

# **Integrated Chassis Control Strategies For Multi-Wheel Combat Vehicle**

by

Moataz Aboelfadl Ahmed

A thesis submitted to the  
School of Graduate and Postdoctoral Studies in partial  
fulfillment of the requirements for the degree of

Doctor of Philosophy in Mechanical Engineering

Department of Automotive and Mechatronics Engineering  
Faculty of Engineering and Applied Science

University of Ontario Institute of Technology (Ontario Tech University)  
Oshawa, Ontario, Canada  
November, 2021

© Moataz Aboelfadl Ahmed ,2021

## THESIS EXAMINATION INFORMATION

Submitted by: **Moataz Aboelfadl Ahmed**

**Doctor of Philosophy (PhD) in Mechanical Engineering**

Thesis title:

**Integrated Chassis Control Strategies for Multi-Wheel Combat Vehicle**

An oral defense of this thesis took place on November 1st, 2021, in front of the following examining committee:

### **Examining Committee:**

Chair of Examining Committee	Dr. Martin Agelin-Chaab
Research Supervisor	Dr. Moustafa El-Gindy
Research Co-supervisor	Dr. Haoxiang Lang
Examining Committee Member	Dr. Jing Ren
Examining Committee Member	Dr. Xianke Lin
University Examiner	Dr. Sheldon Williamson
External Examiner	Dr. Johan Wideberg, University of Seville

The above committee determined that the thesis is acceptable in form and content and that a satisfactory knowledge of the field covered by the thesis was demonstrated by the candidate during an oral examination. A signed copy of the Certificate of Approval is available from the School of Graduate and Postdoctoral Studies



# ABSTRACT

Combat vehicles are exposed to high risks due to their high ground clearance and nature of operation in harsh environments. This requires robust stability controllers to cope with the rapid change and uncertainty of driving conditions on various terrains. Moreover, it is required to enhance vehicle stability and increase safety to reduce accidents' fatality probability. This research focuses on investigating the effectiveness of different lateral stability controllers and their integration in enhancing the cornering performance of an 8x8 combat vehicle when driving at limited handling conditions.

In this research, a new Active Rear Steering (ARS) stability controller for an 8x8 combat vehicle is introduced. This technique is extensively investigated to show its merits and effectiveness for human and autonomous operation. For human operation, the ARS is developed using Linear Quadratic Regulator (LQR) control method, which is compared with previous techniques. Furthermore, the controller is extended and tested for working in a rough and irregular road profile using a novel adaptive Integral Sliding Mode Controller (ISMC). In the case of autonomous operation, a frequency domain analysis is conducted to show the benefits of considering the steering of the rear axles in the path-following performance at different driving conditions. The study compared two different objectives for the controller; the first is including the steering of the rear axles in the path-following controller, while the second is to integrate it as a stability controller with a front-steering path-following controller.

In addition, this research introduces a novel Differential Braking (DB) controller. The proposed control prevents the excessive use of braking forces and consequently the longitudinal dynamic's deterioration. Besides, it introduces an effective DB controller with less dependency and sensitivity to the reference yaw model.

Eventually, two various Integrated Chassis Controllers (ICC) are developed and compared. The first is developed by integrating the ISMC-ARS with the DB controller using a fuzzy logic controller. The second ICC integrates the ISMC-ARS with a developed robust Torque Vectoring Controller (TVC). This integration is designed based on a performance map that shows the effective region of each controller using a new technique based on Machine Learning (ML).

**Keywords:** Chassis control; Lateral stability; Intelligent control; Multi-axle; Combat vehicles

## **AUTHOR'S DECLARATION**

I hereby declare that this thesis consists of original work of which I have authored. This is a true copy of the thesis, including any required final revisions, as accepted by my examiners.

I authorize the Ontario Tech University to lend this thesis to other institutions or individuals for the purpose of scholarly research. I further authorize Ontario Tech University to reproduce this thesis by photocopying or by other means, in total or in part, at the request of other institutions or individuals for the purpose of scholarly research. I understand that my thesis will be made electronically available to the public.

\_\_\_\_\_ Moataz Aboelfadl Ahmed

## STATEMENT OF CONTRIBUTIONS

**Part of the work described in Chapter 2 has been accepted for publication in:**

**Ahmed M**, El-Gindy M, Lang H. "Vehicles Directional Stability Control: Literature Survey." International Journal of Vehicle Systems Modelling and Testing (In press).

**Part of the work described in Chapter 3 has been accepted for publication in:**

**Ahmed M**, Omar M, El-Gindy M. "Investigation of Various Passive Steering Modes for a multi-wheeled Combat Vehicle." International Journal of Vehicle Systems Modelling and Testing (In press).

**Part of the work described in Chapter 4 has been published in:**

**Ahmed M**, El-Gindy M, Lang H, Omar M. "Development of Active Rear Axles Steering Controller For 8X8 Combat Vehicle." SAE Technical Paper 2020-01-0174, 2020, <https://doi.org/10.4271/2020-01-0174>.

**Ahmed M.**, El-Gindy, M. and Lang, H. "A novel adaptive-rear axles steering controller for an 8X8 combat vehicle." Proceedings of the Institution of Mechanical Engineers, Part C: Journal of Mechanical Engineering Science. May 2021. doi:10.1177/09544062211009926

**Ahmed M**, El-Gindy M, Lang H." Path-Following Enhancement of an 8x8 Combat Vehicle Using Different Rear Axles Steering Strategies. Proceedings of the Institution of Mechanical Engineers, Part K: Journal of Multi-body Dynamics. 2021;235(4):539-552. doi:10.1177/14644193211036455

**Part of the work described in Chapter 5 has been published in:**

**Ahmed M**, El-Gindy M, Lang H. "A novel Genetic-programming based differential braking controller for an 8x8 combat vehicle." International Journal of Dynamics and Control. 2020 Dec;8(4):1102–1116. <https://doi.org/10.1007/s40435-020-00693-0>

**Ahmed M**, El-Gindy M, Lang H. "Handling performance of an 8x8 combat vehicle." In IOP Conference Series: Materials Science and Engineering 2020 Nov 1 (Vol. 973, No. 1, p. 012009). IOP Publishing.

**Part of the work described in Chapter 6 has been published in:**

**Ahmed M**, El-Gindy M, Lang H. "Handling performance of an 8x8 combat vehicle." In IOP Conference Series: Materials Science and Engineering 2020 Nov 1 (Vol. 973, No. 1, p. 012009). IOP Publishing.

**Ahmed M**, El-Gindy M, Lang H. "A Novel Coordination method for an Integrated Chassis Controller of an 8x8 Combat Vehicle." SAE Technical Paper No. 22MIL-0009, WCX SAE World Congress Experience, April 5-7, 2022, Detroit, Michigan, USA - (Submitted)

I performed the majority of the synthesis, testing of membrane materials, and writing of the manuscripts.

## ACKNOWLEDGMENTS

I would like to express my special thanks and gratitude to my supervisors, Dr. Moustafa El-Gindy, and Dr. Haoxiang Lang, for their great support and encouragement to conduct this research. Their extensive knowledge and significant experience have not only helped me throughout my research but has also allowed me to overcome any obstacles throughout this process.

I would like appreciatively to acknowledge the Egyptian Ministry of Defense for the financial support extended to this research project.

I wish to express my gratitude to Mark Thompson, Gregoire Chevarie, and Steven Trepanier of General Dynamics Land Systems – Canada (GDLS-Canada) for their continuous technical support during the course of this study.

Furthermore, I would like to thank my colleagues Zeinab El-sayegh, Fatemeh Gheshlaghi, and Mohamed Omar for their support, help, and encouragement.

Last but not least, I would like to express my genuine appreciation to my wife Nancy whom without I wouldn't be able continue this journey. No words can describe my gratitude to my mother for her emotional support and sacrifice. My warmest appreciation to my children Malak and Hamza, your are such a bless.

# TABLE OF CONTENTS

<b>Thesis Examination Information</b>	<b>ii</b>
<b>Abstract</b>	<b>iii</b>
<b>Author's Declaration</b>	<b>iv</b>
<b>Statement of Contributions</b>	<b>v</b>
<b>Acknowledgments</b>	<b>vii</b>
<b>Table of Contents</b>	<b>viii</b>
<b>List of Figures</b>	<b>xi</b>
<b>List of Tables</b>	<b>xxii</b>
<b>List of Symbols</b>	<b>xxiii</b>
<b>List of Abbreviations</b>	<b>xxv</b>
<b>Chapter 1    Introduction</b>	<b>1</b>
1.1    Motivation . . . . .	1
1.2    Objectives . . . . .	2
1.3    Major contributions . . . . .	2
1.4    Thesis outline . . . . .	3
<b>Chapter 2    Literature Review</b>	<b>6</b>
2.1    Introduction . . . . .	6
2.2    Direct yaw control . . . . .	7
2.2.1    Summary on direct yaw control . . . . .	15
2.3    Active steering control . . . . .	16
2.3.1    Summary on active steering control . . . . .	20
2.4    Integrated chassis control . . . . .	21
2.4.1    ICC utilizing top-down method . . . . .	22

2.4.2	ICC utilizing bottom-up method . . . . .	27
2.4.3	Summary on integrated chassis control . . . . .	31
2.5	Lateral dynamic control in path-following application . . . . .	32
2.6	Chapter summary . . . . .	36
<b>Chapter 3</b>	<b>Investigation of Various Passive Steering Modes</b>	<b>39</b>
3.1	Introduction . . . . .	39
3.2	Vehicle model and validation . . . . .	39
3.3	Steering modes . . . . .	40
3.3.1	Conventional front steering mode . . . . .	41
3.3.2	Parallel crab steering mode . . . . .	43
3.3.3	Fixed 3 <sup>rd</sup> axle steering mode . . . . .	43
3.3.4	All-wheel counter steering mode . . . . .	44
3.4	Steering modes evaluation . . . . .	45
3.4.1	Curb-to-Curb test . . . . .	46
3.4.2	Minimum road width test (90-degree turn) . . . . .	48
3.4.3	Closed-loop slalom test . . . . .	50
3.5	Chapter summary . . . . .	56
<b>Chapter 4</b>	<b>Active Rear Axles Steering Controller</b>	<b>58</b>
4.1	Introduction . . . . .	58
4.2	Development of an optimal ARS controller . . . . .	58
4.2.1	Single-track model . . . . .	59
4.2.2	ZSS controller . . . . .	61
4.2.3	Optimal controller design . . . . .	63
4.2.4	Evaluation and simulation results . . . . .	65
4.3	Development of an ARS for rough-rigid terrains operation . . . . .	72
4.3.1	Disturbed single-track model . . . . .	73
4.3.2	The adaptive-ISMC design . . . . .	74
4.3.3	Evaluation and simulation results . . . . .	81
4.4	Active rear axles' steering in path-following application . . . . .	91
4.4.1	Path-follow mathematical models . . . . .	91
4.4.2	$H_\infty$ path-following controllers . . . . .	93
4.4.3	$H_\infty$ -ARS lateral stability controller . . . . .	96
4.4.4	Implementation and frequency domain analysis . . . . .	96

4.4.5	Evaluation and simulation results . . . . .	101
4.5	Chapter summary . . . . .	110
<b>Chapter 5</b>	<b>Direct Yaw Moment Controllers</b>	<b>112</b>
5.1	Introduction . . . . .	112
5.2	Differential braking controllers . . . . .	112
5.2.1	Yaw motion reference model . . . . .	112
5.2.2	Three stages controllers' design . . . . .	114
5.2.3	Evaluation and simulation results . . . . .	123
5.3	Torque vectoring controller . . . . .	130
5.3.1	SMC design . . . . .	130
5.3.2	Evaluation and simulation results . . . . .	132
5.4	Chapter summary . . . . .	137
<b>Chapter 6</b>	<b>Integrated Chassis Controllers</b>	<b>139</b>
6.1	Introduction . . . . .	139
6.2	TVC-ARS integration and coordination . . . . .	139
6.3	ARS-DB integration and coordination . . . . .	143
6.4	Controllers evaluation . . . . .	144
6.4.1	Slalom maneuver . . . . .	144
6.4.2	DLC maneuver . . . . .	150
6.4.3	FMVSS maneuver . . . . .	155
6.4.4	J-turn maneuver . . . . .	159
6.4.5	Increased-step Slalom . . . . .	163
6.5	Chapter summary . . . . .	164
<b>Chapter 7</b>	<b>Conclusions and Future Work</b>	<b>182</b>
7.1	Conclusions . . . . .	182
7.2	Future work and recommendations . . . . .	184
<b>List of Publications</b>		<b>186</b>
<b>List of References</b>		<b>188</b>



## LIST OF FIGURES

Figure 2.1	Relation between corrective moment and vehicle sideslip . . . .	8
Figure 2.2	$\beta - \dot{\beta}$ phase plane . . . . .	8
Figure 2.3	Effect of wheels' braking on the vehicle yaw rate . . . . .	9
Figure 2.4	Control input with (right) and without (left) approximation function	10
Figure 2.5	Scheme of ASMC . . . . .	11
Figure 2.6	IMC Scheme . . . . .	12
Figure 2.7	Upper and lower control scheme as illustrated . . . . .	13
Figure 2.8	Combined $H_\infty$ mixed sensitivity and extension control scheme .	18
Figure 2.9	Rear wheel to front wheel steer ratio in feedforward ZSS . . . .	19
Figure 2.10	MMC schematic diagram . . . . .	19
Figure 2.11	Effective working region of each chassis controller . . . . .	22
Figure 2.12	Combined DYC and ARS using feedback-feedforward controller	23
Figure 2.13	Optimization-based control allocation scheme . . . . .	25
Figure 2.14	Three-level controller method . . . . .	26
Figure 2.15	Coordination using fuzzy logic controller . . . . .	27
Figure 2.16	Controllers configurations . . . . .	29
Figure 2.17	Overview on fuzzy logic controller . . . . .	30
Figure 2.18	G-G diagram . . . . .	36
Figure 3.1	Simulated 22 degrees of freedom vehicle model on TruckSim (a) Front-axle steering (b)8-WS vehicle . . . . .	40
Figure 3.2	The developed passive steering modes . . . . .	41
Figure 3.3	Bicycle model representation of the conventional front steering mode . . . . .	41
Figure 3.4	Conventional front steering (a)1 <sup>st</sup> axle's wheels (b)2 <sup>nd</sup> axle's wheels . . . . .	42
Figure 3.5	Bicycle model representation of the crab steering mode . . . . .	43
Figure 3.6	Fixed 3 <sup>rd</sup> axle steering mode bicycle model representation based on Ackermann . . . . .	44
Figure 3.7	The steering angles of the (a)1 <sup>st</sup> axle's wheels (b)2 <sup>nd</sup> axle's wheels (c)4 <sup>th</sup> axle's wheels with respect to the average steering angle for the fixed 3 <sup>rd</sup> steering mode . . . . .	45

Figure 3.8	All-wheel counter steering mode bicycle model representation based on Ackermann . . . . .	45
Figure 3.9	The steering angles of the (a)1 <sup>st</sup> axle's wheels (b)2 <sup>nd</sup> axle's wheels (c)3 <sup>rd</sup> axle's wheels (d)4 <sup>th</sup> axle's wheels with respect to the average steering angle of the counter steering mode . . . . .	46
Figure 3.10	Trajectory of each steering mode at Curb-to-Curb test . . . . .	47
Figure 3.11	Average steering angles of the (a)1 <sup>st</sup> axle (b)2 <sup>nd</sup> axle (c)3 <sup>rd</sup> axle (d)4 <sup>th</sup> for Curb-to-Curb test . . . . .	48
Figure 3.12	(a) Vehicle longitudinal speed (b) Lateral acceleration (c) Yaw response (d) Vehicle sideslip response for Curb-to-Curb test . . . . .	49
Figure 3.13	Trajectory of each steering mode for 90-degree turn test . . . . .	49
Figure 3.14	Average steering angles of the (a)1 <sup>st</sup> axle (b)2 <sup>nd</sup> axle (c)3 <sup>rd</sup> axle (d)4 <sup>th</sup> for 90-degree turn test . . . . .	50
Figure 3.15	(a) Vehicle longitudinal speed (b) Lateral acceleration (c) Yaw response (d) Vehicle sideslip response for 90-degree turn test . . . . .	51
Figure 3.16	NATO AVTP-1 03-30 slalom course (not in scale) . . . . .	51
Figure 3.17	(a)Trajectory of each steering mode (b) Lateral error from the desired trajectory at for Slalom maneuver at speed 5 km/h . . . . .	52
Figure 3.18	Average steering angles of the (a)1 <sup>st</sup> axle (b)2 <sup>nd</sup> axle (c)3 <sup>rd</sup> axle (d)4 <sup>th</sup> for Slalom maneuver at speed 5 km/h . . . . .	53
Figure 3.19	(a) Vehicle longitudinal speed (b) Lateral acceleration (c) Yaw response (d) Vehicle sideslip response for Slalom maneuver at speed 5 km/h . . . . .	54
Figure 3.20	(a)Trajectory of each steering mode (b) Lateral error from the desired trajectory for Slalom maneuver at speed 50 km/h . . . . .	55
Figure 3.21	Average steering angles of the (a)1 <sup>st</sup> axle (b)2 <sup>nd</sup> axle (c)3 <sup>rd</sup> axle (d)4 <sup>th</sup> for Slalom maneuver at speed 50 km/h . . . . .	55
Figure 3.22	(a) Vehicle longitudinal speed (b) Lateral acceleration (c) Yaw response (d) Vehicle sideslip response for Slalom maneuver at speed 50 km/h . . . . .	56
Figure 4.1	Four-axle steering 8x8 vehicle bicycle model . . . . .	59
Figure 4.2	Figure 2 ZSS controller block diagram . . . . .	63
Figure 4.3	The ratio between 4 <sup>th</sup> and 1 <sup>st</sup> steering axles for zero sideslip condition as a function of forward speed . . . . .	63

Figure 4.4	LQR controller block diagram . . . . .	64
Figure 4.5	Average steering angles of the (a)1 <sup>st</sup> axle (b)2 <sup>nd</sup> axle (c)3 <sup>rd</sup> axle (d)4 <sup>th</sup> for skid-pad test . . . . .	67
Figure 4.6	(a) Vehicle longitudinal speed (b) Lateral acceleration (c) Yaw response (d) Vehicle sideslip response skid-pad test . . . . .	67
Figure 4.7	Vehicle trajectory for FMVSS maneuver at $\mu=0.2$ and speed 60 km/h . . . . .	68
Figure 4.8	Average steering angles of the (a)1 <sup>st</sup> axle (b)2 <sup>nd</sup> axle (c)3 <sup>rd</sup> axle (d)4 <sup>th</sup> for FMVSS maneuver at $\mu=0.2$ and speed 60 km/h . . . . .	69
Figure 4.9	(a) Vehicle longitudinal speed (b) Lateral acceleration (c) Yaw response (d) Vehicle sideslip response for FMVSS maneuver at $\mu=0.2$ and speed 60 km/h . . . . .	70
Figure 4.10	Vehicle trajectory for step slalom test . . . . .	70
Figure 4.11	Illustration of the conventional vehicle in blue in comparison with controlled one in red . . . . .	71
Figure 4.12	Average steering angles of the (a)1 <sup>st</sup> axle (b)2 <sup>nd</sup> axle (c)3 <sup>rd</sup> axle (d)4 <sup>th</sup> for for step slalom test . . . . .	72
Figure 4.13	(a) Vehicle longitudinal speed (b) Lateral acceleration (c) Yaw response (d) Vehicle sideslip response for step slalom test . . . . .	73
Figure 4.14	Genetic programming structure . . . . .	78
Figure 4.15	Mean execution time per step for each time step . . . . .	79
Figure 4.16	Profile of the road surface irregularities in the vertical direction . . . . .	81
Figure 4.17	DLC on a road with $\mu = 0.85$ at speed 100 km/h (a)Vehicle trajectory (b)Lateral error . . . . .	82
Figure 4.18	DLC on a road with $\mu = 0.85$ at speed 100 km/h (a)1 <sup>st</sup> axle average steering angle (b)3 <sup>rd</sup> axle average steering angle (c)4 <sup>th</sup> axle av- erage steering angle . . . . .	83
Figure 4.19	DLC on a road with $\mu = 0.85$ at speed 100 km/h (a)Vehicle lon- gitudinal velocity (b)Lateral acceleration response (c)Yaw rate response (d)Vehicle sideslip response . . . . .	83
Figure 4.20	DLC on a road with $\mu = 0.2$ at speed 60 km/h (a)Vehicle tra- jectory (b)Lateral error . . . . .	84

Figure 4.21 DLC on a road with $\mu = 0.2$ at speed $60 \text{ km/h}$ (a)1 <sup>st</sup> axle average steering angle (b)3 <sup>rd</sup> axle average steering angle (c)4 <sup>th</sup> axle average steering angle . . . . .	85
Figure 4.22 DLC on a road with $\mu = 0.2$ at speed $60 \text{ km/h}$ (a)Vehicle longitudinal velocity (b)Lateral acceleration response (c)Yaw rate response (d)Vehicle sideslip response . . . . .	85
Figure 4.23 Profile of the road surface irregularities . . . . .	86
Figure 4.24 DLC on a road with $\mu = 0.85$ at speed $100 \text{ km/h}$ (a)Vehicle trajectory (b)Lateral error . . . . .	87
Figure 4.25 DLC on a road with $\mu = 0.85$ at speed $100 \text{ km/h}$ (a)1 <sup>st</sup> axle average steering angle (b)3 <sup>rd</sup> axle average steering angle (c)4 <sup>th</sup> axle average steering angle . . . . .	87
Figure 4.26 DLC on a road with $\mu = 0.85$ at speed $100 \text{ km/h}$ (a)Vehicle longitudinal velocity (b)Lateral acceleration response (c)Yaw rate response (d)Vehicle sideslip response . . . . .	88
Figure 4.27 DLC on a road with $\mu = 0.2$ at speed $60 \text{ km/h}$ (a)Vehicle trajectory (b)Lateral error . . . . .	89
Figure 4.28 DLC on a road with $\mu = 0.2$ at speed $60 \text{ km/h}$ (a)1 <sup>st</sup> axle average steering angle (b)3 <sup>rd</sup> axle average steering angle (c)4 <sup>th</sup> axle average steering angle . . . . .	89
Figure 4.29 DLC on a road with $\mu = 0.2$ at speed $60 \text{ km/h}$ (a)Vehicle longitudinal velocity (b)Lateral acceleration response (c)Yaw rate response (d)Vehicle sideslip response . . . . .	90
Figure 4.30 $H_\infty$ Controller block diagram . . . . .	95
Figure 4.31 Controller block diagram of the augmented plant . . . . .	96
Figure 4.32 CLS frequency response of the (a)Lateral error (b)Lateral error integration (c)Control input $\delta_1$ to the reference inputs . . . . .	98
Figure 4.33 (a)Stability and (b)Performance robustness of the front steering CLS . . . . .	98
Figure 4.34 CLS frequency response of the (a)Lateral position tracking (b)Heading angle tracking (c) Lateral error integration (d)Heading angle error integration . . . . .	100
Figure 4.35 CLS frequency response of the control input (a) $\delta_1$ to the reference inputs (b) $\delta_3$ to the reference inputs (c) $\delta_4$ to the reference inputs . .	100

Figure 4.36 (a)Stability and (b)Performance robustness of the AWS CLS . . .	101
Figure 4.37 CLS frequency response of the (a)Lateral velocity (b)Control input $\delta_3$ to the reference inputs (c)Control input $\delta_4$ to the reference inputs	102
Figure 4.38 (a)Stability and (b)Performance robustness of the ARS CLS . . .	102
Figure 4.39 NATO AVTP 03-160 W Double Lane Change setup . . . . .	102
Figure 4.40 (a)Executed trajectory (b) Lateral error . . . . .	103
Figure 4.41 (a)1 <sup>st</sup> axle (b)3 <sup>rd</sup> axle (c)4 <sup>th</sup> axle average steering angle . . . . .	104
Figure 4.42 (a)Forward speed (b) Vehicle lateral acceleration (c) Yaw rate of change (d) Sideslip responses . . . . .	105
Figure 4.43 (a) Executed trajectory (b) Lateral error . . . . .	105
Figure 4.44 (a) Executed trajectory (b) Lateral error . . . . .	106
Figure 4.45 (a)1 <sup>st</sup> axle (b)3 <sup>rd</sup> axle (c)4 <sup>th</sup> axle average steering angle . . . . .	107
Figure 4.46 (a)Forward velocity(b) Vehicle lateral acceleration (c) Yaw rate of change (d) Sideslip responses . . . . .	108
Figure 4.47 (a) Executed trajectory (b) Lateral error . . . . .	109
Figure 4.48 (a)1 <sup>st</sup> axle (b)3 <sup>rd</sup> axle (c)4 <sup>th</sup> axle average steering angle . . . . .	109
Figure 4.49 (a)Forward velocity(b) Vehicle lateral acceleration (c) Yaw rate of change (d) Sideslip responses . . . . .	110
Figure 5.1 Four-axle steering 8x8 vehicle bicycle model . . . . .	113
Figure 5.2 Effect of changing the driving and road conditions on the phase- plane . . . . .	116
Figure 5.3 Stability region at $\dot{\beta}, \beta$ phase-plane to activate the vehicle differ- ential braking controller . . . . .	117
Figure 5.4 ANFS network . . . . .	119
Figure 5.5 Comparison between ANFS output for (a) high dimensional data- set and (b) low dimensional data-set . . . . .	120
Figure 5.6 GA-DB output for low dimensional data-set . . . . .	121
Figure 5.7 Mean execution time per step for each time step . . . . .	121
Figure 5.8 (a) Vehicle trajectory (b) Average Steering angle of the 1 <sup>st</sup> axle for FMVSS maneuver at $\mu=0.2$ and speed 80 km/h . . . . .	124
Figure 5.9 (a) Vehicle longitudinal speed (b) lateral acceleration (c) Yaw response (d) Vehicle sideslip response for FMVSS maneuver at $\mu=0.2$ and speed 80 km/h . . . . .	125

Figure 5.10	Wheels longitudinal slip for FMVSS maneuver at $\mu=0.2$ and speed 80 km/h . . . . .	126
Figure 5.11	(a) Vehicle trajectory (b) Average Steering angle of the 1 <sup>st</sup> axle for DLC maneuver at $\mu=0.2$ and speed 110 km/h . . . . .	126
Figure 5.12	(a) Vehicle longitudinal speed (b) lateral acceleration (c) Yaw response (d) Vehicle sideslip response for DLC maneuver at $\mu=0.2$ and speed 110 km/h . . . . .	127
Figure 5.13	Wheels longitudinal slip for DLC maneuver at $\mu=0.2$ and speed 110 km/h . . . . .	127
Figure 5.14	(a) Vehicle trajectory (b) Average Steering angle of the 1 <sup>st</sup> axle for Slalom maneuver at $\mu=1$ and speed 65 km/h . . . . .	128
Figure 5.15	(a) Vehicle longitudinal speed (b) lateral acceleration (c) Yaw response (d) Vehicle sideslip response for Slalom maneuver at $\mu=1$ and speed 65 km/h . . . . .	128
Figure 5.16	Wheels longitudinal slip for Slalom maneuver at $\mu=1$ and speed 65 km/h . . . . .	129
Figure 5.17	Braking moment for slalom maneuver at $\mu=1$ and speed 65 km/h	129
Figure 5.18	Four-axle steering 8x8 vehicle bicycle model . . . . .	130
Figure 5.19	Double-track vehicle model . . . . .	132
Figure 5.20	FMVSS maneuver at $\mu=0.85$ and speed 80 km/h (a) Vehicle trajectory (b) Close up to the vehicle's lateral shift . . . . .	133
Figure 5.21	FMVSS maneuver at $\mu=0.85$ and speed 80 km/h (a) Vehicle longitudinal speed (b) lateral acceleration (c) Yaw response (d) Vehicle sideslip response . . . . .	134
Figure 5.22	FMVSS maneuver at $\mu=0.2$ and speed 80 km/h (a) Vehicle trajectory (b) Close up to the vehicle's lateral shift . . . . .	135
Figure 5.23	FMVSS maneuver at $\mu=0.2$ and speed 80 km/h (a) Vehicle longitudinal speed (b) lateral acceleration (c) Yaw response (d) Vehicle sideslip response . . . . .	136
Figure 5.24	Slalom maneuver at $\mu=0.85$ and speed 75 km/h (a) Vehicle trajectory (b) Lateral error . . . . .	136
Figure 5.25	Slalom maneuver at $\mu=0.85$ and speed 75 km/h (a) Vehicle longitudinal speed (b) lateral acceleration (c) Yaw response (d) Vehicle sideslip response . . . . .	137

Figure 6.1	Performance map for TVC and ARS with respect to different vehicle's speed and road's coefficient of friction . . . . .	140
Figure 6.2	Neuro-fuzzy representation . . . . .	141
Figure 6.3	Mean execution time per step for each time step . . . . .	142
Figure 6.4	ARS coordination factor with respect to the road friction coefficient	143
Figure 6.5	Road friction membership functions . . . . .	143
Figure 6.6	Slalom maneuver at $\mu=0.85$ and speed 70 km/h (a) Vehicle trajectory (b) Lateral error . . . . .	145
Figure 6.7	Slalom maneuver at $\mu=0.85$ and speed 70 km/h (a) Average Steering angle of the $1^{st} axle$ (b) Average Steering angle of the $3^{rd} axle$ (c) Average Steering angle of the $4^{th} axle$ . . . . .	146
Figure 6.8	Slalom maneuver at $\mu=0.85$ and speed 70 km/h (a) Vehicle longitudinal speed (b) lateral acceleration (c) Yaw response (d) Vehicle sideslip response . . . . .	146
Figure 6.9	Slalom maneuver at $\mu=0.85$ and speed 70 km/h; Corrective driving torque of the right and left wheels' side . . . . .	147
Figure 6.10	Slalom maneuver at $\mu=0.85$ and speed 70 km/h; Braking forces at each wheel . . . . .	148
Figure 6.11	Slalom maneuver at $\mu=0.5$ and speed 50 km/h (a) Vehicle trajectory (b) Lateral error . . . . .	149
Figure 6.12	Slalom maneuver at $\mu=0.5$ and speed 50 km/h (a) Average Steering angle of the $1^{st} axle$ (b) Average Steering angle of the $3^{rd} axle$ (c) Average Steering angle of the $4^{th} axle$ . . . . .	149
Figure 6.13	Slalom maneuver at $\mu=0.5$ and speed 50 km/h (a) Vehicle longitudinal speed (b) lateral acceleration (c) Yaw response (d) Vehicle sideslip response . . . . .	150
Figure 6.14	Slalom maneuver at $\mu=0.5$ and speed 50 km/h; Corrective driving torque of the right and left wheels' side . . . . .	151
Figure 6.15	Slalom maneuver at $\mu=0.5$ and speed 50 km/h; Braking forces at each wheel . . . . .	152
Figure 6.16	Slalom maneuver at $\mu=0.2$ and speed 30 km/h (a) Vehicle trajectory (b) Lateral error . . . . .	153

Figure 6.17 Slalom maneuver at $\mu=0.2$ and speed 30 km/h (a) Average Steering angle of the 1 <sup>st</sup> axle (b) Average Steering angle of the 3 <sup>rd</sup> axle (c) Average Steering angle of the 4 <sup>th</sup> axle . . . . .	153
Figure 6.18 Slalom maneuver at $\mu=0.2$ and speed 30 km/h (a) Vehicle longitudinal speed (b) lateral acceleration (c) Yaw response (d) Vehicle sideslip response . . . . .	154
Figure 6.19 Slalom maneuver at $\mu=0.2$ and speed 30 km/h; Corrective driving torque of the right and left wheels' side . . . . .	155
Figure 6.20 Slalom maneuver at $\mu=0.2$ and speed 30 km/h; Braking forces at each wheel . . . . .	156
Figure 6.21 DLC maneuver at $\mu=0.85$ and speed 100 km/h (a) Vehicle trajectory (b) Lateral error . . . . .	157
Figure 6.22 DLC maneuver at $\mu=0.85$ and speed 100 km/h (a) Average Steering angle of the 1 <sup>st</sup> axle (b) Average Steering angle of the 3 <sup>rd</sup> axle (c) Average Steering angle of the 4 <sup>th</sup> axle . . . . .	157
Figure 6.23 DLC maneuver at $\mu=0.85$ and speed 100 km/h (a) Vehicle longitudinal speed (b) lateral acceleration (c) Yaw response (d) Vehicle sideslip response . . . . .	158
Figure 6.24 DLC maneuver at $\mu=0.85$ and speed 100 km/h; Corrective driving torque of the right and left wheels' side . . . . .	159
Figure 6.25 DLC maneuver at $\mu=0.85$ and speed 100 km/h; Braking forces at each wheel . . . . .	160
Figure 6.26 DLC maneuver at $\mu=0.5$ and speed 100 km/h (a) Vehicle trajectory (b) Lateral error . . . . .	161
Figure 6.27 DLC maneuver at $\mu=0.5$ and speed 100 km/h (a) Average Steering angle of the 1 <sup>st</sup> axle (b) Average Steering angle of the 3 <sup>rd</sup> axle (c) Average Steering angle of the 4 <sup>th</sup> axle . . . . .	161
Figure 6.28 DLC maneuver at $\mu=0.5$ and speed 100 km/h (a) Vehicle longitudinal speed (b) lateral acceleration (c) Yaw response (d) Vehicle sideslip response . . . . .	162
Figure 6.29 DLC maneuver at $\mu=0.5$ and speed 100 km/h; Corrective driving torque of the right and left wheels' side . . . . .	163
Figure 6.30 DLC maneuver at $\mu=0.5$ and speed 100 km/h; Braking forces at each wheel . . . . .	164



Figure 6.31	DLC maneuver at $\mu=0.2$ and speed 100 km/h (a) Vehicle trajectory (b) Lateral error . . . . .	165
Figure 6.32	DLC maneuver at $\mu=0.2$ and speed 100 km/h (a) Average Steering angle of the 1 <sup>st</sup> axle (b) Average Steering angle of the 3 <sup>rd</sup> axle (c) Average Steering angle of the 4 <sup>th</sup> axle . . . . .	165
Figure 6.33	DLC maneuver at $\mu=0.2$ and speed 100 km/h (a) Vehicle longitudinal speed (b) lateral acceleration (c) Yaw response (d) Vehicle sideslip response . . . . .	166
Figure 6.34	FMVSS maneuver at $\mu=0.85$ and speed 100 km/h (a) Vehicle trajectory (b) Close up to the vehicle's lateral shift . . . . .	167
Figure 6.35	FMVSS maneuver at $\mu=0.85$ and speed 100 km/h (a) Average Steering angle of the 1 <sup>st</sup> axle (b) Average Steering angle of the 3 <sup>rd</sup> axle (c) Average Steering angle of the 4 <sup>th</sup> axle . . . . .	167
Figure 6.36	FMVSS maneuver at $\mu=0.85$ and speed 100 km/h (a) Vehicle longitudinal speed (b) lateral acceleration (c) Yaw response (d) Vehicle sideslip response . . . . .	168
Figure 6.37	FMVSS maneuver at $\mu=0.85$ and speed 100 km/h; Corrective driving torque of the right and left wheels' side . . . . .	168
Figure 6.38	FMVSS maneuver at $\mu=0.85$ and speed 100 km/h; Braking forces at each wheel . . . . .	169
Figure 6.39	FMVSS maneuver at $\mu=0.5$ and speed 100 km/h (a) Vehicle trajectory (b) Close up to the vehicle's lateral shift . . . . .	169
Figure 6.40	FMVSS maneuver at $\mu=0.5$ and speed 100 km/h (a) Average Steering angle of the 1 <sup>st</sup> axle (b) Average Steering angle of the 3 <sup>rd</sup> axle (c) Average Steering angle of the 4 <sup>th</sup> axle . . . . .	170
Figure 6.41	FMVSS maneuver at $\mu=0.5$ and speed 100 km/h (a) Vehicle longitudinal speed (b) lateral acceleration (c) Yaw response (d) Vehicle sideslip response . . . . .	170
Figure 6.42	FMVSS maneuver at $\mu=0.5$ and speed 100 km/h; Corrective driving torque of the right and left wheels' side . . . . .	171
Figure 6.43	FMVSS maneuver at $\mu=0.2$ and speed 100 km/h (a) Vehicle trajectory (b) Close up to the vehicle's lateral shift . . . . .	171

Figure 6.44 FMVSS maneuver at $\mu=0.2$ and speed 100 km/h (a) Average Steering angle of the 1 <sup>st</sup> axle (b) Average Steering angle of the 3 <sup>rd</sup> axle (c) Average Steering angle of the 4 <sup>th</sup> axle . . . . .	172
Figure 6.45 FMVSS maneuver at $\mu=0.2$ and speed 100 km/h (a) Vehicle longitudinal speed (b) lateral acceleration (c) Yaw response (d) Vehicle sideslip response . . . . .	172
Figure 6.46 J-turn maneuver at $\mu=0.85$ and speed 100 km/h (a) Vehicle trajectory (b) Close up to the vehicle's lateral shift . . . . .	173
Figure 6.47 J-turn maneuver at $\mu=0.85$ and speed 100 km/h (a) Average Steering angle of the 1 <sup>st</sup> axle (b) Average Steering angle of the 3 <sup>rd</sup> axle (c) Average Steering angle of the 4 <sup>th</sup> axle . . . . .	173
Figure 6.48 J-turn maneuver at $\mu=0.85$ and speed 100 km/h (a) Vehicle longitudinal speed (b) lateral acceleration (c) yaw response (d) vehicle sideslip response . . . . .	174
Figure 6.49 J-turn maneuver at $\mu=0.85$ and speed 100 km/h; Corrective driving torque of the right and left wheels' side . . . . .	174
Figure 6.50 J-turn maneuver at $\mu=0.85$ and speed 100 km/h; Braking forces at each wheel . . . . .	175
Figure 6.51 J-turn maneuver at $\mu=0.5$ and speed 100 km/h (a) Vehicle trajectory (b) Close up to the vehicle's lateral shift . . . . .	175
Figure 6.52 J-turn maneuver at $\mu=0.5$ and speed 100 km/h (a) Average Steering angle of the 1 <sup>st</sup> axle (b) Average Steering angle of the 3 <sup>rd</sup> axle (c) Average Steering angle of the 4 <sup>th</sup> axle . . . . .	176
Figure 6.53 J-turn maneuver at $\mu=0.5$ and speed 100 km/h (a) Vehicle longitudinal speed (b) lateral acceleration (c) Yaw response (d) Vehicle sideslip response . . . . .	176
Figure 6.54 J-turn maneuver at $\mu=0.5$ and speed 100 km/h; Corrective driving torque of the right and left wheels' side . . . . .	177
Figure 6.55 J-turn maneuver at $\mu=0.2$ and speed 100 km/h (a) Vehicle trajectory (b) Close up to the vehicle's lateral shift . . . . .	177
Figure 6.56 J-turn maneuver at $\mu=0.2$ and speed 100 km/h (a) Average Steering angle of the 1 <sup>st</sup> axle (b) Average Steering angle of the 3 <sup>rd</sup> axle (c) Average Steering angle of the 4 <sup>th</sup> axle . . . . .	178

Figure 6.57 J-turn maneuver at $\mu=0.2$ and speed 100 km/h (a) Vehicle longitudinal speed (b) lateral acceleration (c) Yaw response (d) Vehicle sideslip response . . . . .	178
Figure 6.58 Step slalom maneuver at $\mu=1$ and speed 65 km/h . . . . .	179
Figure 6.59 Step slalom maneuver at $\mu=1$ and speed 65 km/h (a) Average Steering angle of the 1 <sup>st</sup> axle (b) Average Steering angle of the 3 <sup>rd</sup> axle (c) Average Steering angle of the 4 <sup>th</sup> axle . . . . .	179
Figure 6.60 Step slalom maneuver at $\mu=1$ and speed 65 km/h (a) Vehicle longitudinal speed (b) lateral acceleration (c) Yaw response (d) Vehicle sideslip response . . . . .	180
Figure 6.61 Step slalom maneuver at $\mu=1$ and speed 65 km/h; Corrective driving torque of the right and left wheels' side . . . . .	180
Figure 6.62 Step slalom maneuver at $\mu=1$ and speed 65 km/h; Braking forces at each wheel . . . . .	181

## LIST OF TABLES

Table 3.1	Low-speed Slalom test summary . . . . .	53
Table 4.1	Path-following controllers weighted functions . . . . .	97
Table 4.2	Controllers design parameters . . . . .	101
Table 5.1	Fuzzy rules for $(i)^{th}$ right side . . . . .	123
Table 5.2	Fuzzy rules for vehicle's wheels right side . . . . .	123
Table 6.1	GP solution statistics . . . . .	142

# LIST OF SYMBOLS

Symbol	Description	Unit
$\alpha_i$	Slip angle of $i^{th}$ tire	$rad$
$\beta$	Vehicle sideslip	$rad$
$\delta_i$	Average steering angle of $i^{th}$ tire	$rad$
$\epsilon_{p_i}$	Tuning parameter that controls the maximum desired error	--
$\epsilon_{u_i}$	Tuning parameter that controls the maximum control gain	--
$\rho$	Path curvature	$1/m$
$\theta$	Vehicle heading angle	$rad$
$\bar{\sigma}$	Singular value	--
$\omega_{p_i}$	Differences between the upper and lower cut-off frequencies for the system	$Hz$
$\omega_{u_i}$	Differences between the upper and lower cut-off frequencies for the control input	$Hz$
$\mu$	Road coefficient of friction	--
$\rho$	Tuning positive scalar	--
$a_i$	Distance between vehicle Center of Gravity $i^{th}$ axle	$m$
$A$	System states matrix	--
$B$	System Input matrix	--
$c_{ij}$	Steering ratio between the average steering angle of the $i^{th}$ to the $j^{th}$ axles	--
$C_{\alpha_i}$	Cornering stiffness of $i^{th}$ tire	$kN/rad$
$e$	Augmented plant controller input	--
$F_1$	Lower fractional transformation	--
$F_{xi}$	Longitudinal (tractive) force on $i^{th}$ tire	$kN$
$F_{yi}$	Lateral forces on $i^{th}$ tire	$kN$
$F_{zi}$	Vertical force on $i^{th}$ tire	$kN$
$G_{aug}$	Augmented/interconnected plant	--
$I_{zz}$	Vehicle's mass moment of inertia about the Z axis	$kg.m^2$
$K$	Controller gain	--
$M_{p_i}$	System maximum sensitivity	--

$M_{ui}$	Maximum control input gain	--
$m_u$	Number of control inputs	--
$m$	Vehicle mass	$kg$
$n_{pi}$	Parameter that control the performance weight function steep	--
$n_u^i$	Parameter that control the controller weight function steep	--
$P$	Positive definite matrix	--
$Q$	States weight matrix	--
$r$	Vehicle yaw rate	$rad/s$
$r_d$	Desired yaw rate	$rad/s$
$R$	Control input weight matrix	--
$u$	Controller output or system control input	--
$U$	Vehicle longitudinal velocity	$m/s$
$V$	Vehicle lateral velocity	$m/s$
$W_p$	Performance weight function	--
$W_u$	Control weight function	--
$w$	Augmented plant inputs	--
$x$	System states	--
$X_1$	Maximum allowed error in tracking the desired vehicle sideslip	$rad$
$X_2$	Maximum allowed error in tracking the desired yaw rate	$rad/s$
$X$	Desired path X-coordinates	$m$
$X$	State vector	--
$Y$	Desired path Y-coordinates	$m$
$Y_1$	Maximum steering angles for the 4 <sup>th</sup> axle	$rad$
$Y_2$	Maximum steering angles for the 3 <sup>rd</sup> axle	$rad$
$z$	Augmented plant output	--

## LIST OF ABBREVIATIONS

<i>AFS</i>	Active Front Steer
<i>ARS</i>	Active Rear Steer
<i>ASC</i>	Active Steering Control
<i>AWS</i>	All Wheel Steer
<i>CoF</i>	Coefficient of Friction
<i>CG</i>	Center of Gravity
<i>DYC</i>	Direct Yaw Control
<i>DB</i>	Differential Braking
<i>DLC</i>	Double Lane Change
<i>ESC</i>	Electronic Stability Control
<i>FMVSS</i>	Federal Motor Vehicle Safety Standards
<i>IAW</i>	In Accordance With
<i>ICC</i>	Integrated Chassis Control
<i>ISMC</i>	Integral Sliding Mode Control
<i>NF</i>	Neuro-Fuzzy
<i>NF</i>	Neural Network
<i>NHTSA</i>	National Highway Traffic Safety Administration
<i>GA</i>	Genetic Algorithm
<i>GP</i>	Genetic Programming
<i>LPV</i>	Linear Parameter Varying
<i>LQR</i>	Linear Quadratic Regulator
<i>LTl</i>	Linear Time Invariant
<i>MPC</i>	Model Predictive Control

<i>SMC</i>	Sliding Mode Control
<i>TOP</i>	Test Operations Procedures
<i>VMT</i>	Vehicle Miles Traffic
<i>ZSS</i>	Zero Side Slip



# CHAPTER 1

## Introduction

### 1.1 Motivation

Multi-axles vehicles are widely used in the military field due to the better distribution of the vehicle weight over the wheelbase. Furthermore, it provides better reliability because of its capability of enduring problems such as tire damage or perforation, so the vehicle can operate effectively with such problems. Despite these advantages, multi-axles combat vehicles have a tendency to rollover compared to conventional 2-axles vehicles, as a result of their higher ground clearance and center of gravity. Besides, its nature of operation in harsh environments and off-road driving conditions that need higher safety standards and ensuring stability.

The motivation of this research is to enhance the handling performance and stability of multi-axles combat vehicles to reduce accidents possibility and fatality of the cabin crew. Accordingly, several active chassis control approaches will be investigated at normal and severe driving conditions to attain the desired objectives utilizing various actuators allocation.

Nowadays, many safety features are commercially available for safety-demand such as Anti-lock Braking System (ABS), Electronic Stability Control (ESC) or Vehicle Stability Control (VSC), Active Suspension (AS) systems, Traction Control Systems (TCS), lane departure warning, and so on. These systems aim to maximize the driver's control in normal driving conditions and support him with aids at severe maneuvers. Thanks to these and other systems, in (2019) National Highway Traffic Safety Administration (NHTSA) reported that the fatality rate per 100 million Vehicle Miles Traffic (VMT) decreases by 66 % since 1975 [1]. In addition, ESC shows the ability to decrease the road fatalities ratio by 0.25, drifting from the road by 0.4, and vehicle's tip over by 0.5 [2]. Notwithstanding, it was reported that around 5 % of the crashes related to the vehicle failure and the weather condition [3].

## 1.2 Objectives

The objectives of this thesis work include:

- Examining the vehicle's maneuverability for multiple passive steering configurations at very low speed for different maneuver courses.
- Presenting a new approach using Active Rear Steering (ARS) without a yaw reference model and comparing it with the existing techniques.
- Investigate the merits of ARS in terms of; enhancing the vehicle's lateral stability with and without considering the road's irregularities, and the incorporation of ARS for path-following application.
- Introducing a differential braking control strategy based on an activation criterion to avoid the drop in vehicle's speed associated with the excessive use of the braking torque.
- Designing a robust Direct Yaw Controller (DYC) using a Torque Vectoring Control (TVC) as allocation strategy.
- Developing and testing different Integrated Chassis Control (ICC) methods at limited handling driving conditions.

## 1.3 Major contributions

The major contributions of this research are as follows:

1. A novel investigation approach of the multi-wheeled vehicle maneuverability was introduced.
2. A new approach of developing a lateral stability controller was introduced using the interdependent steering of the rear axles with zero reference model, which eliminated the controller dependency on the reference model.
3. A novel ARS based on AISMC was developed to ensure minimum use of the actuator, smooth operation, and high stability for rough-rigid road operation.
4. A frequency domain analysis was conducted to show the advantages of incorporating the steering of the rear axles in a path-following application and to give an

insight for the best utilization of the rear axles.

5. A novel GP-based DB controller was designed that needs a low-dimension dataset for training and ensured continuous output in comparison with a neuro-fuzzy-based controller.
6. A new comprehensive performance map was developed, which showed the effective operating conditions of different controllers.
7. A novel coordinator controller based on GP optimization that significantly decreased the processing time in comparison with the fuzzy rules was developed.

## 1.4 Thesis outline

Chapter 2 presents a comprehensive literature review of the most recent research studies that have been done in the field of vehicles' lateral stability. The importance of implementing lateral stability controllers such as DYC, which includes differential braking and TVC, and active steering stability controllers have been discussed. Besides, methods of integrating different chassis controllers were reviewed in detail. Also, an overview on considering stability controllers for autonomous vehicles is presented. Eventually, the gaps in the reviewed research works were summarized at the end.

In chapter 3, the configuration of the 8x8 combat vehicle that was utilized in this research was introduced. Then, the maneuverability of the vehicle was assessed and compared with various passive steering configurations; parallel (crab) All-Wheel Steering (AWS), counter AWS, and 3-axes steering with fixed 3<sup>rd</sup> axle. The chapter presents the advantages and limitations of each controller using standard maneuvers such as curb-to-curb, minimum road width, constant step slalom and Nato double lane change (DLC). Finally, the steering configurations' limitations at high speed were examined by conducting a slalom maneuver.

Chapter 4 investigates the influence of incorporating the steering of the rear axle on the vehicle performance in the case of conventional and autonomous driving. For conventional driving, a new approach for ARS stability controller is introduced in chapter 4. This approach utilizes a Linear Quadratic Regulator (LQR) controller that uses the independent steering of the rear 3<sup>rd</sup> and 4<sup>th</sup> axles to maximize its effect in the ARS controller. Besides, a feedforward ARS system is integrated with the developed LQR

controller for low-speed operation only. The feedforward ARS objective is to ensure a Zero Side Slip (ZSS) at a speed below  $20 \text{ km/h}$ . The integrated controller is compared with an LQR ARS that utilizes the steering of the rear  $4^{th}$  axle with a fixed  $3^{rd}$  axle and an AWS-ZSS controller, which were presented previously in [4, 5].

After that, a novel Adaptive ARS controller is developed for driving on a hard road with irregularities. Based on the developed LQR-ARS controller, an Integral Sliding Mode Control (ISMC) is developed to stabilize the vehicle when driving on a rough-rigid road. The ISMC utilizes the integration of a linear controller with a nonlinear control term. A gain-scheduled LQR controller is used instead of the linear term, where the scheduled gains are optimized by the Genetic Algorithm (GA) using a new synthesized cost function. Furthermore, the scheduled gains are replaced by equations to ensure a smooth transition between the operating points where Genetic-Programming (GP) is used to derive these equations. The developed controller is tested against the uncontrolled (conventional) vehicle and traditional LQR-ARS controller.

In order to investigate the advantages of incorporating the steering of the rear axles for autonomous operation, a frequency domain analysis is conducted later in chapter 4. In addition, the integration of a stability-ARS system with a path-following controller that utilizes a front-steering is compared with a path-following AWS controller.  $H_\infty$  control theory is used to develop the aforementioned controllers with considering uncertain vehicle's velocity.

In chapter 5, two Direct Yaw Moment (DYC) are developed. The first is a novel Differential Braking (DB) controller that is developed using machine learning control theory. Neuro-Fuzzy (NF) is used to generate the control rules using a high-dimension dataset that is obtained from a series of simulations. The NF controller is compared with a GP-based controller that used a low-dimension dataset in the training process. The second controller is a hierarchical-TVC. The controller consists of high-level and low-level controllers. The high-level controller is designed based on conventional SMC theory to generate a corrective moment to stabilize the vehicle. The low-controller level is used to allocate this corrective moment to the vehicle's driving torque, which is distributed on the right and left wheels' sides based on the friction circle. In addition, the importance of considering the vehicle's sideslip in the control design to enhance the controller's performance is presented.

In chapter 6, two ICCs are introduced and their performance is evaluated versus the conventional uncontrolled vehicle. The first ICC exploits the integration of the ARS with TVC, where a novel coordination controller that is developed by a GP optimization technique is used for the integration. The developed GP-coordinator is trained on a dataset that presents a performance map, which presents the effective operating region of ARS and TVC controllers for various driving speeds and different roads' coefficient of frictions. The second ICC utilizes the integration of the ARS with the DB controller using fuzzy rules based on the road friction coefficient.

Finally in chapter 7, the conclusions, future work, major contributions from this research, list of refereed journals and conferences papers are presented.

## CHAPTER 2

### Literature Review

#### 2.1 Introduction

In 2018, Singh [3] mentioned in a technical report that most vehicle accidents occur while negotiating a maneuver or avoiding an obstacle. Therefore, a large number of published studies considering the vehicles handling stability or so-called lateral stability are performed. These studies were introduced to enhance the vehicles' directional performance by controlling either the vehicles' sideslip and/or yaw rate. A review study was conducted by Manning and Crolla [6] in 2007 on the yaw rate and sideslip controllers. The study showed that controlling the yaw rate reinforces the driver's feeling of confidence when handling the vehicle while controlling the vehicle sideslip has more influence on the vehicle stability. Commonly, the lateral dynamics are controlled using two methodologies. The first method is Direct Yaw Control (DYC), in which an external yaw moment is applied to the vehicle to limit its yaw motion or meet a desired yaw signal. This moment can be developed by manipulating the traction/braking forces on the vehicle's right and left wheels. The second method is Active Steering Control (ASC) systems, where an additional lateral force can be generated by actively steering the front and/or rear axle's wheels.

Integrated Chassis Control (ICC) systems have been developed to combine multiple objectives. The objectives of delivering a better driving feeling and improving vehicle stability by integrating the DYC and the ASC systems. The integration of these two methods is usually done by using either top-down or bottom-up techniques. In the top-down technique, all controllers and actuators are considered in a high-level controller that generates the control actions. However, in most cases, a lower-level controller is needed to transform the control inputs into an actuation. This controller is known as the allocation controller. On the other hand, in the Bottom-up technique, all controller is designed separately and a lower-level controller is developed to prevent the interference between each control action, and arrange the actuation signals, which is known as a coordination controller [6].

In this research, previous studies on controlling the ground vehicles' lateral dynamics using DYC and ASC will be reviewed. Furthermore, the method of integration of both controllers will be illustrated to define the state of art and lack in the published work. Subsequently, consideration of lateral dynamic and stability control in path tracking applications will be presented.

## 2.2 Direct yaw control

All-wheel drive vehicles provide traction for the front and rear wheels. In the case of cornering, any loss of traction at the front wheels will increase the chance of oversteering. In contrast, a loss of traction at the rear wheels exposes the vehicle to understeer. Both cases could occur near the traction limit while driving in severe conditions. This situation is called limit handling conditions. In a study done by Shibahata et al. 1993 [7],  $\beta$ -method was introduced. This method introduced vehicle stability as a function of its sideslip and the tires' slip angles. Based on that relation, a corrective moment was determined for different steering angles and longitudinal acceleration as shown in figure 2.1. The corrective moment was then allocated through the distribution of the traction/braking torque between the right and left wheels of the rear axle based on the lateral and longitudinal acceleration. In another study in 1995 on DYC and its effect on vehicle stability, Ikushima and Sawase [8] studied the feasibility of using a new torque distribution technique utilizing Continuous Variable Transmission (CVT)-based differential, which was mounted on the rear axle. This technique aimed to decrease the energy losses that the existed differentials at this time were suffering from. Then, to generate the required corrective moment, a feedback Proportional-Integral (PI) controller was used. The proposed method was able to improve the vehicle handling performance in terms of reducing the sideslip and the yaw rate at high speed and efficiently increasing the limit of lateral acceleration.

A more efficient method to address the vehicle's stability was introduced in 1995 by Inagaki et al. [9]. The authors utilized phase-plane nonlinear analysis to introduce the  $\beta - \dot{\beta}$  phase plane method. This method defined a stability region as in figure 2.2, where the vehicle is stable and the sideslip  $\beta$  and sideslip rate  $\dot{\beta}$  satisfies equation 2.1, where  $A$  and  $B$  are constants.

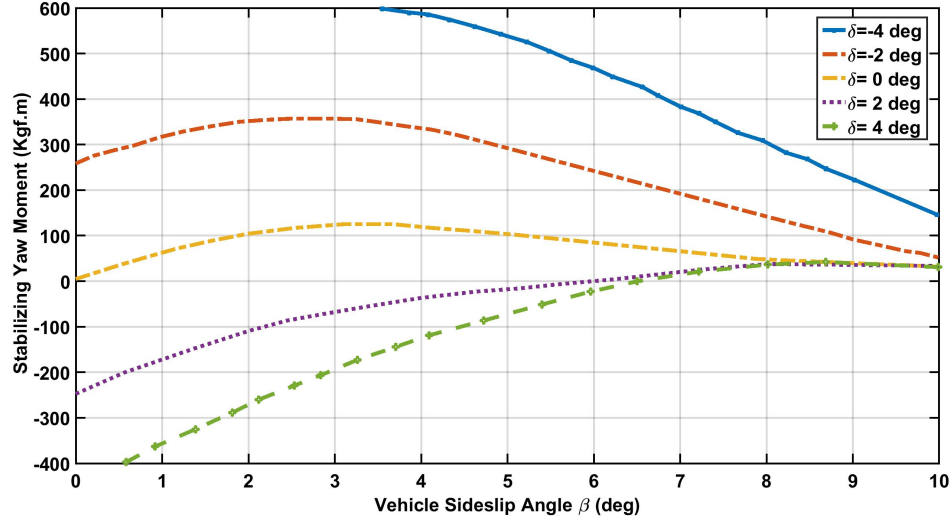


Figure 2.1: Relation between corrective moment and vehicle sideslip at different front steering angles[7]

$$|A\dot{\beta} + B\beta| < 1 \quad (2.1)$$

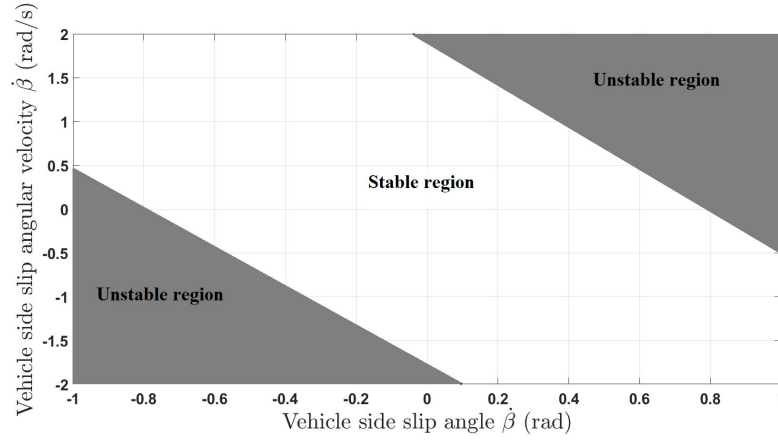


Figure 2.2:  $\beta - \dot{\beta}$  phase plane [9]

Koibuchi et al. [10] used this method later in 1996 within a study on the effectiveness of braking an individual wheel on the generated corrective yaw moment required to stabilize the vehicle. The study showed that braking inner-rear and outer-front has the maximum effect in producing inward and outward yaw moments, respectively, as shown in figure 2.3. The study showed that the vehicle stability and handling improved but with



deteriorating the longitudinal performance. A similar braking scheme was introduced in 2000 by Youn and Song [11] based on feedback Proportional-Derivative (PD) controller. The controller was used to generate the required corrective moment to stabilize the vehicle and follow the desired yaw signal. After that, a lower controller was used to generate this corrective moment using the braking forces based on two stability factors. The first was obtained based on the  $\beta - \dot{\beta}$  method, while the second was determined based on the yaw rate error that implies whether the vehicle follows the driver's commands or not. The proposed controller prevented the vehicle from losing its stability. Nevertheless, the stability index was highly dependent on the estimation of the road friction coefficient, which was not considered in the study.

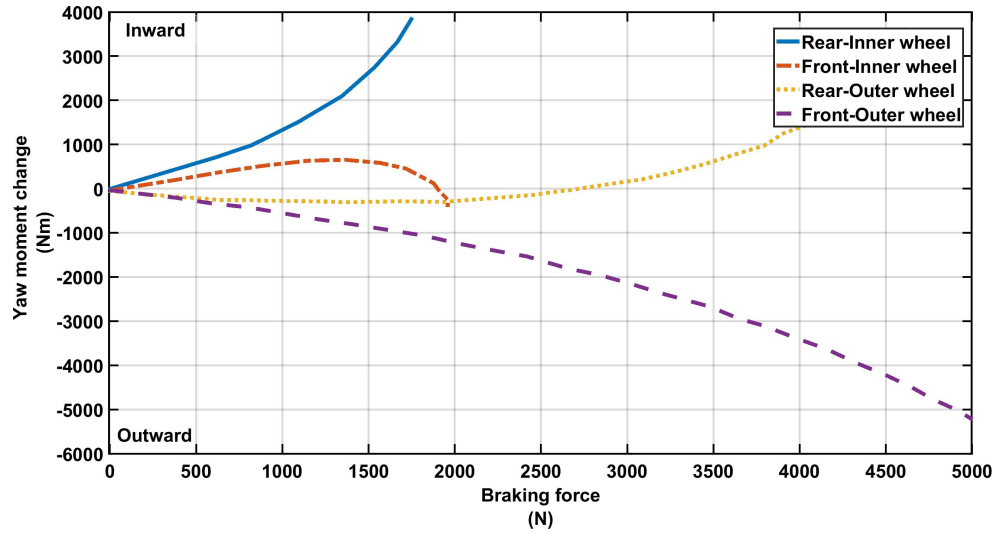


Figure 2.3: Effect of wheels' braking on the vehicle yaw rate [10]

The contentious variation in driving conditions and vehicle parameters, e.g road friction, vehicle velocity, and weight, required a robust controller to accommodate these variations and modelling uncertainty. For this reason, a Sliding Mode Controller (SMC) was adopted in several studies as it was known for its robustness against model uncertainty and bounded disturbance. An SMC based on two degrees of freedom (2-DOF) model was introduced in 1999 by Abe et al. [12] utilizing  $\beta - \dot{\beta}$  method. In that study, the SMC was used to generate the desired corrective moment to stabilize the vehicle. The corrective moment was then allocated by generating an additional driving force to one wheel and braking force to the opposite one. Further, in 2003, Yi et al. [13] compared a simple DYC with an SMC-DYC based on a 2-DOF model that utilized the wheels'

braking pressure. The study showed that it was more efficient to include the yaw rate and vehicle sideslip in the sliding surface design. It has been found that the proposed controller gave smoother and better lateral performance than simple DYC.

Generally, SMC offers a robust solution for modelling uncertainties and disturbance by introducing discontinuous control term [14], which did not consider in the previous studies. However, by adding this term the controller will suffer from the chattering phenomena, which add difficulties in practical implementation. One method to get rid of this phenomenon is using approximation and saturation functions to smooth the output, as shown in figure 2.4. However, using this approximation makes the error convergence time not guaranteed, which is known as quasi-SMC [15].

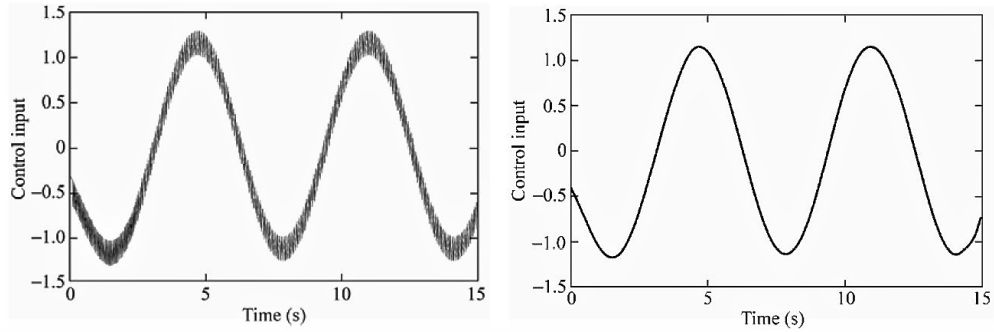


Figure 2.4: Control input with (right) and without (left) approximation function [16]

In 2007, Zhao et al. [17] introduced a quasi-SMC to track a reference yaw rate and sideslip at steady-state driving condition utilizing the braking/driving forces using similar distribution as in [13]. They included the roll motion in the control design using a 4-DOF model. Furthermore, a frequency-based sideslip estimator was introduced by combining kinematic and dynamic-based estimators. In SMC, it was assumed that knowledge about the uncertain dynamics was available, which is not always valid. Therefore, a simulation-based study was introduced by Asiabar et al. in 2019 [18] using Adaptive-SMC (ASMC), as shown in figure 2.5. The adaptation role was developed based on the estimated tires' cornering stiffness, which didn't require information about the uncertainties bounds. The proposed controller was tested on a four-in-wheel electric motors vehicle, which gave good stability and lateral performance. However, the implementation of the real vehicle was not verified. In 2020, Li et al. [19] proposed an ASMC to control the wheel's driving torque of an electric vehicle. The controller was designed to cope with the vehicle and tires parameters uncertainties due to the continuous change in

the tires' vertical load.

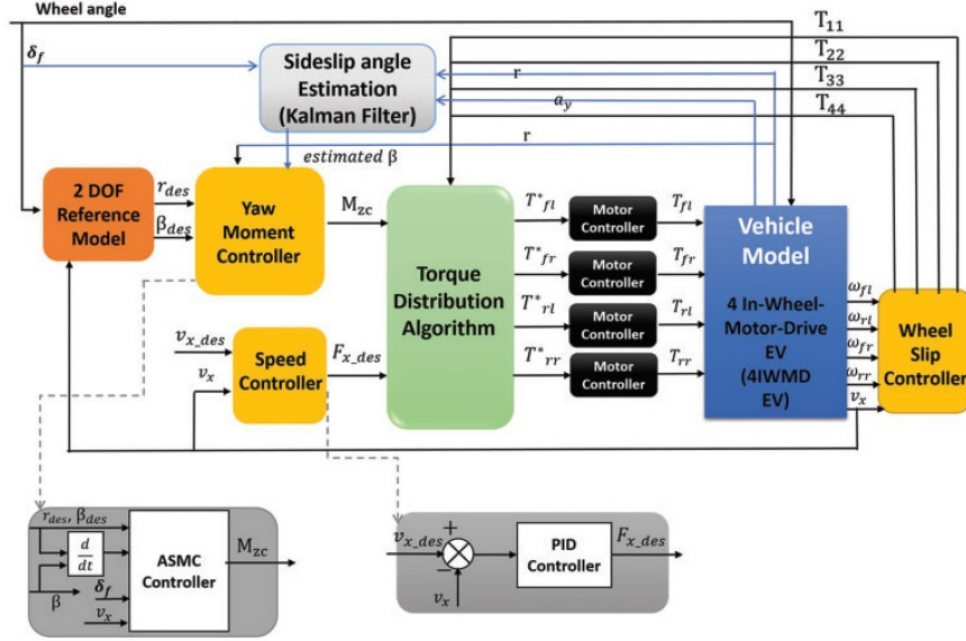


Figure 2.5: Scheme of ASMC as proposed by Asiabar et al. [18]

An alternate method that offers robustness against uncertain vehicle parameters and unmodeled dynamics is Linear parametric Variable (LPV)-based controllers, in which any uncertain or varied parameter can be considered in the LPV model. Then, the control gains are scheduled based on these parameters. In 2015, an LPV- $H_\infty$  controller was introduced by Raharijaona et al. [20] based on a 2-DOF bicycle model considering various longitudinal speeds. The control objective was the rejection of side wind effects in normal driving conditions to assist the driver in keeping the desired path. Better stability was obtained by the controller when compared with conventional  $H_\infty$  control methodology.

In a study introduced in 2008, an  $H_\infty$ -based Internal Model Controller (IMC) was compared with SMC by Canale et al. [21]. IMC controller offered robustness besides the ability to handle the actuator saturation using an anti-windup method, as showed in figure 2.6. A reference model based on a nonlinear tire model was introduced to improve the transient response of the vehicle. Furthermore, the proposed IMC controller considered the vehicle model uncertainty as a transfer function, which was determined from simulations using a 14-DOF nonlinear model. The results showed that both IMC and

SMC controllers gave a good transient performance and small tracking error. However, the behaviour on a low coefficient of friction road was not evaluated and the uncontrolled vehicle offered better performance in braking in turn maneuver at high speed.

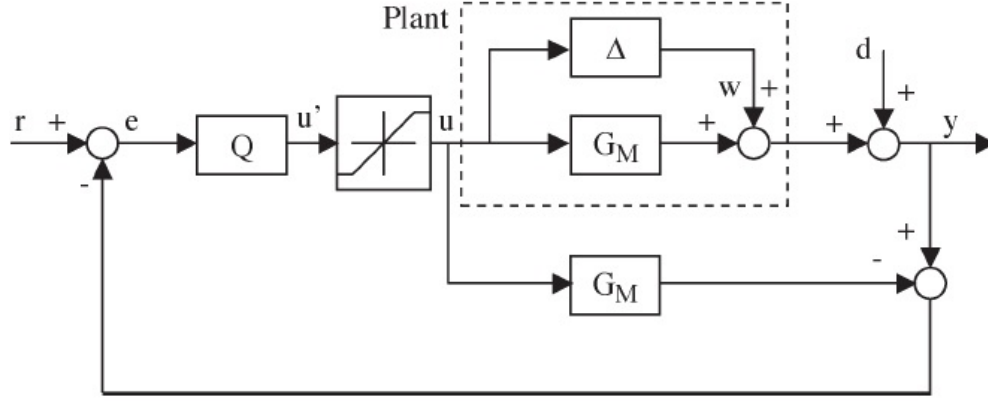


Figure 2.6: IMC Scheme as proposed by Canale et al. [21]

Different vehicle varied parameters were considered in further studies, such as tire cornering stiffness, vehicle mass and inertia. In 2018, LPV- $H_\infty$  controller considering nonlinear tires characteristics was introduced by Weiss et al. [22]. The controller aimed to improve lateral stability using a rear axle's in-wheel electric motors by applying TVC. In 2018, Zhang et al. [23] considered the variation of the mass moment of inertia associated with the fuel consumption in the controller design. Nevertheless, in that study, the tire characteristics were considered to be linear. In 2018, another study based on a gain-scheduling controller that used optimal Linear Quadratic Regulator (LQR) was introduced by Wang et al. [24]. A robust LQR gain-scheduled controller was designed to cope with the unmodelled and varied vehicle parameters and disturbances. The controller included three terms. A feedforward term based on the driver input and the desired yaw rate to give a better transient response, and a conventional LQR feedback term for better reference tracking. The third was a robust feedback term to cope with the variation in the vehicle's parameters. The controller was verified for testing on a dry road only and implemented on a Rang rover, where it showed better performance and stability than the conventional gain-scheduled LQR controller.

Most of the aforementioned controllers used an upper-controller to generate the corrective moment, while a lower-level controller was used to allocate and execute the control

action, as illustrated in figure 2.7. Besides that, it was found that integrating a slip controller with the lower allocation controller can increase the effectiveness of DYC that utilizes tires driving/braking forces [8, 17, 18]. Optimization-based controllers were used to offer the reduction of two-level controllers into one controller, where different optimal-constrained control signals and the vehicle dynamics were included together.

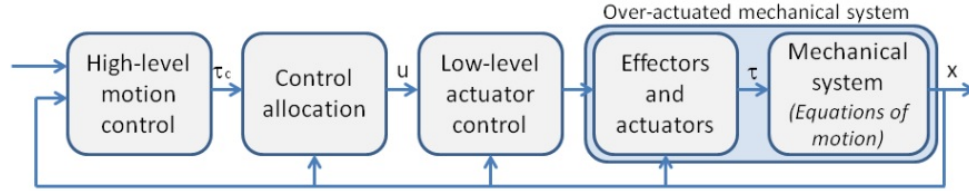


Figure 2.7: Upper and lower control scheme as illustrated [25]

In 2014 and 2015, Kasinathan et al. [26, 27] developed an optimized constrained Holistic Corner Controller (HCC). This method utilized linear-constrained quadratic programming that solved the formulated cost function to assist the driver in keeping the desired path. The formulation of that cost function aimed to minimize the error between the generated lateral and longitudinal forces and the desired ones. In addition, different DYC schemes were introduced exploiting All-Wheel Drive (AWD), and combined rear-wheel braking and opposite front-wheel driving as an application for the proposed constrained HCC. The controller was tested for high and moderate speed at various road coefficients of friction and the implementation on a real vehicle was considered with significantly low processing time.

A most widely used optimization-based controller is the Model Predictive Controller (MPC), in which the optimization problem is solved to satisfy the desired objective function and constraints based on the prediction of vehicle states and control action. In (2016), Jalali et al. [28] proposed an MPC that combined tire slip control and DYC, utilizing the distribution of driving/braking force on each wheel based on a 2-DOF bicycle model. A quadratic optimization was used to minimize the yaw rate error, vehicle sideslip, and wheel velocity error between the vehicle and the desired signals. An electric Chevrolet Equinox was used to implement and test the controller, which showed an improvement in the handling performance and stability of the vehicle. Despite the advantages of MPC controllers, exploiting a linear bicycle model in the controller design makes it difficult at some points to cope with the change in the nonlinear dynamic.

Therefore, a nonlinear MPC is required. In 2018, Metzler and Tavernini [29] developed an explicit Nonlinear MPC (NMPC) to control vehicle lateral stability. This method offered an offline suboptimal solution to the controller, in which the complexity of the calculations of the online (NMPC) was avoided. The optimization problem cost function reformulated to be solved numerically using the direct method. After that, it was approximated to have a suboptimal solution using multi-parametric quadratic programming, where the approximation inaccuracy was controlled using iteration. The proposed method was tested using simulations, where it showed a bounded yaw rate with a decrease in the rear tires' slip angles. However, the complexity of the proposed controller was not tested for real-time processing.

All of the introduced studies concerned two axles vehicles and didn't consider the control of multi-axles vehicles because of the complexity that may appear with the increase in the actuators numbers. However, these vehicles have several applications in the commercial and military fields for many advantages that they offer. The distribution of load over more than two axles gives better stability and maneuverability. Furthermore, they show better safety characteristics as they can tolerate faults such as tire malfunction.

In 2011, Kim et al. [30] utilized the distribution of traction forces on each wheel to track the reference yaw model for an 8 wheel drive/4 wheel steer (8WD/4WS) combat vehicle using 8-in wheel electric motors. An upper controller using a quasi-SMC was designed to generate the required corrective yaw moment, which was allocated through a lower controller to distribute the traction forces. The lower controller allocation was based on a quadratic programming optimization technique, where a quadratic cost function was synthesized to constraint the traction forces based on the friction circle. The proposed method was evaluated through a simulation environment against an equal force distribution method and showed enhancement in yaw tracking accuracy and vehicle stability. Another study on TVC was developed in 2014 by Ragheb [31] to control an 8x8 front-steering combat vehicle utilizing an active differential. In that study, three decoupled Proportional-Derivative-Integral (PID) were designed to control the vehicle lateral acceleration, yaw rate, and longitudinal velocity. To track the desired signal determined by a steady-state bicycle model and follow the driver's command, a combined corrective moment was generated from the PIDs controllers. Then, this corrective moment was distributed by a lower-level controller, in which the required torque was divided equally then added to one side of the vehicle's wheels and subtracted from the opposite.

The controller improved the vehicle handling and prevent rollover at severe maneuvers. In 2016, Ni et al.[32] performed a study on a hybrid 8WD combat vehicle to reduce the turning radius, increase maneuverability at low speed, and enhance stability at high speed. The study utilized differential steering to increase vehicle maneuverability when driving at low speed. The traction forces were distributed over the rear axles based on the difference between the actual steering and the desired one using a P-controller. Furthermore, to improve the lateral stability a neutral-steer ratio was introduced. This ratio was defined as a function of the yaw rate and yaw rate gain to ensure the tendency to understeer at high speed and decrease the understeer tendency at low speed. However, the interference between control action and the driver command did not discuss.

### 2.2.1 Summary on direct yaw control

1.  $\beta - \dot{\beta}$  method proofed to be highly effective than any other method to implement a braking-based DYC, as the vehicle sideslip and sideslip rate gave a better indication of the stability.
2. Stabilizing the vehicle using the distribution of braking forces is efficient in improving vehicle stability, especially in the limited handling conditions. However, the longitudinal performance becomes deteriorated.
3. The integration between braking and driving forces distribution is considerably effective to control the vehicle lateral performance with less effect on the longitudinal performance.
4. Most of the introduced studies use in-wheels electric motors to implement TVC, which results in a good performance. Nevertheless, this option may not be feasible in some cases, especially in heavy vehicles, i.e. multi-axles, and combat vehicles. Meanwhile, DYC based on braking forces distribution is considered to be the best alternative if the effect on longitudinal dynamics is not important.
5. The utilization of braking force in DYC was implemented by either the use of the most effective wheel on the yaw rate or the optimal distribution based on the friction circle and tires' longitudinal slip. Still, the implementation of both methods together was rarely considered. Therefore, more studies in this area are needed.

6. Generally, there is a lack in studying the lateral stability of multi-axles vehicles.
7. Unity-SMC, which uses one control input, was used often in developing DYC because of its robustness. However, most studies included the approximation function to avoid chattering, which reduces the controller effectiveness.
8. MIMO-SMC was almost not considered in the studies. Furthermore, to include the vehicle's varied parameters in the control design, adaptive-SMC was presented, while gain-scheduled SMC was not introduced.
9. Controller robustness against model uncertainty and disturbance rejection were satisfied using  $H_\infty$ -based controller. However, frequency domain analysis of this robustness is almost not considered and needs more clarification. Moreover, optimization-based controllers were effective but work on minimizing the complexity and processing time are still going.

## 2.3 Active steering control

It was concluded from the previous section that controlling the braking/driving forces has a great effect on improving vehicle lateral stability. Even when it comes to stability limits, braking-based control systems were found to be beneficial in stabilizing the vehicle. However, the use of braking forces has a significant effect on deteriorating longitudinal performance. Therefore, another method to control the vehicle stability utilizing the Active Steering Control (ASC) was introduced by adding additional lateral forces on the front or/and rear wheels to offer comfort driving and improve stability without affecting the longitudinal dynamic.

The development of Active Front Steering (AFS) systems was introduced as an effective way to control the vehicle yaw rate. However, as AFS interferes directly with the driver's steering command, a robust controller is needed to ensure smooth action and limit that interference. Therefore, the  $H_\infty$  control method was widely used as it utilizes a frequency domain weighting function to constraint the inputs and the desired performance over the frequency domain. In 1996, Ono et al. [33] introduced a robust  $H_\infty$  using a 2-DOF model to prevent lateral force saturation on the rear wheels by controlling its slip angles utilizing an AFS controller. In this work, a phase-plane analysis was conducted for the vehicle sideslip-yaw rate. The analysis defined the stability region



for different front steering angles and determine the front steering angle at which instability occurs or at which a saddle-node bifurcation exists. The proposed controller was designed to be robust against the uncertainty in modelling the front wheels' cornering stiffness and cope with the variation in the front wheel slip angle. Furthermore, the controller prevented the vehicle from spinning when tested on a low coefficient of friction surface. The importance of including the roll motion in the controller design was introduced in 1998 by Feng et al. [34]. In this study, an analysis of the vehicle dynamics in the frequency domain was compared with experimental data. The analysis showed that the vehicle lateral acceleration drastically decreased at a certain frequency, which is not collected by analyzing the 2-DOF model. This drop may result in oscillations that affect the roll motion of the vehicle, which made it more convenient to include the roll motion in the controller design to damp it. Simulation results showed that oscillation, that measured at the front and rear dampers, was significantly decreased in comparison with a controller-based only on the 2-DOF model that did not include roll motion.

Later in 2002, Mammar and Koenig [35] conducted a phase-plane analysis of the vehicle yaw rate and sideslip at different road coefficients of friction, front steering angles, and speed. The analysis showed that at certain initial states, as driving at a low coefficient of friction road or high steering angle, the vehicles may lose their stability. Based on that, a feedforward controller was introduced to damp the yaw response of the vehicle. This feedforward controller was combined with feedback  $H_\infty$  controller and applied to reject the side wind effect. Later in (2011),  $H_\infty/H_2$  was introduced by Zhao et al.[36], which showed good performance. However, there was an opposition between the control effect and the control output, which was addressed in (2019) by Zhao et al. [37] when using  $H_\infty/H_2$  controllers. This opposition indicated that if better performance is required, so more control effort is needed, which may not be always feasible due to the actuators' limitations. To maximize lateral dynamic performance with minimum control effort, an AFS based on a combined  $H_\infty$  mixed sensitivity and extension controllers was presented, as in figure 2.8. The extension controller analyzed the vehicle status and data to obtain adequate control output from three controllers outputs namely,  $H_\infty$ , extension, and  $H_\infty$ -extension controllers for three datasets. The evaluation on dry and wet surfaces showed the preference of using the proposed controller over  $H_\infty/H_2$ , where better performance and stability were obtained.

Despite the merits of using AFS, it was found to be only effective in controlling the yaw

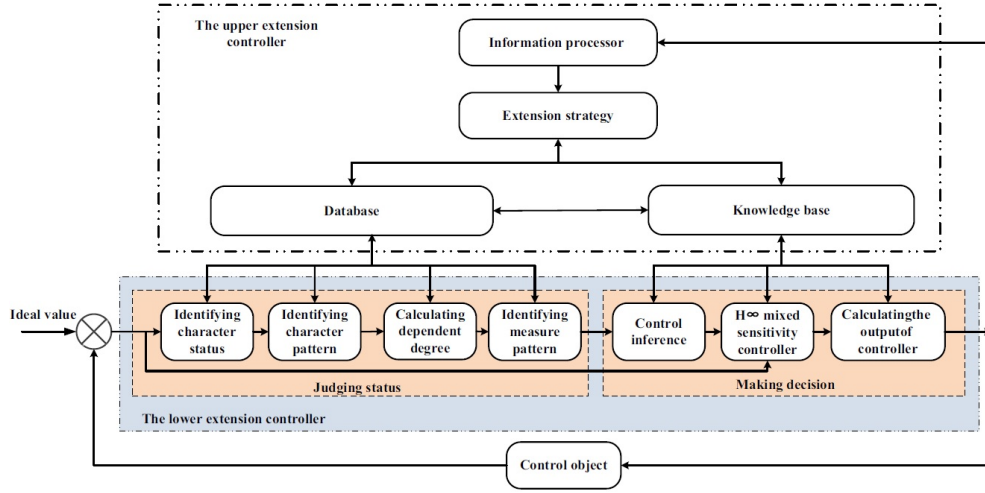


Figure 2.8: Combined  $H_\infty$  mixed sensitivity and extension control scheme[37]

rate, while the effect on the sideslip is not assured. In addition, there was a limitation in controlling the front steering angle to prevent contradiction with the driver's command and generate a feeling of losing control. Besides that, in the case of lateral force saturation on the front wheels, no more control effort can be added. Hereby, Active Rear Steering (ARS) was introduced to offer a higher degree of controllability for vehicle stability that generates additional lateral force without increasing the vehicle sideslip.

In 1986, a study done by Shibahata et al. [38] introduced two feedforward ARS configurations to ensure a vehicle zero sideslip (ZSS), as shown in figure 2.9. One configuration aimed to control the vehicle at low speed to increase the maneuverability and minimize the turning radius, while the other was used to enhance stability at high speed. For more robustness, a combined  $H_\infty$  feedback and feedforward ZSS controllers were developed in 1997 by Hirano et al. [39]. ZSS was designed based on the steady-state single-track (bicycle) model, while the introduced feedback controller was designed based on the Model Matching controller (MMC) technique, which is illustrated in figure 2.10. This method was conducted to achieve better yaw tracking performance in comparison with a standalone feedback controller. Later in 1998, a study conducted by Fujita et al. [40] on the effect of ARS on vehicle stability showed that the driver feeling of safety was increased as the vehicle sideslip angle was decreased. In that work, an  $H_\infty$  based on structured singular values ( $\mu$  synthesized) was introduced to control the vehicle sideslip, which showed the effectiveness of ARS to prevent the vehicle from reaching stability

limits. This effectiveness was confirmed later in a study performed in 2010 by Canale and Fagiano [41]. The study introduced a comparison between Rear Differential Braking (RDB) and ARS to control the vehicle yaw rate and sideslip utilizing a robust  $H_\infty$  controller, which was used also previously in Canale et al. (2008) [21]. The comparison showed the superiority of ARS in controlling the vehicle lateral motion and stability in all driving conditions.

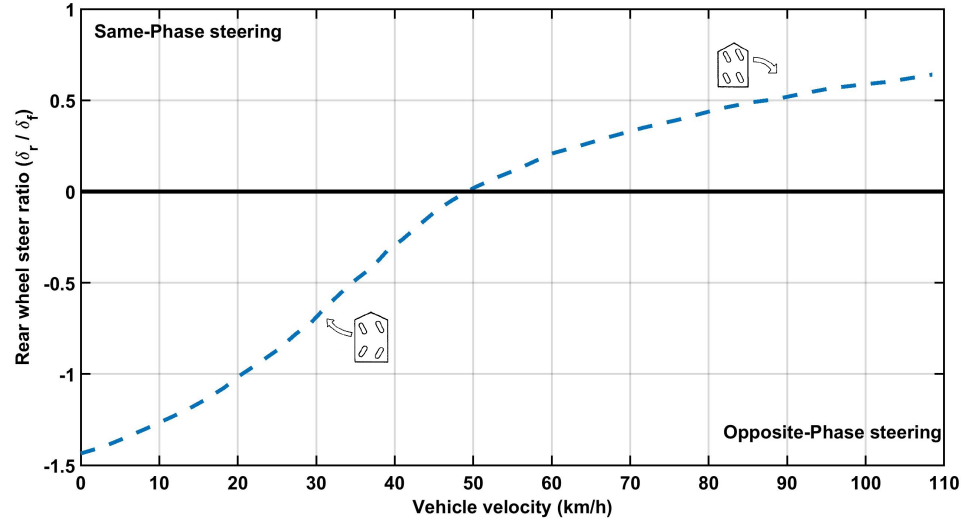


Figure 2.9: Rear wheel to front wheel steer ratio in feedforward ZSS [38]

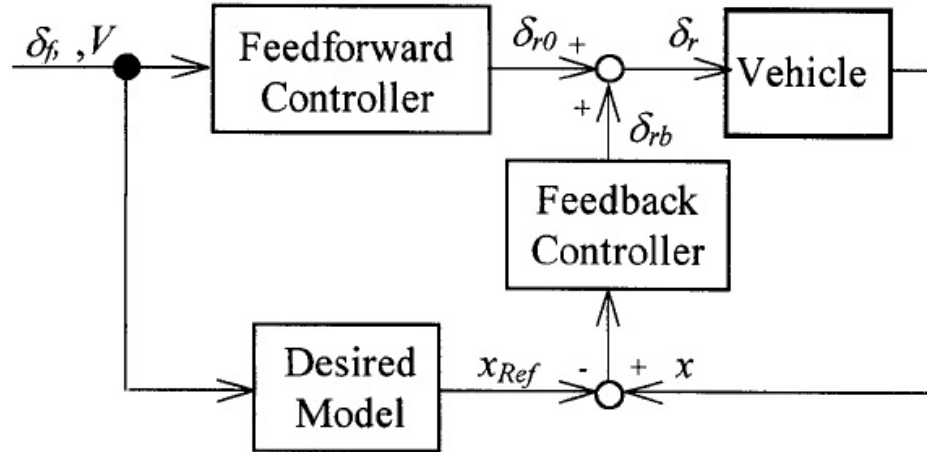


Figure 2.10: MMC schematic diagram [39]

$H_\infty$  controller was used to include the tire nonlinear characteristics and offer robustness

against the cornering stiffness and road friction uncertainty. A less sophisticated robust controller was introduced in 2019 by Park et al. [42]. The controller didn't depend on the road friction or the tire dynamics. The controller consisted of two terms. The first was a feedforward term that was designed based on the ratio between the understeer coefficient of the front and rear axle. The second was a feedback controller based on the rate of change in the vehicle sideslip. The controller showed good performance on dry and wet asphalt in comparison with an uncontrolled vehicle. However, the robustness of the proposed controller needed more analysis.

Several studies on multi-axle vehicles were introduced to exploit different steering configurations. In a study on the handling performance of a six-wheeled vehicle, different steering configurations were analyzed by Huh et al. in 2002 [43]. The analysis showed that the non-active 6-WS configuration has high lateral acceleration and yaw rate gain with a higher response in the yaw motion than other configurations. However, by designing an ARS system, it was proved that vehicle sideslip, lateral acceleration, and yaw rate gains can be decreased and consequently increase stability. The proposed ARS system adopted the steering of the middle axle by a ratio based on the front axle's steering angle, while the rear axle actively steered to track the desired yaw rate signal and obtain vehicle ZSS. Later in 2007, Chen et al. [44] combined feedback-LQR, integral feedback, and feedforward ZSS controllers to achieve robustness and higher maneuverability than the one proposed by Huh et al. (2000) [43]. However, the study only considered testing the vehicle at low speed (36km/h), which makes the performance at high speed and low coefficient of friction road questionable. In 2018, Russel [4] studied the handling performance of an 8x8 combat vehicle by comparing an LQR controller and a feedforward ZSS controller. The LQR objective was tracking a reference yaw rate and vehicle sideslip that were generated from a steady-state 2-DOF bicycle model. The controllers utilized only the active steering of the fourth axle, while the third one was fixed. The study recommended the use of two separate controllers at low and high speed as the ZSS is only effective at low speed, while the LQR controller is more effective at high speed.

### **2.3.1 Summary on active steering control**

1. Investigating some of the work done on ASC showed that it is a powerful method to control the vehicle with less effect on the longitudinal performance. In addition,

it can effectively prevent the vehicle from reaching limited handling conditions.

2. For AFS, robust controllers were widely used, especially  $H_\infty$ . These controllers were used to ensure limited additional steering and robust performance against uncertainty and disturbance.
3. ARS has an outstanding effect in limiting the vehicle sideslip, maintaining stability and consequently increasing the driver's feeling of safety and control. Nonetheless, the excessive use of ARS will give the driver a weird feeling as driving with snow or flat tires. Besides, the driver may feel that the vehicle is pointing out of the turning curvature [45].
4. AFS has a better effect on controlling the vehicle yaw rate, while ARS has more influence on vehicle sideslip. Hence, the integration between them can assure both driving comfortability and stability as will be illustrated in the next section.
5. It is more convenient to use AFS and ARS with limitations on the additional steering angle and steering rate in passenger cars. On contrary, ARS can be used unconditionally in multi-axle combat vehicles as it offers more stability and with the fact that these kinds of vehicles need specially trained drivers anyway.
6. Most of the aforementioned studies used  $H_\infty$  controllers, while SMC was rarely introduced as it has more complicity in considering the actuators' limitations and the vehicle's varied parameters.
7. It is preferred to combine feedback and feedforward controllers when developing ASC, as it will control the vehicle in both linear and nonlinear regions.
8. A sensitivity analysis for the effect of the wheels kinematics on the ASC performance is needed to be covered.

## 2.4 Integrated chassis control

Every chassis controller has an effective region, where it gives maximum performance. Figure 2.11 demonstrates the effective region of each chassis controller, where the circle's center presents normal driving conditions and the borders present limited stability [10]. Therefore, it is more convenient to integrate different chassis controllers to obtain a higher degree of controllability on vehicle dynamics. This integration is known as

Integrated Chassis Controller (ICC). However, without proper coordination and allocation between the integrated control inputs, an interference and contradiction between the controllers' objectives may occur and the overall performance will deteriorate consequently.

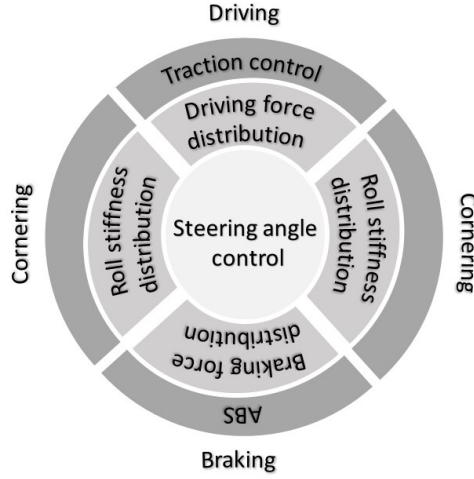


Figure 2.11: Effective working region of each chassis controller [10]

There are two methods of integration used in the ICC system. The first is the top-down method, where all control inputs are considered in the high-level controller. The other is the bottom-up method, in which each controller is designed separately and a lower allocation is used to arrange the interaction between the final control inputs [6]. The following subsection introduces a review of publications about ICC from the coordination point of view with the consideration of the most used lower controller allocation methods.

### 2.4.1 ICC utilizing top-down method

The integration of ARS with DYC in 1997 and 1998 by Nagai et al. [46, 47]. A robust  $H_2$  controller based on the MMC method was used to generate the required corrective moment and the rear axle's steering angle. The controller was designed as a feedback-feedforward controller as shown 2.12. However, the corrective moment allocation was not considered in that study, but just suggestions. In 1998, Fujita [40] developed an  $H_\infty$ - $\mu$  controller to combine a braking-based Vehicle Stability Controller (VSC) and

an ARS. The study concluded that the integration was more efficient in controlling the stability in extreme driving conditions than exploiting VSC alone. Also, the distribution of the DYC's corrective moment was not represented in the study.

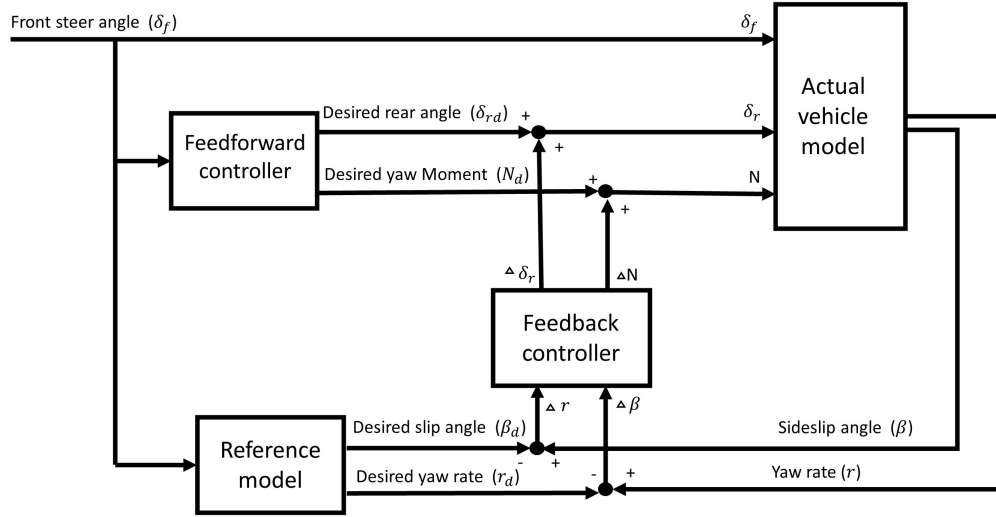


Figure 2.12: Combined DYC and ARS using feedback-feedforward controller [46]

Some studies coordinate the control actions based on the actuator readiness, road and/or driving conditions. Such as in Selmanaj et al. (2013) [48], where a gain-scheduled LPV- $H_\infty$  was developed for that objective. The controller was used to coordinate an AFS, ARS, and rear-axle braking controller. Each actuator was assigned to a weight, which was considered to be the varied parameter in the model. These weights were determined according to controller activation conditions, such as sideslip and yaw rate errors threshold. The proposed controller gave a preference to the AFS to be continuously activated. Meanwhile, ARS was activated according to a threshold based on the  $\beta - \dot{\beta}$  method and the braking controller was activated based on the yaw rate error. That coordination method showed promising results and gave an insight into the importance of using ARS. In addition, the study showed that this method can be extended to handle the actuators' saturation problem by activating an alternative one. A similar study was introduced later in 2013 by Wang et al. [49]. The study utilized an LPV- $H_\infty$  controller to activate the actuators based on their availability as a fault-tolerance controller. later,

Zhang and Wang (2015, 2018) [50, 51] used the same uncertain model to study the effectiveness of a gain scheduled PI controller to enhance the vehicle stability in different driving conditions. The controller was designed based on an energy-to-peak method. However, the distribution of the corrective moment was not considered.

Later in 2018, Jing et al. [52] presented an  $LPV-H_\infty$  controller to integrate AFS and DYC. The controller design considered the uncertainty of the vehicle mass, velocity, tires characteristics, and the actuators' failure. The proposed controller could cope with any actuator failure and obtain a stable performance. The controller performance was compared with an LQR controller, where no significant enhancement was observed. The authors related that to the poor distribution of the driving force, which was simplified and considered to be equal on each wheel. Furthermore, the contradiction of tracking the yaw rate and obtaining a zero-sideslip affected the performance, negatively.

In 2018, The performance of a  $\mu$ -synthesis and an  $H_\infty$  controllers were compared by Zhao et al. [53] in the case of integrating an AFS with ARS in a four-wheel steer-by-wire vehicle (FSV). The controllers accommodated the model uncertainty and perturbation. The comparison showed that tracking a steady-state yaw rate and obtaining the minimum vehicle sideslip using the  $\mu$ -synthesis controller resulted in better transient response. In 2020, Chokor et al. [54] compared a centralized  $LPV-H_\infty$  based controller with a decentralized Super-twisting sliding mode controller based controller to integrate AFS and DYC. The result showed that the proposed novel controller could ensure the Closed-Loop (CL) system stability, however, it is more complex than the decentralized controller, which didn't ensure CL stability. A Linear Matrix Inequality (LMI)-based controller for an  $LPV$ -polytropic vehicle model was introduced by Chen et al. (2020) [55] to integrate AFS and DYC, which resulted in a performance comparable to conventional MPC.

Optimization-based controllers were very common to integrate multi-objective controllers by considering the vehicle dynamics, actuators constrain, and limitations. The objectives were defined as soft constraints, so if a contradiction happened the constraints can be violated without affecting the operation of the actuators. Furthermore, optimization-based controllers were used as a lower controller to allocate the desired corrective moment generated from the upper controller. For example, Mokhiamar et al. (2004) [56] used a sliding controller to generate the corrective moment. After that, an optimal lateral and longitudinal forces distribution was obtained using a lower-level



optimization-based allocation strategy to determine the desired wheels' steering angles and traction forces, as in figure 2.13. This method showed better vehicle performance and stability than the integration of AFS, ARS, and DYC without the proper coordination, especially on slippery surfaces. In 2009, a quasi-SMC was also used with the optimization-based allocation method by Wang and Longoria [57]. In this study, a cost function was formulated and solved using an accelerated fixed-point method, which had the advantages of low computational cost and low complexity. By solving the optimization problem, an optimal tire longitudinal slip and slip angle were obtained to determine the desired longitudinal forces and steering action.

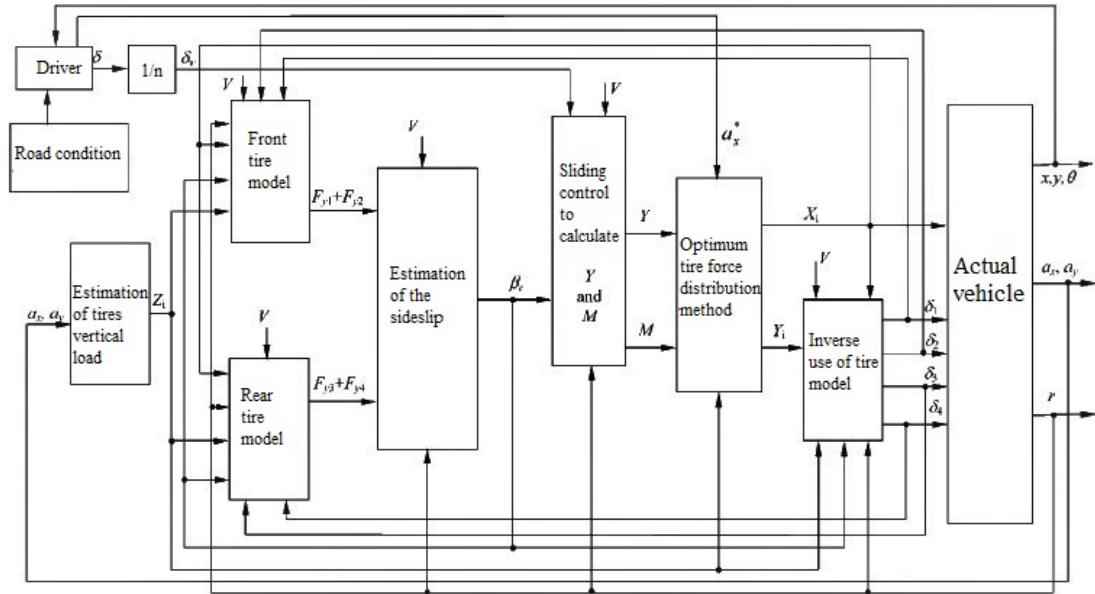


Figure 2.13: Optimization-based control allocation scheme [56]

Notable work was introduced by Tjønnås and Johansen (2009) [58] to integrate AFS and differential braking (DB). In their study, a three-level controller was introduced as shown in figure 2.14. The first was a high-level controller that produced the corrective yaw moment. The middle controller generates the desired tire longitudinal slip and the corrective front-steering angle. The last level was responsible for distributing the braking forces optimally to satisfy the determined longitudinal slip and corrective yaw moment. The control allocation was solved based on the dynamic optimum-seeking method, which ensures an asymptotic optimal solution by adapting the Lyapunov stability function. Another method for integrating AFS and DYC was introduced in 2018

by Mang et al. [59] utilizing a novel non-smooth controller to generate the corrective moment. Then this moment was optimally distributed on the vehicle wheels by penalizing the longitudinal forces of each wheel based on the available vertical load. The controller gave comparable results and better performance in comparison with a conventional SMC.

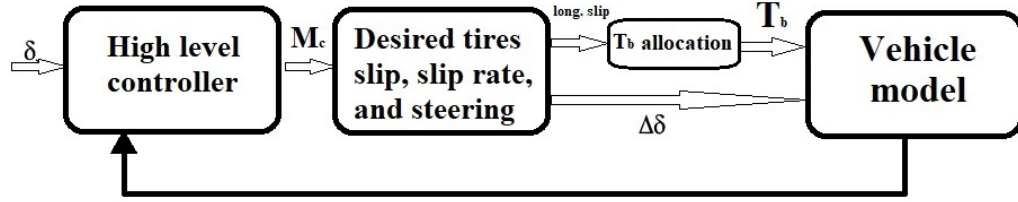


Figure 2.14: Three-level controller method by Tjønnås and Johansen [58]

Recently in 2019, Nah and Yim [60] developed an optimal lower allocation controller based on the pseudo-inverse method. This method was used to allocate the corrective moment, which was generated by an upper SMC. The corrective moment was allocated by a lower controller to integrate an ARS, AFS, TVC, and a differential braking controller. In the proposed optimization problem, a quadratic cost function was formulated to penalize the longitudinal and lateral forces using the friction circle. Different combinations of the aforementioned control systems were compared in terms of maximum yaw rate error (MAYRE), maximum sideslip angle (MASSA), and maximum fluctuation in longitudinal velocity (MFVx). It was concluded that ARS alone could give a competent performance. However, the combined ARS and ESC, ARS and TVC, and ARS with both ESC and TVC hold the best performance with minor differences. In 2020, Feng et al. [61] solved an optimal allocation of DYC, AFS, and differential-ESC using the Fixed-point method to reach the optimal distribution of the tire forces. The results were compared with every single controller and showed the preference of the developed ICC.

MPC was also used to integrate AFS and DB in a study introduced in 2017 by Jalali et al. [62]. A quadratic cost function was formulated to limit the vehicle's sideslip and maintain stability. It was notable that the proposed controller had comparable performance with utilizing only DB when tested on slippery roads. The controller didn't require information about the road friction but used the estimated tires' slip angles in the



more, any additional chassis controller can be designed and added to the existing ones without redesigning all controllers. However, some modifications need to be added to include the new controller in the coordination scheme. Commonly, the lower-level allocation controllers (controller's coordinator) utilize simple rule-base and/or fuzzy logic rules.

In 1990, a simple rule-based was applied by Yokoya et al. [67] with an upper-feedforward controller to integrate an ARS and active suspension (AS) system in a conventional front steering vehicle. The integration was achieved by mapping two ARS modes, normal and sport driving, with three different suspension configurations controlled by a roll gain. This gain was changing through the front and rear axles according to the lateral acceleration feedback and the steering angular velocity. The integration resulted in extending the vehicle stability limits to a higher speed when compared with 4-WS and the front-steering vehicle. Later in 1992, a feedback controller with a rule-based method was utilized by Kawakami et al. [68] to study the integration of different combinations from AS, ARS, TC, and ABS. The ARS was controlled according to the front steering angle and a yaw rate feedback to increase the vehicle controllability. However, using the ARS at high speeds increased the roll gain. Therefore, the AS was used to reduce the vehicle roll angle. Furthermore, TC, ABS, and the braking controller were activated to stabilize the vehicle in case of failure of AS to retain stability.

SMC was widely used in designing ICCs, where separate unity SMCs were developed then integrated through a coordinator and/or an allocation scheme. The combination of quasi-SMC and rule-based allocation was presented in 2006 by He et al. [69] to integrate AFS with Dynamic Stability Control (DSC). In the rule-base allocation algorithm, the activation region of each controller was mapped according to the  $\beta - \dot{\beta}$  method in the form of stability index  $S_i$ . The same method was used in 2019 by Termous et al. [70] to integrate AFS, DB, and AS controllers. A super-twisting SMC was used to develop the AFS and DB to avoid chattering, while the AS was designed using back-stepping. Rule-based allocation functions were designed as a function of the vehicle maximum lateral acceleration,  $\beta - \dot{\beta}$  phase-plane for coordination. This method showed a sufficient lateral stability performance without considering the optimal distribution of braking forces. Other researchers used a threshold to switch between the controllers and mapped it to ensure a smooth transition. Yu et al. (2020) [71] used a Feedforward yaw moment map to coordinate TVC with Electronic Power Steering (EPS) in order to compensate for

the steering-disturbance generated by the torque difference between the right and left wheels.

FLC was found to be an effective method for integrating different chassis controllers by addressing rules to organize the controllers' overlap. Song (2013 and 2018) [72, 73, 74] worked on integrating different combinations from AFS, ARS, and DYC systems. The combinations included ARS with AFS, AFS with rear-axle DB, ARS with front-axle DB, and DB at the front and rear axles, which were denoted as IDCS, IDCF, IDCR, and IDCB, respectively as in figure 2.16. Figure 2.17 shows an overview of the FLC, which was developed for pairing every two controllers, while quasi-SMC was used for allocating the control actions to the actuators. The comparison showed a preference for using ICDR when driving on a snowy road, while IDCF and IDCB made, somewhat, better performance on a dry road. Another study in 2018 performed by Rahimi et al. [75] to integrate AFS, DB, drive-line control, and Active Roll Control (ARC), exploited the FLC algorithm to define each controller weight and activation criteria. A quasi-SMCs were utilized to design the AFS and DB controllers, while a PI controller was used to design the drive-line control. In the DB controller, the quasi-SMC was developed to limit the sideslip utilizing the inner rear and outer front wheels instead of optimal braking force distribution. Meanwhile, a Roll-Index (RI) was defined to activate an active roll bar to decrease the roll angle. In 2020, Zhang et al. [76] integrated a PID-DYC with an active suspension that forces continuous damping on the vehicle vertical dynamic using a multi objectives-FLC.

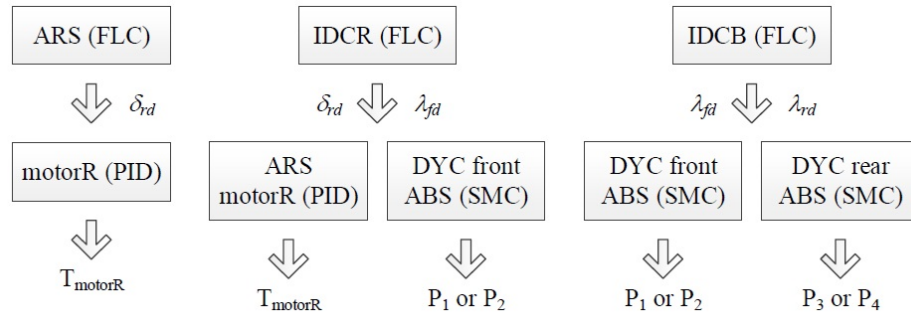


Figure 2.16: Controllers configurations as in [74]

The combination between an LQR controller and a rule-based allocation was not widely used in the development of ICCs, despite the good lateral performance that it achieved.

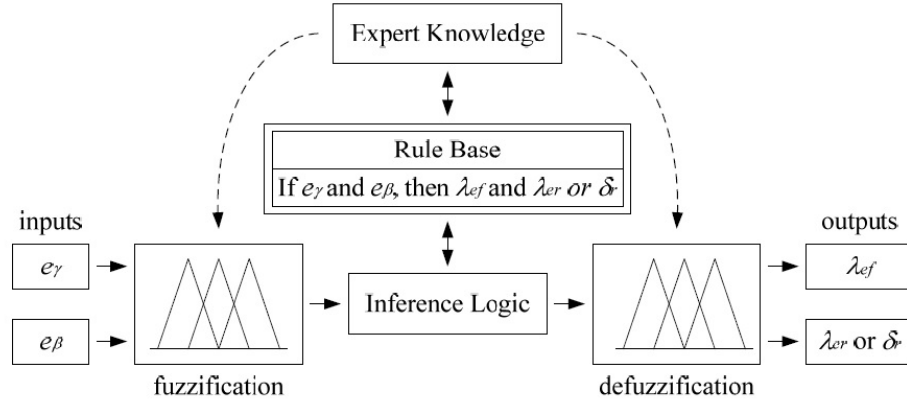


Figure 2.17: Overview on fuzzy logic controller as in [74]

In 2009, Yang et al. [77] integrated AFS and DYC using two robust LQR controllers that included uncertain vehicle parameters in the control design. One controller was designed to use the AFS, while the other was designed to use both AFS and DYC. A rule-based function based on the  $\beta - \dot{\beta}$  method was used to switch between the controllers, where the AFS has priority. After that, the braking force was executed using the inner rear or outer front wheel and the selection of the braking wheel was determined based on the corrective moment direction. Besides, the braking force was limited by a wheel slip controller. Another study using conventional LQR controller and rule-based allocation was introduced by Ahangarnejad et al. (2019) [78]. The integration of ARS, TVC, active suspension, and active aerodynamic was adopted to improve the lateral stability of a high-speed vehicle. The rule base was generated based on the yaw rate, sideslip, steering angle, and vehicle velocity.

Some other studies were dedicated to designing ICC for multi-axles vehicles to exploit the plenty of available actuators. In 2012, Kim et al. [79] integrated middle wheel steering with DYC utilizing the distribution of the longitudinal forces to improve the lateral stability of a 6WD-6WS combat vehicle. A feedforward controller was utilized to determine the middle wheel steering angle exploiting the vehicle steady-state model. On the other hand, quasi-SMC and velocity-PI controllers were used to generate the desired corrective yaw moment and desired traction force, respectively. Moreover, an optimal quadratic problem was solved to determine the traction/braking force distribution on each wheel according to the friction circle. The proposed controller resulted in a better lateral performance in comparison with a braking controller that applied the braking

forces based on the percentage of effectiveness of each wheel. Later on (2016), D’Urso [5] developed a TVC system based on an LPV- $H_\infty$  controller to enhance the lateral stability of an 8-WD combat vehicle at varying speeds. A TVC was integrated with an ARS controller that applied to the fourth axle only. For coordination, a Gaussian distribution rule-based was used to switch between the controllers and ensure smooth operations. In 2017, a study to improve the lateral performance of three axles electric bus was introduced by Liu et al. [80] utilizing the ARS and the distribution of driving forces. Two unity SMCs were developed, one to control the vehicle speed to limit the vehicle sideslip and prevent rollover, and the other was TVC to achieve better handling performance. The rear axle’s steering angle was determined based on the front steering, vehicle yaw rate, and the vertical forces distribution. The ARS was adopted to decrease the wear on the driving tires. The integration was done based on objectives decoupling, while the effect of each controller on the other was not analyzed.

### 2.4.3 Summary on integrated chassis control

1. Top-down integration method has the privilege of considering all actuators and constraints in one controller. Notwithstanding this advantage, it is not easy to add another controller/actuator in the future.
2. Bottom-up method requires the development of each controller separately with the need for a lower controller for coordination/allocation. This method permits adding of another controller but with applying modification to the coordinator.
3. Because of the existence of multi-objectives in ICC, a contradiction may occur between tracking the yaw rate and obtaining a zero-sideslip, which may require improvements on the reference model.
4. Practically, the introduction of a scheme that allows the inclusion of other actuators and controllers for future purposes is very important.
5. Most of the introduced controllers gave preference to one controller over another. Yet, there is fewer clarifications and analysis to the criteria on which this preference is based.
6.  $H_\infty$ -based and optimization-based controllers were often used in the top-down method since it was possible to include the actuators’ saturation, limitations, and

availability with considering the performance objectives and constraints. Meanwhile, SISO-SMC was used in the studies to generate the desired corrective moment as an upper controller, while a lower optimization-based controller allocates this moment on the available actuators. Even so, MIMO-SMC was rarely introduced, which required more concern.

7. It has been shown that optimization-based allocation methods are very effective in integrating different controllers. Nevertheless, a comprehensive study for different optimization techniques that trade between solution optimality, performance, processing time, and complexity is required.

## **2.5 Lateral dynamic control in path-following application**

The development of an autonomous ground vehicle has a great concern in several fields, i.e. civil transportation and passenger cars, commercial, and military applications to increase transporting and driving integrity. Several tasks should be addressed to develop a fully autonomous vehicle such as mapping, localization, path planning, tracking, vehicle dynamics, and stabilization control systems. In this section, the work done on the path-following/tracking controllers considering the vehicle dynamic was reviewed.

Late in the 90s, path-tracking controllers were designed based on the AFS systems as it was the default actuator to control the vehicle heading. In 1994, Guldner et al. [81] utilized a unity SMC using regular form method [15] to design a path-follow controller using the AFS. Vehicle lateral dynamics was addressed by using the 2-DOF bicycle model in the control design, without consideration of vehicle nonlinear and varied parameters or limitations on the vehicle dynamics. In 1999, an integration between longitudinal and lateral vehicle dynamics was presented by Lim et al. [82]. This integration aimed to minimize the lateral error from the lane centerline and keep a fixed distance with the vehicle ahead. The authors discussed the integration as a dynamic and kinematic coupling. Three SMCs were used for the integration. One was developed for controlling the vehicle velocity based on the leader vehicle. The second was designed to produce the proper traction force to control the vehicle velocity and tire longitudinal slip. The third controller was responsible for producing the required engine torque to satisfy the required traction forces. The controller was evaluated in a simulation environment and exper-



imentally without the consideration of tires' slip and resulting in better path-tracking accuracy when compared with a PID-gain scheduled controller. The previous studies did not ensure robustness as the uncertainty and disturbance were not considered in the control design. In 2013, Tagne et al. [83] introduced a super-twisted SMC that avoided the chattering phenomena and improve the path-tracking accuracy using the AFS.

Utilizing the torque distribution on the right and left wheels for path tracking application was presented in 2016 by Wang et al. [84]. The authors performed a two-step path-following controller to track a planned trajectory for a lane-changing maneuver. First, a kinematic-based controller was designed based on the backstepping method to generate the desired longitudinal velocity and yaw rate to follow the desired planned trajectory. Then, a dynamic model-based SMC was developed to ensure accurate execution of the desired vehicle velocity and yaw rate by distributing the driving torque on the left and right wheels. It was noted that most of the previous studies focused only on tracking accuracy, where the controller's objective was to minimize the lateral error between the vehicle and the desired path. Moreover, the vehicle response, dynamics limitations, and driving at the handling limit were not considered.

Limiting the vehicle sideslip was considered later in several studies for better tracking accuracy and stabilization. In 2016, Wang et al. [85] developed a Composite Nonlinear Feedback (CNF) controller based on integral SMC. The controller then generated a front steering and corrective moment to track the desired yaw rate, which was generated according to the path-following reference model with targeting a zero vehicle sideslip. A lower controller was used to assure an optimal distribution of the corrective moment based on the traction force on each wheel. The controller performance was comparable to an LQR controller. However, it was not tested for severe maneuvers. A high-speed evaluation on a dry road only was conducted later by Chuan (2017) [86]. Liu et al. (2020) [87] utilized two separate super twisted SMC to control the front axle steering and the yaw moment to avoid vehicle crash while negotiating a single lane-change maneuver.

Backstepping-SMC, using saturation function approximation, was adopted in 2019 by Wang et al. [88] to develop an AFS controller for path-tracking. The controller gave accurate curvature tracking performance in comparison with conventional SMC and was validated experimentally using a real vehicle. Additionally, the author suggested that the integration with longitudinal vehicle dynamics in the future will give better results.

Backstepping-SMC was used also by Norouzi et al. (2019) [89] to improve the handling and tracking performance for DLC maneuver using AFS. Also, a saturation function was used instead of a discrete sign function to avoid chattering. Furthermore, the controller's adjusted gain was obtained using Particles Swarm Optimization (PSO) method, in which a cost function including the sliding manifolds and the control input was minimized through iterations. The controller gave a good result when driving on a dry road, however, it gave less accuracy in comparison with a conventional backstepping controller when driving on a slippery road.

MPC-based controllers are widely used in path following as they can include different objectives and tasks in the controller design, i.e. trajectory planning and tracking. In 2009, an MPC path-following controller based on a kinematic model was designed by Raffo et al. [90] for low-speed tracking utilizing AFS. Furthermore, this model generated set-points for a dynamic-based controller to take action in case of high-speed operation. The authors demonstrated the importance of considering the vehicle dynamic for path-following at high speed as it achieves better accuracy. Later in 2012, a trajectory planning and tracking controller was introduced by Shim et al. [91]. The controller aimed to avoid collisions and mitigate crashes for an autonomous vehicle. AFS and TVC were integrated to follow the desired path that was generated to avoid the collision. The controller succeeded to avoid the collision at low-speed operation. However, high-speed maneuvers were postponed for future study.

Cui et al. (2018) [92] and Sun et al. (2018) [93] discussed the value of considering the vehicle sideslip limitation in the design of a lateral dynamic controller for path-following application. In the first study, [92], an AFS controller using multi-constraints MPC was compared with conventional MPC. The vehicle sideslip was constrained in the first controller, while it was not considered in the conventional controller. In addition, a  $\beta - \dot{\beta}$  phase-plane analysis was conducted along with that comparison. The analysis showed better performance and stability for multi-constrained MPC than the conventional MPC. The comparison was conducted on wet and dry roads, however, the performance on slippery roads was not assessed. In the second study [93], the front lateral forces were used as the controller input instead of the steering of the front axle. This approach allowed the variation in the tire's slip angle and cornering stiffness to be included in the lateral force allocation.

Explicit MPC was introduced in 2018 by Lee and Chang [94] to decrease the computa-

tional time of an MPC controller for online optimization. The computational time was decreased by exploiting a multi-parameters quadratic programming method that was used to design an AFS controller for path-tracking. The proposed controller showed less processing time with better performance in comparison with conventional MPC. A quadratic programming method was also used later in 2019 by Wang et al. (2019) [95] to develop a Multi-constrained Quadratic programming-based controller to integrate AFS and DYC utilizing traction forces with motion planning for crash mitigation applications. This controller focused on the vehicle's longitudinal velocity and lateral position as the desired output. In addition, the MPC quadratic cost function was formulated based on three objectives. The first was lateral error minimization, while the second used an obstacle avoidance cost function based on the potential field method. The third was an accident severity factor, which was determined based on the weight and velocity of the vehicle and obstacle. Furthermore, in 2019, DYC was integrated with AFS by Yang et al. [96] using a quadratic programming-based MPC as an upper controller. A lower controller based on a weighted-constrained least square method was adopted to generate optimal torque distribution between the vehicle's wheels. Furthermore, the formulated cost function included the tracking error, and actuator saturation and was solved using the active set method.

Other controllers were used recently for better robustness against uncertain parameters and road conditions to achieve better performance near the handling and friction limit. Wachter (2016) [97] utilized an AFS controller, where the control inputs were generated by solving Riccati Equation. The equation was solved online to create a real-time optimal controller considering the varied vehicle parameters and driving conditions. Besides, a vehicle slip controller was designed using ARS, which showed better tracking performance. However, the ARS was not integrated with the proposed AFS controller and tested separately. In another study done by Wnag et al. (2017) [98], the tracking performance of a  $\mu$ -synthesis and an  $H_\infty$  controllers were compared, considering the uncertainty of tires' corner stiffness. The comparison showed that the  $\mu$ -synthesis achieved better performance and stability in the presence of uncertain parameters.

Recently in 2019, Feng et al. [99] proposed an observer-based  $H_\infty$  controller for path-following utilizing an AFS with limitation on the vehicle sideslip. The authors introduced the consideration of vehicle speed variation using the Takagi-Sugeno fuzzy-modelling method. In addition, the controller was evaluated by performing a DLC ma-

neuver under different driving conditions. The controller showed better performance than conventional LQR and SMC. However, the SMC controller results were comparable with slight differences. An  $H_\infty$  controller was also used to design a path-following controller for an autonomous race car by Ni et al. (2019) [100] utilizing the AFS. Furthermore, the tire characteristics uncertainties were considered in the controller design. The developed  $H_\infty$  controller was integrated with a driving controller utilizing the traction/braking forces using a G-G diagram, as in figure 2.18. This diagram mapped the lateral and longitudinal acceleration required to make a predefined race lap to the desired driving force required to successfully finish it. The controller showed good results in comparison with a linear controller. However, it required full foreknowledge about the path.

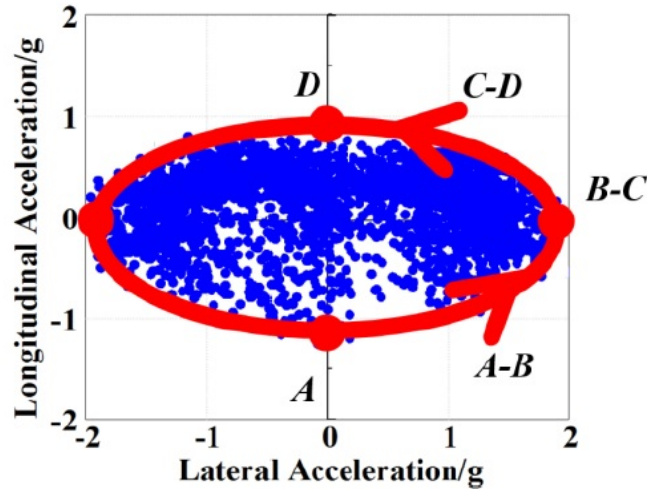


Figure 2.18: G-G diagram introduced in [100]

In late 2020, Chen et al. [101] combined AFS and ARS but for different objectives. The AFS was developed to track the desired trajectory for path following applications while ARS was designed to maintain the vehicle's stability.

## 2.6 Chapter summary

In this chapter, a review of publications that deal with lateral stability control for the traditional and autonomous ground vehicle has been discussed. Direct Yaw Control (DYC) using differential braking and Torque Vectoring Control (TVC) was introduced at the beginning. After that Active Steering Control (ASC) utilizing both Active Front Steering

(AFS) and Active Rear Steering (ARS) was reviewed. Moreover, the methods that are used to integrate DYC and ASC for Integrated Chassis Controllers (ICCs) application were discussed in detail. Eventually, the published work regarding the consideration of vehicle lateral stability and ICCs for path-following application were reviewed. The literature leads to the following closing remarks:

1. Designing lateral stability controllers based on vehicle sideslip and sideslip rate gave the best performance among the reviewed studies. Hence, it can be used to stabilize the vehicle at handling limits.
2. Differential braking reduces the longitudinal performance of the vehicle, so the excessive use of the braking forces should be limited to the handling limit and critical stability conditions.
3. TVC were commonly utilized in-wheel electric motors as the actuators. In the case of heavy vehicles, a feasibility study is required to evaluate the cost/performance.
4. There are limited publications regarding lateral stability and automation of multi-axle combat vehicles, which need to be covered. In addition, lateral stability of multi-axes vehicles considering the model uncertainty, actuators saturation, fault control, and stability over rough terrains was not covered.
5. SMC showed high reliability in designing chassis controllers. However, the consideration of MIMO-SMC for chassis controllers is limited.
6. ARS was found to be an effective controller for the vehicle's lateral stability as it prevents the vehicle from reaching the handling limits. However, based on several studies it will be more efficient to use such a controller in multi-axes combat vehicles as the driver can easily train to adapt to its behaviour.
7. ICCs bottom-up technique has several advantages over the top-down method for the ability to be modified.
8. Machine learning-based controllers are merely used in the design of lateral stability controllers except for Fuzzy Logic Control (FLC), which was used in the coordination of ICCs.
9. A comprehensive study that shows the effective working region of multiple lateral stability controllers is needed to facilitate the controllers' integration.

10. It has been shown that optimization-based allocation methods are very effective. Nevertheless, a comprehensive study for different optimization technique that trades between performance, processing time, and complexity is required.
11. The consideration of ARS for autonomous multi-axle vehicles and its effect on the tracking accuracy near the handling limit is not covered.

## CHAPTER 3

### Investigation of Various Passive Steering Modes

#### 3.1 Introduction

This chapter introduces the configuration of the 8x8 combat vehicle that is used to perform this thesis. In addition, it includes a summary of the vehicle model's validation that was done in previous studies. Moreover, the development and investigation of different steering modes for an 8x8 combat vehicle are introduced. These steering modes are front, crab, counter, and front-rear steering with fixed 3<sup>rd</sup> axle. The vehicle's maneuverability and dynamic response for all steering modes, except the crab steering, are evaluated by conducting the curb-to-curb and minimum road width tests. In addition, all modes are assessed at low and high speeds by conducting a series of slalom maneuvers.

#### 3.2 Vehicle model and validation

A nonlinear 22 degrees of freedom 8x8 combat vehicle model was developed to represent the vehicle motion and dynamics. The model presents the vehicle's lateral, longitudinal, and vertical dynamics, including the pitch, yaw and roll motions. Besides, 2 degrees of freedom that present the vertical motion and spinning of each wheel (16 in total). In addition, a nonlinear tire model was incorporated into that model. The tire model characteristics were tabulated in look-up tables based on measured data that were provided by the manufacturer. Besides, the model includes nonlinear characteristics of the vehicle's pneumatic suspensions. The vehicle is equipped with 4-axles and independent suspensions and powered by an internal combustion diesel engine. In addition, four mechanical differentials, one per axle, are utilized to distribute the engine torque to each axle. The vehicle model uses the steering of the front two axles with the capability of steering the 3<sup>rd</sup> and 4<sup>th</sup> axles, as shown in figure 3.1.

The developed vehicle model was validated by comparing its response with the field measured data that was acquired from the real vehicle by the US army. The validation was done by conducting a series of J-turn, DLC, and constant step slalom maneuvers



Figure 3.1: Simulated 22 degrees of freedom vehicle model on TruckSim (a) Front-axle steering (b)8-WS vehicle

at various vehicle speeds and roads friction coefficients, where each test was repeated four times. The validation criteria were defined so the Root Mean Square (RMS) value of lateral acceleration provided from virtual testing should meet 90% of the measured data. In addition, the data acquired from the time domain response of the virtual testing should achieve kurtosis and skewness within  $\pm 50\%$  of the measured data as provided in [102, 103, 31].

The model was implemented in TruckSim software for research purposes to conduct all virtual testing. The model showed high-fidelity in previous research studies [31, 5, 104, 105]. This high-fidelity encouraged to use that model to perform all virtual testing and simulations in the rest of this thesis. For this chapter, several steering modes are developed and implemented in this full vehicle model to evaluate the vehicle's steerability, as will be presented in the following sections.

### 3.3 Steering modes

This section introduces four different steering modes of the vehicle as illustrated in figure 3.2. The first mode is the conventional steering, which utilizes the steering of the 1<sup>st</sup> and 2<sup>nd</sup> axles with fixed rear axles, as shown in figure 3.2 (a). The second is a parallel-wheels steering mode commonly named crab steering as can be seen in figure 3.2 (b). The third steering mode is presented in figure 3.2 (c) and exhibit the steering of the 1<sup>st</sup>, 2<sup>nd</sup>, and 4<sup>th</sup> axles while the 3<sup>rd</sup> axle is fixed. The last steering mode is shown in figure 3.2 (d) and presents an all-wheel steering vehicle, in which the rear axles move



counter to the front axes.

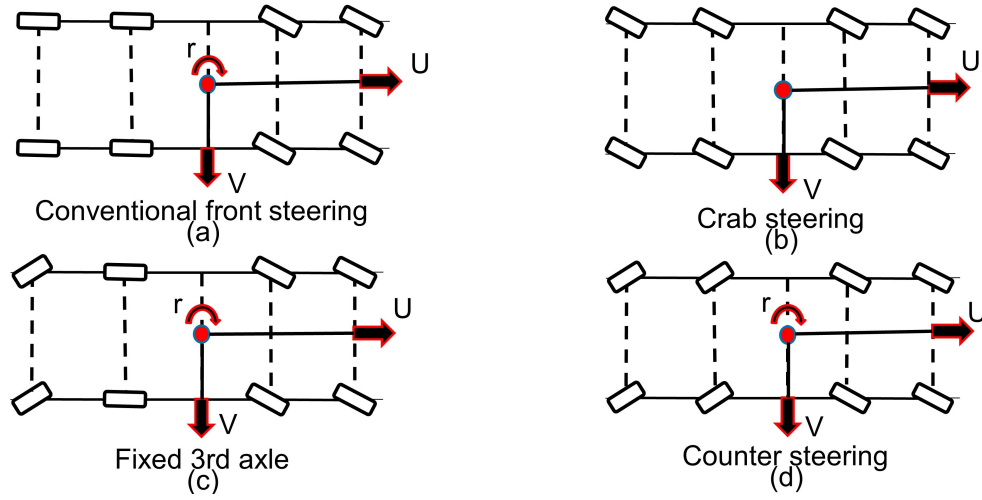


Figure 3.2: The developed passive steering modes

### 3.3.1 Conventional front steering mode

In the conventional front steering mode only the 1<sup>st</sup> and 2<sup>nd</sup> axle are steerable, while the 3<sup>rd</sup> and 4<sup>th</sup> axles are fixed as can be seen in the bicycle model representation of this case in figure 3.3. In that representation, both wheels at the same axles have been combined into one wheel with double cornering stiffness and average steering and slip angles.

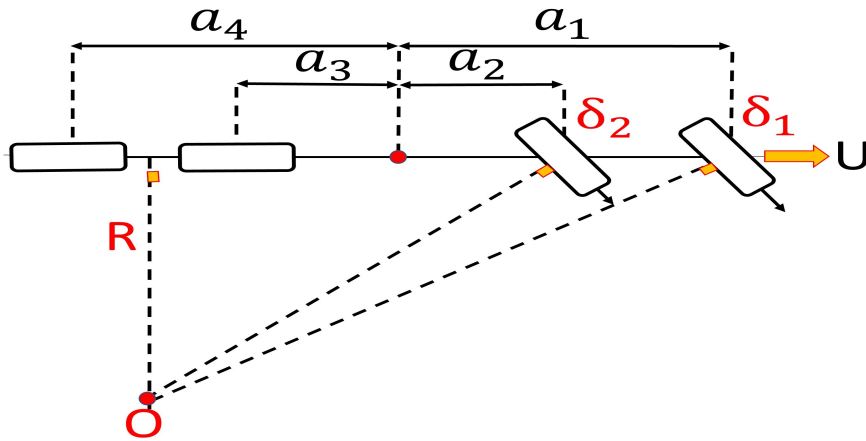


Figure 3.3: Bicycle model representation of the conventional front steering mode

The steering of the 2<sup>nd</sup> axle is linked to the 1<sup>st</sup> axle by a constant ratio, which is provided in TruckSim. The steering box output is related to the driver's wheel steering input by

a fixed ratio (same ratio for both axles). Moreover, the steering box output is then controlling the 1<sup>st</sup> axle average steering angle  $\delta_{av}$ , which is related to the outer steering angle  $\delta_o$  and inner wheel steering angle  $\delta_i$  by equation 3.1.

$$\delta_{av} = \frac{\delta_o - \delta_i}{2} \quad (3.1)$$

After that,  $\delta_o$  and  $\delta_i$  can be calculated for different average steering angles using equation 3.2, where  $t_w$  is the vehicle track width and  $L_i$  is the distance between the  $i^{th}$  axle and the vehicle turning center. For the front steering case,  $L_{1st}$  is defined as in equation 3.3 for the 1<sup>st</sup> axle. Based on the steering direction the outer and inner wheels can be redefined as the right and left wheels of the vehicle.

$$\cot(\delta_o) - \cot(\delta_i) = \frac{t_w}{L_i} \quad (3.2)$$

$$L_{1st} = a_1 + a_3 + \frac{a_4 - a_3}{2} \quad (3.3)$$

Figure 3.4 (a) and (b) show the 1<sup>st</sup> and 2<sup>nd</sup> axles' right and left wheels steering angle with respect to the steering box output angle, respectively.

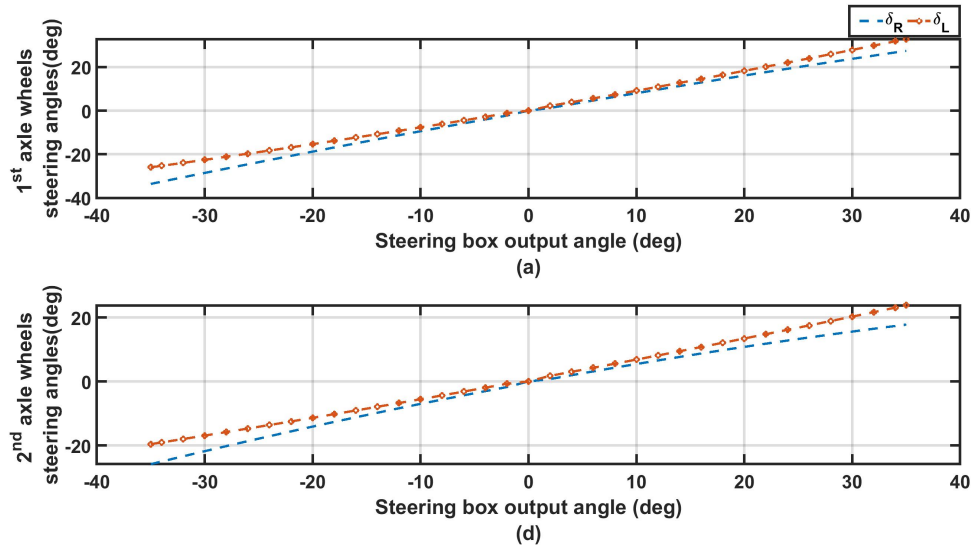


Figure 3.4: Conventional front steering (a) 1<sup>st</sup> axle's wheels (b) 2<sup>nd</sup> axle's wheels

### 3.3.2 Parallel crab steering mode

Figure 3.5 shows the bicycle model representation of the parallel crab steering mode. This mode utilizes perfect parallel steering for all axles, which means that all axles steer with the same steering angle (same direction). It should be noticed that there are no differences between the right and left wheels steering angles, where the ratio between the steering angle of the left and right wheel of each axle is constant and equal to 1. In addition, all axles steering are dependent on the driver's wheel steering by a constant ratio.

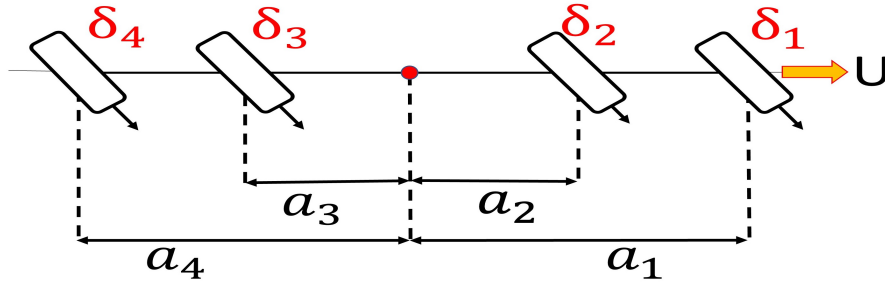


Figure 3.5: Bicycle model representation of the crab steering mode

### 3.3.3 Fixed 3<sup>rd</sup> axle steering mode

In the case of the fixed 3<sup>rd</sup> axle steering mode, the steering of the 1<sup>st</sup>, 2<sup>nd</sup>, and 4<sup>th</sup> axles are developed to satisfy Ackermann steering geometry, which determines the steering ratios between the axles. The steering ratios between the axles can be presented by the ratios of the distance from each axle to the vehicle turning center between the axles [106]. The perpendicular line of each wheel meets with the extension of the vehicle turning center at the 3<sup>rd</sup> axle. For example,  $L_{1st}$  is defined as in equation 3.4 for the 1<sup>st</sup> axle. The steering ratio between the 1<sup>st</sup> axle average steering angle and the average steering angles of other axles can be determined based on the Ackermann steering geometry as in figure 3.6.

$$L_{1st} = a_1 + a_3 \quad (3.4)$$

The average steering angle  $\delta_{av}$  of each axle can be related to the outer and inner wheels,  $\delta_o$  and  $\delta_i$ , at the same axle according to equation 3.1. This equation and equation 3.2 are

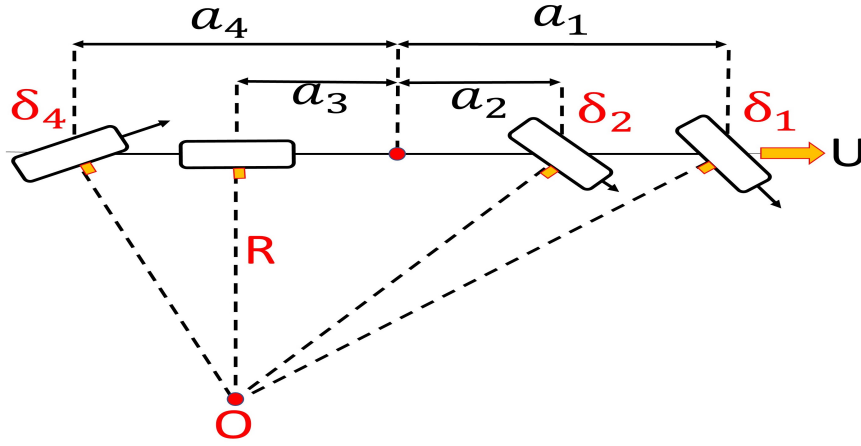


Figure 3.6: Fixed 3<sup>rd</sup> axle steering mode bicycle model representation based on Ackermann

solved for each axle separately to determine  $\delta_o$  and  $\delta_i$  for all possible average steering angles. The determined steering angles of the 1<sup>st</sup>, 2<sup>nd</sup>, and 4<sup>th</sup> axles are presented in figure 3.7 (a), (b), and (c), respectively. In these figures, the relation between the average steering angle of the axle and the right and left wheels is presented. The negative steering angles present that the vehicle turning counterclockwise, while the positive present turning clockwise, according to the TruckSim coordination system. Note that despite determining the steering angles for a large steering angle on the 1<sup>st</sup> axle, the actual wheel steering angles for all cases are constrained to be 36 degrees at maximum.

### 3.3.4 All-wheel counter steering mode

For the all-wheel counter steering mode, all-axles are also steered based on Ackermann steering geometry. The steering of the rear two axles behind the vehicle's Center of Gravity (CG) exhibit a steering angles counter to the front two axles and the perpendicular line on each wheel intersects with the extended line from the vehicle turning center, which lays at the vehicle CG. The steering angles are determined based on equations 3.1 and 3.2, similar to the previous section. However, the vehicle's turning center  $L_i$  is moved to meet the extension of the vehicle's CG, as shown in figure 3.8. For example,  $L_{1st}$  is defined as in equation 3.5 for the 1<sup>st</sup> axle.

$$L_{1st} = a_1 \quad (3.5)$$

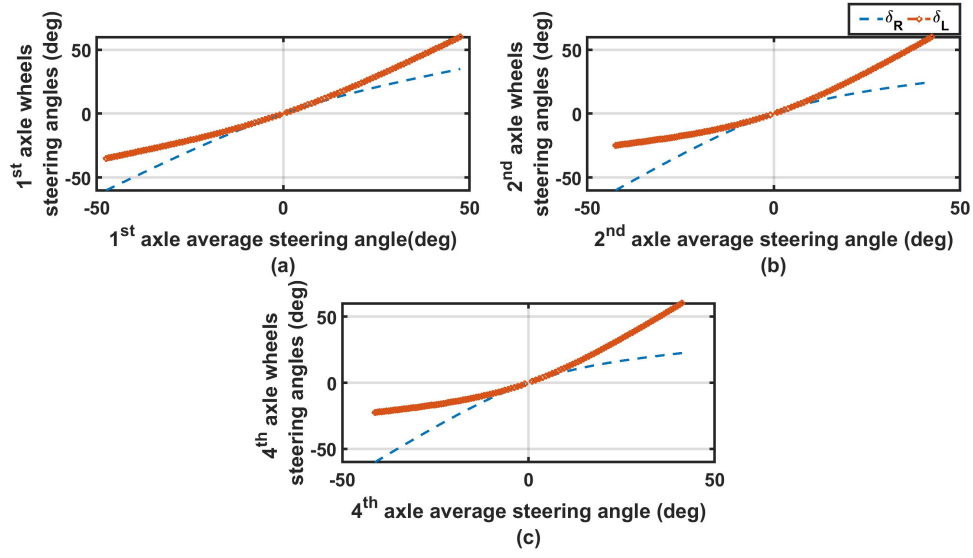


Figure 3.7: The steering angles of the (a)1<sup>st</sup> axle's wheels (b)2<sup>nd</sup> axle's wheels (c)4<sup>th</sup> axle's wheels with respect to the average steering angle for the fixed 3<sup>rd</sup> steering mode

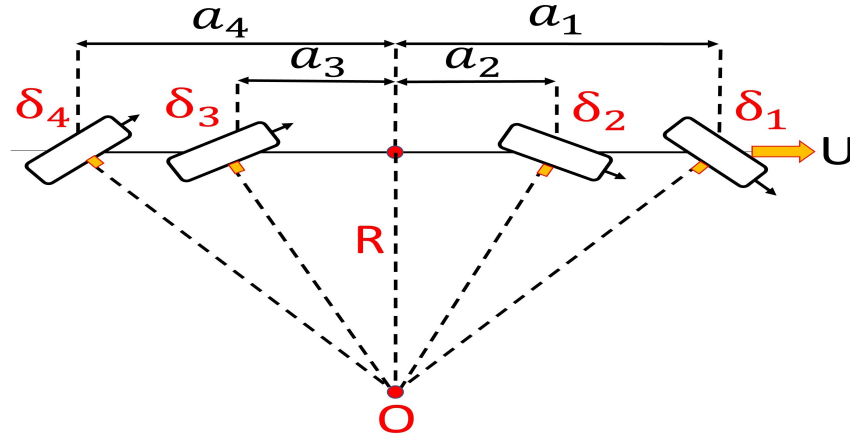


Figure 3.8: All-wheel counter steering mode bicycle model representation based on Ackermann

Figure 3.9 shows the determined steering angles of right and left wheels concerning the average steering angle of all axles.

### 3.4 Steering modes evaluation

The evaluation of the steerability and limitation assessment for each steering mode is determined In Accordance With (IAW) the Test Operations Procedures (TOP) standard

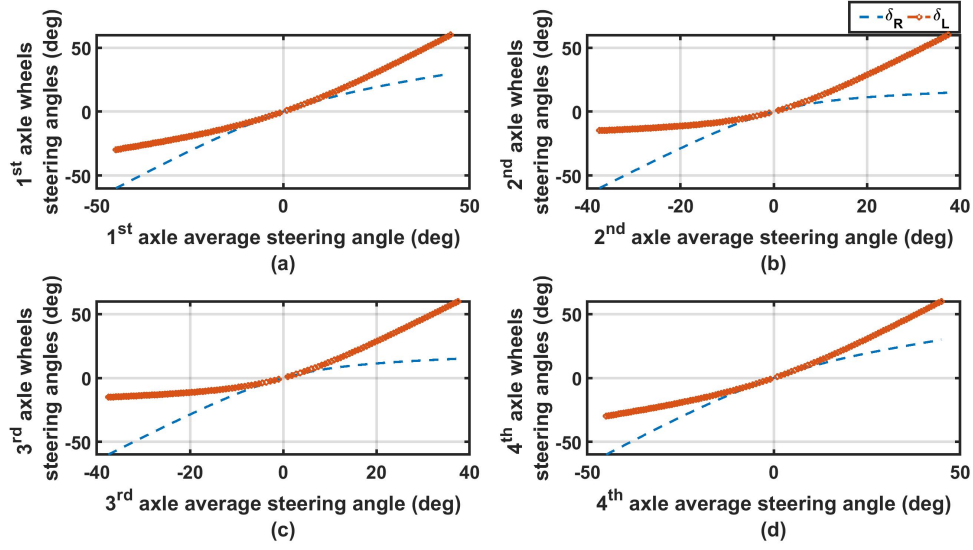


Figure 3.9: The steering angles of the (a)1<sup>st</sup> axle's wheels (b)2<sup>nd</sup> axle's wheels (c)3<sup>rd</sup> axle's wheels (d)4<sup>th</sup> axle's wheels with respect to the average steering angle of the counter steering mode

number 2-2-609 (TOP-2-2-609) to perform a curb-to-curb test and the minimum road width at a turn test. Besides, the NATO AVTP-1 03-30, and a modified version from it are used to perform slalom maneuvers at high and low speeds, respectively. All tests are performed at a dry road while driving at a very low speed ( $V_x = 5 \text{ km/h}$ ), except the high-speed slalom test, which is performed at speed  $50 \text{ km/h}$ .

### 3.4.1 Curb-to-Curb test

This test is conducted to determine the minimum distance between two curbs that are required to perform a successful full turning. The crab steering mode is excluded from this test for the fact that crab steering can only perform a diagonal movement. The test is performed by holding the driver steer wheel at the maximum steering angle and performing a full turn with the vehicle in each case. Then, the turning diameter is calculated from the far point at the outer wheel of the front axle. The trajectory made by each case is presented in figure 3.10 where the distance presenting the curb-to-curb distance is illustrated in the figure. It can be noticed that the conventional front steering mode shows the maximum distance ( $16.53 \text{ m}$ ), followed by the fixed 3<sup>rd</sup> axle steering mode ( $13.2 \text{ m}$ ), while the minimum distance is achieved by the all-wheel counter steering mode ( $10.82 \text{ km/h}$ ). These results show that moving the vehicle center of rotation

from the middle point between the 3<sup>rd</sup> and 4<sup>th</sup> axle toward the vehicle CG increases the vehicle maneuverability in narrow places.

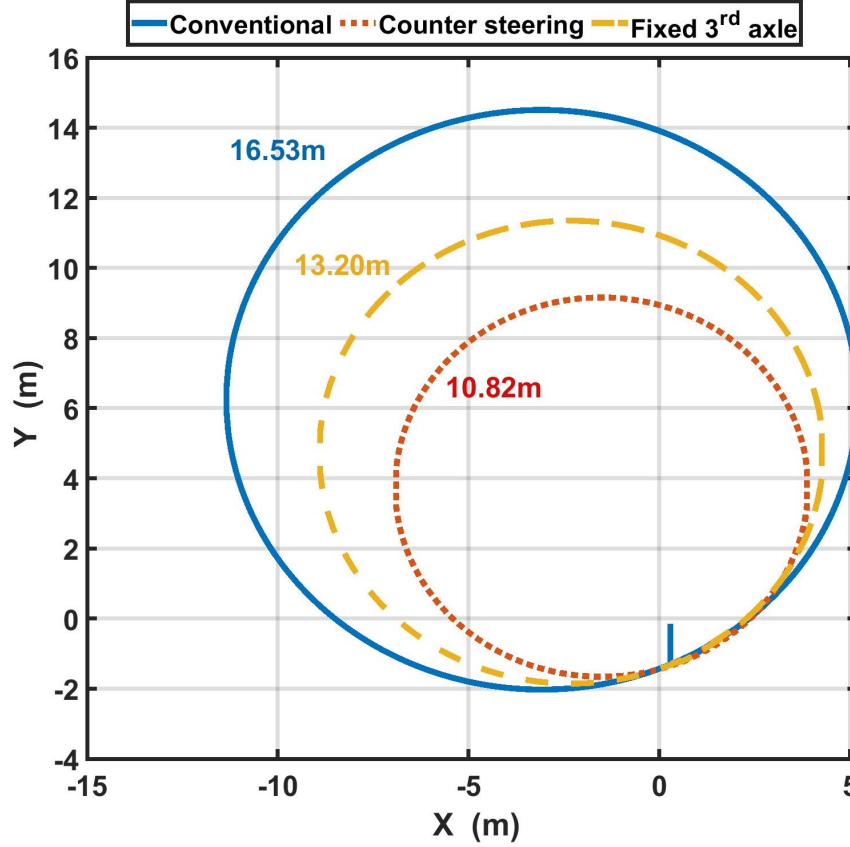


Figure 3.10: Trajectory of each steering mode at Curb-to-Curb test

The corresponding average steering angle of the 1<sup>st</sup>, 2<sup>nd</sup>, 3<sup>rd</sup>, and 4<sup>th</sup> axles are presented in figure 3.11 (a), (b), (c), and (d), respectively. It is observed that, despite exhibiting the same steer wheel angle, the average steering angle of each case defers from one mode to another. This is due to the unequal steering ratio between the right and left wheel on the same axle for the different steering modes because of the different vehicle turning centers of each case.

At such a very low speed, the vehicle dynamic is not dominant on the vehicle performance and can be neglected. However, the vehicle's dynamic response is illustrated for a better understanding of the influence of each case on the vehicle's performance. The vehicle's longitudinal speed, lateral acceleration, yaw rate, and sideslip are shown in figure 3.12 (a), (b), (c), and (d), respectively. From figure 3.12 (c), it can be noticed that

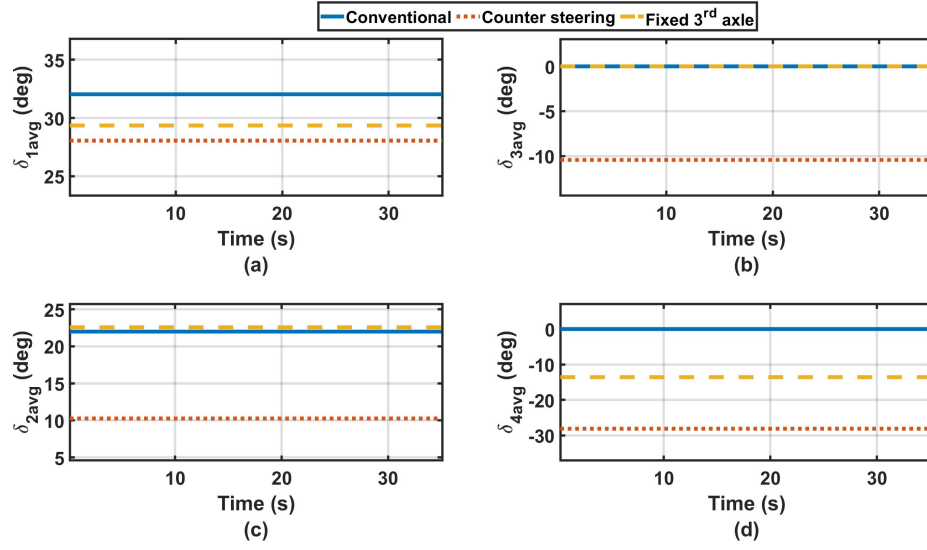


Figure 3.11: Average steering angles of the (a) 1<sup>st</sup> axle (b) 2<sup>nd</sup> axle (c) 3<sup>rd</sup> axle (d) 4<sup>th</sup> axle for Curb-to-Curb test

there is no considered change in the vehicle velocity. Nevertheless, the counter-steering mode generates higher lateral acceleration, as shown in figure 3.12 (b), which can be related to the higher yaw rate at figure 3.12 (c). In addition, the counter-steering at such low speed generates almost zero vehicle sideslip angle, in terms of better tracking performance [107, 108] and low tires' wear [80].

### 3.4.2 Minimum road width test (90-degree turn)

The minimum road width test is conducted at low speed in a tee road's intersection, the vehicle is required to negotiate a 90-degree turn to the right or the left in the intersection and the road width should be determined. The test was repeated by reducing the road width to the least dimension, where a successful turn can be achieved. The crab steering mode is also excluded from this test.

Figure 3.13 shows the path required by the vehicle for each steering mode to make a 90-degree turn. It can be seen that the minimum and narrowest turn is produced by the counter-steering mode, while the largest is performed by the conventional vehicle. It is also recorded that the minimum road widths to perform the maneuver by the counter, fixed 3<sup>rd</sup> axle, and conventional steering modes are 3.7 m, 4.3 m, and 5 m, respectively.

The corresponding average axles' steering angles to perform the maneuver for each



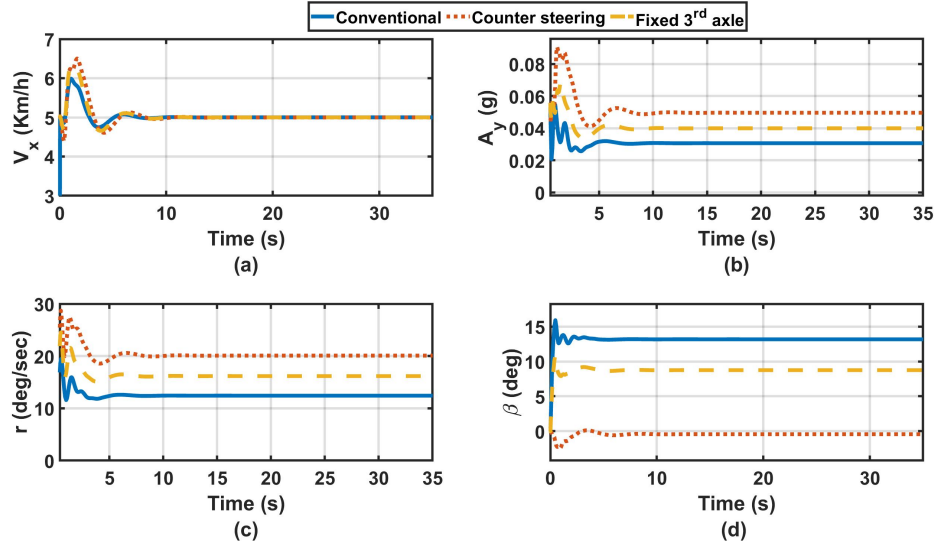


Figure 3.12: (a) Vehicle longitudinal speed (b) Lateral acceleration (c) Yaw response (d) Vehicle sideslip response for Curb-to-Curb test

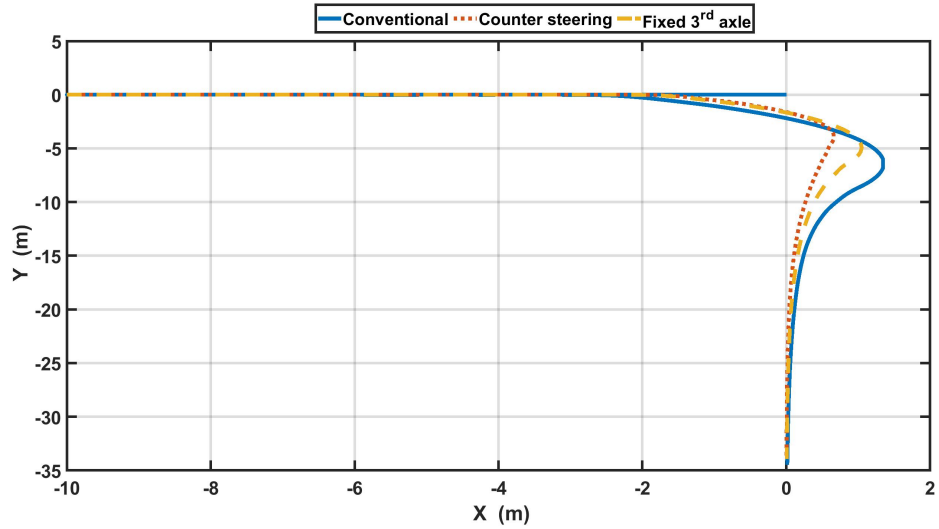


Figure 3.13: Trajectory of each steering mode for 90-degree turn test

case are presented in figure 3.14. It can be observed that the least front steering angle is exhibited by the counter-steering mode, which also performs the maneuver faster than other cases, as can be seen in figure 3.14 (a).

Moreover, the counter-steering mode obtains less longitudinal speed fluctuation and faster settling time as illustrated in figure 3.15 (a). According to figure 3.15 (b), the

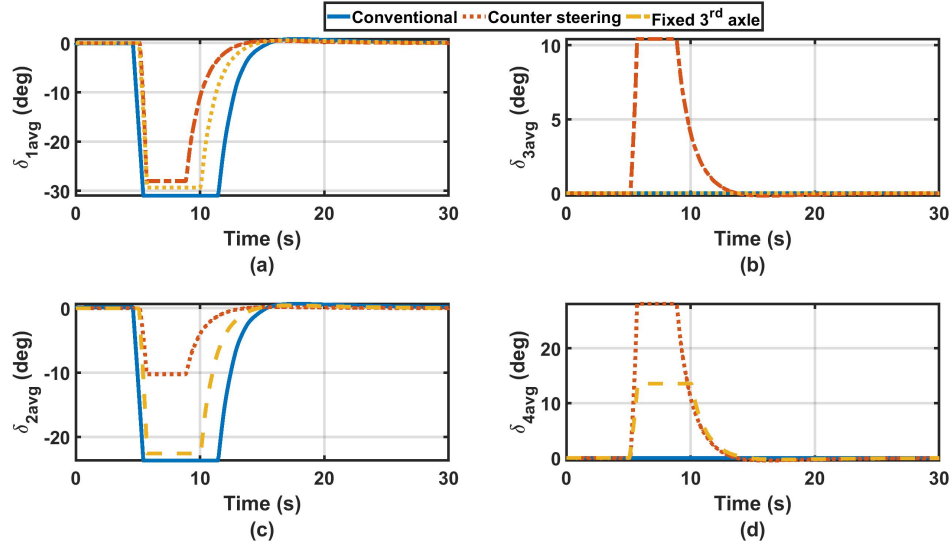


Figure 3.14: Average steering angles of the (a) 1<sup>st</sup> axle (b) 2<sup>nd</sup> axle (c) 3<sup>rd</sup> axle (d) 4<sup>th</sup> for 90-degree turn test

counter-steering also provides less fluctuation but higher lateral acceleration than other cases. Furthermore, steering all wheels in the counter-steering mode resulted in the largest yaw rate, which means higher maneuverability, and almost zero vehicle sideslip. On the other hand, The conventional front steering vehicle has the least maneuverability and the largest sideslip that exceeds 13 degrees.

### 3.4.3 Closed-loop slalom test

In this test, a predefined desired path is generated while the TruckSim's driver model uses the driver sight as feedback to correct the vehicle heading and follow the desired path. The slalom test is performed to assess the maneuverability of all steering modes. The dimension of the conducted test is illustrated in figure 3.16, where  $C_1$  is an entering distance,  $C_2$  and  $C_3$  are the longitudinal and lateral spacing between the cones, respectively. The distance  $Y$  is the lateral distance between the desired path and the cones and  $X$  is the longitudinal distance from the point at which the vehicle starts the maneuver to the end of  $C_2$ .  $d_1$  is the amplitude of the slalom path and  $d_2$  is the distance between one peak (tip) and the following bottom on the desired path. In addition,  $X$  is set to be zero and  $Y$  is set to be equal to half  $C_3$ , and  $d_2$  is equal to  $C_2$ .

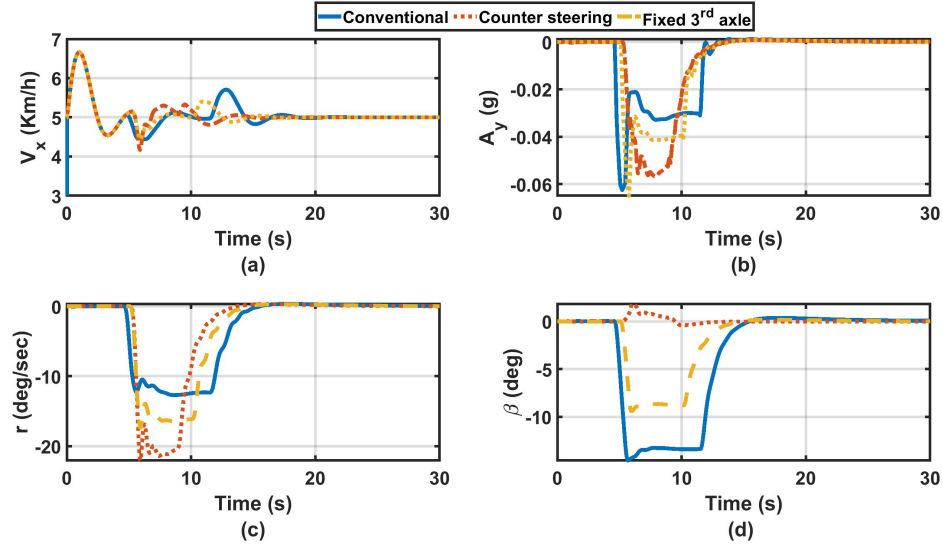


Figure 3.15: (a) Vehicle longitudinal speed (b) Lateral acceleration (c) Yaw response (d) Vehicle sideslip response for 90-degree turn test

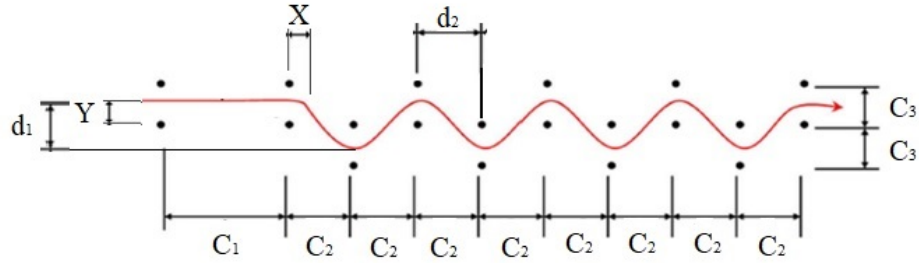


Figure 3.16: NATO AVTP-1 03-30 slalom course (not in scale)

### 3.4.3.1 Low-speed assessment

The test is conducted on a dry surface at low speed ( $V_x = 5 \text{ km/h}$ ). The Cones' longitudinal spacing is set to be  $30 \text{ m}$  and reduced until it reaches the distance at which all steering modes achieve a successful maneuver at  $C_2 = d_2 = 15 \text{ m}$ . Figure 3.17 (a) shows the trajectory for each steering mode, while the corresponding lateral error is shown in figure 3.17 (b). It can be seen that the counter-steering mode has the least lateral error, while the crab steering has the largest error. However, the crab steering maintained the maneuver faster (with the least settling time among all cases). Note that the vehicle position is measured from the vehicle center, however, the TruckSim driver model follows the path from the driver's point of view.

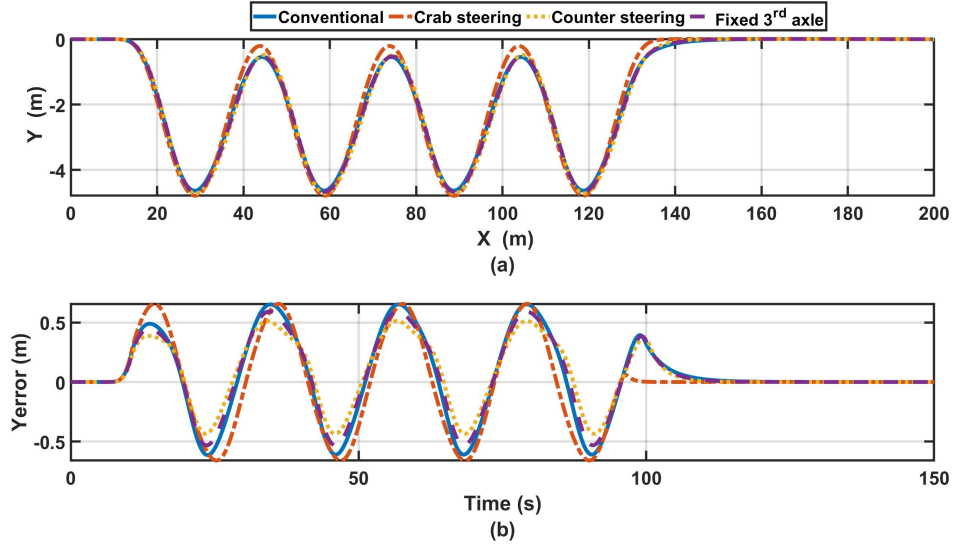


Figure 3.17: (a)Trajectory of each steering mode (b) Lateral error from the desired trajectory at for Slalom maneuver at speed 5 km/h

Figure 3.18 shows the average steering angle exhibited by each axle. It can be observed that the crab steering mode exhibits the largest steering angle, while the counter-steering shows the least, as shown in figure 3.18 (a).

By observing the longitudinal speed response in figure 3.19 (a), it is noticed that the counter-steering has less fluctuation than other cases while the crab steering is the largest. Besides, figure 3.19 (b) shows that the crab steering generates the largest lateral acceleration among the other cases. The crab steering exhibits zero yaw rate due to its diagonal movement which causes a large sideslip that exceeds 20 degrees, as shown in figures 3.19 (c) and 3.19 (d), respectively. On contrary, the counter-steering shows the largest and least yaw rate and sideslip, respectively.

Table 3.1 demonstrates the dimensions of the slalom course at which each case has failed to perform a successful maneuver. Remarkably, the conventional steering and the crab steering modes fail to complete the maneuver without hitting the cones at  $d_2 = 10 \text{ m}$ . Meanwhile, the fixed 3<sup>rd</sup> axle fails at  $d_2 = 8 \text{ m}$  while the counter-steering fails at  $d_2 = 7.5 \text{ m}$ . The slalom course is modified according to each case to achieve a successful maneuver. Moreover, the path is shifted upward with the distance  $\Delta Y$  and/or forward with the distance  $\Delta X$ . The dimension  $d_2$  is increased for certain modes, while the cone spacing is kept the same at  $C_2 = 5 \text{ m}$  for all tests.

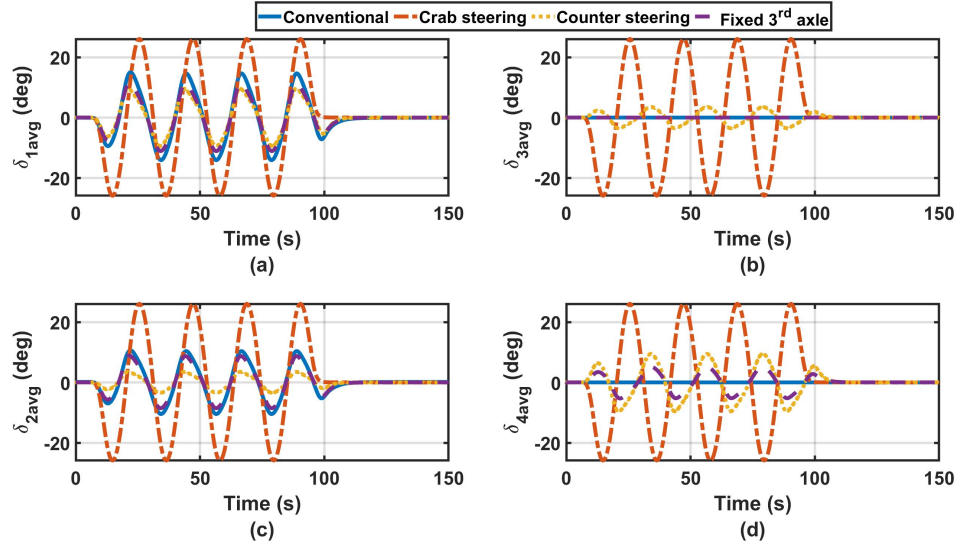


Figure 3.18: Average steering angles of the (a) 1<sup>st</sup> axle (b) 2<sup>nd</sup> axle (c) 3<sup>rd</sup> axle (d) 4<sup>th</sup> for Slalom maneuver at speed 5 km/h

Table 3.1: Low-speed Slalom test summary

Steering mode	Failure	Path modification to pass
Conventional front	$d1 = 5m, d2 = 10m$	$d1 = 6m, \Delta Y = 0.6m$
Crab steering	$d1 = 5m, d2 = 10m$	$d1 = 5m, \Delta X = 1.5m$
Fixed 3 <sup>rd</sup> axle	$d1 = 5m, d2 = 8m$	$d1 = 6.1m, \Delta Y = 0.8m, \Delta X = 1m$
Counter	$d1 = 5m, d2 = 7.5m$	$d1 = 5.35m, \Delta Y = 0.47m, \Delta X = 0.75m$

The impact of the modified course according to each steering mode is interpreted as the driver's steering actions required to maintain a successful maneuver. This is because of the change in the vehicle turning center which changes the turning geometry, except for crab steering mode that performs a diagonal motion. e.g. in the case of the crab steering mode, the driver has to delay the steering action to ensure that the vehicle will perform the diagonal motion to avoid hitting the cones, justifying the changing of  $\Delta X$  to be 1.5 m. For the counter-steering mode, the driver has to consider the swing of the vehicle's rear end. Hence, the driver has to delay the turning action to avoid hitting the cones. In addition, he has to take a wider turn, which reflects the changing of  $\Delta Y$  and  $d_1$  to 0.47 m and 5.35 m, respectively.

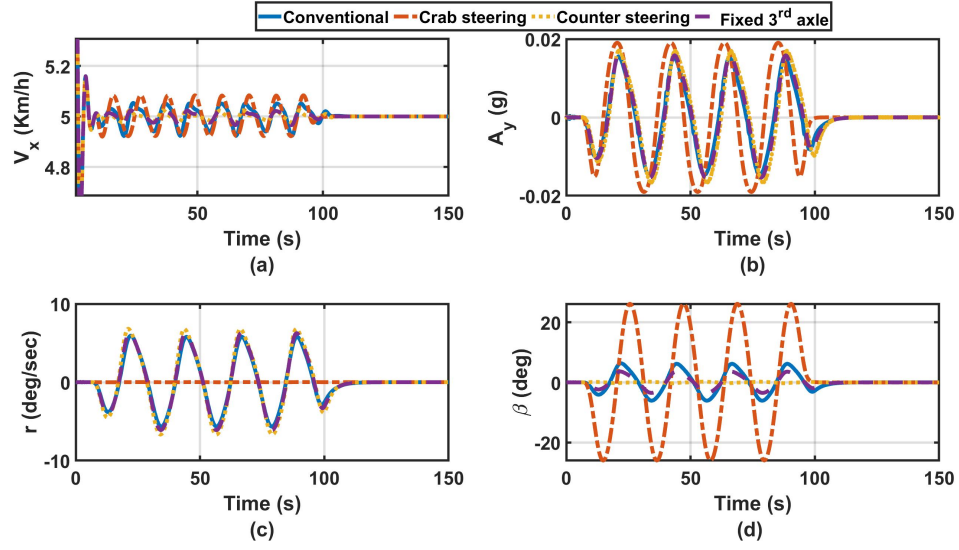


Figure 3.19: (a) Vehicle longitudinal speed (b) Lateral acceleration (c) Yaw response (d) Vehicle sideslip response for Slalom maneuver at speed 5 km/h

### 3.4.3.2 High-speed assessment

The slalom maneuver is conducted at a relatively high speed of 50  $km/h$  with cones' spacing  $C_2 = d_2 = 30\ m$  to have an overview of the vehicle's stability under each steering mode. Figure 3.20 (a) presents the vehicle trajectory for each steering mode. Moreover, the corresponding lateral error is shown in figure 3.20 (b). It is observed that the crab steering has the largest lateral error with a phase shift from other cases, while the counter-steering has the smallest error among all cases.

The average steering angle of the 1<sup>st</sup>, 2<sup>nd</sup>, 3<sup>rd</sup>, and 4<sup>th</sup> axles are shown in figure 3.21 (a), (b), (c), and (d), respectively. The crab steering exhibits the largest axles' steering angle, while other cases almost have less and same front steering angles. It is also observed that the steering angles in the case of the crab steering take a long time to return to zero.

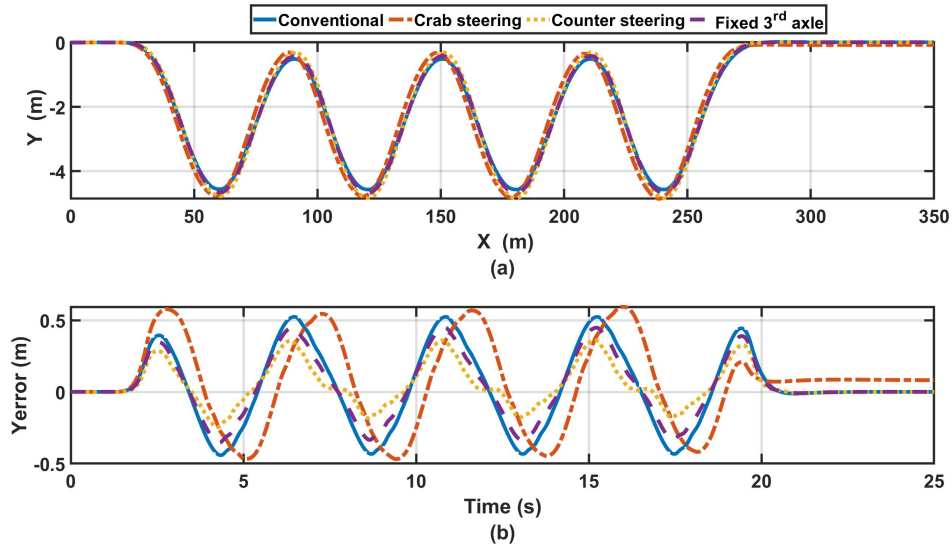


Figure 3.20: (a) Trajectory of each steering mode (b) Lateral error from the desired trajectory for Slalom maneuver at speed 50 km/h

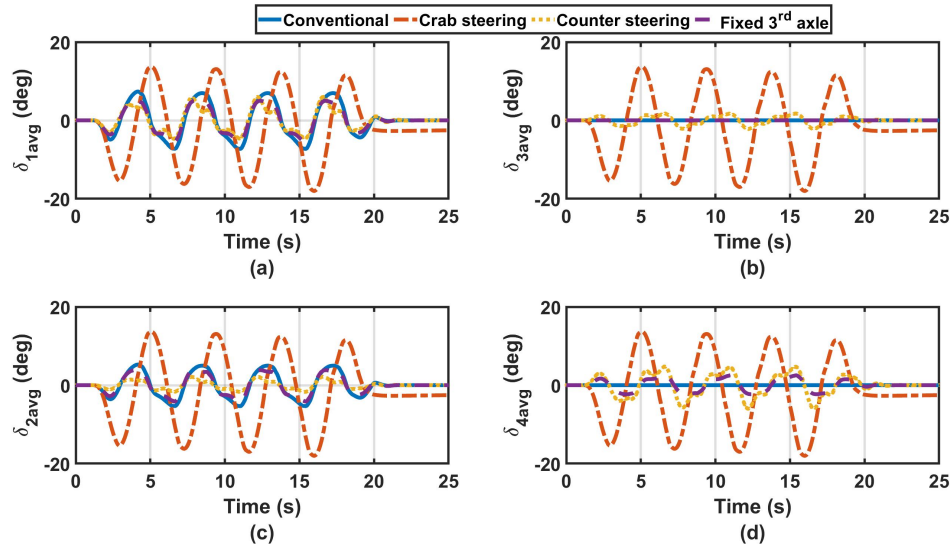


Figure 3.21: Average steering angles of the (a) 1<sup>st</sup> axle (b) 2<sup>nd</sup> axle (c) 3<sup>rd</sup> axle (d) 4<sup>th</sup> for Slalom maneuver at speed 50 km/h

There is no significant change in the longitudinal speed response except for the crab steering mode that generates large speed variations, as figure 3.22 (a). In addition, the lateral acceleration response is almost the same for all cases as can be shown in figure 3.22 (b). By observing the yaw response in figure 3.22 (c), it's remarkable that the

counter-steering generates the largest yaw rate, while the crab steering has the smallest. The crab steering generates the largest sideslip followed by the counter steering, as shown in figure 3.22 (d).

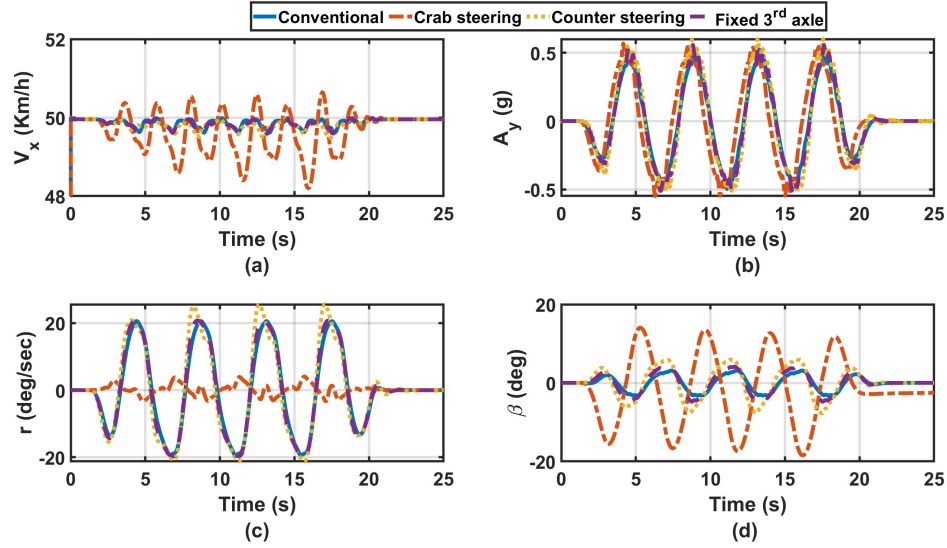


Figure 3.22: (a) Vehicle longitudinal speed (b) Lateral acceleration (c) Yaw response (d) Vehicle sideslip response for Slalom maneuver at speed 50 km/h

It is deserved to be mentioned that by performing the slalom maneuver at higher speed, the conventional steering and fixed 3<sup>rd</sup> axle steering modes failed at speed 60 *km/h*, while the counter-steering failed at 55 *km/h* due to the large yaw rate and sideslip generated. Moreover, the crab steering mode fails at a speed equal to 65 *km/h*.

### 3.5 Chapter summary

In this chapter, several steering modes named; front, crab, fixed 3<sup>rd</sup> axle, and counter steering were developed for an 8x8 combat vehicle. The vehicle steerability and maneuverability were evaluated for each steering mode by conducting standard TOP-2-2-609 and modified NATO AVTP-1 03-30 maneuvers and the closing remarks are as follows:

- As the vehicle center of turning shifts towards the vehicle center of gravity, the maneuverability at low speed is enhanced.
- The counter-steering mode generates almost zero vehicle's sideslip at low speed



hence decreasing the tires' wear.

- The crab steering shows the ability to generate a perfect diagonal motion with no rear-end swing, which can be effective in performing tight maneuvers where there are limitations on performing yaw motion.

The following recommendations can be applied to maximize vehicle maneuverability:

- Considering a steering combination by switching between the crab and counter steering modes is very effective at low speed, based on the available spaces to perform tight maneuvers.
- The high-speed test shows that implementing parallel steering for the rear axles has a tremendous effect on reducing the vehicle yaw rate. Consequently, it decreases the vehicle's rear-end swing and enhances vehicle stability.
- An active rear steering controller is needed at high speed to independently control the rear axles' steering angles to provide high stability and agility for different driving conditions and also increases the tires' life span due to less wear.
- The modifications made in the low-speed slalom test can give an insight into some perspectives that have to be considered in path generation for future autonomous applications.

## CHAPTER 4

### Active Rear Axles Steering Controller

#### 4.1 Introduction

This chapter investigates the effect of the incorporation of the active steering of the rear axles on the vehicle cornering performance for conventional and autonomous driving. For normal operation, a new ARS technique that utilizes the steering of the rear 3<sup>rd</sup> and 4<sup>th</sup> axles with no dependency on the reference model is introduced. The controller is developed using an LQR controller, which is integrated with a low-speed feedforward ZSS controller. Furthermore, the controller is evaluated and compared with the uncontrolled vehicle and an active 4<sup>th</sup> axle steering that was introduced in previous study [4]. After that, the same ARS technique is utilized to develop a novel adaptive Integral Sliding Mode controller, which is suitable for driving on a rough-rigid terrain. Eventually, autonomous driving is investigated in terms of path-following and stability performances. For that purpose,  $H_\infty$  controllers are developed to design a front-steering and AWS path-following controllers, and an ARS stability controller. Moreover, a frequency domain analysis is conducted to study the controllers' robustness. Then, the path-following controllers are compared with an integrated front steering-ARS controller to show the advantages and limitations of each controller.

#### 4.2 Development of an optimal ARS controller

In this technique, the rear axles are controlled independently using a Linear Quadratic Regulator (LQR). In addition, the controller is designed to attain a zero vehicle's sideslip, where a large weight is assigned to the sideslip. Moreover, to prevent contradiction between generating a sufficient yaw rate and maintaining a Zero SideSlip (ZSS), a zero yaw rate reference is applied. However, a small weight is assigned to the yaw rate so the controller can violate the zero yaw rate constrain and generate a sufficient yaw rate to perform a maneuver. The proposed controller consists of another control term that is added to the LQR controller. This term is a feedforward controller that is designed to

maintain a ZSS at a very low speed ( $<20$  km/h). The 4<sup>th</sup> axle's steering angle is determined based on the steady-state equation of the vehicle sideslip as a function of the front axle steering angle and the vehicle velocity to satisfy a ZSS condition. In addition, the 3<sup>rd</sup> axle's steering angle is determined by a ratio to the 4<sup>th</sup> axle's steering angle based on Ackermann steering geometry.

### 4.2.1 Single-track model

Figure 4.1 shows 2-DoF bicycle model of the four-axle steering combat vehicle. A single-track mathematical model (bicycle model) is used to drive the state-space equation to the vehicle. The mathematical model has been linearized based on the following assumptions:

1. Negligible longitudinal and lateral load transfer.
2. A small angle approximation is used.
3. All tires are identical.
4. Linear tires characteristics on hard surface (No off-road analysis).
5. Wheels' camber, tow, and caster angles are neglected.
6. Constant longitudinal speed.

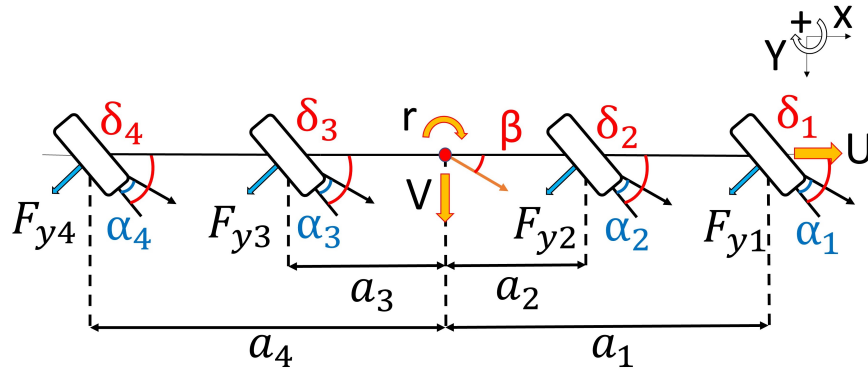


Figure 4.1: Four-axle steering 8x8 vehicle bicycle model

The slip angles of the tire are defined using equation 4.1.

$$\alpha_i = \delta_i - \tan^{-1}\left(\frac{V + a_i r}{U}\right) \quad (4.1)$$

Where  $\delta$  is the average steering angle of the tire,  $V$  and  $U$  are the vehicle's lateral and longitudinal velocities respectively,  $a$  is the distance between the vehicle Center of Gravity (CoG) and the desired axle, where  $a$  has positive value for axles in front of the CoG and negative value for axles behind the vehicle CoG, and  $r$  is the vehicle yaw rate. Applying small slip and steering angles assumptions where  $V/U$  is equal to the vehicle sideslip  $\beta$ :

$$\alpha_i = \delta_i - (\beta + \frac{a_i r}{U}) \quad (4.2)$$

From the linear tire characteristics assumption, the lateral cornering forces  $F_y$  can be determined from the following equation as a function of the tire cornering stiffness  $C_\alpha$  and the tire slip angle  $\alpha$ :

$$F_{yi} = C_{\alpha i} \alpha_i \quad (4.3)$$

According to Ackerman steering geometry, the steering angle of the  $2^{nd}$  steering axles can be determined as function of the  $1^{st}$  axle average steering angle as follows [4, 104], where  $c_{21}$  is the steering ratio between the average steering angle of the  $2^{nd}$  axle to the  $1^{st}$  axle:

$$\delta_2 = c_{21} \delta_1 \quad (4.4)$$

The lateral and yaw equations of motion can be expressed as in equations 4.5 and 4.6, respectively, where  $m$  is the vehicle mass and  $I_{zz}$  is the vehicle mass moment of inertia about the Z axis:

$$m(\dot{V} + Ur) = F_{y1} + F_{y2} + F_{y3} + F_{y4} \quad (4.5)$$

$$I_{zz} \dot{r} = a_1 F_{y1} + a_2 F_{y2} + a_3 F_{y3} + a_4 F_{y4} \quad (4.6)$$

Substituting from equations 4.1 to 4.4 in equation 4.6 will result of equation 4.7. Combining this equation with equation 4.8 presents the state-space model of the vehicle,

where the system states and desired output are presented respectively.

$$\begin{bmatrix} \dot{\beta} \\ \dot{r} \end{bmatrix} = \begin{bmatrix} a_{11} & a_{12} \\ a_{21} & a_{22} \end{bmatrix} \begin{bmatrix} \beta \\ r \end{bmatrix} + \begin{bmatrix} \frac{C_{\alpha 1} + c_{21}C_{\alpha 2}}{mU} & \frac{C_{\alpha 3}}{I_{zz}} & \frac{C_{\alpha 4}}{I_{zz}} \\ \frac{a_1C_{\alpha 1} + a_2c_{21}C_{\alpha 2}}{I_{zz}} & \frac{a_3C_{\alpha 3}}{I_{zz}} & \frac{a_4C_{\alpha 4}}{I_{zz}} \end{bmatrix} \begin{bmatrix} \delta_1 \\ \delta_3 \\ \delta_4 \end{bmatrix} \quad (4.7)$$

$$\begin{aligned} \text{Where } a_{11} &= \frac{-C_{\alpha 1} - C_{\alpha 2} - C_{\alpha 3} - C_{\alpha 4}}{mU} \\ a_{12} &= \frac{-a_1C_{\alpha 1} - a_2C_{\alpha 2} - a_3C_{\alpha 3} - a_4C_{\alpha 4} - mU^2}{mU^2} \\ a_{21} &= \frac{-C_{\alpha 1} - C_{\alpha 2} - C_{\alpha 3} - C_{\alpha 4}}{I_{zz}} \\ a_{22} &= \frac{-a_1^2C_{\alpha 1} - a_2^2C_{\alpha 2} - a_3^2C_{\alpha 3} - a_4^2C_{\alpha 4}}{I_{zz}U} \end{aligned}$$

$$\begin{bmatrix} \beta \\ r \end{bmatrix} = \begin{bmatrix} 1 & 0 \\ 0 & 1 \end{bmatrix} \begin{bmatrix} \beta \\ r \end{bmatrix} + \begin{bmatrix} 0 & 0 & 0 \\ 0 & 0 & 0 \end{bmatrix} \begin{bmatrix} \delta_1 \\ \delta_3 \\ \delta_4 \end{bmatrix} \quad (4.8)$$

#### 4.2.2 ZSS controller

ZSS is a feedforward controller, where the average steering angle of the 4<sup>th</sup> axle is determined based on the vehicle longitudinal velocity and the average steering angle of the 1<sup>st</sup> axle as illustrated in the block diagram as shown in Figure 4.2. The mathematical model for four-wheel steering in equation 4.10 has been used [109] to drive the steady-state equations of the vehicle by rearrange the equations and replace  $\delta_4$  by equation 4.9, where  $c_{34}$  is the average steering angle of the 3<sup>rd</sup> axle to the 4<sup>th</sup> one resulting in equation 4.10:

$$\delta_3 = c_{34}\delta_4 \quad (4.9)$$

$$\begin{bmatrix} \dot{\beta} \\ \dot{r} \end{bmatrix} = \begin{bmatrix} a_{11} & a_{12} \\ a_{21} & a_{22} \end{bmatrix} \begin{bmatrix} \beta \\ r \end{bmatrix} + B_{zss} \begin{bmatrix} \delta_1 \\ \delta_4 \end{bmatrix} \quad (4.10)$$

Where  $B_{zss} =$

$$\begin{bmatrix} \frac{C_{\alpha 1} + c_{21}C_{\alpha 2}}{a_1C_{\alpha 1} + a_2c_{21}C_{\alpha 2}} & \frac{C_{\alpha 4} + c_{34}C_{\alpha 3}}{a_4C_{\alpha 4} + a_3c_{34}C_{\alpha 3}} \\ \frac{mU}{I_{zz}} & \frac{mU}{I_{zz}} \end{bmatrix}$$

The steady-state model for ZSS controller can be derived by substituting in all the transient parameters by zero let  $\dot{\beta} = \dot{r} = 0$  the steady-state model will be as follows:

$$\begin{bmatrix} \beta \\ r \end{bmatrix}_{ss} = - \begin{bmatrix} a_{11} & a_{12} \\ a_{21} & a_{22} \end{bmatrix}^{-1} B_{zss} \begin{bmatrix} \delta_1 \\ \delta_4 \end{bmatrix} \quad (4.11)$$

Using the steady-state model (equation 4.11) for an all-wheel steering vehicle, where all wheels steering angles is related based on Ackermann condition, the steady-state vehicle sideslip equation can be separated as a function of  $\delta_1, \delta_4$  and  $U$ . Starting with this equation the vehicle sideslip can be assumed to be zero and the ratio between  $\delta_1$  and  $\delta_4$  for ZSS at different forward velocities can be determined as in Figure 4.3. In this method, the 3<sup>rd</sup> axle average steering angle  $\delta_3$  is related with  $\delta_4$  by the Ackerman steering geometry.

$$\beta_{ss} = f(\delta_1, \delta_4, U) \quad (4.12)$$

The steering of the rear axle based on a steady-state equation has a great effect while the vehicle is operating in the linear region. However, in the nonlinear region, the steady-state equation is not held anymore. Therefore, the feedforward term of the steering input is taken at a speed range from 0 km/h to 50 km/h and is neglected at a higher speed.

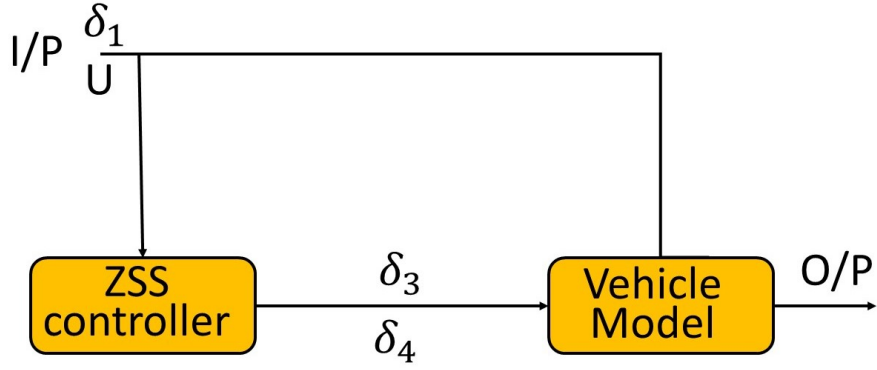


Figure 4.2: Figure 2 ZSS controller block diagram

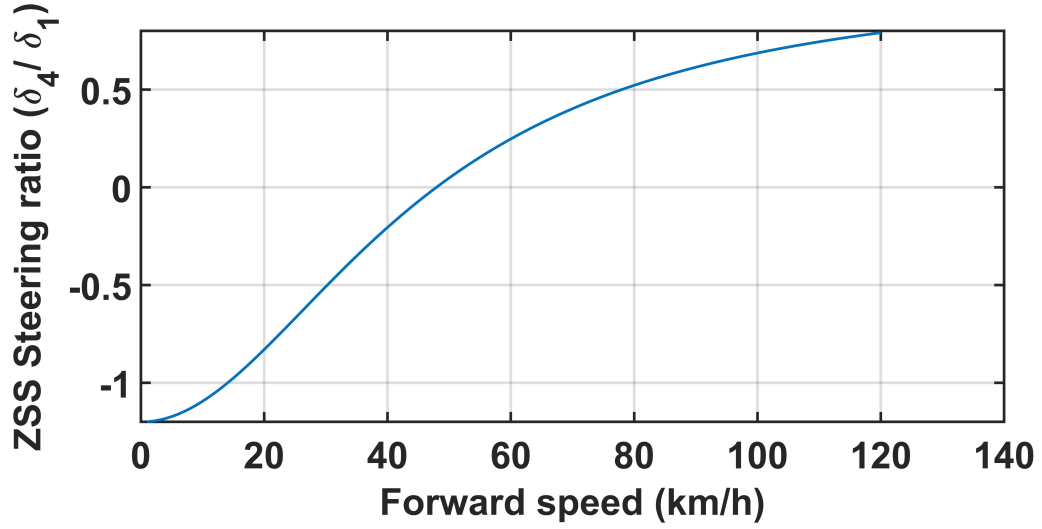


Figure 4.3: The ratio between 4<sup>th</sup> and 1<sup>st</sup> steering axles for zero sideslip condition as a function of forward speed

### 4.2.3 Optimal controller design

LQR is a feedback control system (shown in Figure 4.4), which is designed to satisfy and minimize a quadratic cost function, as shown in equation 4.13, to maximize the required performance, which is limiting the vehicle sideslip. The controller gains matrix is illustrated in equation 4.14 and the controller output (system input) is shown in equation 4.15 :

$$J = \int_{t_o}^t (X^T Q X + u^T R u) dt \quad (4.13)$$

$$K = R^{-1}(B^T P) \quad (4.14)$$

$$u_{LQR} = -KX \quad (4.15)$$

Where  $X$  is the state vector ( $\beta$  and  $r$ ),  $Q$  is the states weight matrix,  $R$  is the control input weight matrix,  $u$  is the control vector ( $\delta_3$  and  $\delta_4$ ),  $K$  is the controller gain, and  $B$  is system Input matrix.  $P$  is a positive definite matrix, which can be determined by solving Riccati's equation [110], as in equation 4.16.

$$A^T P + P A - P B R^{-1} B^T P + Q = 0 \quad (4.16)$$

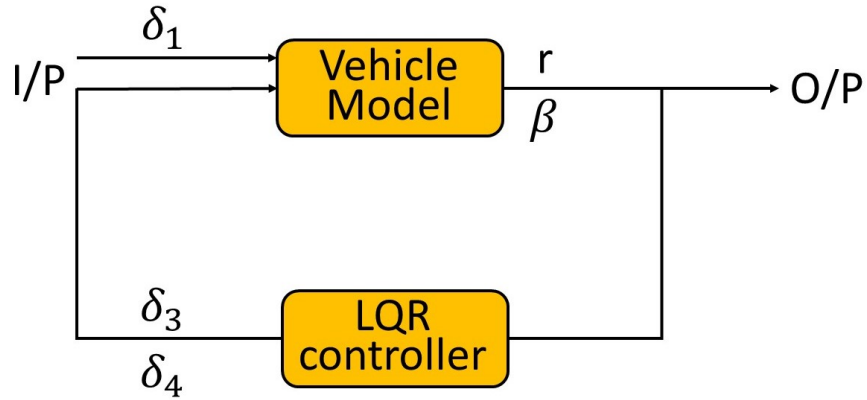


Figure 4.4: LQR controller block diagram

To derive the gain matrix for the LQR control system the weight function of the state variables and output variables  $Q$  and  $R$  should be tuned according to Bryson's rule [111, 112, 113, 114, 84, 115] as follows:

$$Q = \rho \begin{bmatrix} \frac{1}{X_{1(max.)}^2} & 0 \\ 0 & \frac{1}{X_{2(max.)}^2} \end{bmatrix} \quad (4.17)$$



$$R = \begin{bmatrix} \frac{1}{Y_{1(max.)}^2} & 0 \\ 0 & \frac{1}{Y_{2(max.)}^2} \end{bmatrix} \quad (4.18)$$

Where  $\rho$  is a tuning positive scalar,  $X_1$  and  $X_2$  are the maximum allowed error of the states  $(\beta, r)$ , respectively, which are determined from equations 4.19 and 4.20 [4, 104, 116].  $Y_1$  and  $Y_2$  represent the average permissible steering angles for the 3<sup>rd</sup> and 4<sup>th</sup> axles respectively, which can be determined from the physical maximum steering of each axle.

$$X_{1(max.)} = \beta_{max.} = \tan^{-1}(0.02\mu g) \quad (4.19)$$

$$X_{2(max.)} = r_{max.} = \frac{0.75\mu g}{U} \quad (4.20)$$

By determining  $Q$  and  $R$  matrices,  $P$  can be determined by equation 4.16. After that by substituting  $P$  in equation 4.14, the desired controller gain can be determined. Note that, since the control system does not control the steering wheel of the first axle it is considered as a disturbance to the system and final control law to the closed-loop system as follows:

$$u_{total} = u_{ZSS} + u_{LQR} \quad (4.21)$$

#### 4.2.4 Evaluation and simulation results

The evaluation is utilized using the 22 degree of freedom nonlinear model that is presented in chapter 3, section 3.2. A Matlab/Simulink is used as a co-software with Truck-Sim for implementing the controller and performing all simulations in this chapter.

The proposed controller is evaluated and compared with the conventional vehicle and an active 4<sup>th</sup> axle vehicle (using only the LQR controller). The handling characteristics of the vehicle have been assessed by applying several maneuvers that are conducted in previous studies [4, 104, 31, 5]. The Skid Pad test has been conducted to evaluate the steady-state handling characteristics of the vehicle, while FMVSS 126 ESC test was

used to evaluate the transient state handling characteristics on a slippery surface at CoF 0.2.

In addition, the vehicle has been tested under severe maneuvers, where a sinusoidal steering input with increasing amplitude has been applied to the vehicle for a while. Further information about the tests that can be used to judge whether the vehicle has good handling characteristics or not and how to evaluate it can be found in [117, 118].

#### 4.2.4.1 100-ft Circle Skid Pad (Constant Radius):

The 100-ft radius circle Skid Pad test is performed, where the steering input required to maintain a constant radius and the dynamic response are measured. The test is a closed-loop test (driver in the loop) performed to follow the same circular trajectory, where all configurations (conventional and controlled) succeeded to follow the designed path.

It can be noticed from Figure 4.5 that the steering angle of the controlled vehicle using ZSS-LQR is lower than other cases at low speed ( $<40$  km/h). This is because of the effect of the counter-steering of the  $4^{th}$  and  $3^{rd}$  axles. This makes the  $4^{th}$  axle steering angle in the case of ZSS-LQR is more than the vehicle with fixed  $3^{rd}$  axle. This behaviour indicates that the maneuverability and the minimum turning radius of the vehicle will be increased at low speed. Meanwhile, the steering angle increases at a higher speed where the  $3^{rd}$  and  $4^{th}$  axles steer in the same direction as the front axles.

Figure 4.6 (a) shows the longitudinal velocity history with time. The speed drop in case of ZSS-LQR controller within a range not more than  $1$  km/h, while in case of  $4^{th}$  axle steering it has been more. Figure 4.6 (d) shows the vehicle sideslip response with time. The proposed controller shows superiority in maintaining minimum sideslip till the time reaches 12 sec, which corresponds to a speed  $<41$  km/h. After that, the sideslip is maintained at  $0.5$  deg, which is less than the conventional vehicle. Meantime, the vehicle with only active  $4^{th}$  axle produces less sideslip, almost reaches zero, at a high steady speed ( $>41$  km/h), which indicates better stability and priority than other cases. However, this priority can be neglected as the vehicle with active  $4^{th}$  and  $3^{rd}$  axles (ZSS-LQR) is still able to give sufficient sideslip angle to maintain the stability, which makes it recommended to be used at low and high speed.

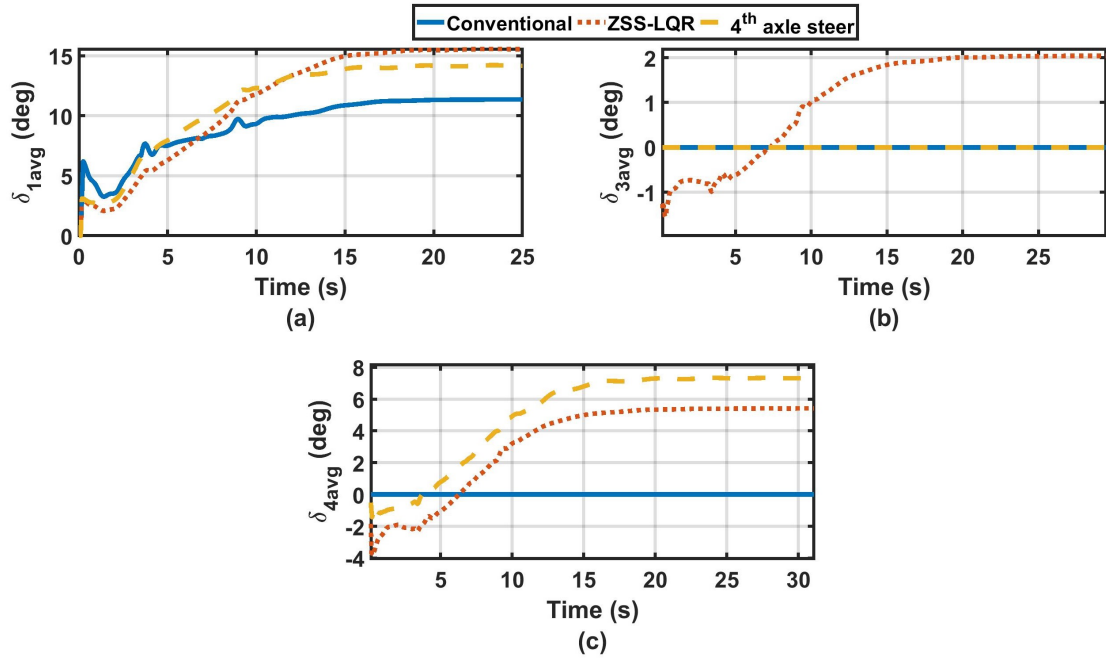


Figure 4.5: Average steering angles of the (a) 1<sup>st</sup> axle (b) 2<sup>nd</sup> axle (c) 3<sup>rd</sup> axle (d) 4<sup>th</sup> for skid-pad test

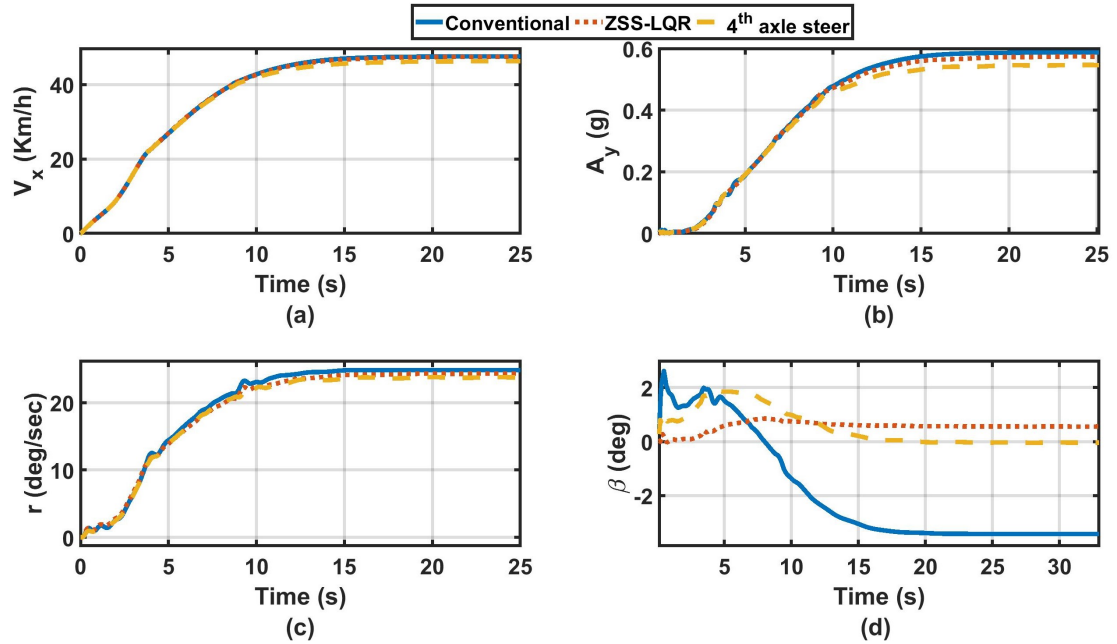


Figure 4.6: (a) Vehicle longitudinal speed (b) Lateral acceleration (c) Yaw response (d) Vehicle sideslip response skid-pad test

#### 4.2.4.2 FMVSS 126 ESC Test at road C.O.F 0.2 at forward speed 60 km/h:

This test has been conducted to evaluate electronic stability control systems (ESC). The test is an open-loop test, where a sine with dwell steering input is applied to the vehicle and the vehicle response versus time should be evaluated [119]. Figure 4.7, shows the vehicle trajectory for all cases at road surface of 0.2 CoF and longitudinal velocity  $60 \text{ km/h}$ . The lateral displacement of the controlled vehicle is less than the conventional vehicle due to the active steering of the rear axles, which are in the same direction as the front axles steering.

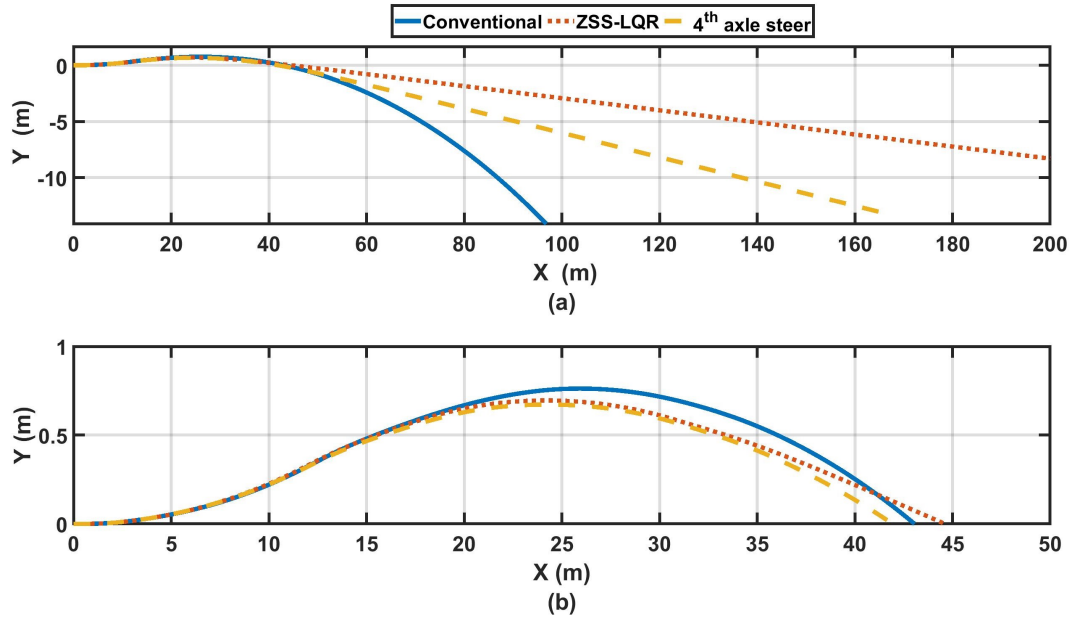


Figure 4.7: Vehicle trajectory for FMVSS maneuver at  $\mu=0.2$  and speed 60 km/h

Figure 4.8, show the variations in the steering wheel angle and the average road wheels steering angles for the 1<sup>st</sup>, 3<sup>rd</sup> and the 4<sup>th</sup> axles. It can be observed that the controlled vehicle same-phase steering behaviour (steering in the same direction as the front axle), which results in decreasing the vehicle maneuverability and increasing stability. From observing the settling time of the steering angles, a faster stabilization can be noticed in the vehicle that is controlled with the ZSS-LQR controller, while the one controlled by LQR utilizes only the 4<sup>th</sup> axle takes a longer time to be stable.

Figure 4.9 (a) shows the lateral accelerations for all cases. Notably, the proposed controller stabilized the vehicle faster than other cases (almost in 2.7 seconds), while the

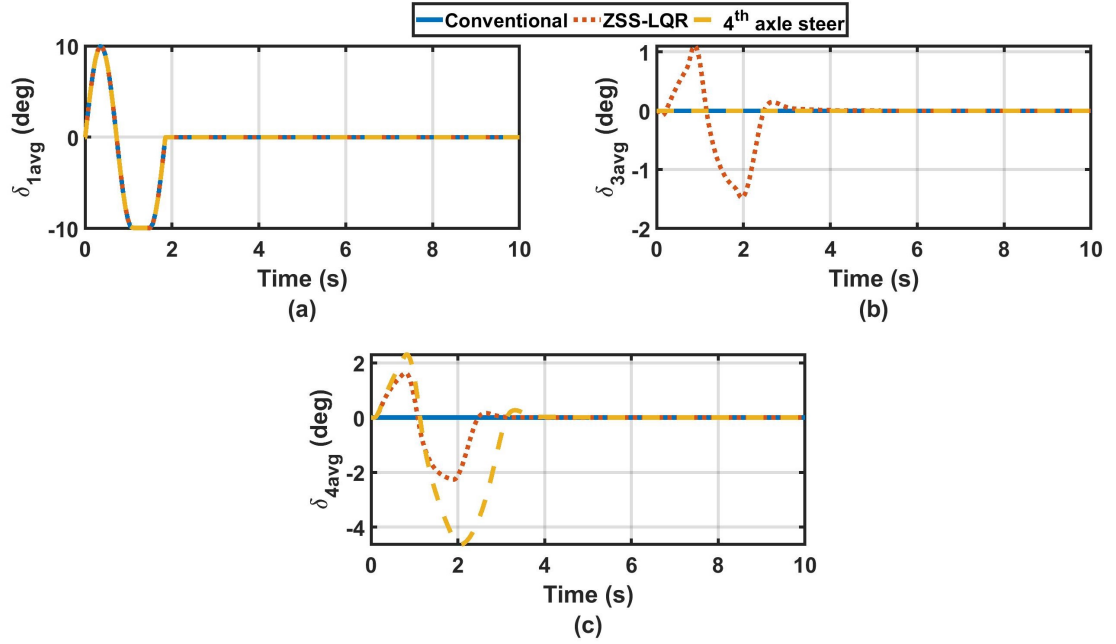


Figure 4.8: Average steering angles of the (a) 1<sup>st</sup> axle (b) 2<sup>nd</sup> axle (c) 3<sup>rd</sup> axle (d) 4<sup>th</sup> for FMVSS maneuver at  $\mu=0.2$  and speed 60 km/h

conventional vehicle took 9 seconds to be stable on such a low friction surface. Similarly, the yaw rate response followed the same behaviour as shown in Figure 4.9 (c).

Figure 4.9 (d) shows the vehicle sideslip angle response, where the vehicle controlled by the ZSS-LQR controller produced the minimum sideslip (maximum  $\pm 0.67$ ) and reaches the steady-state faster than other cases and with fewer oscillations. Meanwhile, the vehicle that has only active 4<sup>th</sup> axle (LQR controller) stabilized faster than the conventional one. This concludes that ARS is recommended to stabilize the vehicle at slippery surfaces generally. Simultaneously, activation of both 3<sup>rd</sup>, and 4<sup>th</sup> axles is better than using only active 4<sup>th</sup> axle.

#### 4.2.4.3 Open Loop Step Slalom Test:

gradually increased. The vehicle is driven with a speed of 65 km/h on a dry surface with CoF equal to 1, which increases the chance of vehicle rollover. Figure 4.10 shows the corresponding vehicle trajectory for the designed steering input. The figure shows that ARS vehicles succeeded to finish the maneuver and maintain stability, while the conventional vehicle didn't, as presented in figure 4.11.

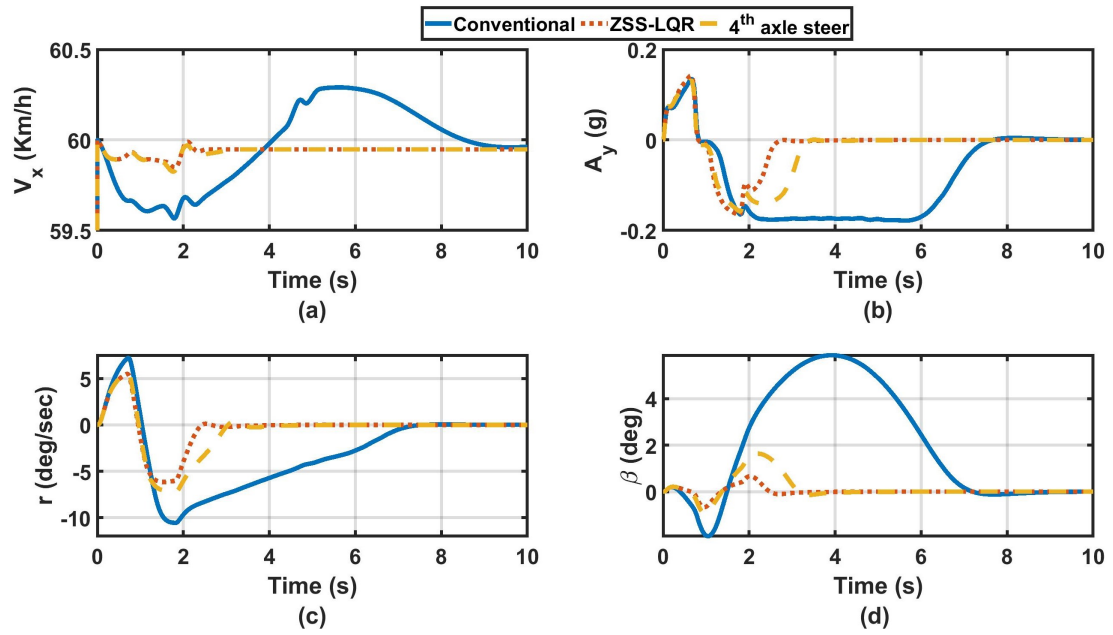


Figure 4.9: (a) Vehicle longitudinal speed (b) Lateral acceleration (c) Yaw response (d) Vehicle sideslip response for FMVSS maneuver at  $\mu=0.2$  and speed 60 km/h

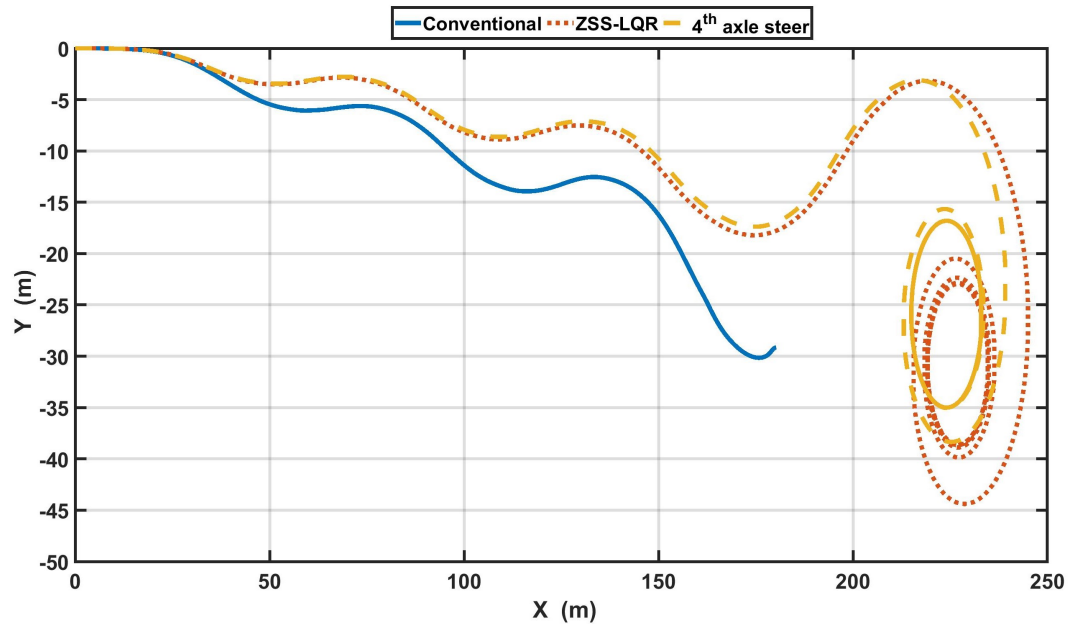


Figure 4.10: Vehicle trajectory for step slalom test

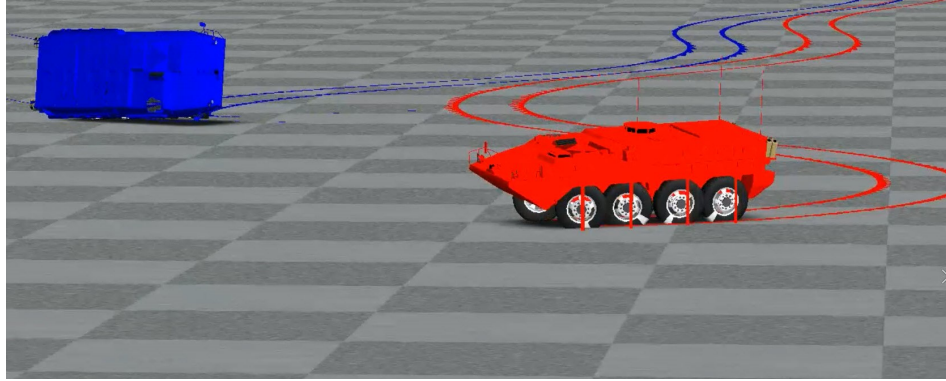


Figure 4.11: Illustration of the conventional vehicle in blue in comparison with controlled one in red

Figure 4.12 (a) shows the designed input average steering angle of the 1<sup>st</sup> axle and the corresponding average steering angle at the 3<sup>rd</sup> and 4<sup>th</sup> axles for all cases is presented in figure 4.12 (b) and (c), respectively. It can be noticed that all the steering axes point in the same direction as the front axle until the front axle steering angle is fixed. After that, the steering angles of the vehicle controlled by both 3<sup>rd</sup>, and 4<sup>th</sup> axles (ZSS-LQR controller) started to change slowly to perform a counter-steering with a small steering angle, which occurred because of the decrease in the speed. On the other hand, the vehicle controlled by only 4<sup>th</sup> axle (LQR controller) performed a same-phase steering behaviour and the 4<sup>th</sup> axle steering angle remains constant regarding the change in the vehicle speed.

The vehicle longitudinal velocity associated with the test has been illustrated in figure 4.13 (a). It is observed that the controlled vehicles' speed kept decreasing until reaching 25 km/h, While the conventional vehicle shows a sudden drop in its velocity. The lateral acceleration and yaw rate response are presented in figure 4.13 (b) and (c), respectively. The figures illustrate that the controlled vehicles kept the lateral acceleration below the rollover threshold and consequently prevent rollover. On the other hand, the conventional vehicle lateral acceleration increased over the rollover threshold resulting in a vehicle rollover. The vehicle sideslip response can be observed from figure 4.13 (d). The figure shows that the vehicle that is controlled with an active 3<sup>rd</sup>, and 4<sup>th</sup> axles produced the minimum sideslip angle (0.04 deg), while the one that is controlled by only the 4<sup>th</sup> axle generated higher sideslip angle (4.6 deg). These results indicate higher stability in the case of actively controlled the 3<sup>rd</sup>, and 4<sup>th</sup> axles than controlling only the

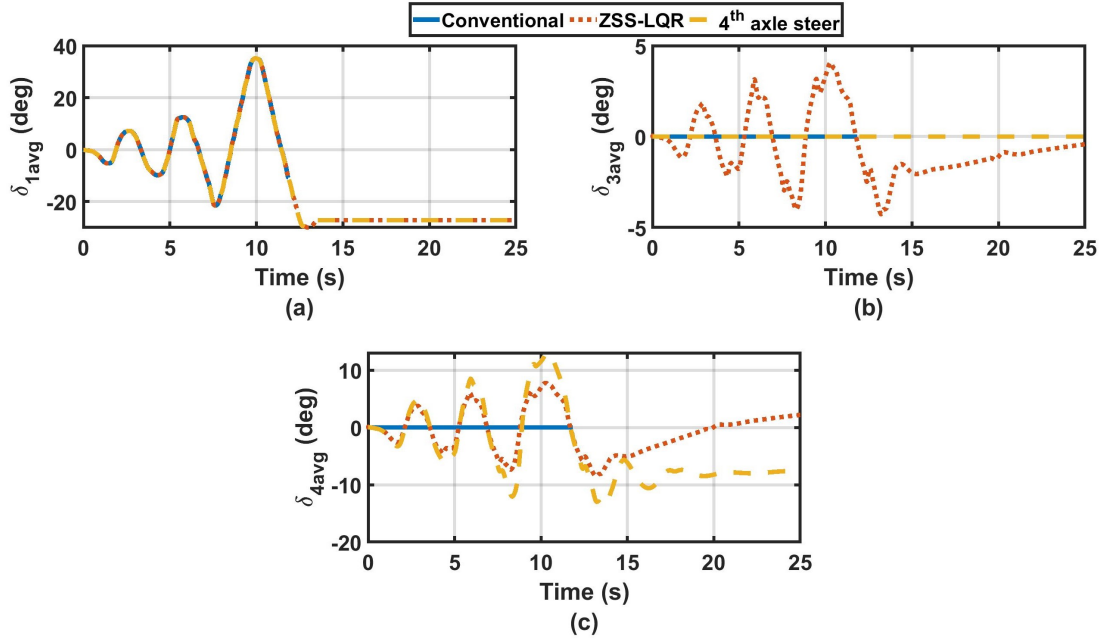


Figure 4.12: Average steering angles of the (a)1<sup>st</sup> axle (b)2<sup>nd</sup> axle (c)3<sup>rd</sup> axle (d)4<sup>th</sup> for for step slalom test

4<sup>th</sup> axle.

### 4.3 Development of an ARS for rough-rigid terrains operation

This section introduces a new synthesized cost function to optimize a gain-schedule controller that ensures the stability of the closed-loop control system at all operating conditions with minimal control effort. Besides, genetic programming is used to introduce a control law that can replace the generated high-dimensional gain-scheduled controller to overcome implementation complexity in the future. Furthermore, due to the lack of research studies that cover multi-axle vehicles' stability over rough terrain, this chapter fills the gap and introduces an ISMC-based controller to enhance the vehicle's lateral stability when operated on rough terrain at different driving conditions. The results are discussed in detail following virtual testing and evaluation in comparison with the optimal LQR controller that was introduced in detail in section 4.2.



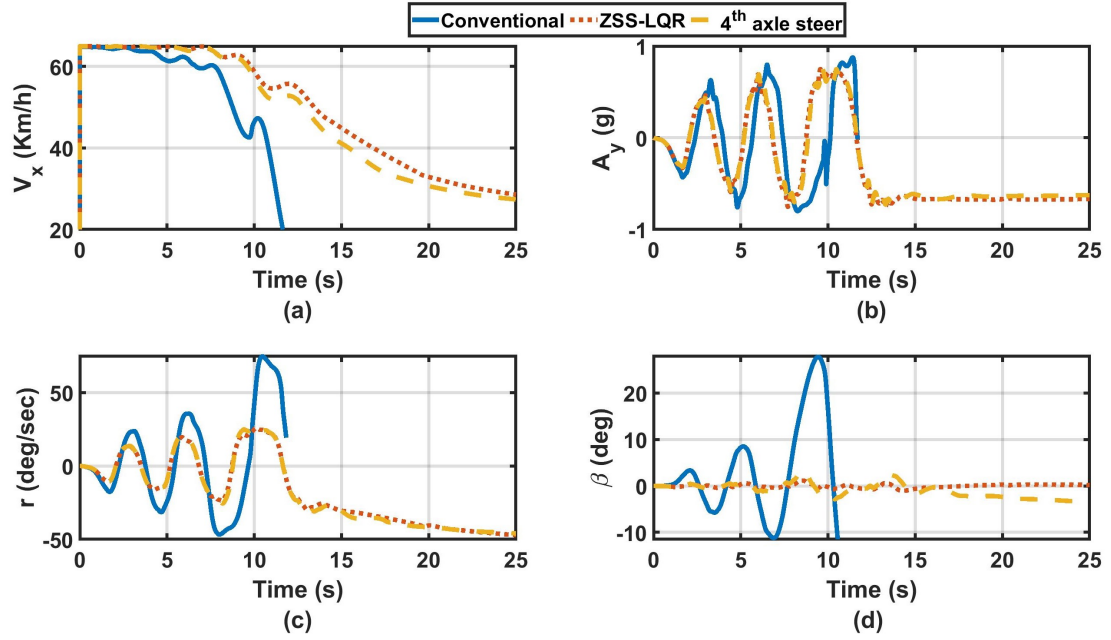


Figure 4.13: (a) Vehicle longitudinal speed (b) Lateral acceleration (c) Yaw response (d) Vehicle sideslip response for step slalom test

### 4.3.1 Disturbed single-track model

The bicycle model that was introduced in section 4.2.1 is used to design the controller. In addition, disturbances are added with the assumption that the upper bounds of all external disturbances are known to drive the disturbed model.

The equation of motion in the lateral direction can be presented as in equation 4.22 where,  $m$  is the vehicle mass,  $V$  and  $U$  are the vehicle lateral and longitudinal velocities,  $r$  is the yaw rate, and  $F_{yi}$  is the lateral force act on  $i^{th}$  axle. In addition, any disturbance  $w_d$  to the vehicle such as side wind or road irregularities can be presented as a force and moment disturbance  $\Delta_{Fy}$  and  $\Delta_{Mz}$ , respectively.

$$m(\dot{V} + Ur) = F_{y1} + F_{y2} + F_{y3} + F_{y4} + \Delta_{Fy} \quad (4.22)$$

Furthermore, the summation moment about the Z-axis can be represented as in equation 4.23, where  $I_{zz}$  is the vehicle's mass moment of inertia about the same axis.

$$I_{zz}\dot{r} = a_1F_{y1} + a_2F_{y2} + a_3F_{y3} + a_4F_{y4} + \Delta_{Mz} \quad (4.23)$$

By substituting from equations 4.1 to 4.4 in equations 4.22 and 4.23, the state-space equation presenting the vehicle's yaw motion can be presented as a function of the vehicle yaw rate and sideslip as in equation 4.24, which is equivalent to equation 4.25.

$$\begin{bmatrix} \dot{\beta} \\ \dot{r} \end{bmatrix} = \begin{bmatrix} a_{11} & a_{12} \\ a_{21} & a_{22} \end{bmatrix} \begin{bmatrix} \beta \\ r \end{bmatrix} + \begin{bmatrix} \frac{C_{\alpha 3}}{mU} & \frac{C_{\alpha 4}}{mU} \\ \frac{a_3 C_{\alpha 3}}{I_{zz}} & \frac{a_4 C_{\alpha 4}}{I_{zz}} \end{bmatrix} \begin{bmatrix} \delta_3 \\ \delta_4 \end{bmatrix} + \begin{bmatrix} \frac{C_{\alpha 1} + c_{21} C_{\alpha 2}}{a_1 C_{\alpha 1} + a_2 c_{21} C_{\alpha 2}} \\ \frac{mU}{I_{zz}} \end{bmatrix} \delta_1 + \begin{bmatrix} \frac{\Delta_{Fy}}{mU} \\ \frac{\Delta_{Mz}}{I_{zz}} \end{bmatrix} \quad (4.24)$$

Where

$$\begin{aligned} a_{11} &= \frac{-C_{\alpha 1} - C_{\alpha 2} - C_{\alpha 3} - C_{\alpha 4}}{mU} \\ a_{12} &= \frac{-a_1 C_{\alpha 1} - a_2 C_{\alpha 2} - a_3 C_{\alpha 3} - a_4 C_{\alpha 4} - mU^2}{mU^2} \\ a_{21} &= \frac{-a_1 C_{\alpha 1} - a_2 C_{\alpha 2} - a_3 C_{\alpha 3} - a_4 C_{\alpha 4}}{I_{zz}} \\ a_{22} &= \frac{-a_1^2 C_{\alpha 1} - a_2^2 C_{\alpha 2} - a_3^2 C_{\alpha 3} - a_4^2 C_{\alpha 4}}{I_{zz} U} \end{aligned}$$

$$\dot{X} = AX + Bu + w_{\delta_1} + w_d \quad (4.25)$$

### 4.3.2 The adaptive-ISM design

The vehicle is subjected to a continuous variation in the driving parameters and road conditions such as the vehicle velocity and the road surface friction. Besides, the road profile irregularities and side wind can produce a disturbance that can be assumed as an additional yaw force and moment to the vehicle motion. Therefore, this section discusses the design procedures of a new Adaptive Integral Sliding Mode Controller (AISM) for an ARS system to enhance the handling performance and stability of the 8x8 combat vehicle when driving at various speeds on rough terrain with different friction coefficients. In general, Integral Sliding Mode Control (ISM) is synthesized from two control terms; linear and nonlinear controllers. In this section, the linear term is

designed based on (Gain Scheduled Linear Quadratic Regulator) GSLQR so the discontinuous (nonlinear) term gains are also scheduled according to it.

#### 4.3.2.1 Optimal GSLQR

LQR is an optimal controller, however, it is developed based on a certain design point that is represented by the nominal model parameters, so the effectiveness of the controller can be decreased when operated far from these parameters. Therefore, the proposed controller gains are determined at different speeds to cover all possible operating speeds. Hence, the state-space equation can be represented as a function of the vehicle longitudinal speed as in equation 4.26. Moreover, the maximum desire states ( $r$  and  $\beta$ ) can be represented as a function of vehicle's speeds and road coefficient of friction ( $\mu$ ) according to equations 4.27 and 4.28, respectively where  $g$  denotes the gravitational acceleration [116].

$$\dot{X} = A(U)X + B(U)u \quad (4.26)$$

$$r(U, \mu)_{max.} = \frac{0.85\mu g}{U} \quad (4.27)$$

$$\beta(\mu)_{max.} = \tan^{-1}(0.02\mu g) \quad (4.28)$$

Eventually, by solving the Riccati equation 4.29 that minimizing the performance index in equation 4.30 [120] the controller gains  $K$  can be calculated as in equation 4.31. In these equations  $\nu$  represents the varied parameters,  $P$  is a positive definite matrix,  $Q$  and  $R$  are the states and control effort weight matrices, respectively. The final control input is then scheduled as a function of the vehicle longitudinal velocity and road coefficient of friction as in equation 4.32.

$$A(\nu)^T P + P A(\nu) - P B(\nu) R(\nu)^{-1} B(\nu)^T P + Q(\nu) = 0 \quad (4.29)$$

$$J(\nu) = \int_{t_o}^t (X^T Q(\nu) X + u^T R(\nu) u) dt \quad (4.30)$$

$$K = R(\nu)^{-1}(B(\nu)^T P) \quad (4.31)$$

$$u(U, \mu)_{LQR} = -KX \quad (4.32)$$

Generally, if a linear system represents a nonlinear one and is found to be asymptotic stable, it indicates that the nonlinear system is also stable [14]. Hence, the weights matrices  $Q$  and  $R$  are continuously optimized for each design parameter variation to ensure asymptotic stability with real negative eigenvalues of the closed-loop control system. The weights matrices  $Q$  and  $R$  are presented according to Bryson's rule [114, 84, 115] and optimized based on a free constant positive number  $C_Q$ , the maximum allowable average steering angle of the 3<sup>rd</sup> and 4<sup>th</sup> ( $\delta_{3max.}$  and  $\delta_{4max.}$ ) as in equations 4.33 and 4.34, consequently. For that purpose, a new cost function is synthesized and introduced as in equation 4.35. The equation is developed to minimize the parameter  $C_Q$ , so it increases the ability of the controller to minimize the vehicle sideslip  $\beta$  and increase the error tolerance on the yaw rate. This method allows designing the controller with reference signals equal to zero to reflect no dependency on the reference model as in previous conventional LQR design [4]. In addition, the cost function also minimizes the steering angles  $\delta_{3max.}$  and  $\delta_{4max.}$  to prevent excessive use and decrease the control effort. Besides, with a very small positive constant  $\epsilon$  the eigenvalues imaginary part  $\lambda_{ij \text{ img}}$  is forced to be zero and the real part  $\lambda_{ij \text{ real}}$  is be maximized.

$$Q(\beta_{max.}, r_{max.}, C_Q) = \begin{bmatrix} \frac{1}{\beta(\mu)_{max.}^2} & 0 \\ 0 & \frac{C_Q}{r(U, \mu)_{max.}^2} \end{bmatrix} \quad (4.33)$$

$$R(\delta_{3max.}, \delta_{4max.}) = \begin{bmatrix} \frac{1}{\delta_{3max.}^2} & 0 \\ 0 & \frac{1}{\delta_{4max.}^2} \end{bmatrix} \quad (4.34)$$

$$\begin{aligned} \text{Cost function} = \\ \left\| C_Q + \delta_3 + \delta_4 + \frac{1}{|\lambda_{ij \text{ real}}|} + \frac{|\lambda_{ij \text{ img}}|}{\epsilon} \right\| \end{aligned} \quad (4.35)$$

#### 4.3.2.2 Genetic programming-based GSLQR

In the late 90s, an evolutionary optimization algorithm known as Genetic Programming (GP) was introduced by John Kozaa. Following the same concept of the Genetic Algorithm (GA), GP uses the techniques of mutation, crossover, and natural selection. GA is usually used to produce a bit-string representation of a certain problem. On the contrary to GA, GP deals with the string data type that presents genetic operators to synthesize an algorithm and apply it to the same problem [121]. Hence, GP generates arithmetic functions and operations in a hierarchical structure to generate a solution to the problem based on the inputs (terminals). In addition, GP applies the genetic operators on the algorithm/equation in form of branches as in figure 4.14 [122].

In this section, a genetic programming tool provided by Eureka software is utilized to represent each scheduled gain by a simple and single optimum equation that can replace and reduce the dimension of the developed GSLQR gains. This technique permits increasing the resolution of the varied parameters and includes more design points in the GSLQR design regardless of the burden of resulting in a high-dimensional gains dataset. Besides, it facilitates future hardware implementation of the controller. Another advantage of using this method is to interpolate between the design point and allow a smooth transition from one point to another and extrapolate for points beyond the one included in the design.

GP is used to represent the GSLQR gain to the one illustrated equation 4.36, which will be stated as GP-GSLQR in the rest of this chapter, as a function of the vehicle's speed and road's friction where  $Cn_{kij}$  presents real constant values. Moreover, to simplify the output equations and consequently reduce the complexity and computational effort, the solution is constrained to basic math operators (\*, protected division /, -, +).

$$K_{GSLQR} = \begin{Bmatrix} K_{11} & K_{12} \\ K_{21} & K_{22} \end{Bmatrix} \quad (4.36)$$

where

$$K_{11} = C1_{k11} + C2_{k11}U + C3_{k11}\mu + C4_{k11}\mu U \\ + C5_{k11}(\mu U)^2$$

$$\begin{aligned}
K_{12} &= C1_{k12} + C2_{k12}U + C3_{k12}(U)^2 \\
&\quad + C4_{k12}\mu(U)^2 \\
K_{21} &= C1_{k21} + C2_{k21}U + \frac{C3_{k21}}{U} + C4_{k21}\mu U \\
&\quad + C5_{k21}\mu(U)^2 \\
K_{22} &= C1_{k22} + \frac{C2_{k22}U}{\mu} + C3_{k22}\mu(U)^3 + C4_{k22}\mu U \\
&\quad + C5_{k22}\mu + \frac{C6_{k22}}{(U)^3}
\end{aligned}$$

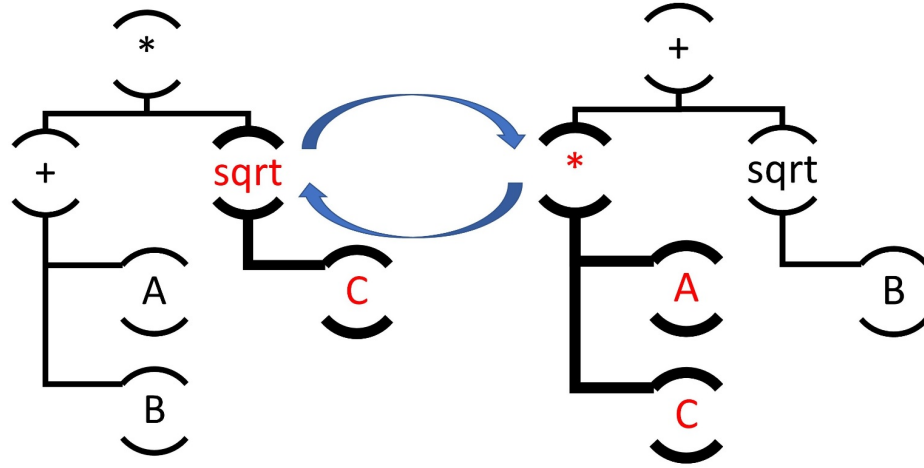


Figure 4.14: Genetic programming structure

Moreover, the execution time of the GS-based and GP-based controllers are compared using the Matlab/Simulink profiler for various time steps using the same solver and simulation time. The execution time per each step for different time steps is introduced in figure 4.15. The figure shows that the GP-based controller has a comparable processing time with the GS-based one as that time is very low for both cases.

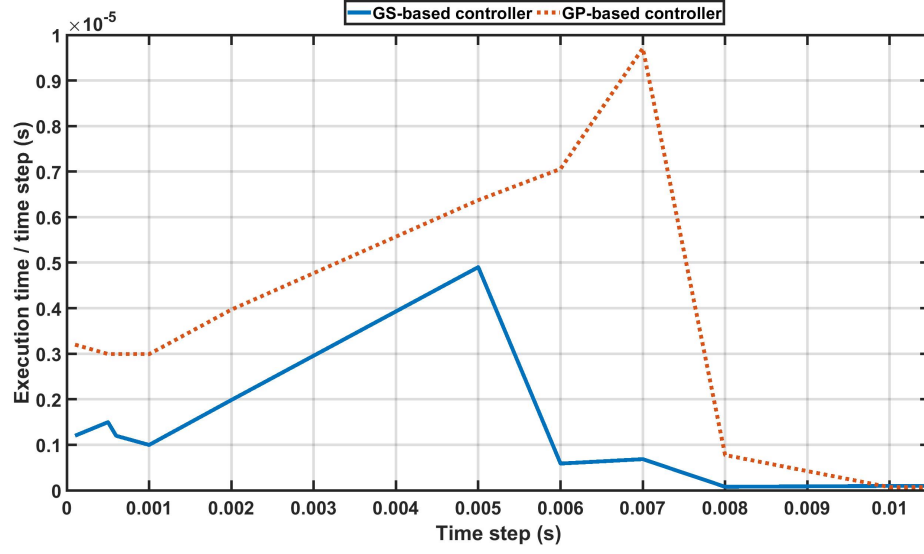


Figure 4.15: Mean execution time per step for each time step

#### 4.3.2.3 Integral sliding mode control design

SMC is known for its effectiveness and robustness in disturbance rejection and parameters uncertainties, however, this compensation only starts after reaching the sliding manifold. On the contrary, ISMC is capable to compensate for that disturbance and uncertainties from the beginning and without the existence of the reaching phase [15]. Lets consider the disturbance  $w_d$  in equation 4.25 is bounded and can be presented as matched disturbance equals to  $B\xi$ , as in equation 4.37. In this equation,  $\xi$  is a disturbance vector,  $\rho_\beta$  and  $\rho_r$  are the upper bounds on the sideslip and yaw rate disturbances that can be determined from equation 4.38.

$$w_d = B\xi \text{ where } \xi = \begin{bmatrix} \rho_\beta \\ \rho_r \end{bmatrix} \quad (4.37)$$

$$\text{and } B = \begin{bmatrix} \frac{C_{\alpha 3}}{mU} & \frac{C_{\alpha 4}}{mU} \\ \frac{a_3 C_{\alpha 3}}{I_{zz}} & \frac{a_4 C_{\alpha 4}}{I_{zz}} \end{bmatrix}$$

$$\begin{bmatrix} \frac{\Delta F_y}{mU} \\ \frac{\Delta M_z}{I_{zz}} \end{bmatrix} = \begin{bmatrix} \frac{C_{\alpha 3}}{mU} & \frac{C_{\alpha 4}}{mU} \\ \frac{a_3 C_{\alpha 3}}{I_{zz}} & \frac{a_4 C_{\alpha 4}}{I_{zz}} \end{bmatrix} \begin{bmatrix} \rho_\beta \\ \rho_r \end{bmatrix} \quad (4.38)$$

ISM has structured form two terms linear controller that controls the nominal system without considering the disturbance and a nonlinear discontinuous control term to compensate for the existed bounded disturbance. The proposed controller includes the developed GP-GSLQR, which is designed based on a linear control theory to stabilize the nominal system at various driving conditions and a nonlinear control term as in equation 4.39.

$$u_{ISM} = u_{GSLQR} + u_{SMC} \quad (4.39)$$

The sliding manifold  $S$  of the ISM is designed and scheduled according to equation 4.40 where,  $G_{SC}$  is a projection matrix that satisfy equation 4.41,  $X_o$  is the system's states initial condition.

$$S = G_{SC} \left( X - X_o - \int_0^t (Ax(\tau) + Bu_{GSLQR}(\tau)) d\tau \right) \quad (4.40)$$

$$G_{SC} = B^+ \quad (4.41)$$

where  $G_{SC}B = I$  and  $\det(G_{SC}B) \neq 0$

Eventually, the discontinuous controller is presented as in equation 4.42 and the sign function is approximated according to equation 4.43 using a very small positive constant  $\epsilon_{smc}$  to prevent chattering phenomena.

$$u_{SMC} = -\rho_{smc} \text{sign}((G_{SC}B)^T S) \quad (4.42)$$

where  $\rho_{smc} \geq \|\xi\|$

$$\text{sign}(S) \approx \frac{S}{|S| + \epsilon_{smc}} \quad (4.43)$$



### 4.3.3 Evaluation and simulation results

The controller is implemented with the 8-WS nonlinear 22-DoF full vehicle model, presented in 3 section 3.2, to perform all simulations. The evaluation is conducted on rough terrain as will be discussed in the next subsections.

#### 4.3.3.1 Evaluation on rough terrain

At first, the controllers are tested on a road with uniform irregularities as shown in figure 4.16. The road surface profile is presented as a sinusoidal wave with a wavelength of 2 m, and peak-to-peak amplitude of 0.05 m. The sinusoidal road irregularity is applied for 300 m length followed by a negative road slope 0.1 m/s.

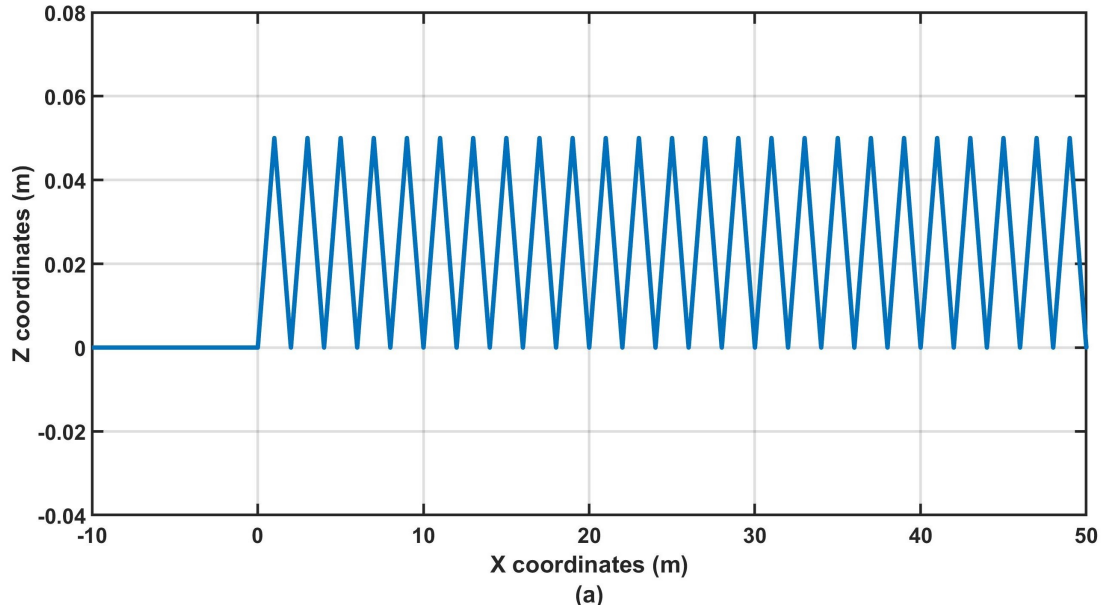


Figure 4.16: Profile of the road surface irregularities in the vertical direction

Figure 4.17a illustrates the vehicle trajectory when it was driven with speed 100 km/h on a road with a coefficient of friction 0.85. It can be seen that the uncontrolled (conventional) vehicle failed to complete the maneuver, while other cases did. Moreover, both controllers resulted in almost the same lateral error as shown in figure 4.17b.

Figure 4.18 shows the corresponding average steering angle for the 1<sup>st</sup>, 3<sup>rd</sup>, and 4<sup>th</sup> axles. It was noticed that the conventional vehicle utilizes only the steering of the 1<sup>st</sup> axle, which is saturated, while the controlled vehicle is not. Besides, the ARS-AISM

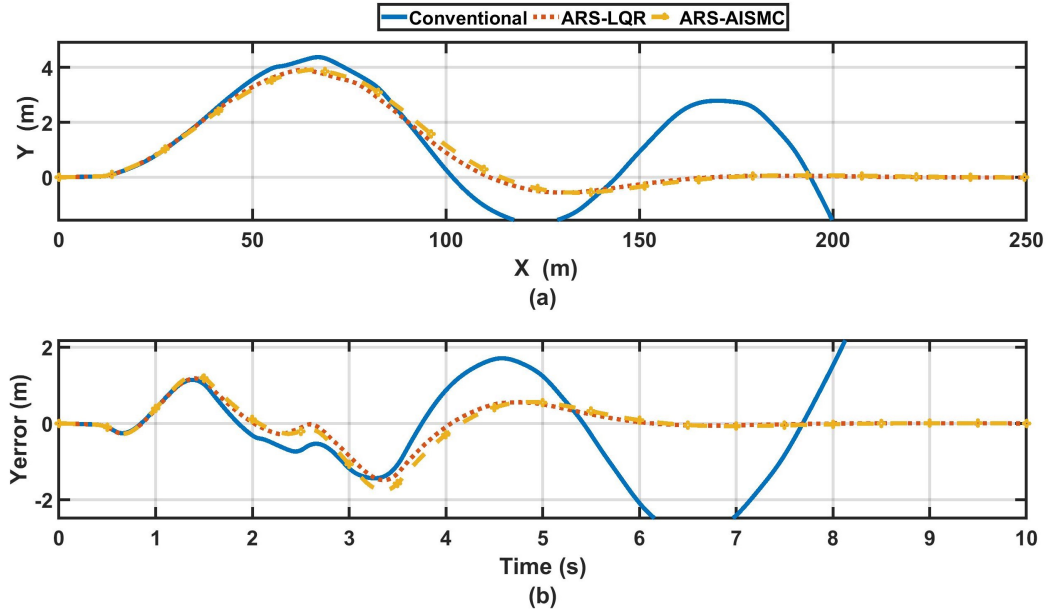


Figure 4.17: DLC on a road with  $\mu = 0.85$  at speed  $100 \text{ km/h}$  (a) Vehicle trajectory  
(b) Lateral error

exhibited a smaller  $3^{rd}$  axle's steering angle than ARS-LQR, which preserves higher lateral forces that can be used for stabilization. Meanwhile, the  $4^{th}$  axle's average steering angle of the ARS-AISM is slightly higher than the ARS-LQR, which can be neglected.

The vehicle dynamic response is illustrated in figure 4.19. It can be seen that the fluctuation in the vehicle longitudinal velocity and lateral acceleration is the same for each case as in figures 4.19a and 4.19b, respectively. Meanwhile, the yaw rate and vehicle's sideslip response of ARS-AISM is less than ARS-LQR as in figures 4.19c and 4.19d, respectively, which indicates higher stability.

The controllers are evaluated at  $60 \text{ km/h}$  speed on a slippery road with a 0.2 coefficient of friction. The vehicle trajectory and corresponding lateral error are shown in figures 4.20a and 4.20b, respectively. The figures indicate that the conventional vehicle failed to complete the maneuver, while the controlled vehicles succeeded. However, the lateral error resulting from the ARS-AISM is less than ARS-LQR.

Figure 4.21 shows the steering axles' average steering angles. The average  $1^{st}$  axle steering angle of ARS-AISM is less than ARS-LQR with a slight value as in figure 4.21a. Also, the Average steering angle of the  $3^{rd}$  axles is lower than ARS-LQR, and the

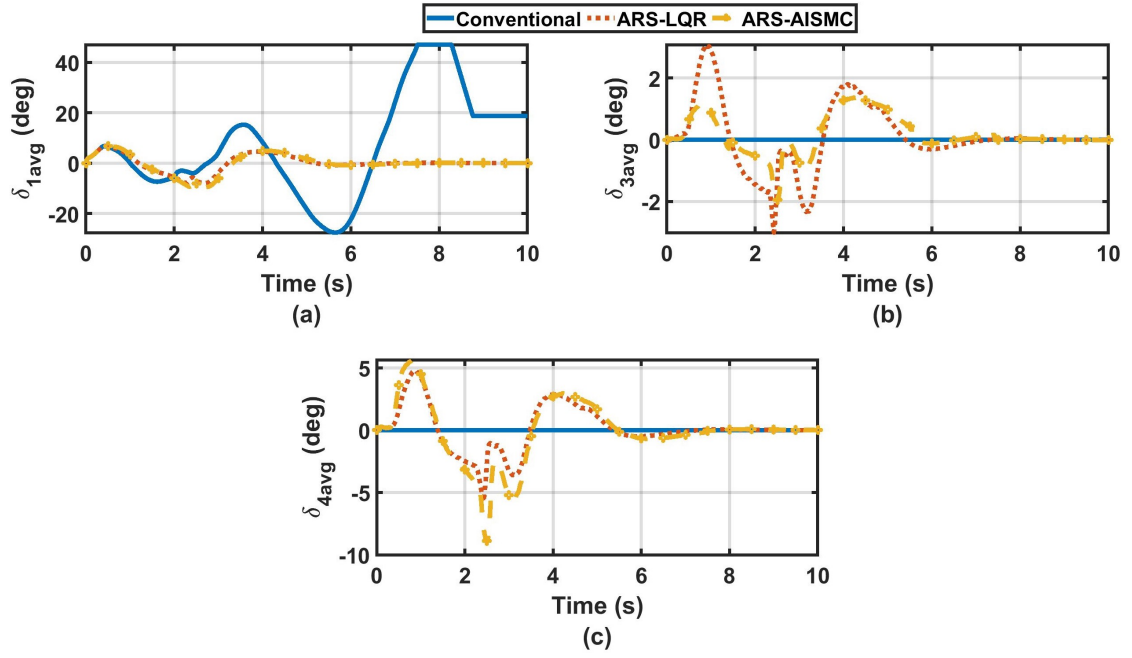


Figure 4.18: DLC on a road with  $\mu = 0.85$  at speed  $100 \text{ km/h}$  (a)  $1^{st}$  axle average steering angle (b)  $3^{rd}$  axle average steering angle (c)  $4^{th}$  axle average steering angle

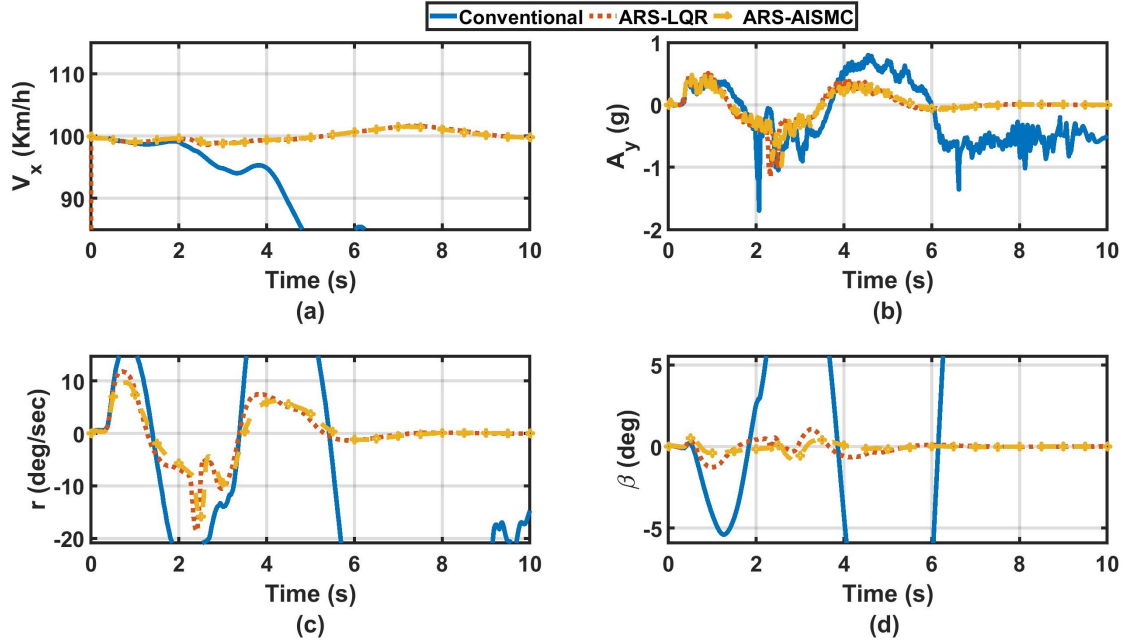


Figure 4.19: DLC on a road with  $\mu = 0.85$  at speed  $100 \text{ km/h}$  (a) Vehicle longitudinal velocity (b) Lateral acceleration response (c) Yaw rate response (d) Vehicle sideslip response

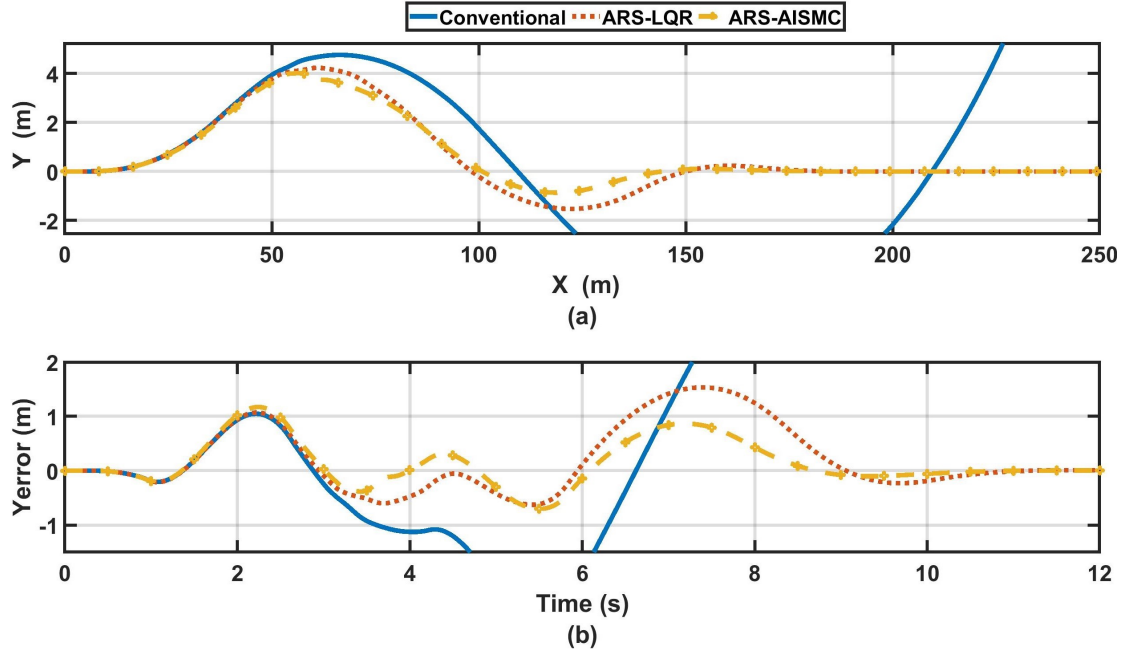


Figure 4.20: DLC on a road with  $\mu = 0.2$  at speed  $60 \text{ km/h}$  (a) Vehicle trajectory  
(b) Lateral error

4<sup>th</sup> axle steering angle of ARS-AISM is only higher at the beginning of the maneuver as shown in figures 4.21b and 4.21c, respectively.

The longitudinal velocity and lateral acceleration almost respond the same for both controllers as in figures 4.22a and 4.22b, respectively. Meanwhile, figure 4.22c shows low differences between the controllers at the beginning. However, the ARS-AISM shows a lower yaw rate and the end and faster stabilization than ARS-LQR. This result can be confirmed by observing lower vehicle sideslip of the ARS-AISM and higher stability than ARS-LQR as in figure 4.22d.

#### 4.3.3.2 Evaluation on extreme rough terrain

In this section, the previous road's surface profile is superimposed with an extreme rough profile that is shown in figure 4.23. First, the controllers are tested on a road with a high coefficient of friction (0.85) and the vehicle is driven with speed  $100 \text{ km/h}$ .

The vehicle trajectory and corresponding lateral error are illustrated in figure 4.24a and 4.24b, respectively. It can be noticed that the conventional vehicle couldn't be stabilized after the maneuver. On the other hand, the controlled vehicle could successfully

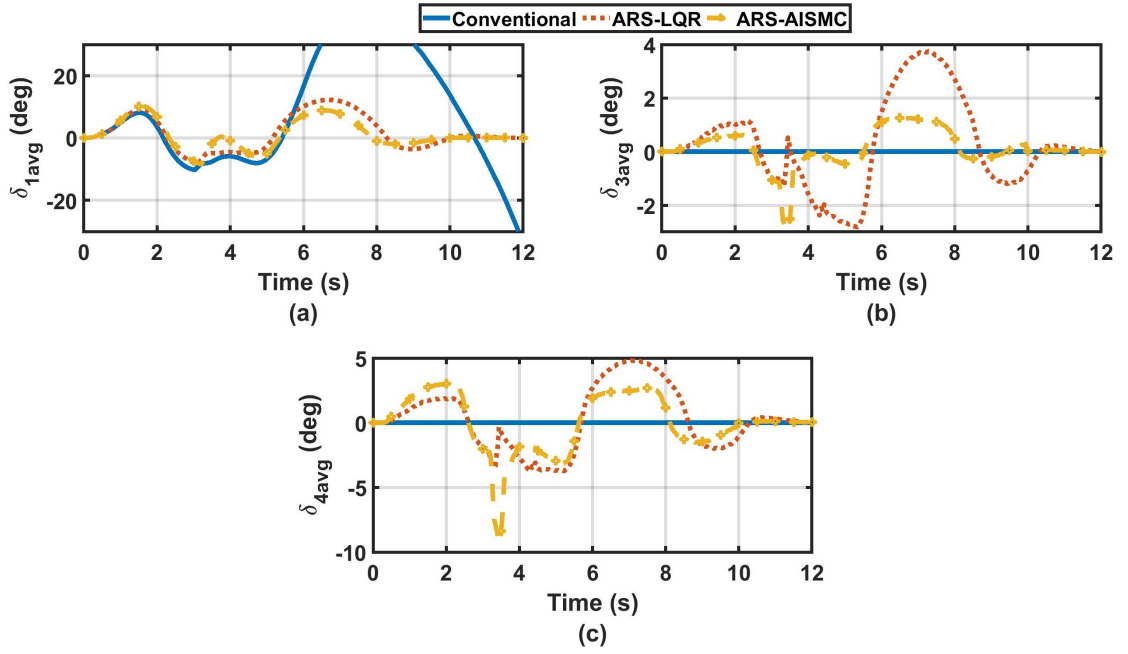


Figure 4.21: DLC on a road with  $\mu = 0.2$  at speed  $60 \text{ km/h}$  (a)  $1^{st}$  axle average steering angle (b)  $3^{rd}$  axle average steering angle (c)  $4^{th}$  axle average steering angle

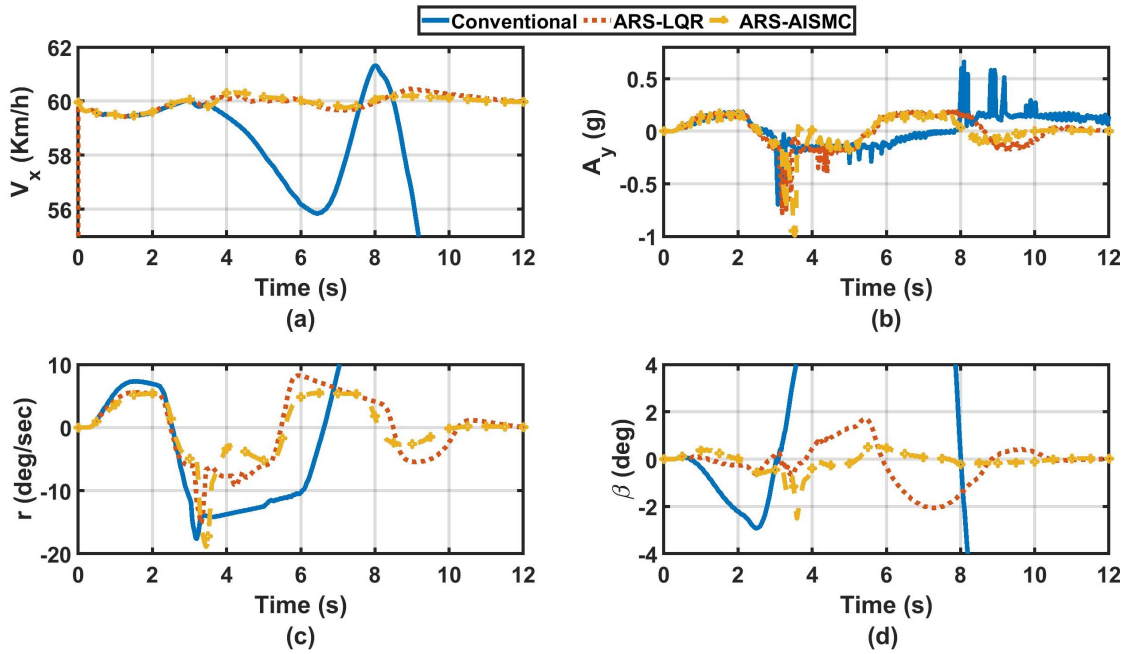


Figure 4.22: DLC on a road with  $\mu = 0.2$  at speed  $60 \text{ km/h}$  (a) Vehicle longitudinal velocity (b) Lateral acceleration response (c) Yaw rate response (d) Vehicle sideslip response

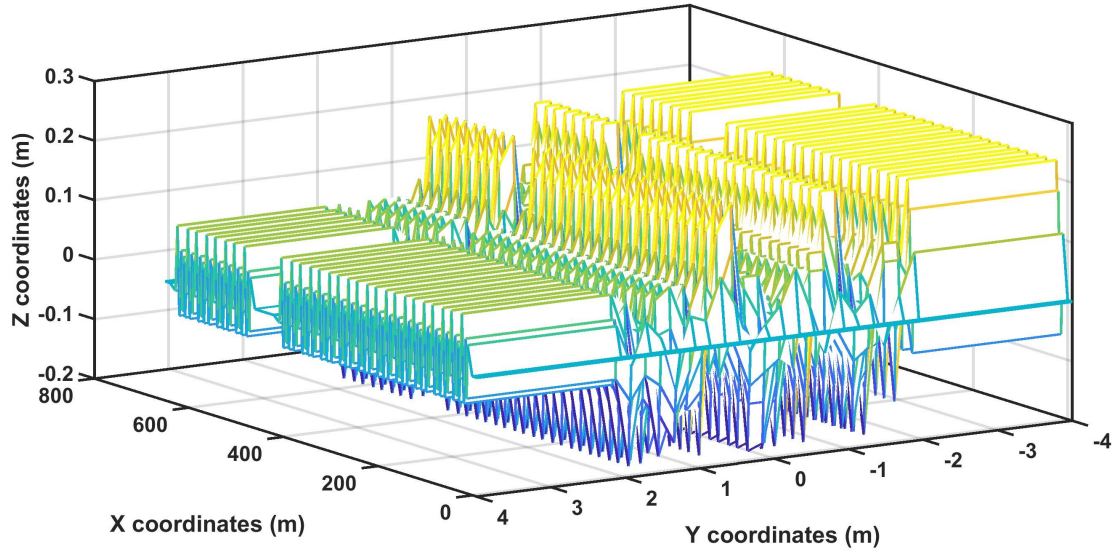


Figure 4.23: Profile of the road surface irregularities

finish the maneuver resulting in almost the same lateral error. It is also noticed that the conventional vehicle has the lowest steerability (maneuverability) as it performed the minimum lateral distance for the maneuver, as shown in figure 4.24a.

Figure 4.25a shows the average steering angle of the 1<sup>st</sup>, it is observed that the conventional vehicle is saturated while controlled cases aren't. In figure 4.25b, the ARS-AISMCM exhibits a smaller average steering angle of the 3<sup>rd</sup> axle than the ARS-LQR. In contrast, the average steering angle of the 4<sup>th</sup> axle is higher than the ARS-LQR, as shown in figure 4.25c. However, it is only higher at  $t = 12$  s.

The vehicle dynamic response in figure 4.26 doesn't show a considerable difference between both controllers and it can be seen that both controllers almost follow the same behaviour and longitudinal speed profile as in 4.26a and can limit the vehicle yaw rate and sideslip, as in figures 4.26c and 4.26d, respectively. Meanwhile, the high lateral acceleration in figure 4.26b indicates that wheels lift off the ground due to the high speed and high irregularities, however, rollover didn't occur.

When repeating the maneuver at a slippery surface with a coefficient of friction  $\mu = 0.2$  and speed  $60 \text{ km/h}$ , it can be seen that the conventional vehicle and ARS-AISMCM succeeded to perform the maneuver and maintain the stability, as shown in figure 4.27a. On the other hand, the ARS-LQR controller failed to keep the vehicle's stability. Besides,

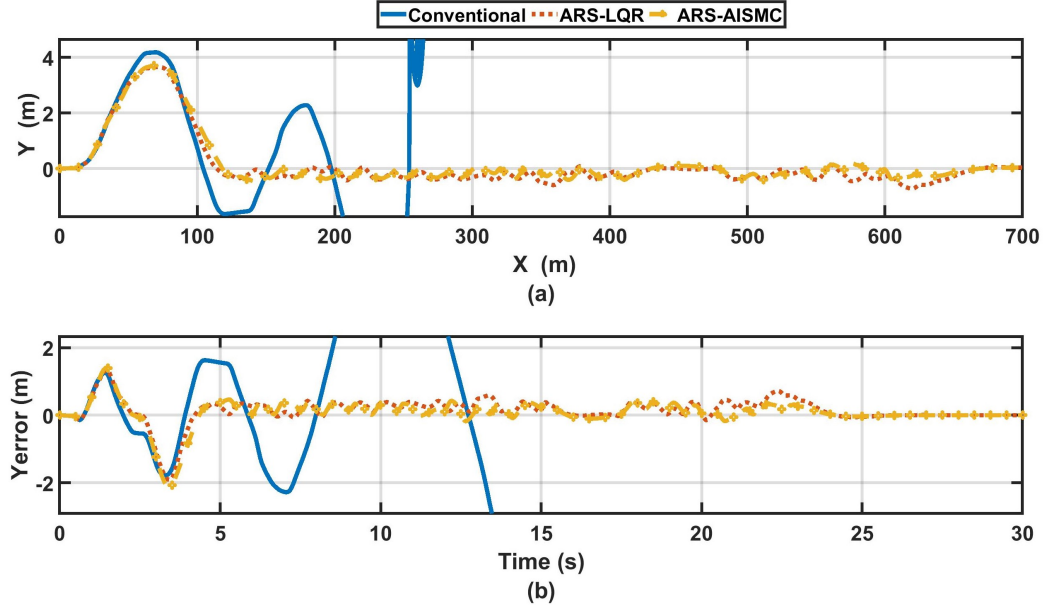


Figure 4.24: DLC on a road with  $\mu = 0.85$  at speed  $100 \text{ km/h}$  (a) Vehicle trajectory  
(b) Lateral error

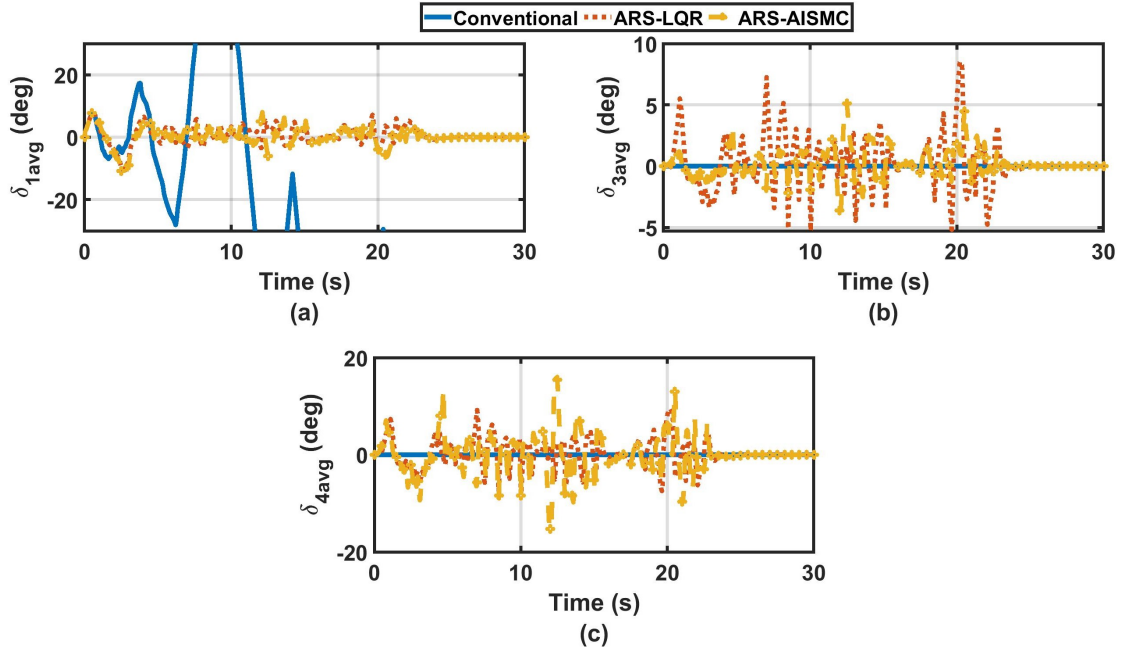


Figure 4.25: DLC on a road with  $\mu = 0.85$  at speed  $100 \text{ km/h}$  (a)  $1^{st}$  axle average steering angle (b)  $3^{rd}$  axle average steering angle (c)  $4^{th}$  axle average steering angle



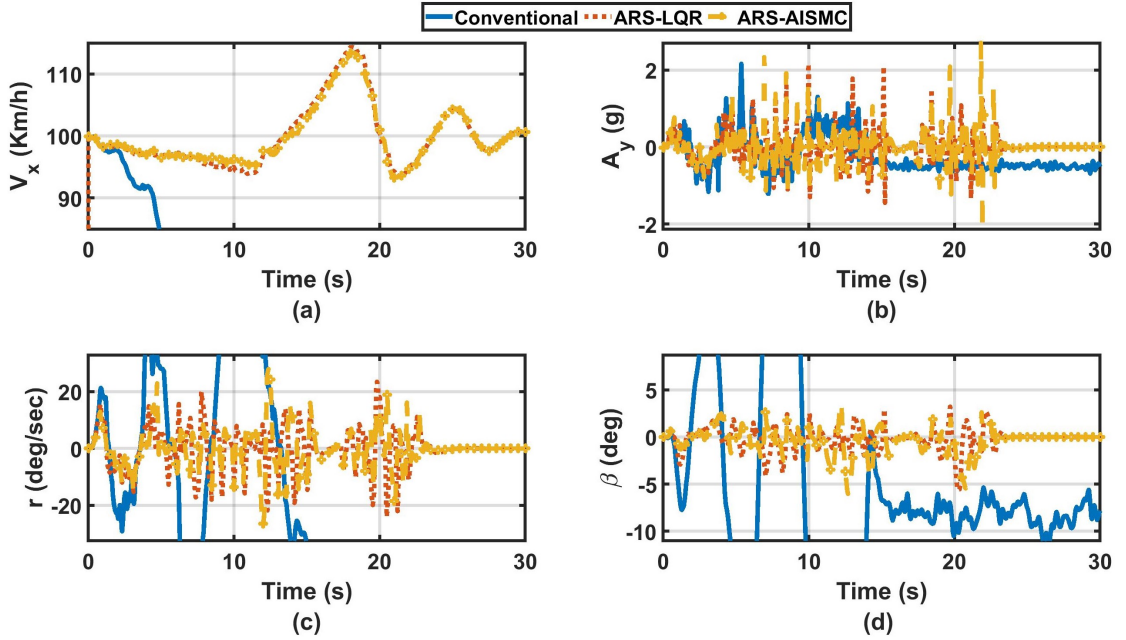


Figure 4.26: DLC on a road with  $\mu = 0.85$  at speed  $100 \text{ km/h}$  (a) Vehicle longitudinal velocity (b) Lateral acceleration response (c) Yaw rate response (d) Vehicle sideslip response

the ARS-AISM produces less lateral error than other cases as can be seen in figure 4.27b.

In figure 4.28, the ARS-AISM shows the minimum consumption of the steering actuators with a low average steering angle than all cases in figure 4.28a, and lower than the ARS-LQR in figure 4.28b and 4.28c.

By observing the fluctuation in the vehicle's longitudinal velocity in figure 4.29a, it can be seen that the ARS-LQR is exposed to high fluctuation (more than  $\pm 10 \text{ km/h}$ ) while the conventional vehicle is the lowest, less than  $\pm 5 \text{ km/h}$ , followed by the ARS-AISM ( $\pm 5 \text{ km/h}$ ). The lateral acceleration response in figure 4.29b, also indicates that there are wheels lift-off occurs for all cases. Figure 4.29c shows bounded yaw rate for the conventional and the ARS-AISM cases and shows instability in the case of the ARS-LQR. Similarly, the vehicle sideslip shows the same behaviour in figure 4.29d and both figures show faster stabilization of the ARS-AISM than the conventional vehicle.

The failure of the ARS-LQR to stabilize the vehicle in comparison to the conventional vehicle is related to several reasons. The first is associated with the less lateral offset that



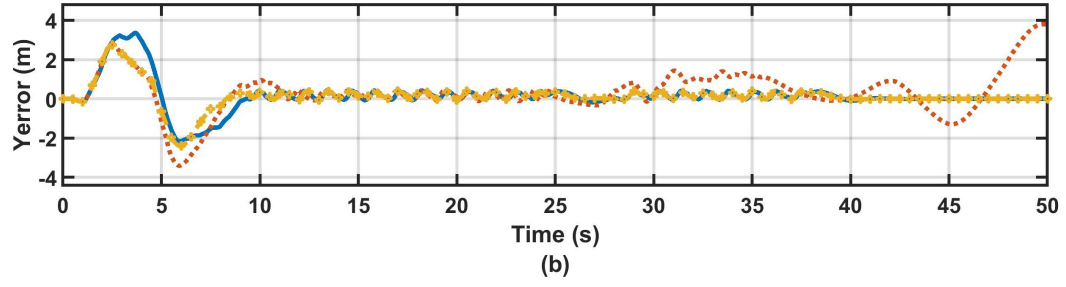
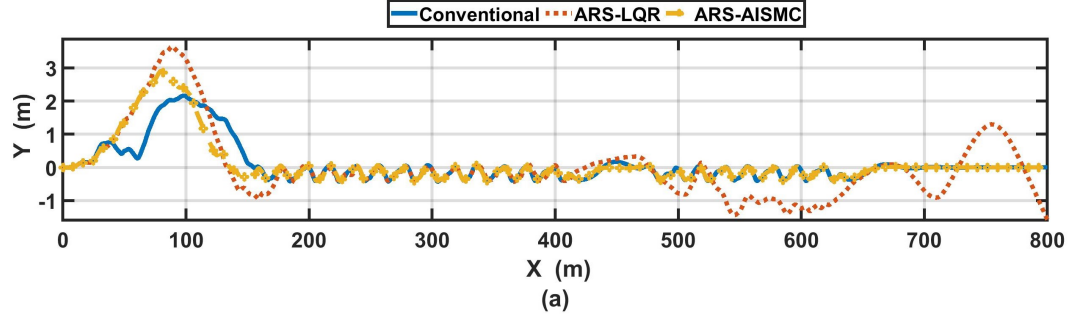


Figure 4.27: DLC on a road with  $\mu = 0.2$  at speed  $60 \text{ km/h}$  (a) Vehicle trajectory  
(b) Lateral error

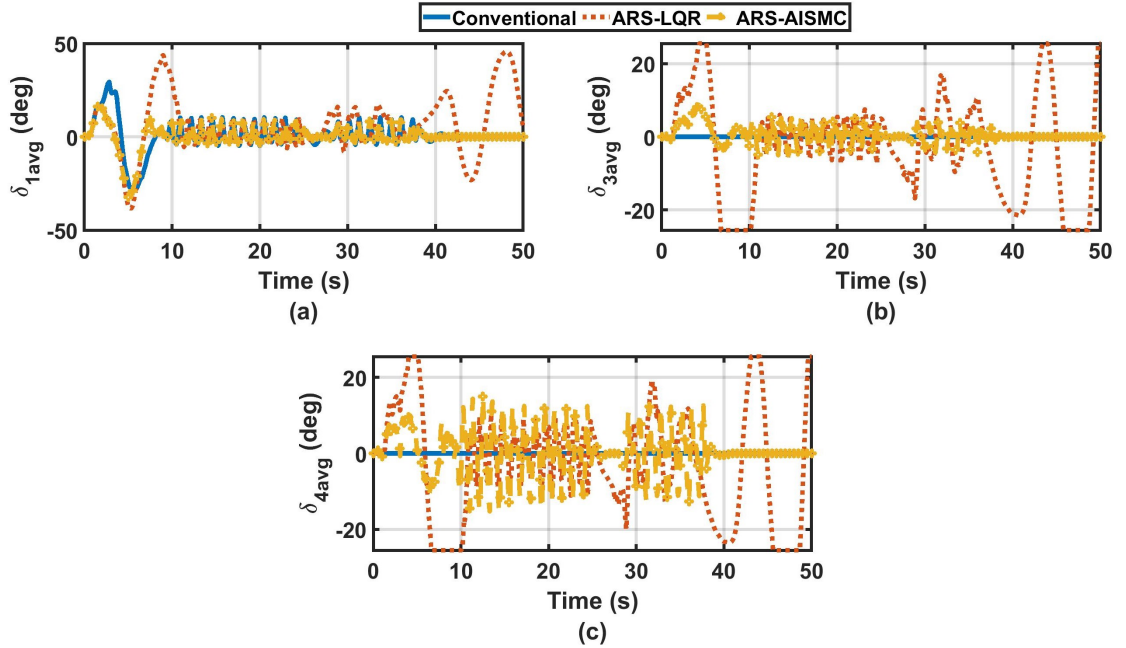


Figure 4.28: DLC on a road with  $\mu = 0.2$  at speed  $60 \text{ km/h}$  (a)  $1^{st}$  axle average steering angle (b)  $3^{rd}$  axle average steering angle (c)  $4^{th}$  axle average steering angle

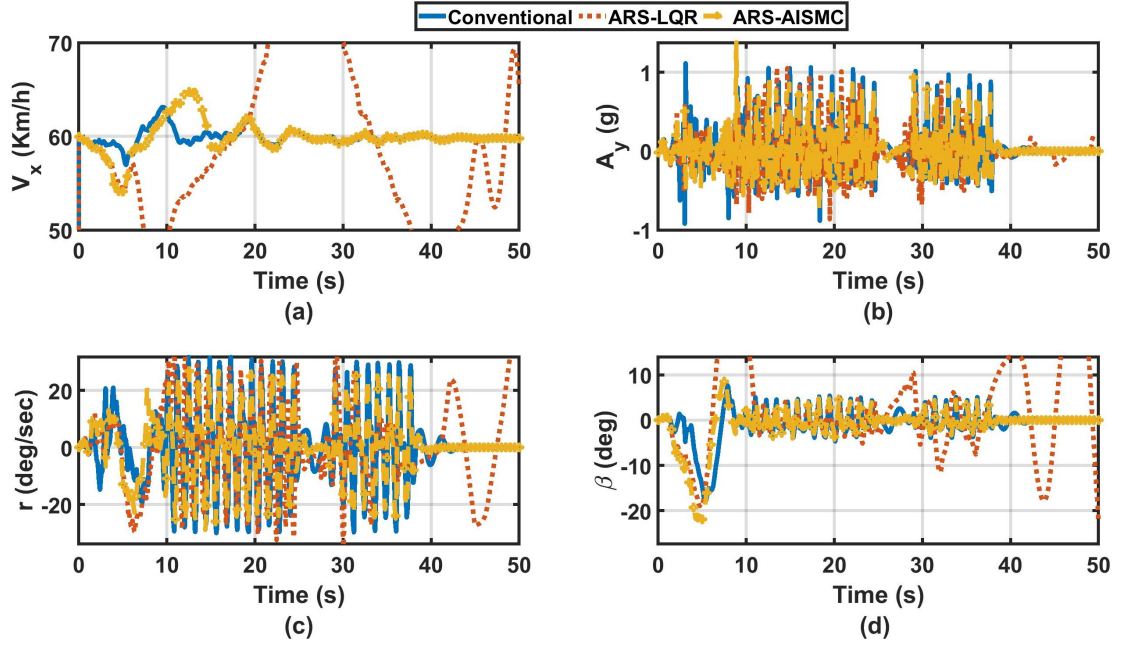


Figure 4.29: DLC on a road with  $\mu = 0.2$  at speed  $60 \text{ km/h}$  (a) Vehicle longitudinal velocity (b) Lateral acceleration response (c) Yaw rate response (d) Vehicle sideslip response

is taken by the conventional vehicle, as shown in figure 4.27a. This small lateral offset resulted in less yaw rate and sideslip, hence, better stability but limited maneuverability. On contrary, the vehicle controlled by the ARS-LQR exhibits higher lateral offset (and demonstrates better maneuverability). Another reason is the large steering angles that are exhibited by the ARS-LQR on the rear axles ( $3^{rd}$  and  $4^{th}$ ), as shown in figures 4.28b and c, respectively. These high lateral motion and large steering angles generated high yaw rate, high fluctuation in the vehicle speed, and consequently high sideslip, as shown in figure 4.29. The generated high sideslip and yaw rate make it difficult for the controller to regain stability with such high maneuverability on a slippery surface. This can be related to the controller design, which is developed at nominal driving conditions (nominal speed and high road friction), so the performance at driving conditions far from this point is not guaranteed.

## 4.4 Active rear axles' steering in path-following application

In this section, three cases of the path-following controller are developed and compared for an 8x8 combat vehicle. At first, an  $H_\infty$  path-following controller is designed and utilized for the steering of the front axles but fixed rear axles. In the second case, the developed  $H_\infty$  path-following controller includes the rear axles' steering with modifying the controller's weight functions and adding constraints to tighten the design requirements. The third case integrates the developed front steering path-following controller side-by-side with a separate  $H_\infty$  ARS controller that is developed to enhance the vehicle's lateral stability by exploiting the independent steering of the rear two axles. Eventually, virtual testing is conducted in TruckSim software in collaboration with Simulink using a series of DLC maneuvers. The testing is performed at different speeds and on various road friction coefficients.

### 4.4.1 Path-follow mathematical models

The bicycle model showed its effectiveness to design lateral stability controllers in previous studies as introduced by [23, 37, 78, 18]. Besides, it is also used for vehicles' automation and path-following applications as presented in [100, 89, 95, 88]. Therefore, the state-space model required to design the controllers can be derived using the linearized 2-DoF bicycle model presented in chapter 4, section 4.2.1. In addition, the developed controllers are incorporated with the nonlinear 22-DoF full vehicle model for virtual testing and evaluation.

By rearranging the equations from 4.1 to 4.6, in section 4.2, and substituting in the lateral velocity ( $V$ ) with the rate of change in the Y-axis coordinate  $\dot{Y}$ , and  $r$  with the rate of change in the vehicle heading angle  $\dot{\theta}$ , the path-following state-space model can be described as in equation 4.44. This equation can represent a front steering vehicle by substituting  $\delta_2$  and  $\delta_3$  by zero, which represent fixed rear axles.

$$\begin{bmatrix} \dot{Y} \\ \ddot{Y} \\ \dot{\theta} \\ \dot{r} \end{bmatrix} = \begin{bmatrix} 0 & 1 & 0 & 0 \\ 0 & a_{11} & 0 & a_{12} \\ 0 & 0 & 0 & 1 \\ 0 & a_{21} & 0 & a_{22} \end{bmatrix} \begin{bmatrix} Y \\ \dot{Y} \\ \theta \\ r \end{bmatrix} + \begin{bmatrix} 0 & 0 & 0 \\ \frac{C_{\alpha 1} + c_{21}C_{\alpha 2}}{m} & \frac{C_{\alpha 3}}{m} & \frac{C_{\alpha 4}}{m} \\ 0 & 0 & 0 \\ \frac{a_1C_{\alpha 1} + a_2c_{21}C_{\alpha 2}}{I_{zz}} & \frac{a_3C_{\alpha 3}}{I_{zz}} & \frac{a_4C_{\alpha 4}}{I_{zz}} \end{bmatrix} \begin{bmatrix} \delta_1 \\ \delta_3 \\ \delta_4 \end{bmatrix} \quad (4.44)$$

Where

$$\begin{aligned} a_{11} &= \frac{-C_{\alpha 1} - C_{\alpha 2} - C_{\alpha 3} - C_{\alpha 4}}{mU} \\ a_{12} &= \frac{-a_1C_{\alpha 1} - a_2C_{\alpha 2} - a_3C_{\alpha 3} - a_4C_{\alpha 4} - mU^2}{mU} \\ a_{21} &= \frac{-C_{\alpha 1} - C_{\alpha 2} - C_{\alpha 3} - C_{\alpha 4}}{I_{zz}U} \\ a_{22} &= \frac{-a_1^2C_{\alpha 1} - a_2^2C_{\alpha 2} - a_3^2C_{\alpha 3} - a_4^2C_{\alpha 4}}{I_{zz}U} \end{aligned}$$

The yaw model that is used for lateral stability controller's design can be derived by isolating the  $\ddot{Y}$  and  $\dot{r}$  from equation 4.44 as follows:

$$\begin{bmatrix} \ddot{Y} \\ \dot{r} \end{bmatrix} = \begin{bmatrix} a_{11} & a_{12} \\ a_{21} & a_{22} \end{bmatrix} \begin{bmatrix} \dot{Y} \\ r \end{bmatrix} + \begin{bmatrix} \frac{C_{\alpha 3}}{I_{zz}} & \frac{C_{\alpha 4}}{I_{zz}} \\ \frac{a_3C_{\alpha 3}}{I_{zz}} & \frac{a_4C_{\alpha 4}}{I_{zz}} \end{bmatrix} \begin{bmatrix} \delta_3 \\ \delta_4 \end{bmatrix} + \begin{bmatrix} \frac{C_{\alpha 1} + c_{21}C_{\alpha 2}}{I_{zz}} \\ \frac{a_1C_{\alpha 1} + a_2c_{21}C_{\alpha 2}}{I_{zz}} \end{bmatrix} \delta_1 \quad (4.45)$$

Now, equations 4.44 and 4.45 are represented as in the state-space equation 4.46.

$$\dot{x} = Ax + Bu \quad (4.46)$$

The reference model considered the desired lateral coordinate of the desired path  $Y_d$ , a zero desired lateral velocity to minimize the vehicle sideslip angle  $\beta$  that is equal to  $\dot{Y}/U$ , the path's desired heading angle  $\theta$  as in equation 4.47, where  $X$  is the X-axes coordinates of the desired path, and the desired yaw rate  $\dot{\theta}_d$  as in equation 4.48 where  $\rho$  is the path curvature, which can be determined from equation 4.49.

$$\theta_d = \tan^{-1} \frac{dY}{dX} \quad (4.47)$$

$$\dot{\theta}_d = \rho U \quad (4.48)$$

$$\rho = \frac{\frac{d^2 Y}{d^2 X}}{\left(1 + \left(\frac{dY}{dX}\right)^2\right)^{3/2}} \quad (4.49)$$

Eventually, the reference model is filtered with a low-pass filter transfer function to smooth the desired signal to match the vehicle dynamics and response as in equation 4.50, where  $\tau$  is a small delay time.

$$s = \frac{1}{\tau s + 1} \quad (4.50)$$

#### 4.4.2 $H_\infty$ path-following controllers

In general,  $H_\infty$  control design is based on minimizing the  $H_\infty$  norm of the lower fractional transformation  $F_1$  of a Closed-looped System (CLS) formed from a plant and controller  $G$  and  $K$ , respectively. The  $H_\infty$  norm can be represented with the singular value ( $\bar{\sigma}$ ) of  $F_1$  for the CLS as in equation 4.51.

$$\|F_1(G, K)\|_\infty \triangleq \sup_{\omega \in R} \bar{\sigma}(F_1(G, K)(j\omega)) \quad (4.51)$$

This problem can be presented as a minimization problem as in equation 4.52, which is called the mixed sensitivity problem. In this equation,  $K$  denotes the desired controller

that stabilizes the system  $G$  and minimize the  $H_\infty$  norm of the sensitivity functions  $S$  and  $KS$ , which are penalized by the performance and control input weight functions  $W_p$  and  $W_u$ , to achieve good tracking performance and less control effort, receptively.

$$\min_{K \text{ stabilizing}} \left\| \begin{bmatrix} W_p S \\ W_u K S \end{bmatrix} \right\|_\infty \quad \text{where } S = (I + GK)^{-1} \quad (4.52)$$

These weight functions can be absorbed in the interconnected or augmented system  $G_{aug}$  as in equation 4.53 and the  $H_\infty$  norm of the system in equation 4.52 can be represented as in equation 4.54 to include the constraints on the system.

$$G_{aug} = \begin{bmatrix} W_p & -W_p G \\ 0 & W_u \\ I & -G \end{bmatrix} \quad (4.53)$$

$$\min_{K \text{ stabilizing}} \|F_1(G_{aug}, K)\|_\infty \quad (4.54)$$

Considering the introduced weighting functions, the whole plant can be augmented as in figure in figure 4.30 for designing the  $H_\infty$  controller. In this figure,  $\triangle$  is the model parameters uncertainty. The performance weight functions matrix is shown in equation 4.55, where  $W_p \in R^{5 \times 5}$ .  $W_{p_{1:4}}$  are the weights that are used to penalize the tracking errors ( $err_{1:4}$ ) between the reference signals ( $ref_{1:4}$ ) and the vehicle's states presented by the lateral position, lateral velocity, heading angle, and the rate of change in the yaw motion. Meanwhile,  $W_{p_{55}}$  is used to penalize the error's integration of the lateral position and ensure the convergence to zero at steady-state.  $W_u \in R^{m \times m}$  is synthesized to penalize the control effort at high frequencies, where  $m$  is the number of control inputs.

$$W_p = \begin{bmatrix} W_{p_{11}} & 0 & 0 & 0 & 0 \\ 0 & W_{p_{22}} & & 0 & 0 \\ 0 & 0 & W_{p_{33}} & 0 & 0 \\ 0 & 0 & 0 & W_{p_{44}} & 0 \\ 0 & 0 & 0 & 0 & W_{p_{55}} \end{bmatrix} \quad (4.55)$$

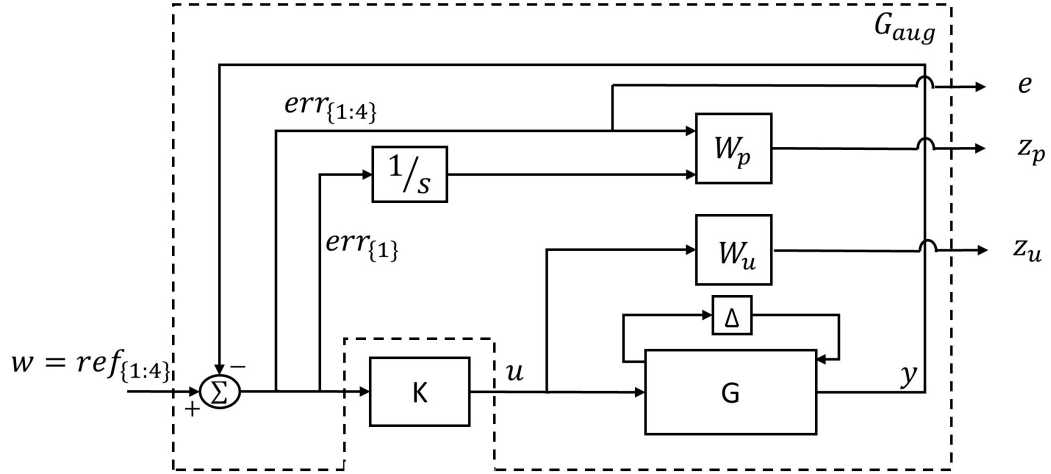


Figure 4.30:  $H_\infty$  Controller block diagram

The weighting functions in the frequency domain can be derived by converting the performance requirements of the CLS from the time domain, as can be presented in the following equations.

Equation 4.56 present the performance weight function.  $M_{p_i}$  is the maximum sensitivity gain,  $\omega_{p_i}$  is the differences between upper and lower cutoff frequencies,  $\epsilon_{p_i}$  is a parameters that present the maximum desired error, and  $n_{p_i}$  is tuned to control the weight function steep [123].

$$W_{p_{ii}} = \left( \frac{S / {}^{n_{p_i}}\sqrt{M_{p_i}} + \omega_{p_i}}{S + \omega_{p_i} {}^{n_{p_i}}\sqrt{\epsilon_{p_i}}} \right)^{n_{p_i}} \quad (4.56)$$

On the other hand, the control input weight functions  $W_{u_{ii}}$  are formulated and tuned as a high pass filter in equation 4.57:

$$W_{u_{jj}} = \frac{(a_{1j}S + a_{2j})^{n_{u1}}}{(S + a_{3j})^{n_{u2}}} \quad (4.57)$$

Eventually, the control system block diagram for the augmented plant can be represented as in figure 4.31, where  $w$  denotes the plant inputs ( $ref_{1:4}$ ),  $z$  is plant output ( $z_p$  and  $z_u$ ),  $e$  is the measured outputs and controller inputs ( $err_{1:4}$ ), and  $u$  is the con-

troller output ( $\delta_{1:4}$ ). The  $H_\infty$  control problem can be solved based on the state-space representation augmented plant as in equation 4.58. Moreover, the solution satisfies the condition  $\|T(S)\|_\infty < \gamma$ , where  $T$  is the CLS formed by the augmented plant  $G_{aug}$  and the controller  $K$ , and  $\gamma$  is constrained to be between  $[0.1, 5]$  to achieve robustness [124].

$$G_{aug} \begin{cases} \dot{x}(t) = Ax(t) + B_1w(t) + B_2u(t) \\ z(t) = C_1x(t) + D_{11}w(t) + D_{12}u(t) \\ e(t) = C_2x(t) + D_{21}w(t) \end{cases} \quad (4.58)$$

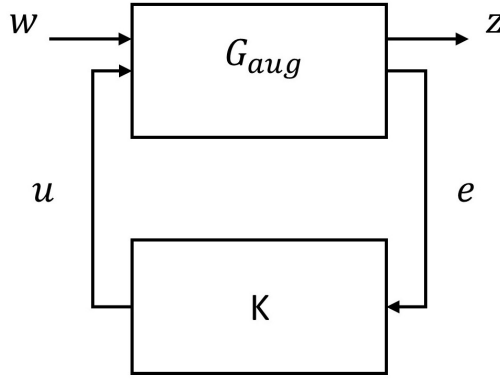


Figure 4.31: Controller block diagram of the augmented plant

#### 4.4.3 $H_\infty$ -ARS lateral stability controller

The same theory and structure of the path-following controller are applied for the lateral stability controller. However, the controlled states and consequently the performance weights are decreased into two ( $Wp_{11}$  and  $Wp_{44}$ ). In addition, the control inputs for this controller are the steering angle of the 3<sup>rd</sup> and 4<sup>th</sup>,  $\delta_3$  and  $\delta_4$ , respectively.

#### 4.4.4 Implementation and frequency domain analysis

This section introduces the design procedure and design requirement limitations for each control case. The design includes the performance and control weighted functions



that are selected and tuned to satisfy an accepted range for stability and performance. Moreover, a frequency domain analysis is conducted to demonstrate the performance and stability robustness against the velocity uncertainty.

#### 4.4.4.1 Front steering path-following controller

Equation 4.44, is used to design the controller, where the steering of the 3<sup>rd</sup> and 4<sup>th</sup> axles  $\delta_3$  and  $\delta_4$  are substituted by zero to demonstrate fixed rear axles. The performance weight functions are selected as in table 4.1, and the  $h_\infty$  problem is solved using Matlab software toolbox with constraining the performance index  $\gamma$  to be between  $[0.1, 5]$ . At first, the optimizer failed to find a solution that satisfies the performance requirements. So, the problem is solved at a fixed nominal speed 20 km/h, with releasing the constrain on the control input.

Table 4.1: Path-following controllers weighted functions

Design parameters	Front-Steering	AWS
$Wp_{11}$	$\frac{s^2+160s+6400}{16s^2+512s+4096}$	$\frac{s+8.944}{0.89s+0.25}$
$Wp_{22}$	0.05	0.05
$Wp_{33}$	0.1	$\frac{s+5}{s+0.112}$
$Wp_{44}$	0.01	0.01
$Wp_{55}$	$\frac{s^2+0.004s}{4s^2+0.00064s}$	$\frac{0.0s^2+0.06s+0.09}{0.0036s^2+0.0036s+0.0009}$
$Wp_{66}$	— — —	$\frac{s+10}{s+1}$
$Wu_{11}$	$\frac{0.0008s+0.038}{0.00032s+15}$	$\frac{0.1s+1.7}{0.00032s+30}$
$Wu_{22}$	— — —	$\frac{0.1s+2.1}{0.0001s+30}$
$Wu_{33}$	— — —	$\frac{0.1s+2.1}{0.00032s+30}$
$\gamma$	0.68	1.6

Figure 4.32 presents the frequency analysis of the uncertain CLS for the determined controller. Figure 4.32 (a) shows that the output lateral position satisfies the designed performance weighted function  $Wp_{11}$ . The function  $Wp_{11}$  is chosen to result in an acceptable lateral error at high frequencies. In addition, the performance weighted function  $Wp_{55}$  penalizes the lateral error integration at low frequencies, to ensure that the steady-state lateral error will reach zero, as presented in figure 4.32 (b). The effect of  $Wp_{55}$  is reflected on the error at figure 4.32 (a) as the gain at low frequencies are very small (below  $-100$  dB). Figure 4.32 (C) shows the control input ( $\delta_1$ ) response to the input reference, and it can be seen that there is almost no constrain on the control input

at high frequency.

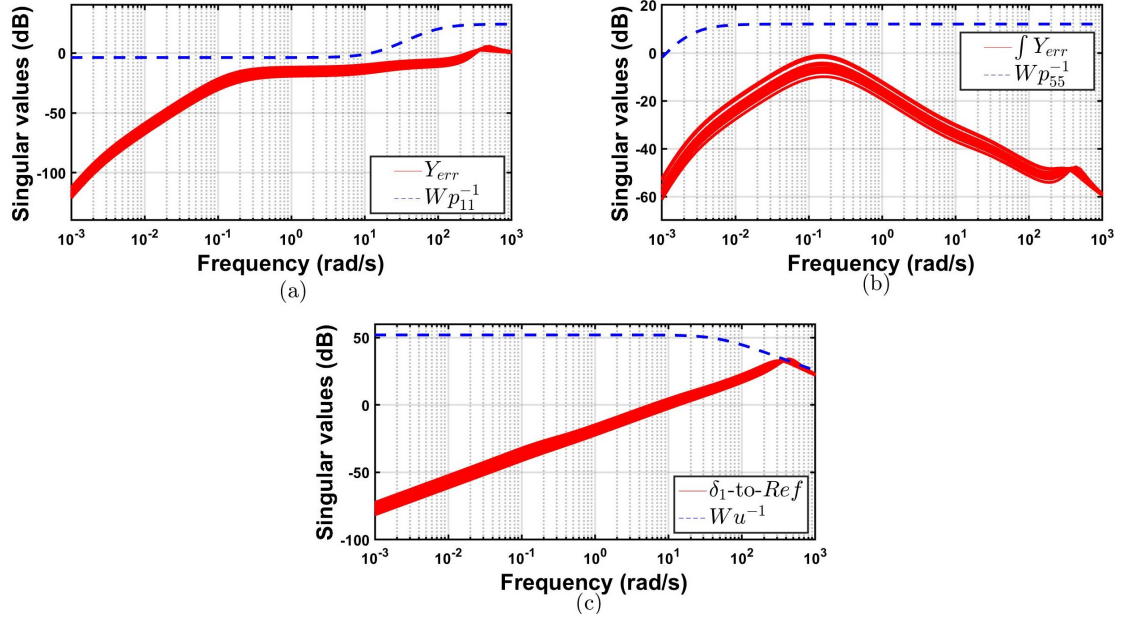


Figure 4.32: CLS frequency response of the (a)Lateral error (b)Lateral error integration (c)Control input  $\delta_1$  to the reference inputs

Figure 4.33 (a) shows the stability performance of the uncertain CLS and shows that the system attains robust stability as the structured singular value bounds  $\mu$  are  $< 1$ . However, the system doesn't achieve robust performance at high frequencies as it violates the controller performance weighted function  $Wu_{11}$ , as in figure 4.33 (b).

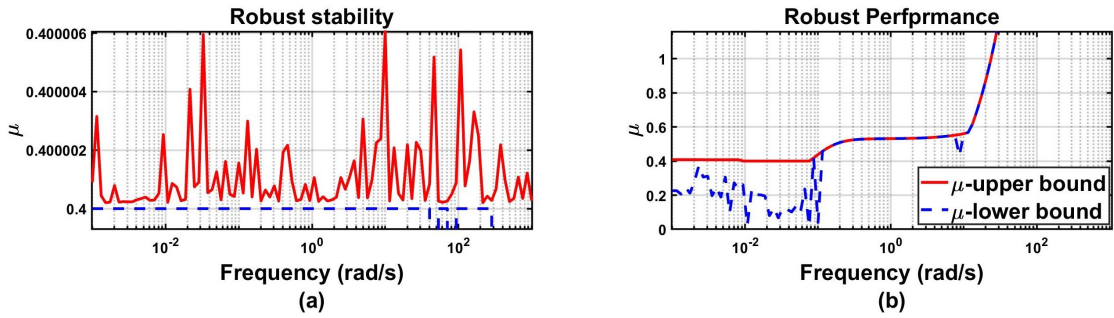


Figure 4.33: (a)Stability and (b)Performance robustness of the front steering CLS

#### 4.4.4.2 AWS path-following controller

Equation 4.44 is used with no modifications to design the AWS path-following controller that utilizes the steering of the 1<sup>st</sup>, 3<sup>rd</sup>, and 4<sup>th</sup> axles, and the selected weighted functions

are illustrated table 4.1. Including the steering of the rear axles in the model reflects several advantages on the tightening procedures as follow:

- The optimizer was able to find a solution considering the velocity uncertainty at nominal forward velocity  $60 \text{ km/h}$ .
- Tightening the constraints on the lateral error by increasing the gain of  $Wp_{11}$  at low frequencies, as can be noticed in figure 4.34 (a).
- Adding constrain on the heading angle tracking error at low frequency ( $Wp_{22}$ ), as presented in figure 4.34 (b), to ensure faster stabilization of the vehicle and less swing.
- Increasing the constrain on the lateral error integration weight function  $Wp_{55}$  for a higher frequency to ensure that the steady-state lateral error will reach zero much faster, as observed in figure 4.34 (c).
- Penalizing the heading angle tracking error integration at low frequency, as shown in figure 4.34 (d), to ensure a zero steady-state heading angle at the end of the maneuver by adding the weighted function  $Wp_{66}$ .
- Penalize the control inputs maximum steering angle at high frequencies, as shown in figure 4.35.

Despite the advantages of adding the steering of the rear axles on the design procedures, the CLS achieves robust stability but lacks performance robustness, as can be concluded from figure 4.36 (a) and (b) respectively. However, by observing figure 4.34 and figure 4.35, it can be noticed that the violation of the performance requirements is in an acceptable range and still, can achieve good performance.

#### 4.4.4.3 ARS lateral stability controller

In this section, an  $h_\infty$ -ARS lateral stability controller is developed to be integrated with the front steering path-following controller. The controller is developed to penalize the vehicle's lateral velocity and consequently limits its Sideslip and improves the stability while performing steering. The performance and control weighted functions of the developed ARS are presented in table 4.2.

Figure 4.37 presented the frequency response of the CLS , where figure 4.37 (a) shows the lateral velocity response and figure 4.37 (b) and (c) show the response of the control

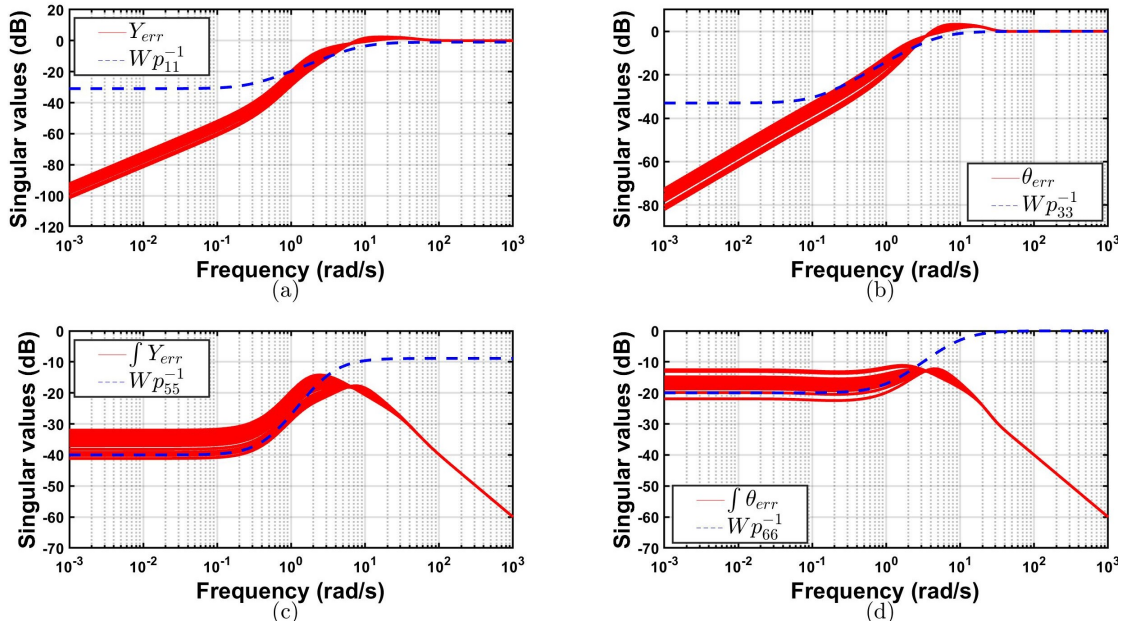


Figure 4.34: CLS frequency response of the (a)Lateral position tracking (b)Heading angle tracking (c) Lateral error integration (d)Heading angle error integration

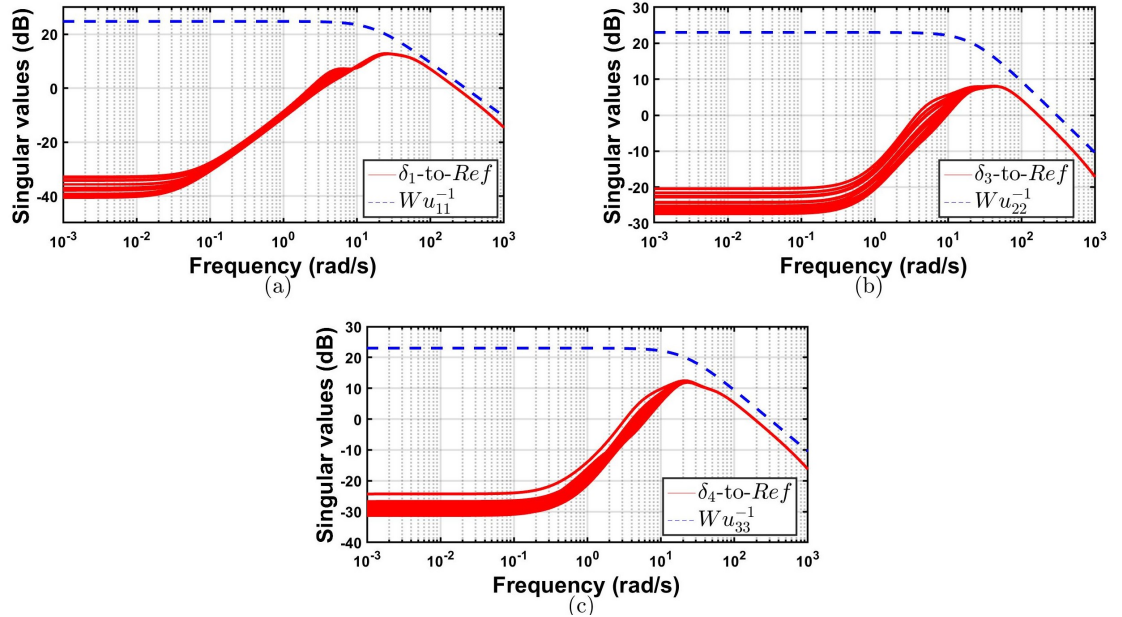


Figure 4.35: CLS frequency response of the control input (a) $\delta_1$  to the reference inputs (b) $\delta_3$  to the reference inputs (c)  $\delta_4$  to the reference inputs

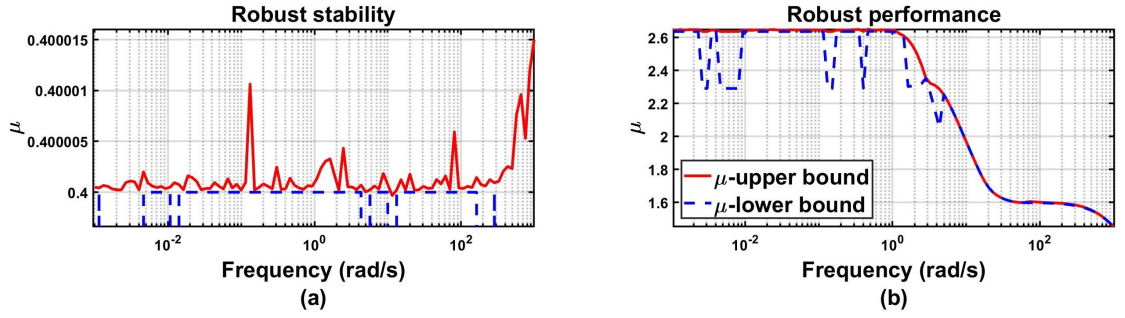


Figure 4.36: (a)Stability and (b)Performance robustness of the AWS CLS

Table 4.2: Controllers design parameters

Design parameters	ARS
$W_{p1}$	$\frac{s^2+80s+1600}{4s^2+120s+900}$
$W_{p2}$	0.01
$W_{u1}$	$\frac{0.05s+11.18}{0.0001s+10}$
$W_{u2}$	$\frac{0.05s+5.97}{0.00032s+10}$
$\gamma$	0.53

inputs  $\delta_3$  and  $\delta_4$  to the reference input, respectively. It can be seen that the response of the uncertain CLS meets the required weighted functions. Furthermore, the control weight functions  $W_{u11}$  and  $W_{u22}$  are chosen to ensure that the steering angle of the 4<sup>th</sup> axle is higher than the 3<sup>rd</sup> axle at high frequencies. Besides, it ensures satisfying the desired performance with minimum use of the rear axles' steering angles.

The CLS stability and performance robustness are illustrated in figures 4.38 (a) and (b), respectively. The figures show that the controlled system attains robust stability and performance, which allows binding the design requirements if needed.

#### 4.4.5 Evaluation and simulation results

The same vehicle configuration that is used in previous chapters and presented in chapter 3, section 3.2 is utilized to perform all simulation and testing. The Controllers are compared and evaluated by performing the NATO Double Lane Change (DLC) as in figure 4.39 at various speeds (from 40 and 100  $km/h$ ) at different coefficients of friction (0.35, 0.5 and 0.85).

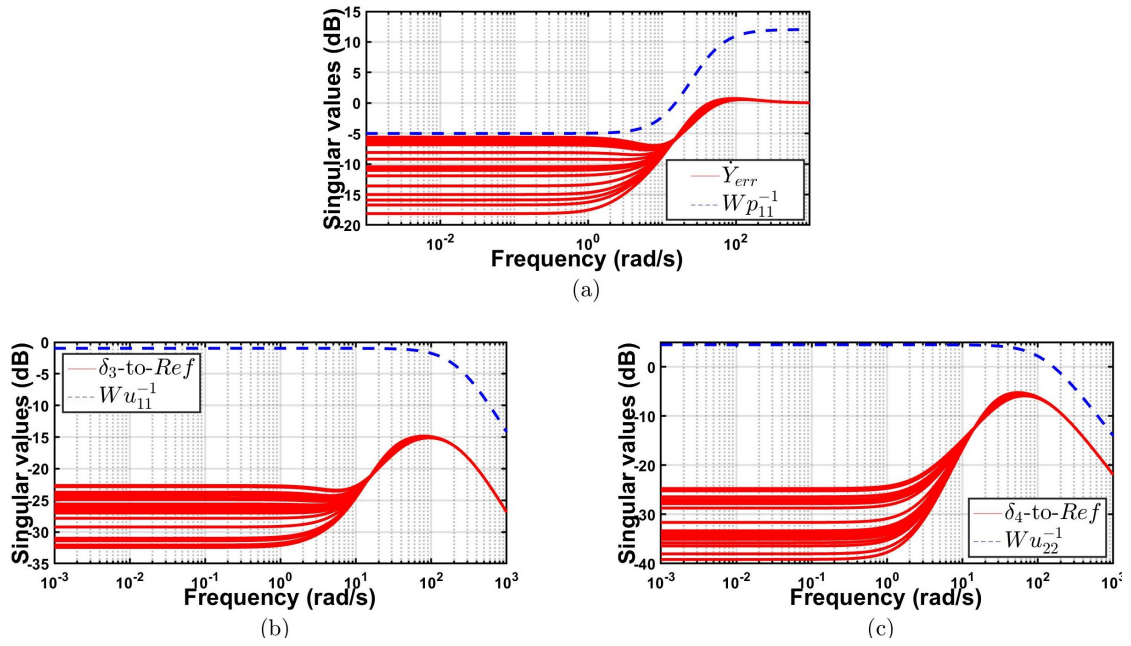


Figure 4.37: CLS frequency response of the (a)Lateral velocity (b)Control input  $\delta_3$  to the reference inputs (c)Control input  $\delta_4$  to the reference inputs

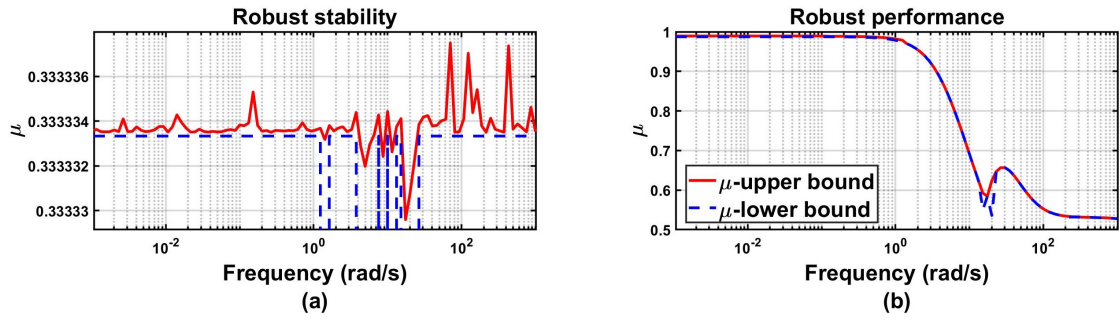


Figure 4.38: (a)Stability and (b)Performance robustness of the ARS CLS

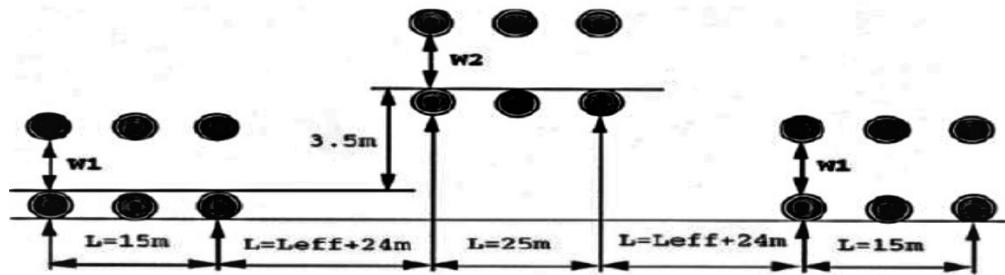


Figure 4.39: NATO AVTP 03-160 W Double Lane Change setup [31, 4]



#### 4.4.5.1 Low-speed evaluation using Double lane change maneuver

In this section the controllers will be evaluated at low speed ( $U = 40 \text{ km/h}$ ) and on roads with various coefficient of friction ( $\mu = 0.85, 0.5$ , and  $0.35$ ).

##### At friction coefficient=0.85 and forward speed=40 km/h

Figures 4.40 (a) and (b) shows the vehicle trajectory and the corresponding lateral error when driving at speed  $40 \text{ km/h}$  over a surface with coefficient of friction 0.85. It can be seen that all cases have finished the maneuver and the AWS results in a minimum error, followed by other cases. However, the error in the case of front steering with and without ARS is generated due to a phase shift from the desired trajectory. Besides, the front steering cases can stabilize the vehicle faster than the AWS case.

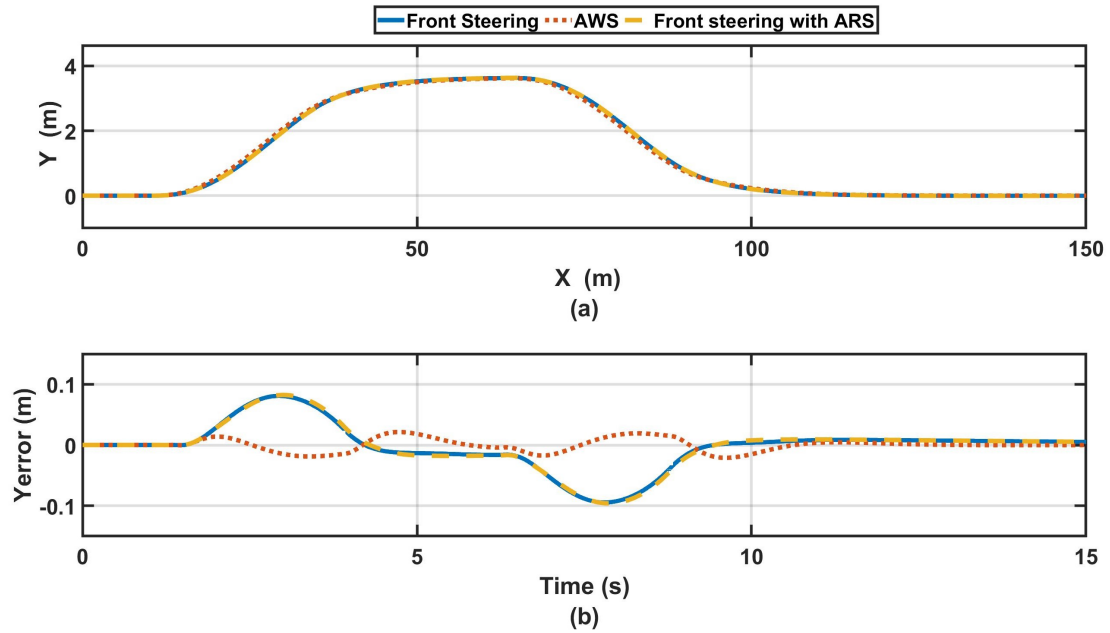


Figure 4.40: (a) Executed trajectory (b) Lateral error

The first, third, and fourth axle' average steering angles are illustrated in figures 4.41 (a), (b), and (c), respectively. It is noticed that there is no huge difference between front steering-based controllers (front steering and front-ARS), while the front steering angle of the AWS is slightly higher. In contrast, there is a big difference in the 3<sup>rd</sup> and 4<sup>th</sup> steering angles between the AWS and front-ARS controllers, where the AWS exhibits higher angles.

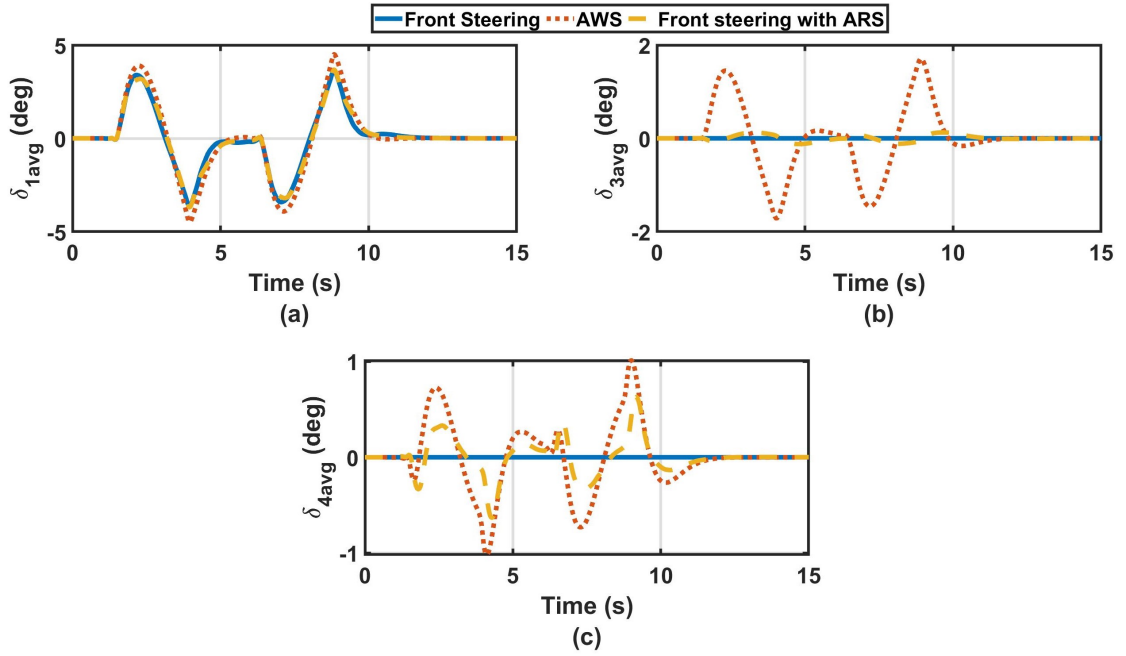


Figure 4.41: (a)1<sup>st</sup> axle (b)3<sup>rd</sup> axle (c)4<sup>th</sup> axle average steering angle

The vehicle's forward velocity is shown in figures 4.42 (a), the lateral acceleration is shown in figures 4.42 (b), and the yaw rate is in is shown in figures 4.42 (c), where there is almost no difference between the three cases. Figure 4.42 (d) presents the vehicle sideslip angle for each case, it is notable that for almost the same yaw rate, the integrated front-ARS generates the least Sideslip. Meanwhile, AWS reaches the same Sideslip as the front steering controller. However, due to the added weight for tracking the yaw angle at low frequencies, AWS generates a uniform Sideslip that has the same shape as the yaw rate signal.

#### At friction coefficient=0.5 and forward velocity=40 km/h

The vehicle trajectory when driving on a surface with friction coefficient 0.5 with speed = 40 km/h is illustrated in figure 4.43 (a), while the corresponding error is presented in figure 4.43 (b). The result is almost the same as manoeuvring with the same speed on a hard surface with Cof 0.85, and it has also the same yaw rate and sideslip response.



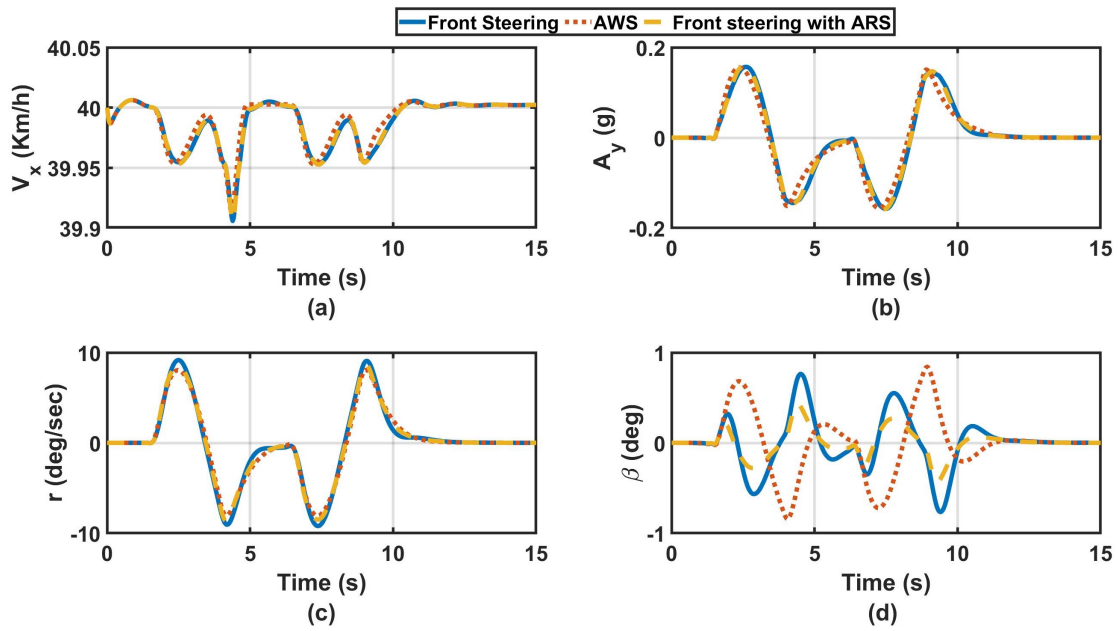


Figure 4.42: (a)Forward speed (b) Vehicle lateral acceleration (c) Yaw rate of change (d) Sideslip responses

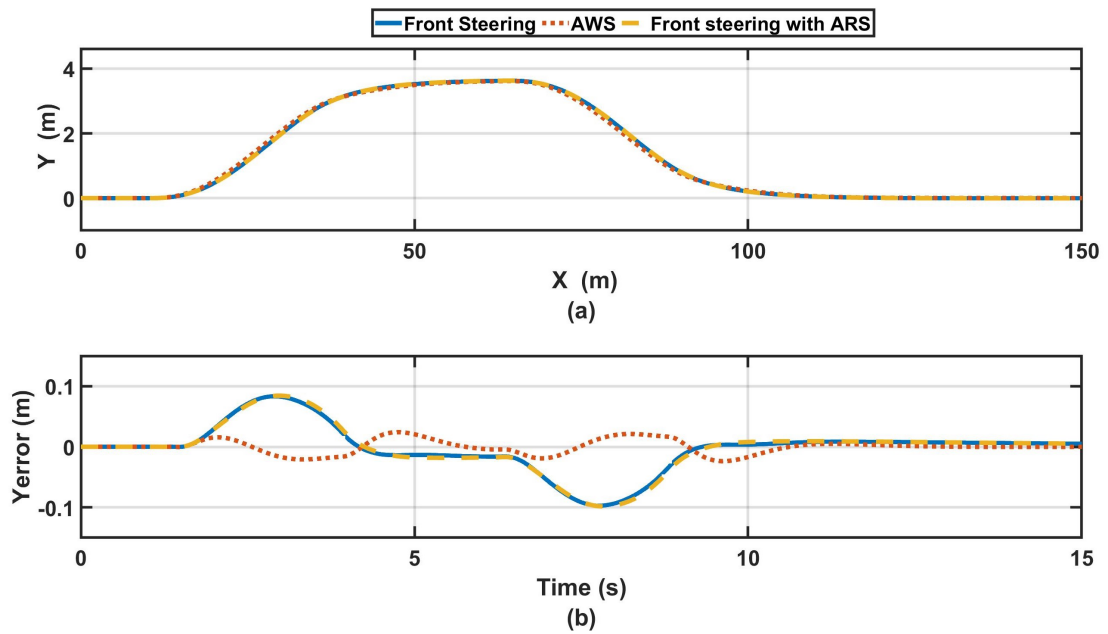


Figure 4.43: (a) Executed trajectory (b) Lateral error

#### 4.4.5.2 High-speed evaluation using Double lane change maneuver

In this section, all cases are evaluated at the maximum speed of each test on roads with various coefficients of friction. This speed is determined based on a pass/fail criteria, where the vehicle should finish the maneuver without stepping on the cones and without losing its stability.

**At friction coefficient=0.85 and forward velocity=100 km/h**

The vehicle trajectory is presented in figure 4.44 (a) when performing the maneuver with speed 100 *km/h* and all cases pass the maneuver successfully. The integrated front-ARS results in less mean square error and stabilize the trajectory faster than other cases, as can be observed from figure 4.44 (b). However, it has a higher steady-state error due to the tracking limitations of the front-steering controller that was integrated with the ARS.

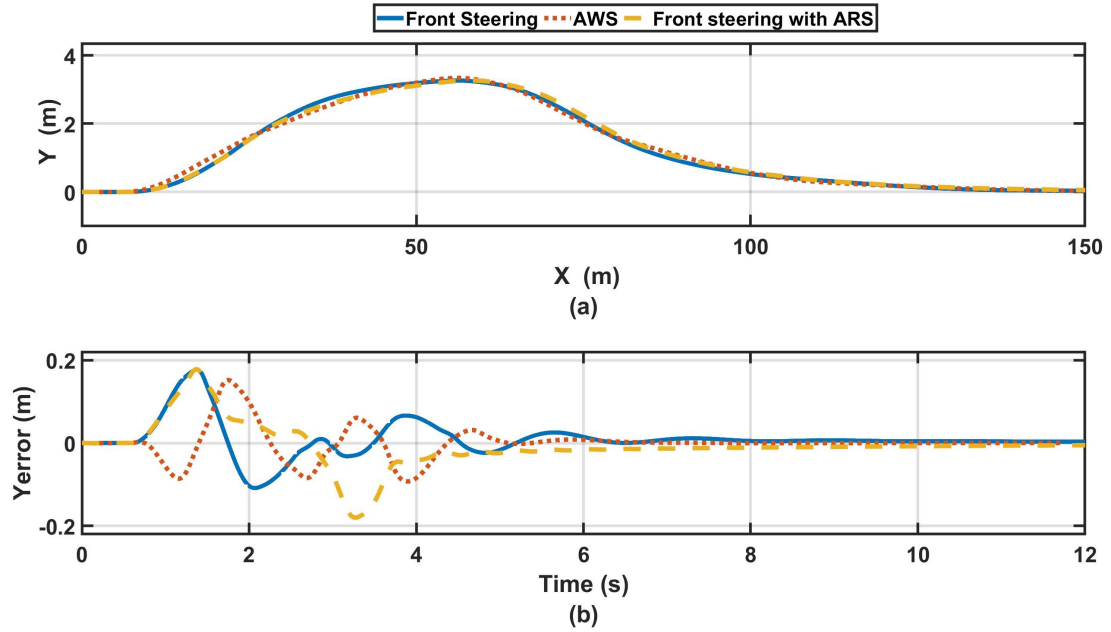


Figure 4.44: (a) Executed trajectory (b) Lateral error

The front steering controller results in the highest average front steering angle among all cases as in figure 4.45 (a). The front-ARS results in a higher 3<sup>rd</sup> axle average steering than the AWS as presented in figures 4.45 (b), meanwhile, they reach the same 4<sup>th</sup> average steering angle as illustrated in figures 4.45 (c). In addition, it can be noticed that

the front-ARS results in parallel steering, which means that the rear and front axles steer in the same direction. On contrary, AWS results in a random steering pattern, which is sometimes parallel and others counter.

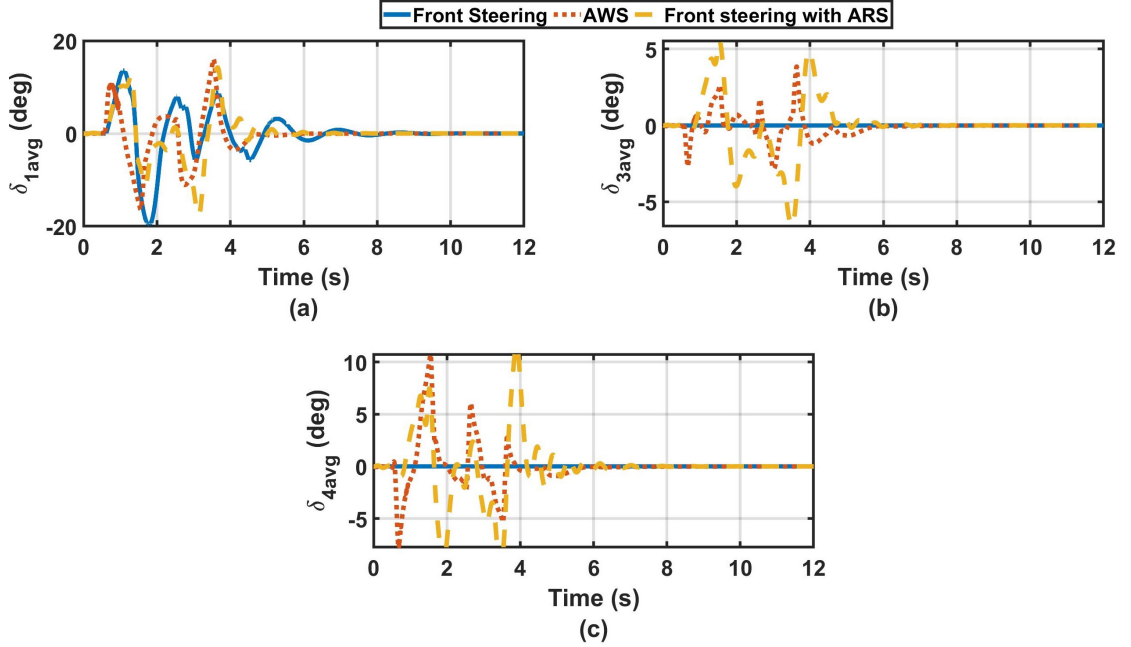


Figure 4.45: (a)1<sup>st</sup> axle (b)3<sup>rd</sup> axle (c)4<sup>th</sup> axle average steering angle

The dynamic response of all cases is illustrated in figure 4.46. The less reduction in the longitudinal velocity is achieved by the integrated front-ARS, followed by the AWS, then the front steering that produces the highest reduction as presented in figure 4.46 (a). By observing figure 4.46 (b), it can be noticed that the lateral acceleration is kept below the rollover threshold for all cases. However, the AWS and the front-ARS stabilize almost at the same time and faster than the standalone front steering. Meanwhile, the front-ARS results in the least yaw rate because of the very low Sideslip as observed in figure 4.46 (c) and (d), respectively.

#### At friction coefficient=0.5 and forward velocity=100km/h:

In this section, the controllers are evaluated at high speed ( $U = 100 \text{ km/h}$ ) and low-CoF (0.5), respectively. This test shows the importance of integrating a lateral stability controller in autonomous vehicles for crash mitigation applications.

It is shown in figure 4.47 (a) that all other cases fail to stabilize the vehicle and finish the

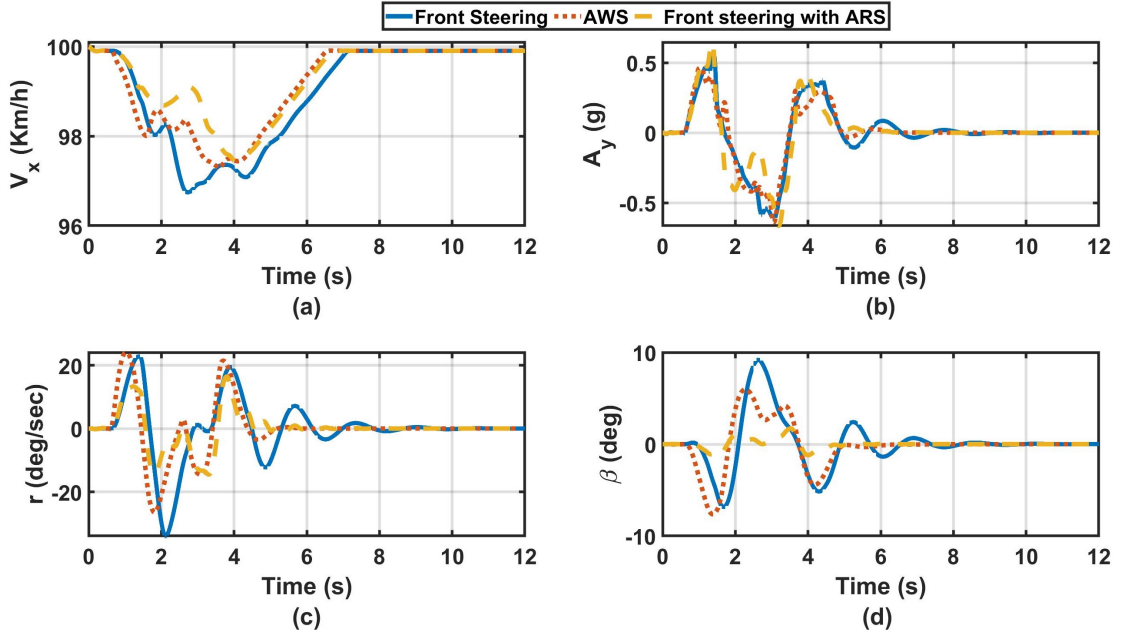


Figure 4.46: (a)Forward velocity(b) Vehicle lateral acceleration (c) Yaw rate of change (d) Sideslip responses

manoeuvre except for the integrated front-ARS controllers, which pass the manoeuvre despite the generated high lateral error, as presented in figure 4.47 (b).

It is shown in figure 4.47 that all other cases fail to stabilize the vehicle and finish the maneuver. On the other hand, the integrated front-ARS controllers pass in the maneuver despite the generated high lateral error.

As can be observed in figure 4.48 (a), there is a saturation in the 1<sup>st</sup> axle's steering angle. Despite that, the ARS controller can stabilize the vehicle by exhibiting small steering angles on the 3<sup>rd</sup> and 4<sup>th</sup> axles, as presented in figure 4.48 (b) and (c), respectively.

Figure 4.49 (a) shows the effectiveness to regain the vehicle stability with a small reduction in the longitudinal velocity, which doesn't exceed 7 km/h. In addition, the yaw rate and sideslip responses show the effectiveness of the ARS in limiting the yaw rate and sideslip as shown in figure 4.49 (c) and (d), respectively and regain the vehicle stability.

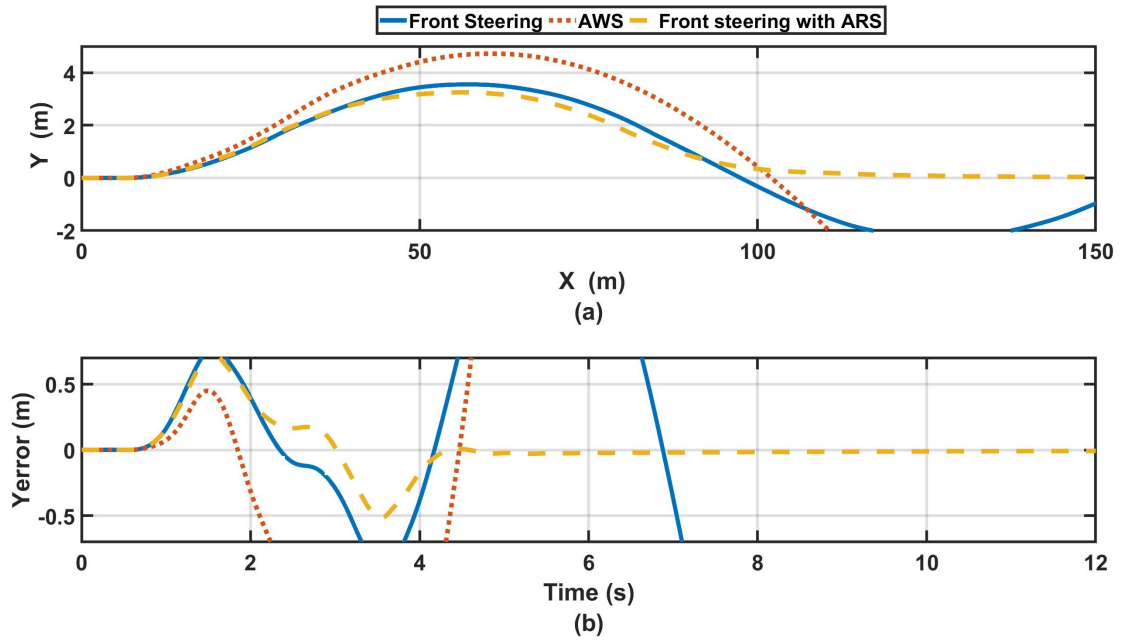


Figure 4.47: (a) Executed trajectory (b) Lateral error

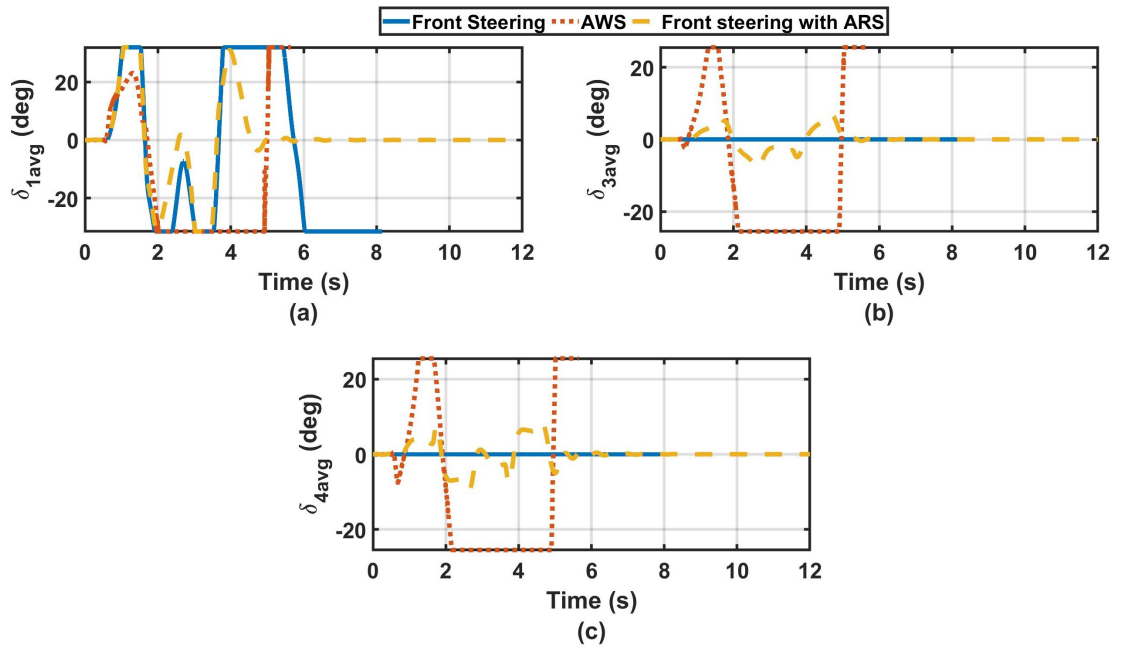


Figure 4.48: (a)1<sup>st</sup> axle (b)3<sup>rd</sup> axle (c)4<sup>th</sup> axle average steering angle

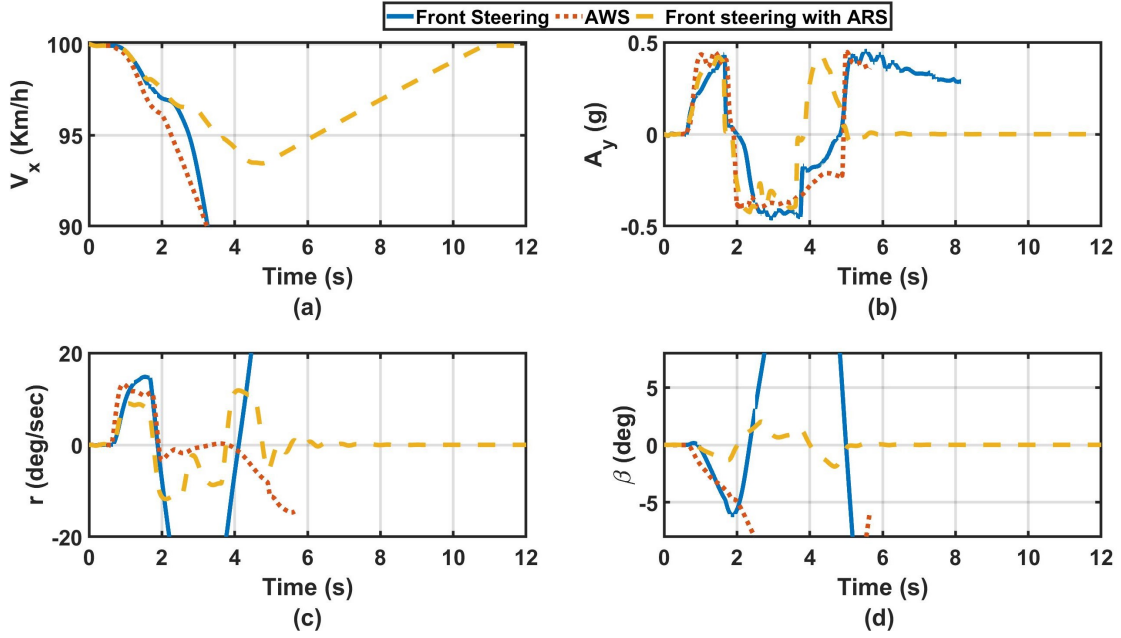


Figure 4.49: (a)Forward velocity(b) Vehicle lateral acceleration (c) Yaw rate of change (d) Sideslip responses

## 4.5 Chapter summary

This chapter investigated the influence of incorporating the independent and active steering of the vehicle's 3<sup>rd</sup> and 4<sup>th</sup> axles on the vehicle lateral stability performance in the case of conventional and autonomous driving.

For conventional driving on a smooth rigid surface, an active rear steering controller was developed for the 8x8 combat vehicle. The controller utilized the independent steering of the rear axles (3<sup>rd</sup> and 4<sup>th</sup>) to minimize the vehicle sideslip and limit the yaw rate. The proposed controller included two terms. The first was a feedback term generated by an optimal LQR controller that controls the vehicle at all driving conditions and was designed with no dependency on the reference model. The second was a feedforward controller to attain a zero sideslip at low-speed. The proposed controller was evaluated by assessing the steady and transient state handling characteristics of the vehicle in comparison with fixed rear axles and active 4<sup>th</sup> axle steering vehicles.

After that, a novel adaptive-ISMIC was designed based on the same aspects of the developed LQR controller. The controller consisted of two terms; the first is a gain-scheduled

LQR controller, which was optimized using a new synthesized cost function to ensure minimum use of rear axles and stability of the controller at various operating conditions. In addition, the scheduled gains were replaced with a GP-based equation to ensure a smooth transition between these operating conditions. The second term is a nonlinear switching controller that considered the lateral dynamics disturbances generated from the road's irregularities and ensured a robust performance. The controller was tested and compared with the conventional LQR and uncontrolled vehicle and showed better stability in different driving conditions over a rough-rigid road.

For autonomous driving on a smooth rigid road, three  $h_\infty$  controllers were developed to control the vehicle path. The first was a path-following controller that utilized the steering of the front axles only. The second was also a path-following controller, which exploited the steering of all axles. The third controller integrated the front steering path-following controller with a lateral stability Active Rear Steering (ARS) Controller. In addition, a frequency-domain analysis was conducted for the closed-loop control systems. The analysis shows that including the steering of the rear axles enhanced the path-following performance by tightening the constraints on the lateral position tracking, heading angle tracking, and control inputs responses. Furthermore, the analysis of the developed ARS-stability controller shows the effectiveness of the rear axles in constraining the vehicle sideslip with minimum utilization of the rear axles. Eventually, the controllers were evaluated using DLC maneuvers to discuss the advantages and limitations of each technique.

## **CHAPTER 5**

### **Direct Yaw Moment Controllers**

#### **5.1 Introduction**

In this chapter, two DYCs are introduced based on differential braking and torque vectoring. The first is a novel differential braking controller based on genetic programming (GP), which is developed to improve the lateral stability of the 8X8 combat vehicle. The controller is compared with a Neuro-fuzzy differential braking (NFDB) controller to show the effectiveness of using the GP in replacement with the Neuro-fuzzy rules. The second controller is a TVC, which is designed based on conventional SMC theory. The vehicle sideslip is constrained in the controllers' design. Moreover, the controller is evaluated with and without the consideration of the sideslip constraint to show its influence on the controller performance.

#### **5.2 Differential braking controllers**

The controllers are designed based on three stages. At first, an activation criterion is developed to decrease the excessive use of braking force, which is based on a phase-plane analysis of the vehicle nonlinear model. The controller isn't designed to track a reference yaw signal but is only activated to push back the vehicle inside the stability regime, which makes the controller has less dependent on the reference signal. In the second stage, an adaptive controller generates an effective braking moment according to the vehicle speed and road conditions based on a pre-generated data set. In the last stage, the braking moment is executed based on the yaw error direction generated and the slip ratio of each wheel using a fuzzy-logic slip controller.

##### **5.2.1 Yaw motion reference model**

In this section, the single track (bicycle) model is used to derive the yaw motion reference model for DYC. The model is derived based on the vehicle model as shown in



figure 5.1. In this model, the 3<sup>rd</sup> and 4<sup>th</sup> axles are considered to be fixed.

$$\begin{bmatrix} \dot{\beta} \\ \dot{r} \end{bmatrix} = \begin{bmatrix} a_{11} & a_{12} \\ a_{21} & a_{22} \end{bmatrix} \begin{bmatrix} \beta \\ r \end{bmatrix} + \begin{bmatrix} \frac{C_{\alpha 1} + c_{21}C_{\alpha 2}}{mU} \\ \frac{a_1C_{\alpha 1} + a_2c_{21}C_{\alpha 2}}{I_{zz}} \end{bmatrix} \delta_1 \quad (5.1)$$

$$\begin{aligned} \text{Where } a_{11} &= \frac{-C_{\alpha 1} - C_{\alpha 2} - C_{\alpha 3} - C_{\alpha 4}}{mU} \\ a_{12} &= \frac{-a_1C_{\alpha 1} - a_2C_{\alpha 2} - a_3C_{\alpha 3} - a_4C_{\alpha 4} - mU^2}{mU^2} \\ a_{21} &= \frac{-a_1C_{\alpha 1} - a_2C_{\alpha 2} - a_3C_{\alpha 3} - a_4C_{\alpha 4}}{I_{zz}} \\ a_{22} &= \frac{-a_1^2C_{\alpha 1} - a_2^2C_{\alpha 2} - a_3^2C_{\alpha 3} - a_4^2C_{\alpha 4}}{I_{zz}U} \end{aligned}$$

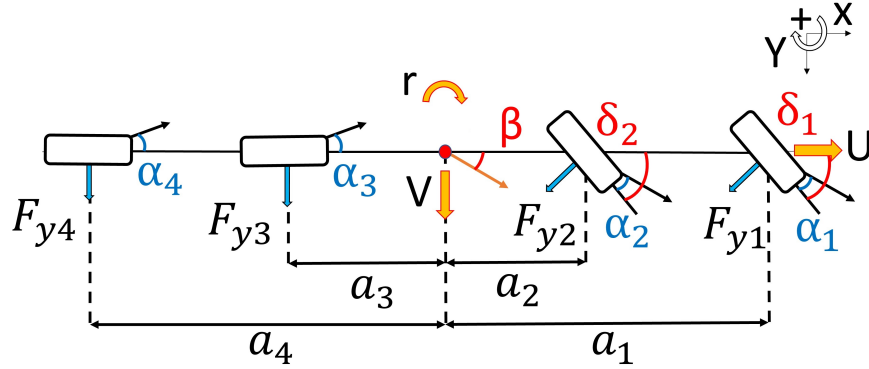


Figure 5.1: Four-axle steering 8x8 vehicle bicycle model

To derive a linear steady-state (ss) reference model all the time-varying parameters ( $\dot{\beta}$  and  $\dot{r}$ ) in equation (5.1) were considered to be equal to zero. After that, the equation is arranged to address the steady-state yaw rate and vehicle sideslip as in equation 5.2. To perform better performance and higher stability, the reference sideslip and yaw rate have to be limited according to equation (5.3) and (5.4) [116]. However, the reference vehicle's sideslip can be considered as zero for higher stability and better tracking per-

formance [38, 44, 84, 52]. Eventually, to generate a traceable yaw rate that is not faster than the vehicle response, a dynamic delay ( $\tau$ ) has to be added as a low-pass filter function according to equation (5.5) [5], where  $\mu$  is the road friction and  $g$  in the gravitational acceleration.

$$\begin{bmatrix} \beta \\ r \end{bmatrix}_{ss} = \begin{bmatrix} a_{11} & a_{12} \\ a_{21} & a_{22} \end{bmatrix}^{-1} \begin{bmatrix} \frac{C_{\alpha 1} + c_{21}C_{\alpha 2}}{mU} \\ \frac{a_1C_{\alpha 1} + a_2c_{21}C_{\alpha 2}}{I_{zz}} \end{bmatrix} \delta_1 \quad (5.2)$$

$$\beta_{max.} = \tan^{-1}(0.02\mu g) \quad (5.3)$$

$$r_{max.} = \frac{0.85\mu g}{U} \quad (5.4)$$

$$r_{ref} = \frac{r_{ss}}{\tau s + 1} \quad (5.5)$$

## 5.2.2 Three stages controllers' design

The control design is presented in this section in three stages. First, an activation condition for the braking controller is presented to minimize the use of the braking force in emergencies only when the vehicle stability is vulnerable. Second, an upper controller is developed to generate the wheels' effective braking moment according to the driving conditions (vehicle speed and road friction). At last, a fuzzy lower controller is designed to execute the braking moment through the eight wheels according to the direction of the yaw rate error signal between the reference model and the vehicle, wheels longitudinal slip, and the activation condition or Stability Index (SI).

### 5.2.2.1 Activation condition based on phase-plane analysis

Studying the stability of linear systems can be mathematically obtained through different analysis approaches such as eigenvalues and Routh stability. On the contrary, nonlinear systems have irregular behaviour in comparison with linear systems, which gave stability analysis some complexity. In many cases, the stability of nonlinear systems can be concluded from its linearized model. However, if the linearized model is marginally

stable, so nothing can be concluded about the stability of the nonlinear system and a nonlinear approach is needed.

Phase plane analysis is a graphical approach to picture the stability of the system and it is usually used for the nonlinear second-order system. Consider a second-order system consists of two states  $x_1, x_2$ , and nonlinear functions  $f, g$  as in equation 5.6.

$$\dot{x}_1 = f(x_1, x_2) \text{ and } \dot{x}_2 = g(x_1, x_2) \quad (5.6)$$

Phase portrait can be obtained by plotting the relation between  $x_1$  and  $x_2$  [14].

For the system described in equations (4.6), and (4.5) considering constant longitudinal velocity. Let's substitute the tire forces by Dugooof's tire model from equation (5.7) to (5.10), where  $f_x$  and  $f_z$  are the longitudinal and vertical forces respectively,  $C_s$  is the longitudinal stiffness of the tire,  $s_i$  is the longitudinal wheel's slip ratio,  $\omega_i$  is the wheel angular velocity, and  $R$  is the tire radius.

$$F_x = \frac{C_s s_i}{1 - s_i} f(\lambda) \text{ and } F_y = \frac{C_{\alpha_i} \tan(\alpha_i)}{1 - s_i} f(\lambda) \quad (5.7)$$

$$s_i = 1 - \frac{R\omega_i}{U} \quad (5.8)$$

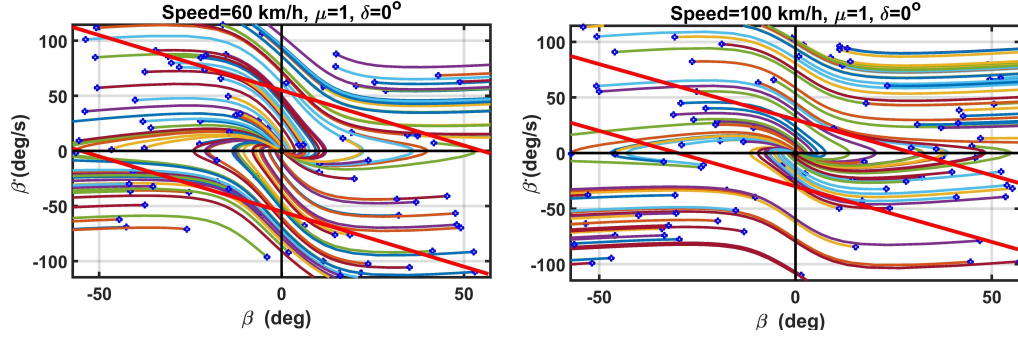
$$\lambda = \frac{\mu f_{zi} [1 - \epsilon_r U \sqrt{s_i^2 + \tan^2(\alpha_i)}]}{2 \sqrt{(C_s s_i)^2 + (C_{\alpha} \tan(\alpha_i))^2}} (1 - s_i) \quad (5.9)$$

$$f(\lambda) = \begin{cases} \lambda(2 - \lambda) & \lambda < 1 \\ 1 & \lambda \geq 1 \end{cases} \quad (5.10)$$

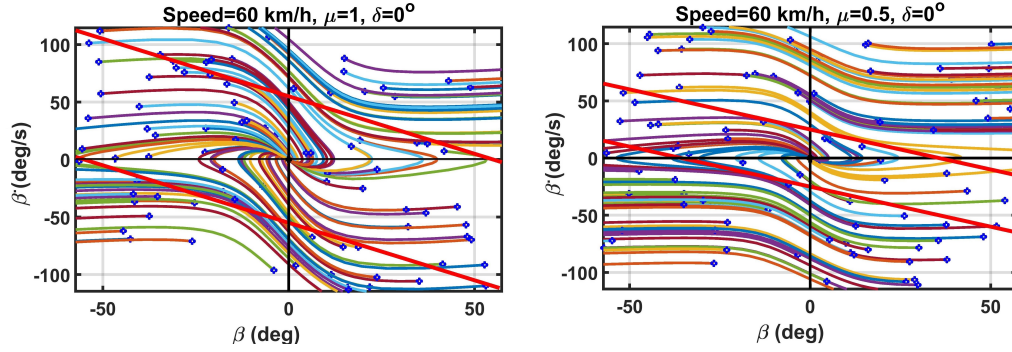
Let  $F_z$  to be obtained from equation 5.11 [125] where the  $\pm$  is to compensate for the right and left wheel respectively and  $t_w, l, h_{cg}$  are the track width, wheel base, and the height of the Center of Gravity (CG).

$$F_{zi} = \frac{m g a_i}{2l} \pm \frac{m a_y h_{cg} a_i}{t_w l} \quad (5.11)$$

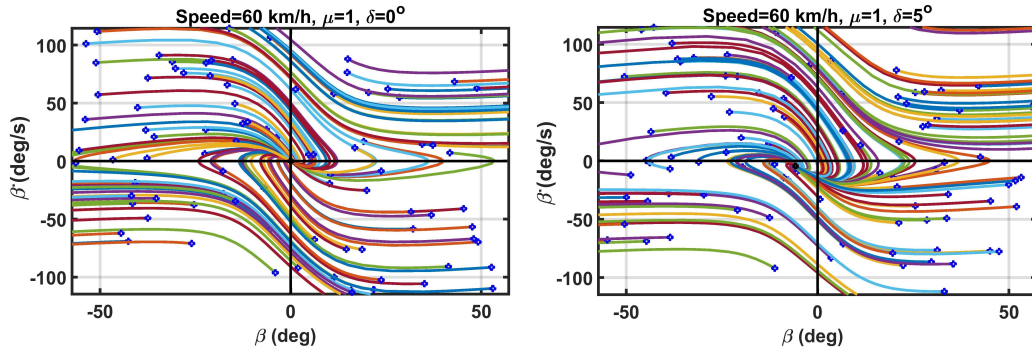
Then, the system's differential equations are solved using Matlab for the yaw rate  $r$  and the vehicle's sideslip  $\beta$ . Eventually, a quasi-linear solution was determined to the system concerning the sideslip  $\beta$  and the sideslip rate of change  $\dot{\beta}$  at each solution of  $r$  and  $\beta$ .



(a) Phase analysis for different longitudinal speeds



(b) Phase analysis for different road's friction coefficients



(c) Phase analysis for different front steering angles

Figure 5.2: Effect of changing the driving and road conditions on the phase-plane

It can be noticed from figure 5.2 (a) and (b) that the states' trajectory will end up at the equilibrium point if started anywhere inside the red lines (stability region) and will end up at infinity if started at anywhere else. This stable region decreases with increasing

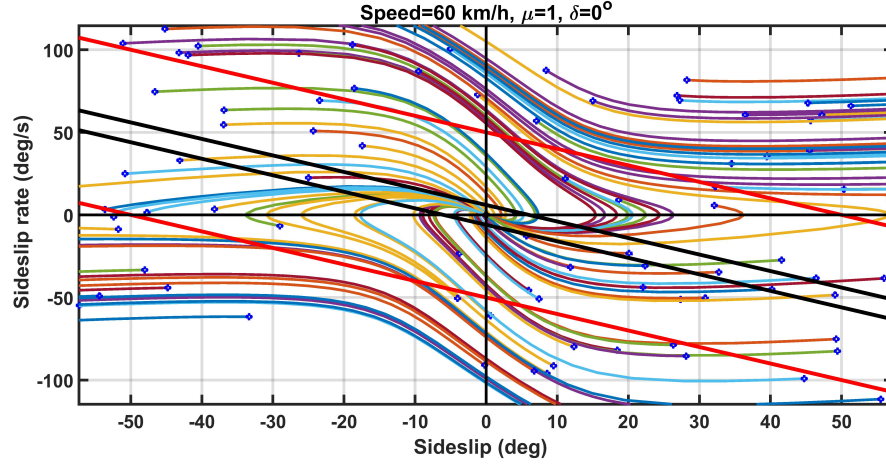


Figure 5.3: Stability region at  $\dot{\beta}, \beta$  phase-plane to activate the vehicle differential braking controller

the vehicle's speed and/or decrease the road coefficient of friction [125]. In addition, the origin position changes with changing the steering angle as shown in figure 5.2 (c). Therefore, the activation condition of the braking controller is defined as shown in figure 5.3, where the new stability region is marked by the black lines to force the states to stay close to the origin for various driving conditions and to cope with changing the driving and road conditions.

The controller activation condition can be defined as the stability index by equation 5.12, where  $k_{\dot{\beta}-\beta}$  is the slope of the black line and  $B$  is the width of the stability region.

$$|\dot{\beta} + k_{\dot{\beta}-\beta}\beta| < B \quad (5.12)$$

#### 5.2.2.2 Neuro-Fuzzy Differential Braking controller (NFDB)

Fuzzy logic was introduced by Zadah in the late 60s which represents the inference of action based on useful knowledge about the system [126, 127]. Fuzzy-Logic Control (FLC) was introduced by Mamdani (1974).

Generally, FLC is done by first fuzzify the crisp input data into fuzzy ones, then determine the membership functions. After that fuzzy inference rules are implied and eventually the fuzzy output is defuzzified into a crisp value. The determination of the

membership function affects the quality of FLC, so a tuning or optimization of the membership functions is needed to ensure high quality.

The neuro-fuzzy controller is a machine learning controller in which a neural network is used to determine and tune the weights ( $w$ ) of the membership functions while maintains the essence of FLC [128]. In neural networks the weights are updated passed on different methods that determine the optimum weights that minimize the cumulative network error  $E_c$  as in equation 5.13, where  $k$  is the target layer,  $i$  represents the  $i^{th}$  neuron of the output layer,  $t_i$  is the target output, and  $o_i$  is the actual output. Two of these methods are the least square (LS), and the gradient method as shown in equations 5.14 and 5.15, where  $X$  and  $\theta$  are the node input and threshold, respectively.

$$\min_w E_c = \min_w \frac{1}{2} \sum_{k=1}^n \sum_{i=1}^q [t_i(k) - o_i(k)]^2 \quad (5.13)$$

$$\Delta w = \eta \left[ t - \left( \sum_{i=1}^q w_i X_i - \theta \right) \right] X_i \quad (5.14)$$

$$\Delta w = -\eta \frac{\partial E(k)}{\partial w} \quad (5.15)$$

In this section, a neuro-fuzzy controller is developed as an upper controller to generate the maximum wheel braking torque. First, a ramp braking moment was applied at each wheel individually and the vehicle was driven in a straight line at a certain speed and a road's coefficient of friction. After that, the maximum braking moment at which the maximum vehicle's sideslip and yaw moment based on equations 5.3, and 5.4 were determined. The simulation was repeated at different speeds (from 20 to 110 km/h) and various road coefficients of friction (from 0.2 to 0.85) to generate a data set. A neural network as in figure 5.4 was trained on the generated data set. The network weights were optimized according to the hybrid optimization method, in which the inputs' weights were determined based on backpropagation while the least square method was used to optimize the output's weights [129]. Eventually, the network optimizes the inputs and outputs membership function of a 36 rules fuzzy controller.

The developed NN is structured by a 4 layers network; the input layer consists of 12 nodes, 2 hidden layers include 36 nodes for each layer and a single-node output layer.

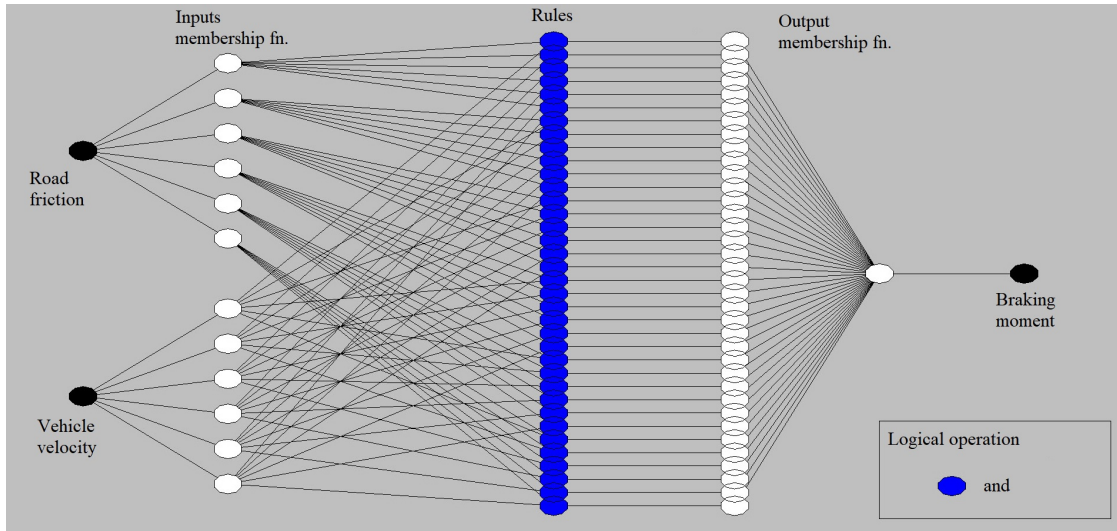


Figure 5.4: ANFS network

The 36 nodes layers represent a 36 fuzzy rule, which will be implemented later in the control algorithm. Furthermore, the network is trained using a hybrid training algorithm, which resulted in a training error of  $1.783e-3$  for 22 epochs.

Note that to generate an accurate ANFS controller (NFDB), a high dimension data-set from the inputs and output is required, which is a time-consuming process. Besides, the higher dimension of the data-set results in a larger rules number. Figure 5.5 represent a comparison between the output of high and low dimensional data-set consequently. It can be observed that the output was missing at road frictions between 0.2 to 0.4 and from 0.55 to 0.7, which means that a high dimensional training data-set is essential, which may be hard to determine and require higher processing effort to execute the corresponding fuzzy rules.

### 5.2.2.3 Genetic Programming Differential Braking controller (GPDB)

This section introduces a novel upper controller that incorporates genetic programming and offers high accuracy correspond to a lower-dimensional data-set, which utilizes an optimized equation that is developed using Eureqa software. Furthermore, the controller will require less computational effort than the NFDB controller.

GP was used in this section to form an equation that generates the maximum braking torque based on the input vehicle speed and road friction. A low-dimensional data set

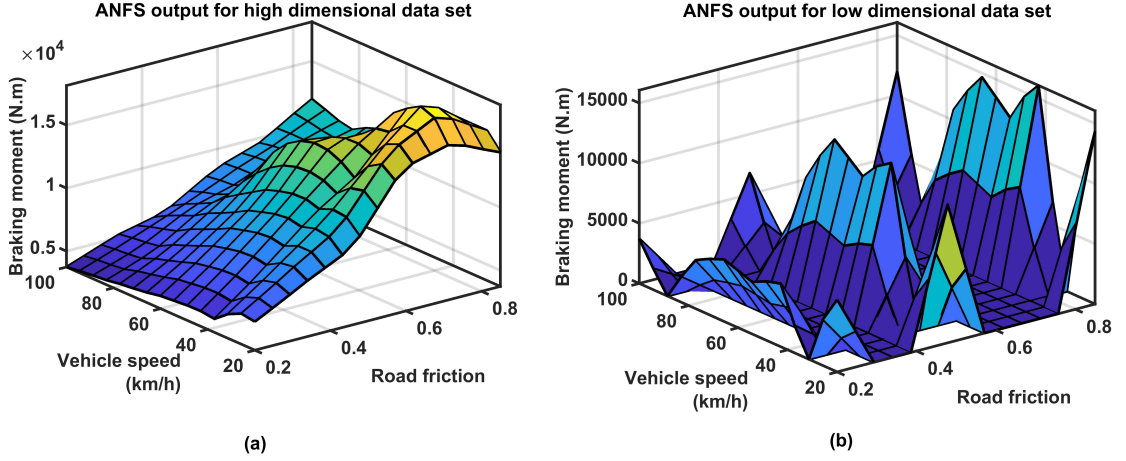


Figure 5.5: Comparison between ANFS output for (a) high dimensional data-set and (b) low dimensional data-set

was used in the process. Also, the output equation was constrained to be generated utilizing basic and simple mathematical operation (+, -, protected division /, \*) to decrease the complexity of the formulated equation and consequently decrease the computational effort for the desired controller as shown in equation 5.16, where  $C_1$  to  $C_6$  are constants. To optimize equation 5.16 and its corresponding constants, Eureka software was utilized. The software was set to minimize the Mean Square Error (MSE) and the output equation resulting in the following statistics:  $R^2$  fitness 0.9978, Correlation coefficient 0.998, Mean absolute error 131.1 N.m, Normalized fit 0.002, and complexity size 45 with constraining it to the mathematical operations that mentioned previously. Moreover, it was used a generation rate of 240 per second at 8 CPU cores, 16 M evaluation per second, and the final equation was developed after 11 minutes.

Contrary to ANFS, the generated equation using low dimensional data-set interpolate for the missing data and resulting in smooth output as can be observed from figure 5.6. However, ANFS has higher accuracy using the high dimensional data-set.

$$M_b = C_1 + C_2U + C_3\mu U + C_4U^2 + \frac{-C_5 - C_6U}{C_7\mu} + C_8\mu^2U^3 - C_9\mu U^2 \quad (5.16)$$



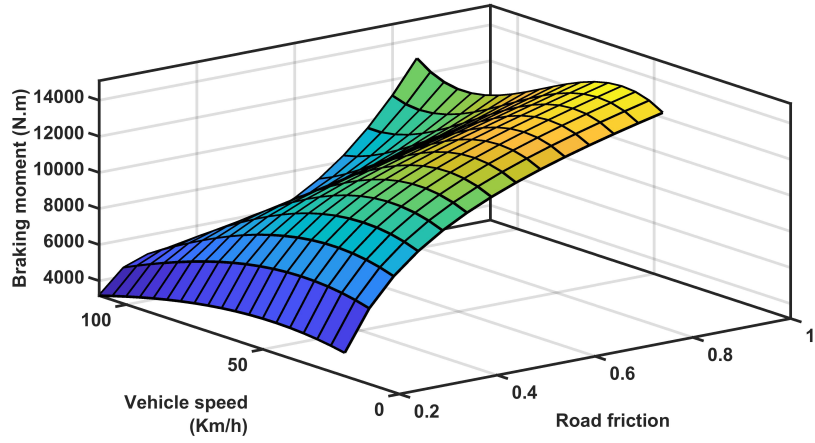


Figure 5.6: GA-DB output for low dimensional data-set

Furthermore, the execution time of the NF-based and GP-based controllers are evaluated using the Matlab/Simulink profiler for various time steps using the same solver and simulation time. The execution time per each step for different time steps is introduced in figure 5.7, where the GP-based controller has significantly less execution time than the NF-based controller.

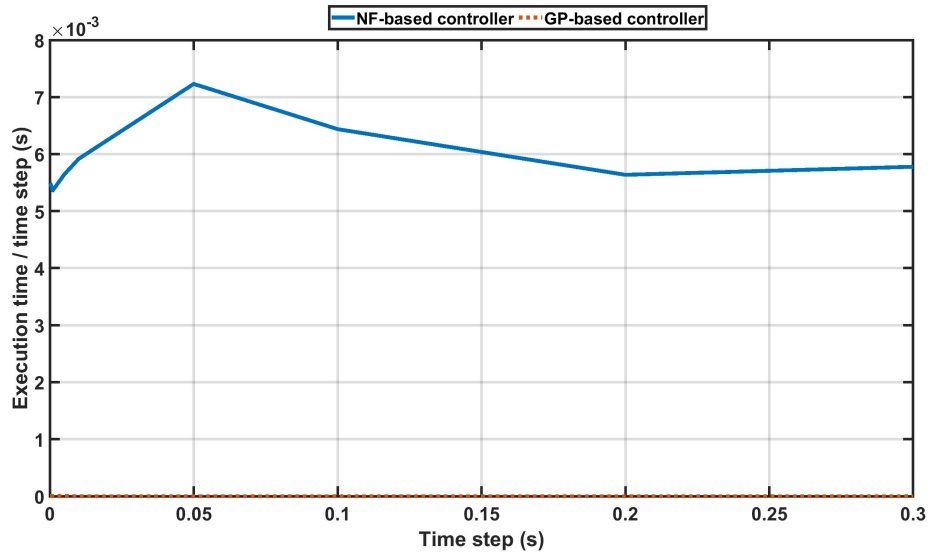


Figure 5.7: Mean execution time per step for each time step

#### 5.2.2.4 Fuzzy-logic slip controller

The traction force and grip between the tire and road surface are drastically decreased as the longitudinal slip increased. To maintain the effectiveness of DYC the longitudinal slip while driving (traction) or braking should be limited to be less than 0.2 (20%) where the maximum traction is achieved [130]. Moreover, to avoid excessive braking, the braking moment is applied on one wheel based on its longitudinal slip. So if the slip becomes more than 0.2 no braking moment will be applied on that wheel and will be executed through the next wheel. The wheels at the vehicle's right side are used to generate a negative yaw moment, while the left ones are used to generate a positive yaw moment. In addition, the longitudinal slip due to traction is controlled in case the braking controller is not active to avoid contradiction between the objectives of decreasing the slip and generating yaw moment in a certain direction.

Based on the previous knowledge and condition, it is convenient to develop the controller utilizing a decision making-knowledge based controller, which in this case is a conventional Fuzzy Logic Controller (FLC). A Mamdani FLC model, which was developed by Zadeh in 1973 [131], was used to design the controller if it is more intuitive and suitable for human input than Sugeno model. The fuzzy rule was created as follows:

$$if \ (i/p_i \text{ is } \mu(i)) \text{ and/or } (i/p_j \text{ is } \mu(j)) \text{ and/or } \dots \text{ then } (o/p_n \text{ is } \mu(n))$$

Where  $\mu(i)$  is the  $i^{th}$  input (i/p) or output (o/p) membership function. And the aggregation is performed based on (min-max) operation on the rules  $R_i$  as in equation 5.17, and the defuzzified output is generated based on equation 5.18 where  $x(i)$  is a point in the universe of discourse along the x-axis.

$$Agg. \{R1, R2, \dots, Rn\} = max. \{R1, R2, \dots, Rn\} \quad (5.17)$$

$$Centroid = \frac{\sum_i \mu(x_i)x_i}{\sum_i \mu(x_i)} \quad (5.18)$$

The developed controller is a composition of the rule base of multiple inputs that represent 8 wheels' longitudinal slip and the corrective moment rate or direction. For more detail, a braking moment is applied on the right wheels in case of a negative rate and applied on the left wheels in case of a positive rate. Table 5.1 represent the rule base of

the right wheel of axle number  $i$ , where  $i$  changes from 1 to 4, concerning the corrective moment rate. In this table, NMR denoted for negative moment rate and PMR for positive moment rate while HNS denoted for high negative slip, NS for negative slip, and PS for zero and positive slip. In addition, table 5.2 represents the control output of wheel number  $i + 1$  with respect to wheel number  $i$  of the same side. For illustration, if wheel number 1 on the right side reaches HNS, a braking moment will be applied to the next wheel (number2) on the same side.

Table 5.1: Fuzzy rules for  $(i)^{th}$  right side

Control Rules for right wheel		Corrective moment rate	
		NMR	PMR
$(i)^{th}$ axle wheel slip	HNS	ZE	ZE
	NS	MB	ZE
	PS	HB	ZE

Table 5.2: Fuzzy rules for vehicle's wheels right side

Control Rules for right side		$(i+1)^{th}$ axle right wheel slip		
		HNS	NS	PS
$(i)^{th}$ axle right wheel slip	HNS	ZE	MB	HB
	NS	ZE	MB	MB
	PS	ZE	ZE	ZE

### 5.2.3 Evaluation and simulation results

The developed differential braking controllers are evaluated and compared with the conventional (uncontrolled) vehicle through simulation-based maneuvers. For evaluating the controllers when driving on a slippery surface with a coefficient of friction of 0.2, Federal Motor Vehicle Safety Standers (FMVSS) test is conducted at first where the vehicle is driven at speed 80 km/h, then Double Lane Change (DLC) maneuver is performed at maximum speed (110km/h). Finally, the vehicle's stability is evaluated when

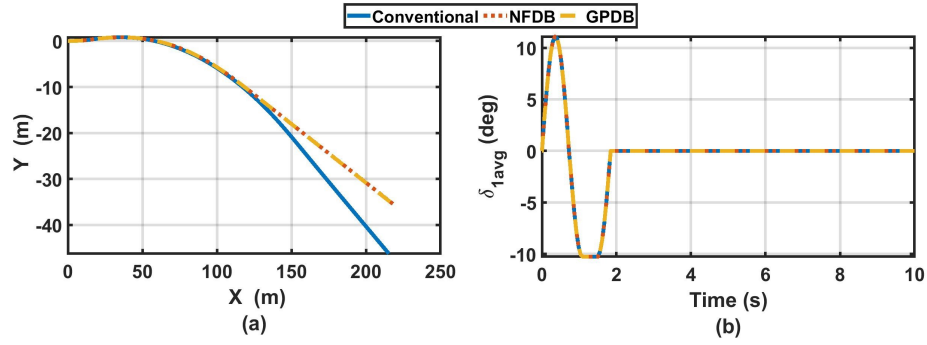


Figure 5.8: (a) Vehicle trajectory (b) Average Steering angle of the 1<sup>st</sup> axle for FMVSS maneuver at  $\mu=0.2$  and speed 80 km/h

driving on a dry surface using a severely modified slalom maneuver by driving the vehicle at 65 km/h on the road with a coefficient of friction 1. Note that the limitations and constraints on the maximum wheels steering angles are removed only in these tests for evaluation purposes.

#### 5.2.3.1 FMVSS maneuver

Figure 5.8 (a) shows a stable trajectory for all cases corresponding to the same steering angle as can be seen in figure 5.8 (b). The vehicle response is shown in Figure 5.9. Notably, the vehicle stability is improved dramatically as it is stabilized faster than the uncontrolled vehicle. The controller was effective in limiting the vehicle sideslip and consequently increase the stability, while the longitudinal velocity doesn't much get affected as seen in Figure 5.8 (d), and (a) respectively. It can be seen from the sideslip graph that the conventional vehicle sideslip exceeds its maximum value, so the activation of the controller in the controlled vehicle can be deduced from this high value as the stability index is violated. Furthermore, from comparing the longitudinal slip of the GPDB controller and the uncontrolled vehicle in figure 5.10, it can be seen that the controller succeeded in improving the stability without excessive use of braking moment as the slip is very small.

#### 5.2.3.2 DLC maneuver

The vehicle trajectory is shown in figure 5.11 (a) shows as it negotiates DLC maneuver at speed 110 km/h on slippery surface ( $\mu = 0.2$ ) and figure 5.11 (b) illustrates the related average steering angle of the first axle. It can be noticed that the uncontrolled vehicle

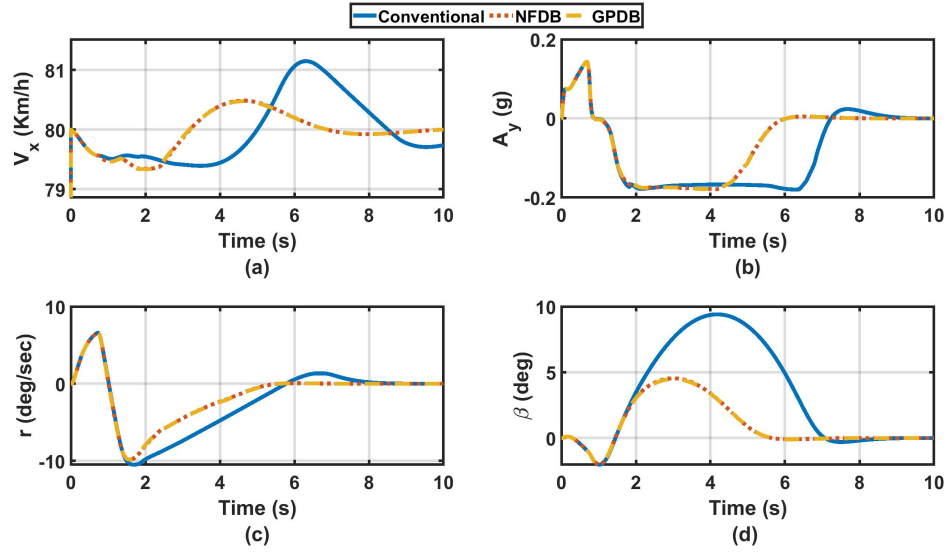


Figure 5.9: (a) Vehicle longitudinal speed (b) lateral acceleration (c) Yaw response (d) Vehicle sideslip response for FMVSS maneuver at  $\mu=0.2$  and speed 80 km/h

experiences high oscillation, which made it difficult to stabilize fast.

In contrast, the controlled vehicles show faster stabilization as it stabilizes 10 seconds faster than the conventional vehicle. The high amplitude oscillation of the conventional vehicle resulting in a decrease of the vehicle velocity as shown in Figure 5.12 (a). On the opposite, the controlled vehicle's longitudinal velocity decreased with a smaller value. The faster stabilization can be seen in the lateral acceleration in figure 5.12 (b). The yaw rate of the controlled vehicle is bounded due to the raking moment effect, while the conventional vehicle yaw rate keeps oscillating as in figure 5.12 (c). Figure 5.12 (d) illustrates that the controller bounds the vehicle sideslip as well and prevents its growth as in the case of the uncontrolled vehicle. A comparison between the longitudinal slip of the conventional and GPDB controlled vehicle can be seen in figure 5.13. The maximum longitudinal slip of the conventional vehicle is 0.3 at the 1<sup>st</sup> wheel of the right side while in the case of the controlled vehicle the slip exceeds 0.5. The slip controller didn't interfere in this case due to applying braking moment at the same time at the 1<sup>st</sup> wheel of the left (opposite) side. Therefore, the controller didn't apply a braking moment to the right side to decrease the slip to prevent interference to the two objectives (decreasing the longitudinal slip and compensate the yaw rate error to maintain stability).

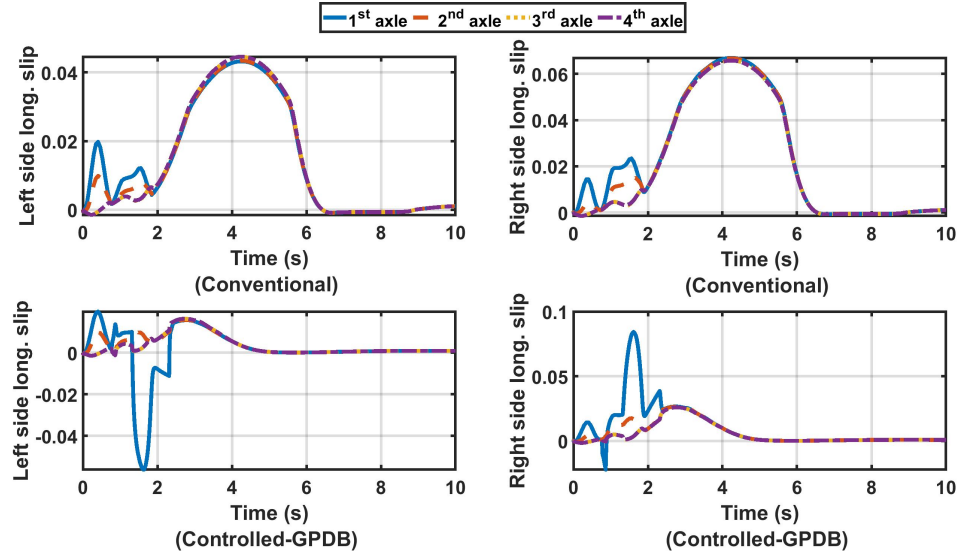


Figure 5.10: Wheels longitudinal slip for FMVSS maneuver at  $\mu=0.2$  and speed 80 km/h

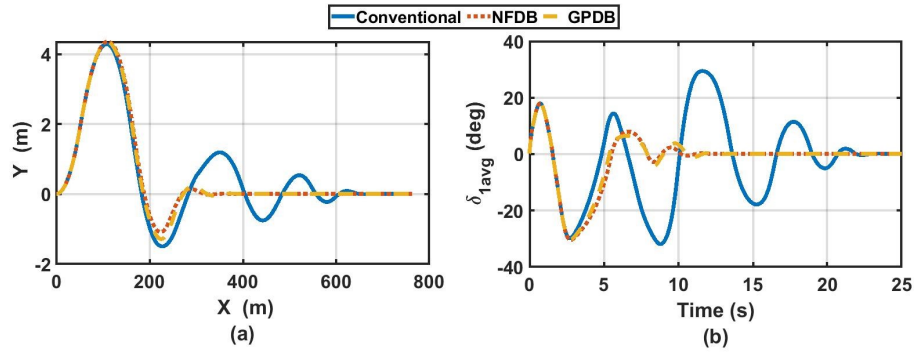


Figure 5.11: (a) Vehicle trajectory (b) Average Steering angle of the 1<sup>st</sup> axle for DLC maneuver at  $\mu=0.2$  and speed 110 km/h

### 5.2.3.3 Modified increased slalom maneuver

At this maneuver, the vehicle is driven at a speed of 65 km/h on a dry surface of a coefficient of friction equal to 1 ( $\mu = 1$ ). Open-loop sinusoidal steering input is applied to the vehicle where its amplitude is increased gradually then held at a constant value at last. Figure 5.14 (a) shows the vehicle trajectory for all cases for the same steering input as appear in figure 5.14 (b). It is noticed that the controlled vehicle completed the maneuver and the trajectory end by circle corresponding to the constant steering input. In contrast, the conventional vehicle failed to complete the trajectory.

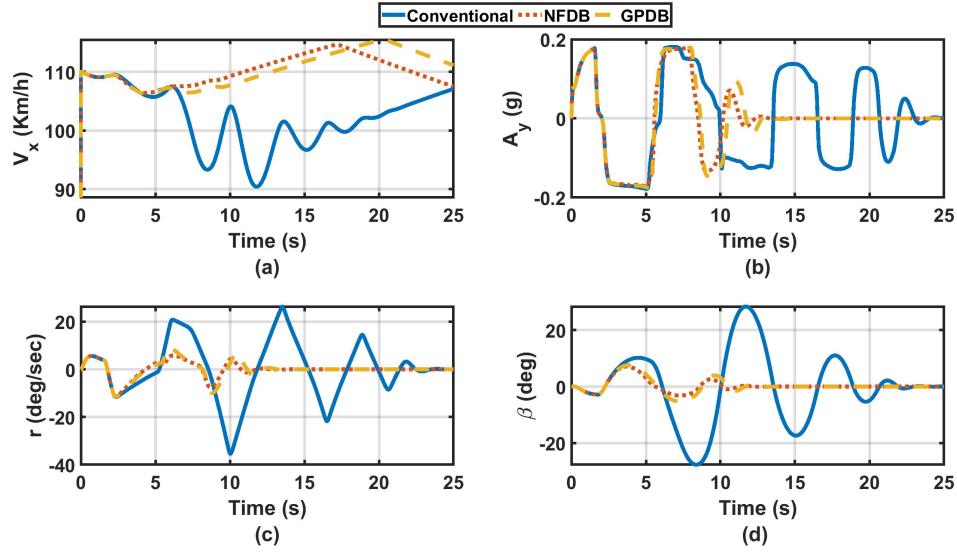


Figure 5.12: (a) Vehicle longitudinal speed (b) lateral acceleration (c) Yaw response (d) Vehicle sideslip response for DLC maneuver at  $\mu=0.2$  and speed 110 km/h

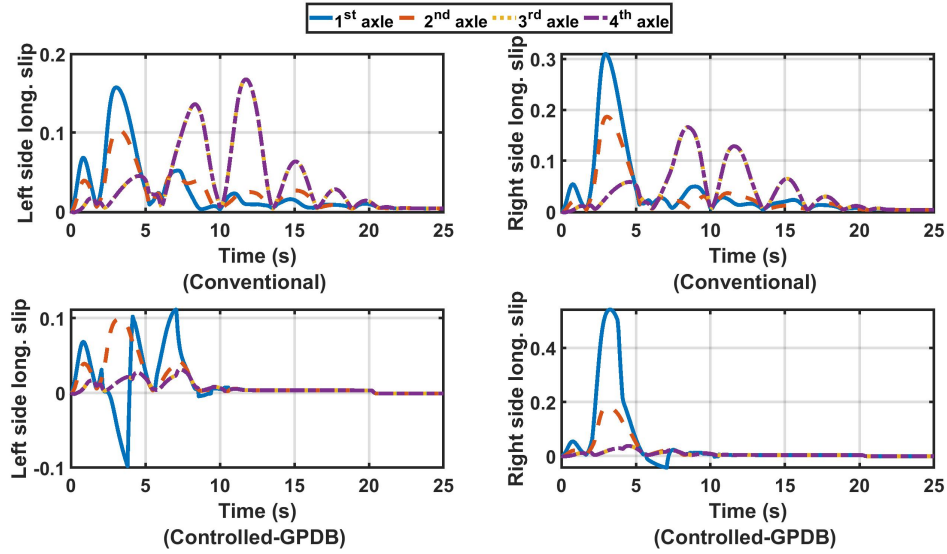


Figure 5.13: Wheels longitudinal slip for DLC maneuver at  $\mu=0.2$  and speed 110 km/h

By observing figure 5.15 (a), a drastic decrease in the vehicle speed appears for all cases. However, the controlled vehicles' speed decreased in a controlled manner until the vehicle restored its stability. Meanwhile, figure 5.15 (b) shows that the uncontrolled vehicle's lateral acceleration exceeded the critical threshold and the vehicle rolled over. Meanwhile, the controlled vehicle succeeded to limit the growth in yaw rate and sideslip

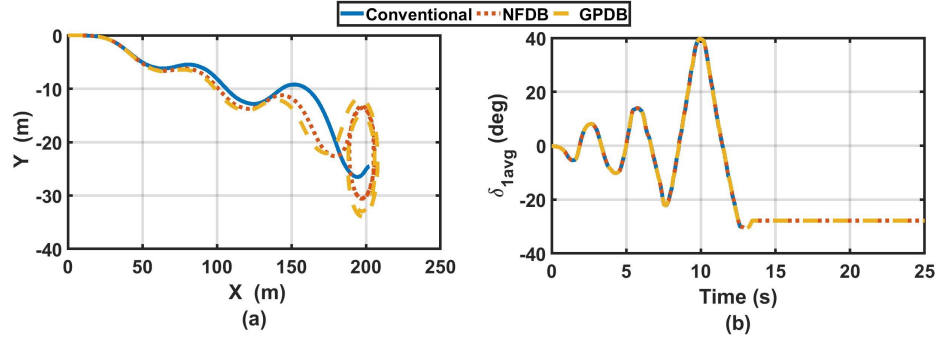


Figure 5.14: (a) Vehicle trajectory (b) Average Steering angle of the 1<sup>st</sup> axle for Slalom maneuver at  $\mu=1$  and speed 65 km/h

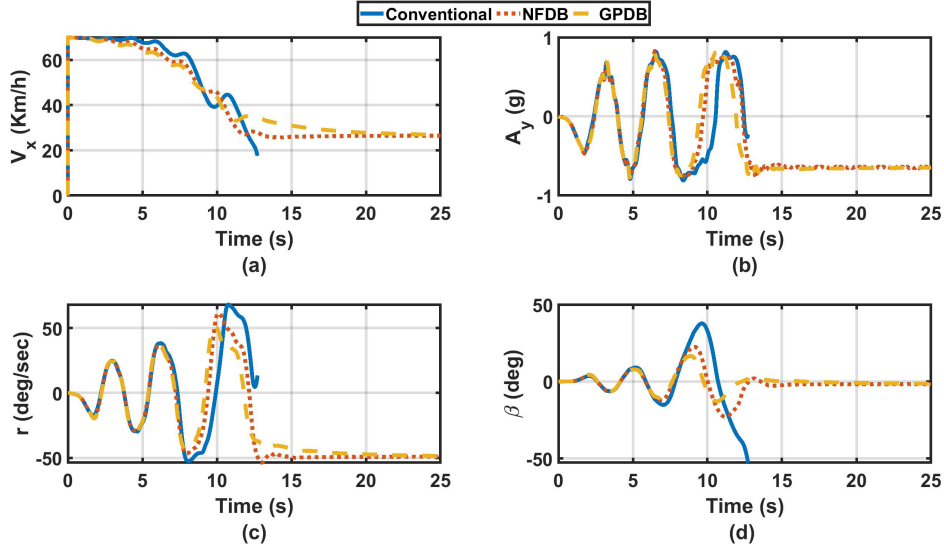


Figure 5.15: (a) Vehicle longitudinal speed (b) lateral acceleration (c) Yaw response (d) Vehicle sideslip response for Slalom maneuver at  $\mu=1$  and speed 65 km/h

as illustrated in figure 5.15 (c), and (d) consequently. It is also noticed that the performance in the case of GPDB is slightly better than the NFDB controller. The reason is that in the case of the NFDB controller, the controller only trained for a maximum coefficient of friction equal to 0.85, while in the case of GPDB the equation is valid and extended to be used for any speed and coefficient of friction. It can be concluded that the braking moment in the GPDB controller is increased with the increase of speed and friction. Meanwhile, the maximum output of the NFDB controller is associated with friction 0.85 and speed 110 km/h.



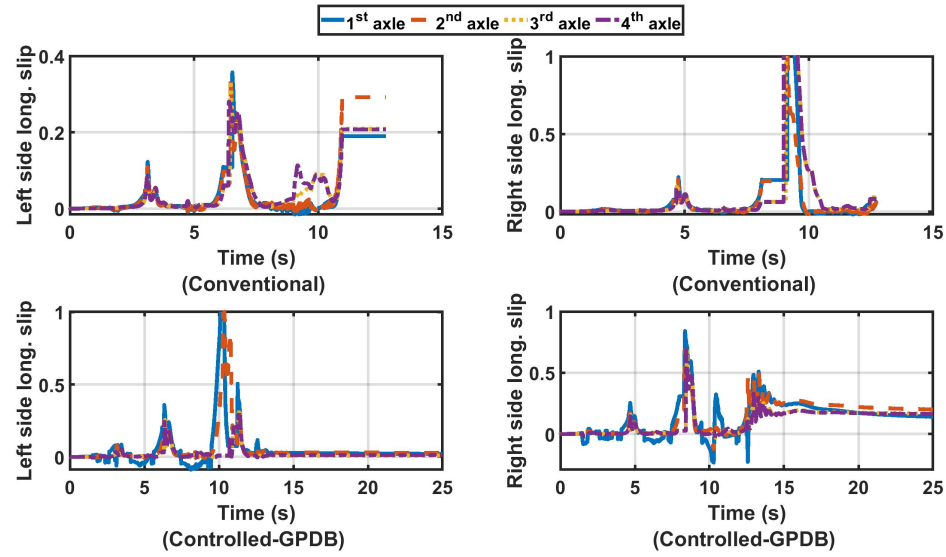


Figure 5.16: Wheels longitudinal slip for Slalom maneuver at  $\mu=1$  and speed 65 km/h

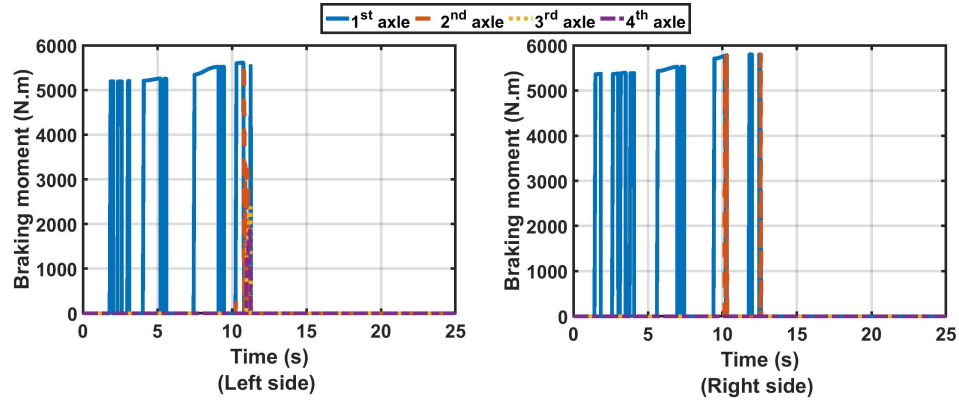


Figure 5.17: Braking moment for slalom maneuver at  $\mu=1$  and speed 65 km/h

Figure 5.16 shows a comparison between the longitudinal slip of the controlled and uncontrolled vehicles. At the upper figures, the conventional vehicle shows an increase of the and reach 100%. The controlled vehicles also show an increase in the longitudinal slip in the middle of the maneuver. This increase is limited and decreased due to the effect of the slip controller as it appears in figure 5.17, where a braking effort is executed through all axles to decrease the slip.

## 5.3 Torque vectoring controller

The TVC is designed in a two-level hierarchical structure. The upper level is developed based on conventional SMC theory, where a corrective moment will be generated to correct the vehicle yaw motion and follow the desired yaw signal as presented in section 5.2.1. After that, the lower level will be used for the control allocation to convert the corrective moment to a driving moment. This driving moment will be distributed on the vehicle's right and left wheels' sides according to the normal load on each side based on the friction circle.

### 5.3.1 SMC design

The single track (bicycle) model is used to derive the state-space mathematical model for DYCs. The model is derived based on the vehicle model as shown in figure 5.18. This model differs from the active steering model in the following points:

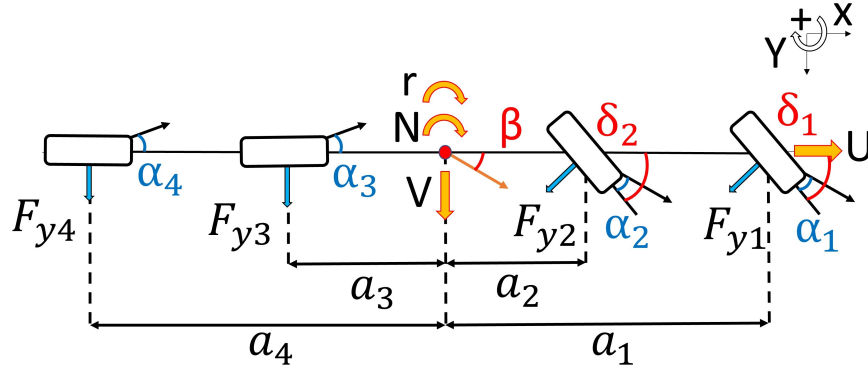


Figure 5.18: Four-axle steering 8x8 vehicle bicycle model

1. The 3<sup>rd</sup> and 4<sup>th</sup> axles are fixed ( $\delta_{3,4} = 0$ ).
2. The moment required to adjust the vehicle yaw motion is considered as  $N$ .

Following same assumptions and equations as in chapter 4, section 4.2.1 with considering  $\delta_{3,4} = 0$ . The yaw equation can be presented as in equation 5.19.

$$I_{zz}\dot{r} = a_1F_{y1} + a_2F_{y2} + a_3F_{y3} + a_4F_{y4} + N \quad (5.19)$$

This controller is developed to follow the desired yaw rate reference generated from the

vehicle's steady-state model. A Single Input-Single Output (SISO) conventional SMC is used in developing the controller, where the sliding manifold  $S_{TVC}$  is considered to be the error signal between the vehicle and the desired yaw rate  $r_d$  as in equation 5.20. The dynamics of the sliding manifold  $\dot{S}_{TVC}$  is presented in equation 5.21.

$$S_{TVC} = r - r_d + C_\beta \beta \quad (5.20)$$

$$\dot{S}_{TVC} = \dot{r} - \dot{r}_d + C_\beta \dot{\beta} \quad (5.21)$$

Substituting by the yaw rate equation 5.19 into equation 5.21 and considering the steering angles of the first and second axles with fixed rear axles resulted in equation 5.22. Using Lyapunov function as in equation 5.23 and a positive constant  $K_{SMC}$  ensures the controller stability.

$$\dot{S}_{TVC} = \sum_{i=1}^4 \frac{a_i F_{yi}}{I_{zz}} \cos \delta_i + \frac{N}{I_{zz}} - \dot{r}_d + C_\beta \dot{\beta} \quad (5.22)$$

$$S_{TVC} \dot{S}_{TVC} \leq -K_{SMC} |S_{TVC}| \quad \text{Where } K_{SMC} > 0 \quad (5.23)$$

By using a constant rate reaching law as in equation 5.24 and substitute in equation 5.22, the corrective yaw moment control action can be calculated as in equation 5.25.

$$\dot{S}_{TVC} = -K_{SMC} \text{sgn}(S_{TVC}) \quad (5.24)$$

$$\begin{aligned} N = & - \sum_{i=1}^4 a_i F_{yi} \cos \delta_i + I_{zz} \dot{r}_d + I_{zz} C_\beta \dot{\beta} \\ & - I_{zz} K_{SMC} \text{sgn}(S_{TVC}) \end{aligned} \quad (5.25)$$

Also, the sign function approximation is used as in equation 5.26 to avoid the chattering phenomena, where  $\epsilon$  is a very small positive constant that tends to zero.

$$\text{sgn}(S_{TVC}) = \frac{S_{TVC}}{|S_{TVC}| + \epsilon} \quad (5.26)$$

Moreover, the control allocation that is used to distribute the longitudinal forces on the left and right wheels' sides ( $F_{xL}$ ,  $F_{xR}$ ) illustrated in equation 5.27. The equation is derived based on the double-track model as illustrated in figure 5.19.

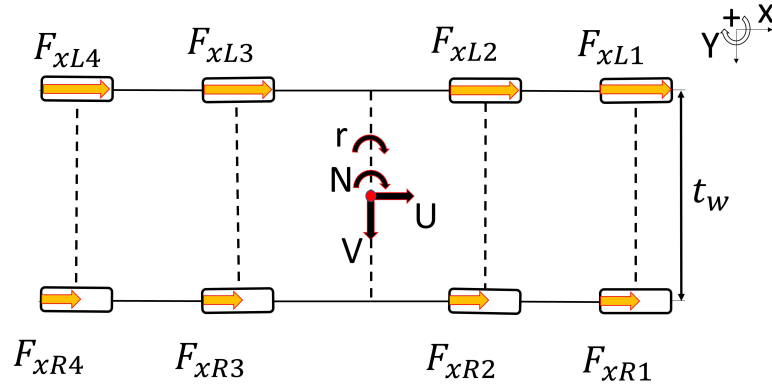


Figure 5.19: Double-track vehicle model

$$N = \frac{t_w}{2} \left( \sum_{i=1}^4 F_{xRi} - \sum_{i=1}^4 F_{xLi} \right) \quad (5.27)$$

Finally, the longitudinal forces on right and left sides are distributed as in [56] according to the vertical forces and road friction based on the friction circle as in equation 5.28. The vehicle longitudinal load transfer is neglected and the vehicle is considered to be mono-axle, which means that all four axles are combined in one axle.

$$F_{x_{max}} = \sqrt{(\mu F_z)^2 - F_y^2} \quad (5.28)$$

### 5.3.2 Evaluation and simulation results

In this section, two TVCs are incorporated with the 22-DoF full vehicle model to be compared and tested. In the first controller, the coefficient  $C_\beta$  is set to be zero to remove the constrain on the vehicle sideslip, while in the second controller this factor is set to be 1. Furthermore, the controllers are compared with the uncontrolled (conventional)

vehicle to show the influence of constraining the vehicle sideslip on the vehicle stability and the overall performance.

The FMVSS open-loop maneuver is conducted at a speed of 80 km/h on a dry and slippery road with CoF 0.85 and 0.2, respectively. In addition, a closed-loop slalom test is conducted, where the vehicle speed is set to be 75 km/h when driving on a dry surface with COF 0.85.

### 5.3.2.1 FMVSS at maneuver CoF=0.85 and forward speed=80 km/h

Figure 5.20 (a) presents the vehicle's path when performing the FMVSS maneuver at speed 80 km/h and CoF of 0.85, while figure 5.20 (b) shows a close-up on that figure to present the lateral offset that is taken by each case. It is noticed that the conventional and the TVC-1 (unconstrained sideslip) has almost the same lateral offset, while the TVC-2 (constrained sideslip) has a lower lateral offset.

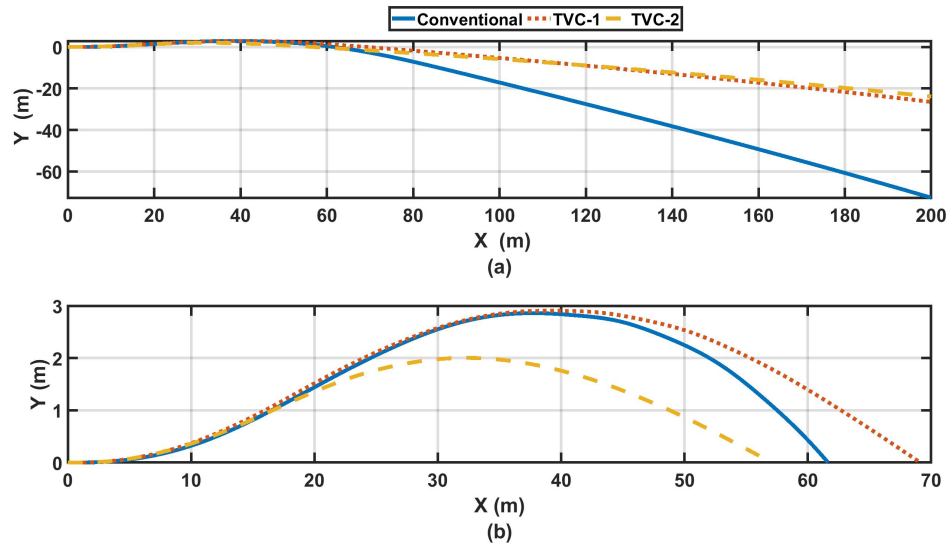


Figure 5.20: FMVSS maneuver at  $\mu=0.85$  and speed 80 km/h (a) Vehicle trajectory (b) Close up to the vehicle's lateral shift

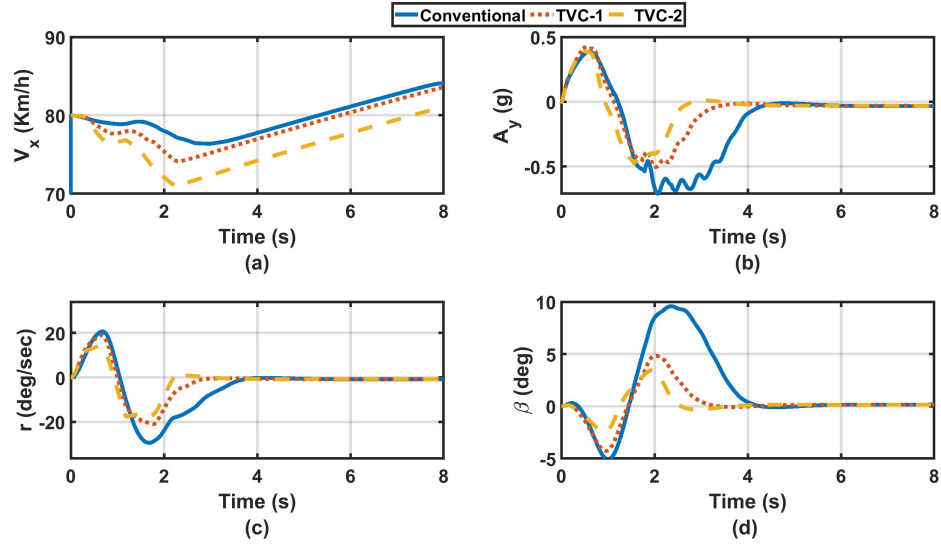


Figure 5.21: FMVSS maneuver at  $\mu=0.85$  and speed 80 km/h (a) Vehicle longitudinal speed (b) lateral acceleration (c) Yaw response (d) Vehicle sideslip response

Figure 5.21 (a) shows that the TVC-2 resulted in a higher drop in the vehicle's longitudinal speed than in other cases. By observing the dynamic response of the vehicle in figure 5.21 (b), (c), and (d), it can be seen that the TVC-2 stabilizes the vehicle faster than the TVC-1 and the conventional vehicle. However, it resulted in less yaw rate and sideslip than the TVC-1, which indicates less maneuverability and higher stability as presented in figures 5.21 (c) and (d), respectively.

### 5.3.2.2 FMVSS maneuver at CoF=0.2 and forward speed=80 km/h

By repeating the maneuver at the same speed but on a slippery road with CoF 0.2, the same behaviour can be noticed as performing the maneuver on a dry surface. It can be seen in figure 5.22 that the TVC-2 has less lateral offset than other cases.

Similarly to testing on dry road, the TVC-2 resulted in higher speed reduction with faster lateral acceleration, yaw rate, and sideslip stabilization, as can be seen in figure 5.23. In addition, the TVC-2 still generates less yaw rate and sideslip than other cases as presented in figure 5.23 (c) and (d), respectively.

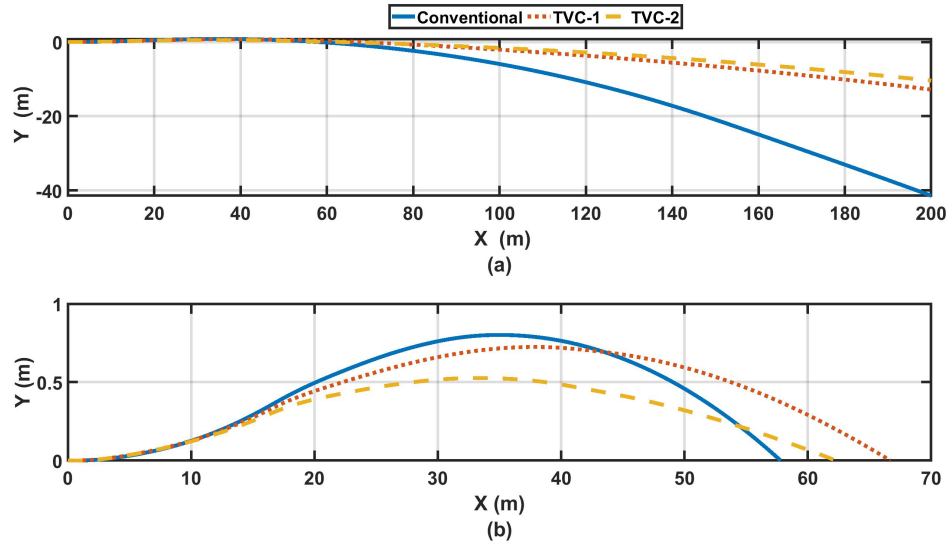


Figure 5.22: FMVSS maneuver at  $\mu=0.2$  and speed 80 km/h (a) Vehicle trajectory (b) Close up to the vehicle's lateral shift

### 5.3.2.3 Slalom maneuver at CoF=0.85 and forward speed=75 km/h

This section presents performing the slalom maneuver at speed of 75 km/h on a dry road with CoF 0.85. The vehicle path and corresponding lateral error is presented in figure 5.24 (a) and (b), respectively. It can be seen that all cases lost their stability and drift from the designed path except the TVC-2, which finish the maneuver successfully.

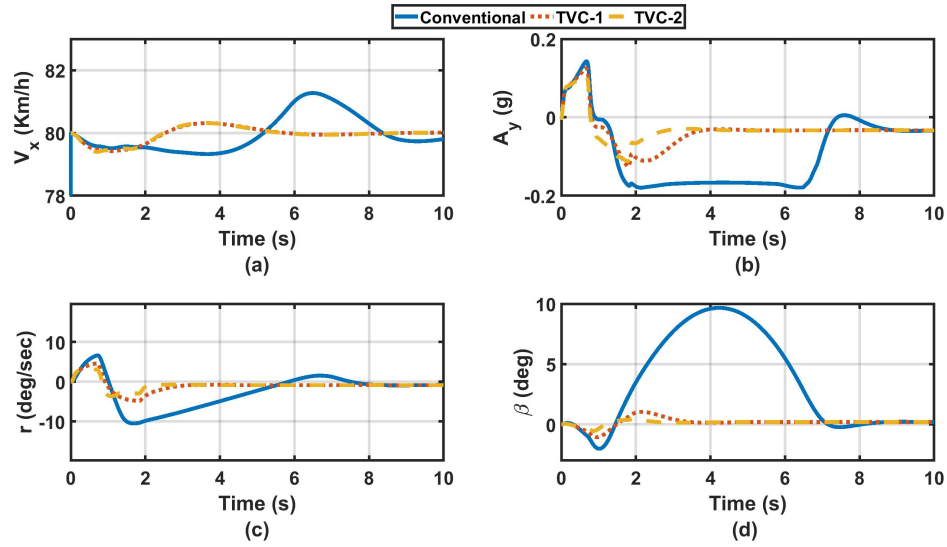


Figure 5.23: FMVSS maneuver at  $\mu=0.2$  and speed 80 km/h (a) Vehicle longitudinal speed (b) lateral acceleration (c) Yaw response (d) Vehicle sideslip response

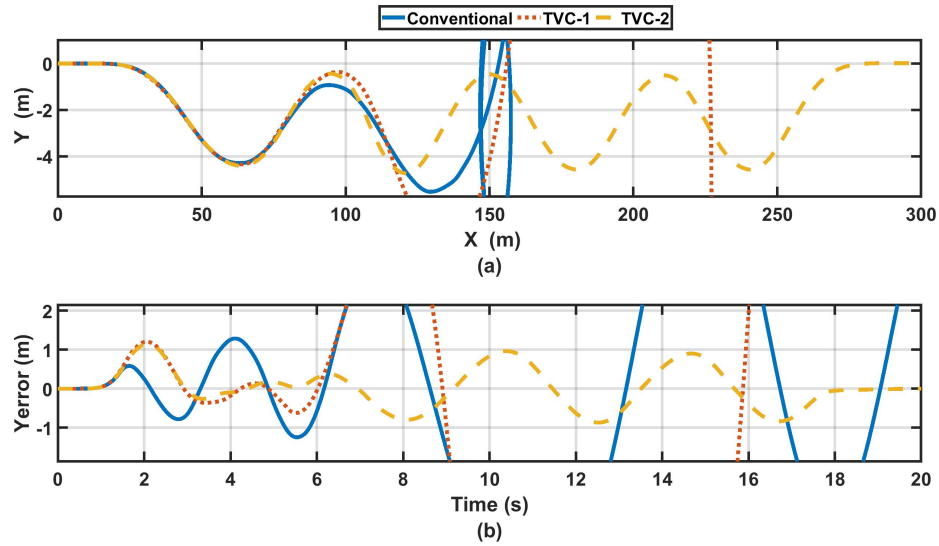


Figure 5.24: Slalom maneuver at  $\mu=0.85$  and speed 75 km/h (a) Vehicle trajectory (b) Lateral error

In figure 5.25 (a), it is noticed that all cases resulted in a high speed drop. However, in the case of the controlled cases, the drop is less than the uncontrolled vehicle. It can be seen also that despite the limitation of the vehicle yaw rate and sideslip in the case of the controlled vehicles, the TVC-1 failed to stabilize the vehicle, as shown in figure



5.25 (c) and (d), respectively. Adding constraint on the vehicle sideslip in the TVC-2 case, resulted in more reduction in the vehicle sideslip than in TVC-1, which resulted in better stability.

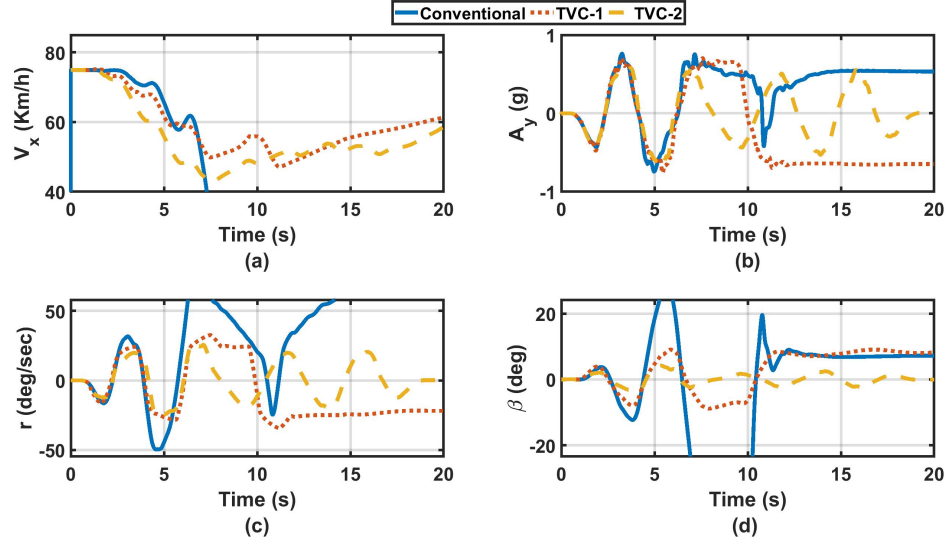


Figure 5.25: Slalom maneuver at  $\mu=0.85$  and speed 75 km/h (a) Vehicle longitudinal speed (b) lateral acceleration (c) Yaw response (d) Vehicle sideslip response

## 5.4 Chapter summary

In this chapter, two DYCs were developed to enhance the vehicle lateral stability. At first, a novel differential braking controller was developed. The reference model has been driven analytically, followed by the design of two layers controller (upper and lower controller). The upper controller was an adaptive controller that was responsible for generating the maximum allowable braking moment at the vehicle's wheels as a function of the vehicle speed and road coefficient of friction. The controller was designed using two different methods. The first was developed based on adaptive neuro-fuzzy control methodology (NFDB), while the second converted the developed fuzzy rules into a single equation that was optimized using genetic programming (GPDB). Furthermore, a lower fuzzy-based controller was designed to execute and allocate the developed braking moment through the vehicle's wheels and decrease the longitudinal slip of each wheel. This strategy ensures that the controller's insensitivity to the reference model. Besides, to avoid excessive use of the braking moment, an activation

condition is developed in the form of a stability index, which is based on phase-portrait analysis of the vehicle's nonlinear model.

The controllers were evaluated using series of simulation-based maneuvers. The comparison showed that the GPDB controller's results were comparable with the NFDB. Moreover, the GPDB controller was more efficient than NFDB in terms of:

- Developing an extensive controller for a low dimensional data-set, which requires fewer simulations and time consumption.
- GPDB controller showed better performance when tested in a working region beyond the trained data-set because the developed equation can interpolate between the provided data-set and extrapolate for future data.
- Developing a non-complex single equation in the case of GPDB will facilitate future hardware implementation in comparison with the NFDB that is resulted in 36 fuzzy rules.

The second DYC was a hierarchical two-level TVC. The first was a high-level controller that was designed based on conventional SMC theory to generate a corrective moment to stabilize the vehicle. The second was a low-controller level that was used to allocate this corrective moment to the vehicle's driving torque, which was distributed on the right and left wheels' side based on the friction circle. A comparison was made to show that considering the vehicle's sideslip in the control design can enhance the controller's performance drastically and increase the vehicle stability.

## CHAPTER 6

### Integrated Chassis Controllers

#### 6.1 Introduction

This chapter introduces two methods of integration for ICCs that are incorporated in the 8x8 combat vehicle. The first method aims to integrate the developed ARS, as in section 4.3, with the TVC, as in section 5.3, by mapping the effective working region of each controller at different speeds and road CoFs based on a series of simulations. Then, a coordination factor is introduced based on that map and is implemented with the full vehicle model using an ML-based controller. The second integration method utilizes FLC-based controller rules that define the working conditions of the ARS and GPDB controller. The FLC rules are generated to ensure activation of the GPDB controller when driving at high speed on a dry surface without any involvement from the ARS. The involvement percentage of the ARS is increased with the decrease in the road friction coefficient. The controllers are denoted as ARS, TVC, and DB in the rest of this chapter.

#### 6.2 TVC-ARS integration and coordination

In order to integrate the developed ARS and TVC controllers, a series of DLC maneuvers are conducted to present a three-dimension map of the vehicle dynamic response. This map is defined by the summation of the dynamics' response settling time for the specified maneuvers concerning the driving conditions which are defined as the vehicle velocity and road coefficient of friction as shown in figure 6.1 (a). The intersection line of these two maps is projected on the  $(U, \mu)$  plane and formed a Qualitative Performance Map (QPM) that defines the recommended operating region for the TVC and the ARS as in figure 6.1 (b), where the colours illustrated the differences in the performance. So the bright colour shows small differences, from the stability point of view, between the controllers' performance, while the dark region demonstrates high-performance differences and superiority of ARS over TVC.

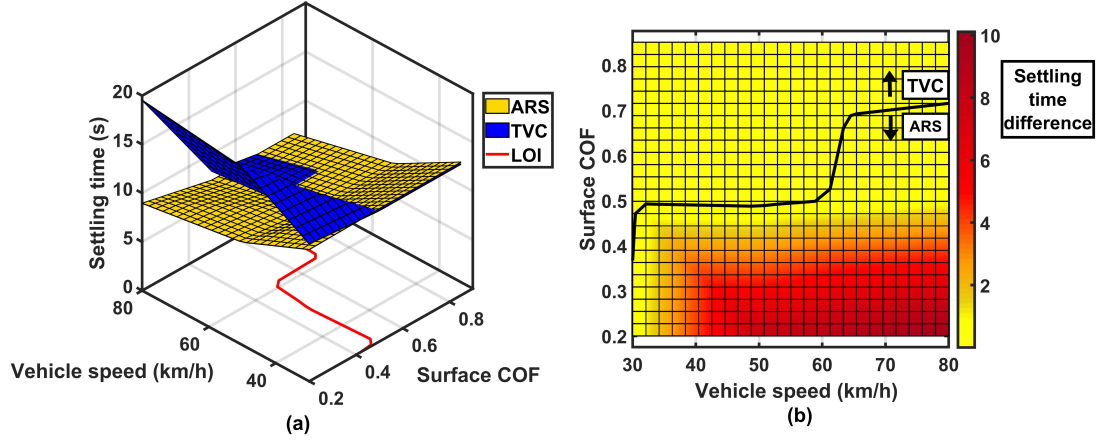


Figure 6.1: Performance map for the TVC and the ARS controllers with respect to different speeds and road coefficient of frictions

Based on the QPM, the ARS is found to be more effective in the limited handling conditions when driving at low friction and high speed. On the other hand, the TVC is more effective which driving at very low speed or when driving on a dry surface with high CoF. Therefore, a new exponential-based equation is defined as in 6.1. The coordination factor  $R$  defines the engagement percentage for the TVC. In this equation,  $Z$  is the numeric representation of the colors in figure 6.1 (b),  $n$  and  $C$  are positive constants. This equation is determined based on two objectives; Attenuating the low-performance controller, and maximizing the effect of the high-performance controller based on the working region.

$$R = \left( \frac{e^{Z/\max(|Z|)}}{C} \right)^n \quad (6.1)$$

$$R_{ARS} = 1 - R \quad (6.2)$$

A fuzzy logic neural network is trained for the data-set formed by two inputs, vehicle velocity  $U$ , road friction  $\mu$ , and the coordination factor  $R$  as the output as in figure 6.2. The network is trained using a hybrid method, in which the input membership functions are optimized using backpropagation, while the output membership functions

are optimized using the least method. The network trained for inputs data dimension 15x15, for 6 epoch, which resulted in an accuracy of 0.008, and 225 fuzzy rules.

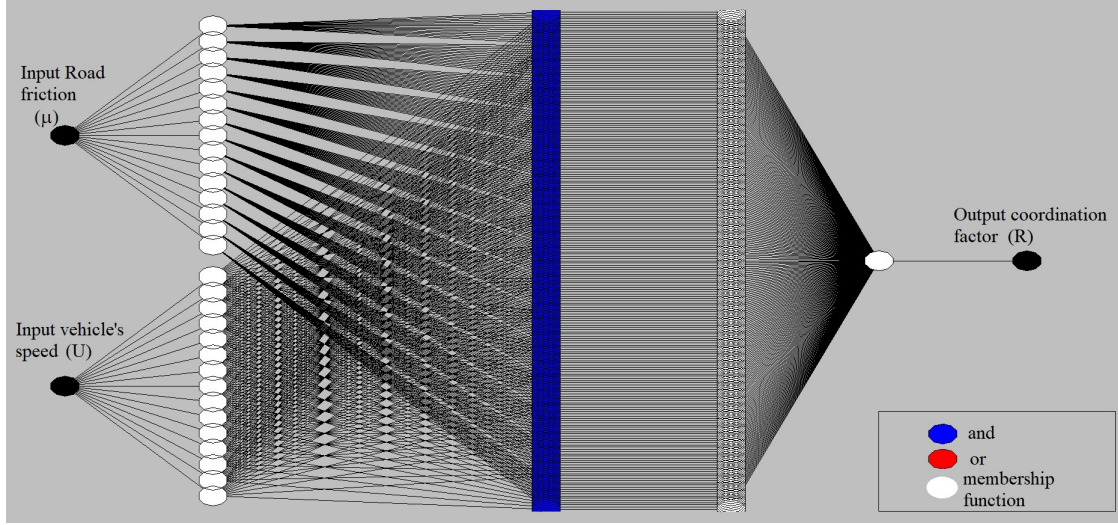


Figure 6.2: Neuro-fuzzy representation

The NFLC resulted in high dimension rules, which need to be decreased in order to facilitate future implementation on a low-cost and low-memory size microprocessor. Therefore, Genetic Programming (GP) is used to train the data-set and develop optimized coordination equations that can replace the Neuro-fuzzy rules efficiently.

Eureqa software is utilized to generate and optimize equation 6.3. Moreover, The searching process is constrained to use simple mathematical operations such as (/ "protected version", \*, +, -) to force the algorithm to generate a low-complexity equation, which will have consequently less computational effort in the future implementation. In that equation the symbols  $a_i, b_j, c_k$  are positive constants, and  $R_{GP}$  is the coordination factor based on GP.

$$R_{GP} = \begin{cases} a_1 + a_2 U^5 + \frac{a_3}{\mu^8} - a_5 U & \text{if } \mu < 0.39 \\ \frac{b_1}{U^6} - \frac{b_2 \mu}{U^4} + \frac{b_3 \mu^2}{U} - b_4 & \text{if } \mu \in [0.390.498] \\ c_1 + c_2 \mu U^2 - c_3 U - c_4 \mu & \text{if } \mu \in [0.4980.71] \\ 1 & \text{if } \mu > 0.71 \end{cases} \quad (6.3)$$

The solution statistics are presented in table 6.1 for each equation, respectively. In addition, the generation rate of this equation is 260/s at 8 CPU cores, 12 M evaluation/second, and the searching process took about 12 minutes.

Table 6.1: GP solution statistics

$R^2$ fitness	Correlation	Mean square error	Complexity size
0.99222334	0.99647751	0.044	30
0.96734402	0.98366793	0.0765	38
0.97725109	0.98877702	0.02948391	17

Eventually, the execution time of the two coordinators (NF-based and GP-based) are evaluated using the Matlab/Simulink profiler for various time steps using the same solver and simulation time (10 sec). The execution time per each step for different time steps is introduced in figure 6.3. Notably, the GP-based coordinator significantly reduces the execution time by 98.8373 in comparison with the fuzzy-based coordinator. Moreover, it can be observed that the fuzzy-based coordinator has a nonlinear relation with the time step. On contrary, the GP-based coordinator has a linear relation with time steps, which makes it easy to predict the execution time at any time step.

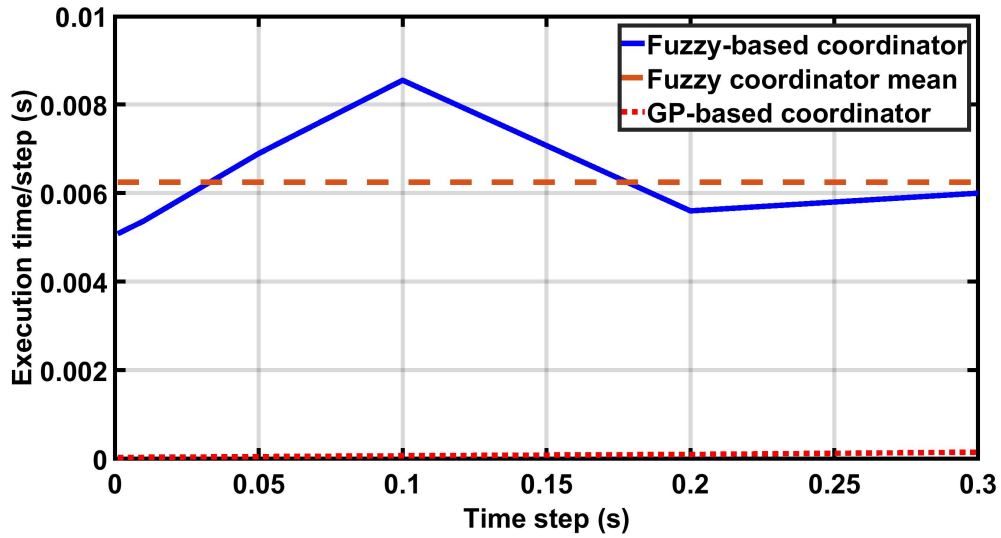


Figure 6.3: Mean execution time per step for each time step

### 6.3 ARS-DB integration and coordination

The coordination factor in this section is introduced to activate the ARS, while the DB controller is activated at all driving conditions. The activation of the DB system is controlled by the activation condition that was introduced in section 5.2.2.1. Figure 6.4 shows the ARS coordination factor, which is developed using Matlab's Sugeno-fuzzy control toolbox.

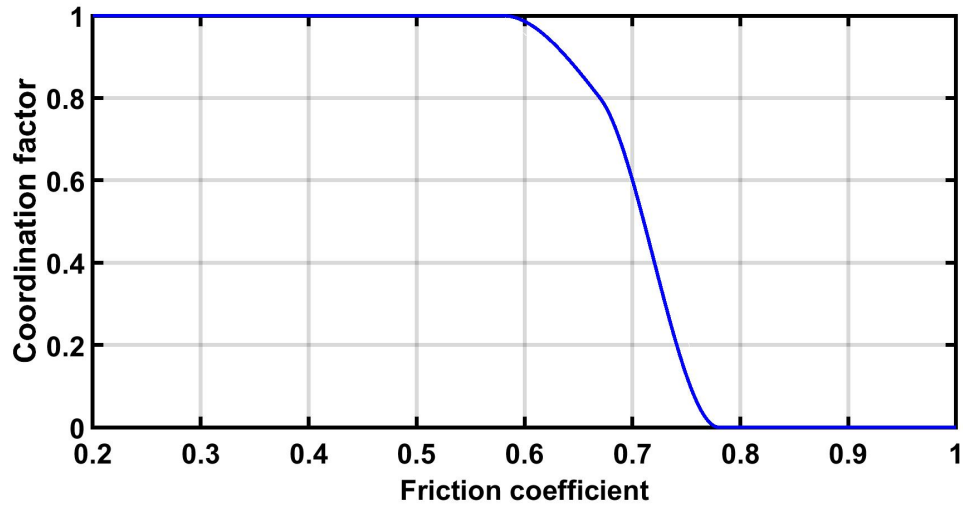


Figure 6.4: ARS coordination factor with respect to the road friction coefficient

The input for the fuzzy system is the road friction coefficient, which is presented using two membership functions; Low Friction (LF), and High Friction (HF) as presented in figure 6.5.

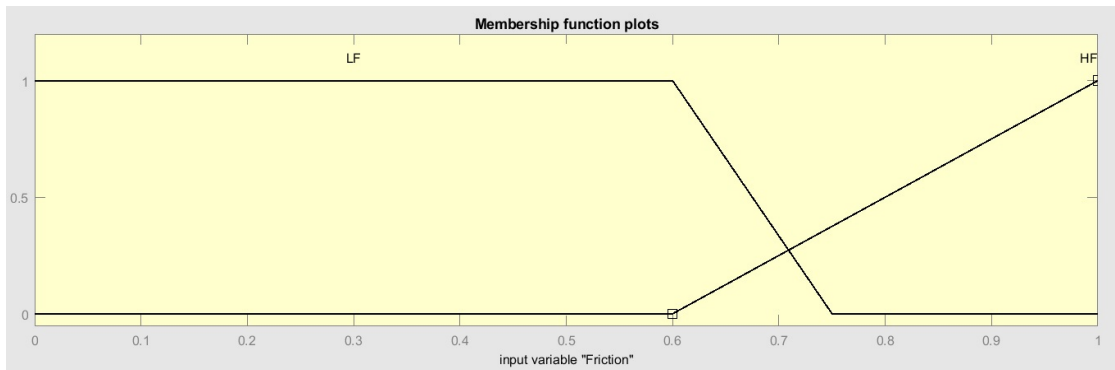


Figure 6.5: Road friction membership functions

Moreover, the output depends on two membership functions; (DB-Only) DBO and ARS with functions type constant and linear and have values of [0] and [0 1], respectively. In addition, the fuzzy rules are as follows:

$$\begin{aligned} & \text{if } (Friction \text{ is } HF) \text{ then } (R \text{ is } DBO) \\ & \text{if } (Friction \text{ is } LF) \text{ then } (R \text{ is } ARS) \end{aligned}$$

The final output (R) is defuzzified using the weighted-sum method as in equation 6.4, where N is the number of the fuzzy rules and Z is the rule output level based on the output membership function.

$$R = \sum_{i=1}^N (w_i Z_i) \quad (6.4)$$

## 6.4 Controllers evaluation

The high fidelity 22-DoF nonlinear full vehicle model is used to perform virtual testing and evaluation as in previous chapters.

The controllers are evaluated using close-loop and open-loop maneuvers. All maneuvers are performed at speed of 100 km/h and different CoFs, except the slalom maneuver and the step slalom maneuver, which are performed at the same CoFs but for maximum obtained speed at each CoF.

### 6.4.1 Slalom maneuver

#### 6.4.1.1 Slalom maneuver at $\mu = 0.85$ and $V = 70 \text{ km/h}$ :

The slalom maneuver is performed on a dry road with  $\mu = 0.85$ , while the vehicle entering speed is  $70 \text{ km/h}$ . Figure 6.6 (a) shows the controllers trajectory in comparison with the uncontrolled vehicle, while figure 6.6 (b) shows the lateral offset from the desired path for each case. The figures show that the uncontrolled vehicle failed to stabilize and drifted away from the desired path. Meanwhile, the TVC-ARS has the least lateral error. However, the difference is not significant.

Figure 6.7 (a), (b), and (c) show the corresponding 1<sup>st</sup>, 3<sup>rd</sup>, and 4<sup>th</sup> axles' average steering angles, respectively. It can be seen that the ARS didn't activate in both controllers



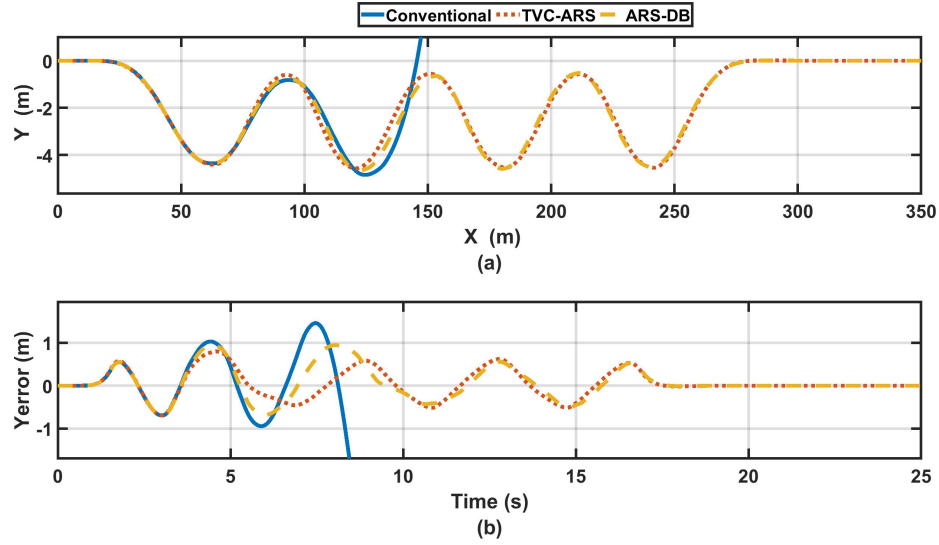


Figure 6.6: Slalom maneuver at  $\mu=0.85$  and speed 70 km/h (a) Vehicle trajectory (b) Lateral error

and only the TVC and DB controllers were in operation. In addition, the TVC-ARS resulted in lower steering input and consequently lower 1<sup>st</sup> axle's steering.

The dynamic response of the vehicle is illustrated in figure 6.8. Notably, the controlled vehicles have a high drop in longitudinal speed (around 20 km/h) as shown in figure 6.8(a). According to figure 6.8(b), the lateral acceleration of the TVC-ARS is slightly less than the ARS-DB. It is observed also from figure 6.8(c) that the ARS-DB have higher maneuverability and yaw rate than other cases, while the TVC-ARS has the lowest maneuverability. From 6.8(d), It can be noticed that the TVC-ARS achieved a limited sideslip.

Figure 6.9 shows the corrective driving torque that is applied on the right and left wheels' sides. It can be observed an unequal distribution on both sides due to the unequal load distribution associated with the lateral load transfer.

The braking torque of the DB controller on each wheel is presented in figure 6.10. It can be seen that the braking is not continuously activated, as it is only activated in case the stability criterion is violated.

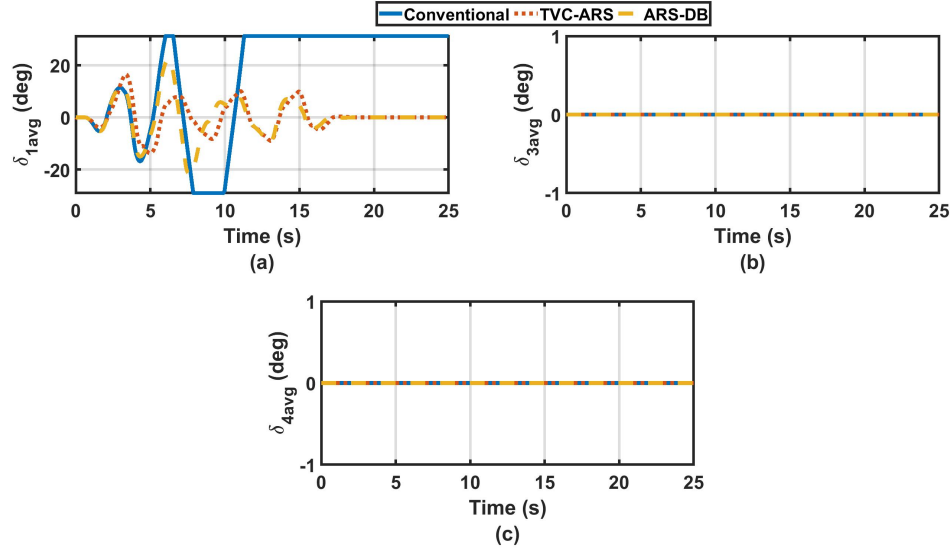


Figure 6.7: Slalom maneuver at  $\mu=0.85$  and speed 70 km/h (a) Average Steering angle of the 1<sup>st</sup> axle (b) Average Steering angle of the 3<sup>rd</sup> axle (c) Average Steering angle of the 4<sup>th</sup> axle

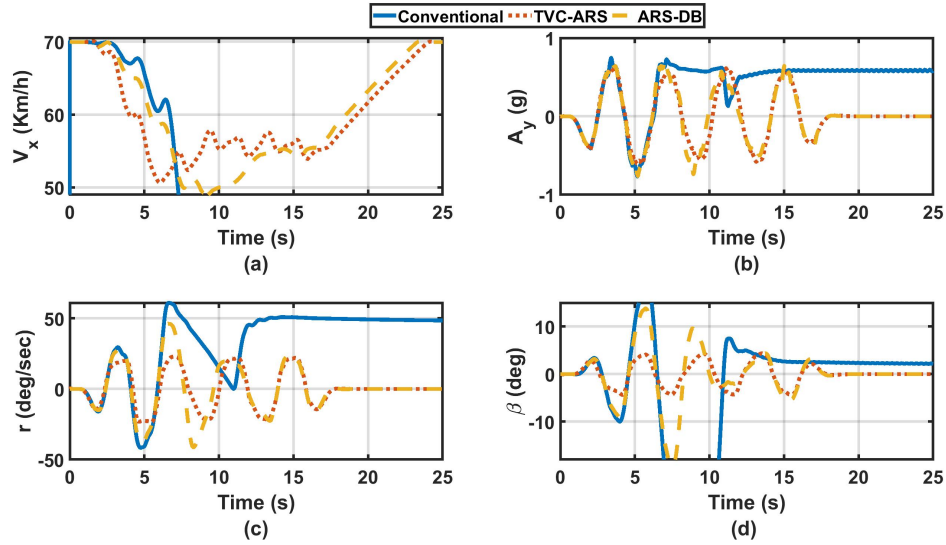


Figure 6.8: Slalom maneuver at  $\mu=0.85$  and speed 70 km/h (a) Vehicle longitudinal speed (b) lateral acceleration (c) Yaw response (d) Vehicle sideslip response

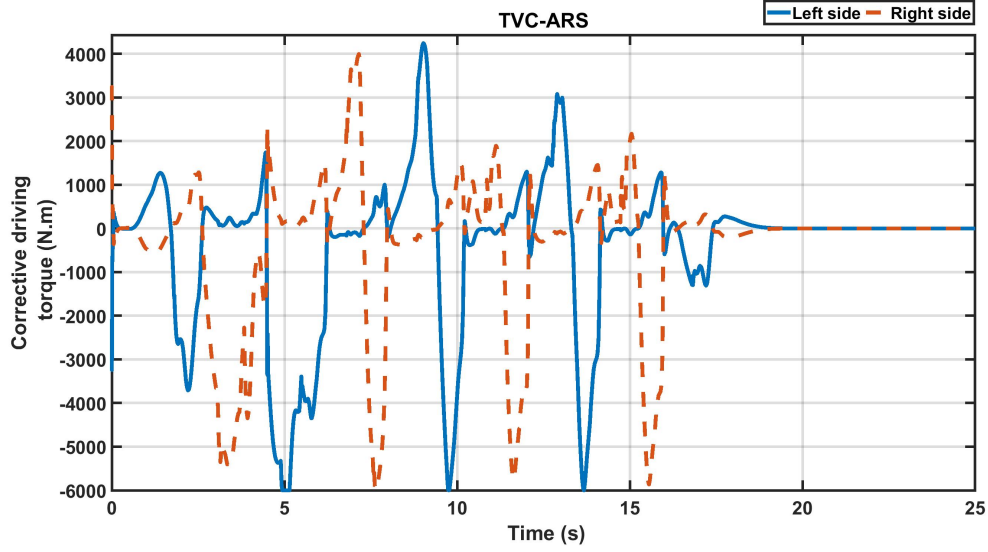


Figure 6.9: Slalom maneuver at  $\mu=0.85$  and speed 70 km/h; Corrective driving torque of the right and left wheels' side

#### 6.4.1.2 Slalom maneuver at $\mu = 0.5$ and $V = 50 \text{ km/h}$ :

By repeating the same maneuver but on a wet asphalt road with  $\mu = 0.5$ , It can be seen from figure 6.11 (a) that the conventional vehicle lost stability. On the other hand, the controllers could stabilize the vehicle and complete the maneuver. Moreover, the TVC-ARS has less lateral error than the ARS-DB, as shown in figure 6.11 (b).

From figure 6.12 (a), it is noticed that there is a slight difference in the 1<sup>st</sup> axle's steering angle in the controlled cases. The average steering angle of the 3<sup>rd</sup> and 4<sup>th</sup> figures 6.12 (b) and 6.12 (c), respectively. It can be observed that the ARS is not activated in case of the TVC-ARS, while it is activated in case of the ARS-DB controller.

Figure 6.13 (a) shows a negligible drop in the vehicle's speed associated with the ARS-DB controller. On the other hand, that drop is increased for the TVC-ARS controller. In addition, the ARS-DB controller resulted in less lateral acceleration, yaw rate, and sideslip than the TVC-ARS, as appear in figures 6.13 (b), (c), and (d), respectively. Besides, the ARS-DB stabilizes the vehicle faster than the TVC-ARS, which can be related to the higher speed.

Figure 6.14 shows the distribution of the corrective torque on the wheels' right and left sides in case of TVC-ARS, while the braking torque associated with the ARS-DB is

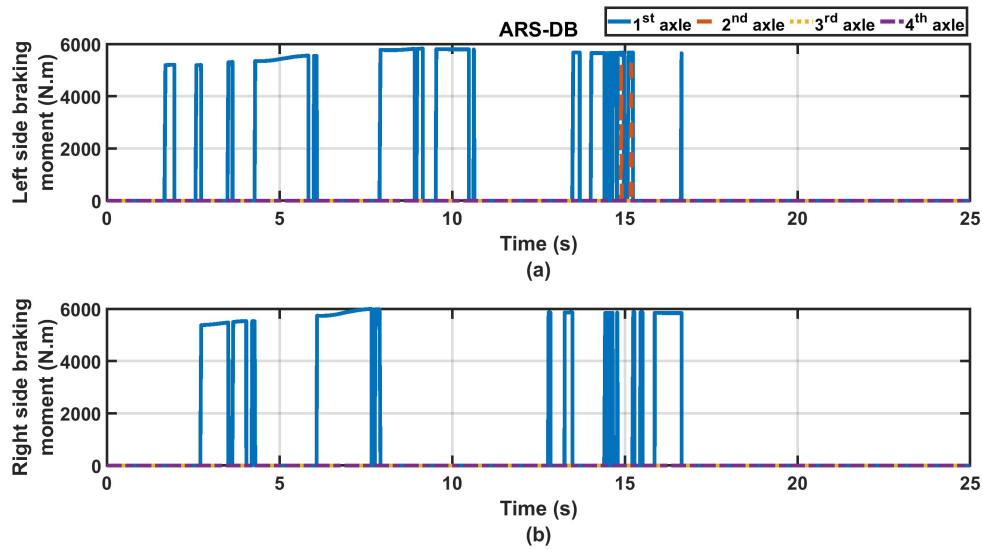


Figure 6.10: Slalom maneuver at  $\mu=0.85$  and speed 70 km/h; Braking forces at each wheel

presented in figure 6.15.

#### 6.4.1.3 Slalom maneuver at $\mu = 0.2$ and $V = 30 \text{ km/h}$ :

Figures 6.16 (a) and (b) show the vehicle trajectory and the corresponding lateral error for each case when performing slalom maneuver at CoF 0.2 and longitudinal speed 30 km/h. Notably, only the TVC-ARS succeeded to complete the maneuver. However, the ARS-DB was about to finish the maneuver but lose the stability at the end, which is still a better result than the uncontrolled vehicle that loses its stability at the beginning of the maneuver.

It can be noticed from figure 6.17 (a) that the 1<sup>st</sup> axle reaches the steering limits in the case of ARS-DB and the conventional vehicle. In addition, the steering angle was larger than the TVC-ARS due to the effect of TVC. Accordingly, the 3<sup>rd</sup> and 4<sup>th</sup> axles steering angle in the case of TVC-ARS were less than its counterpart in the ARS-DB, as shown in figures 6.17 (b) and (c), respectively.

There is no major deviation from the desired velocity for all cases as the maximum was 1 km/h in the case of TVC-ARS, as presented in figure 6.18 (a). In addition, all cases kept the vehicle's lateral acceleration under 0.2 g and a low sideslip under 2 degrees, as shown in figures 6.18 (b) and (d), respectively. Despite that, figure 6.18 (c) shows that

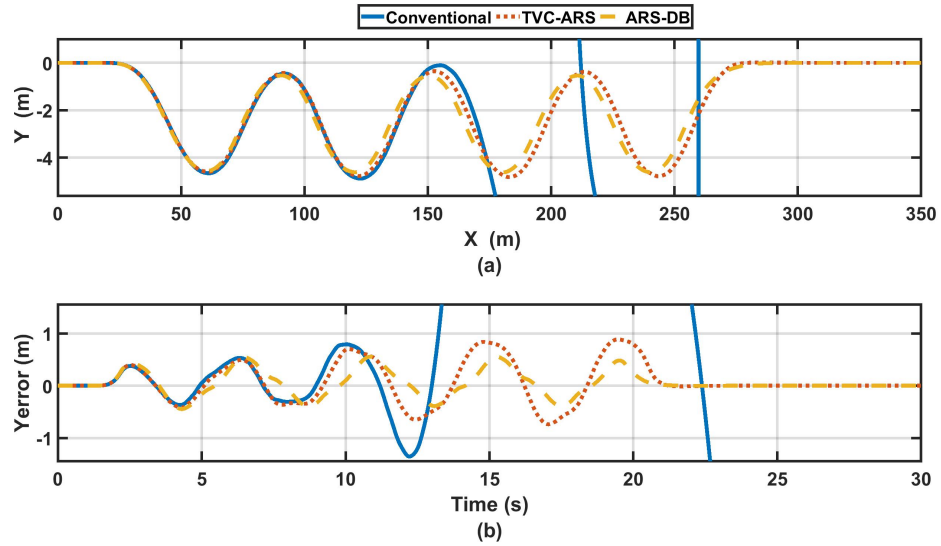


Figure 6.11: Slalom maneuver at  $\mu=0.5$  and speed 50 km/h (a) Vehicle trajectory (b) Lateral error

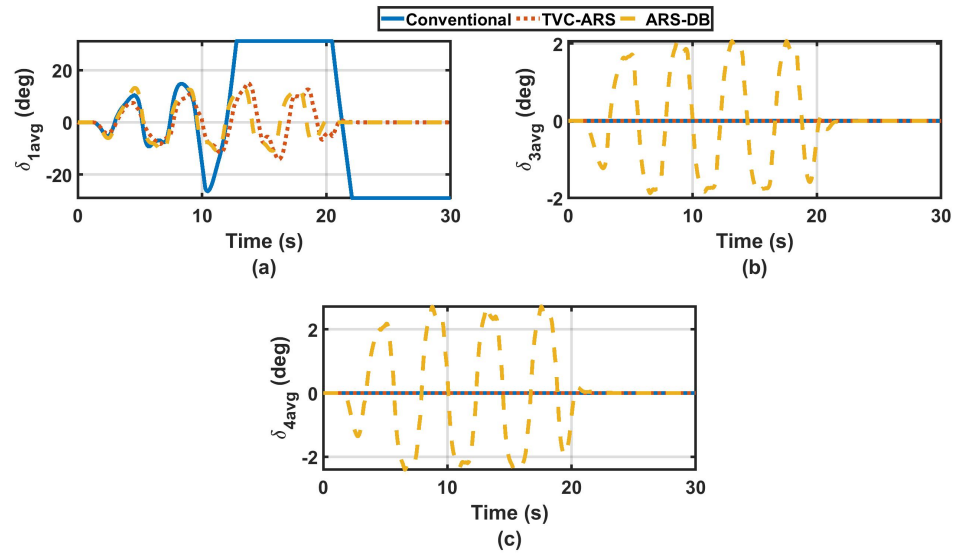


Figure 6.12: Slalom maneuver at  $\mu=0.5$  and speed 50 km/h (a) Average Steering angle of the 1<sup>st</sup> axle (b) Average Steering angle of the 3<sup>rd</sup> axle (c) Average Steering angle of the 4<sup>th</sup> axle

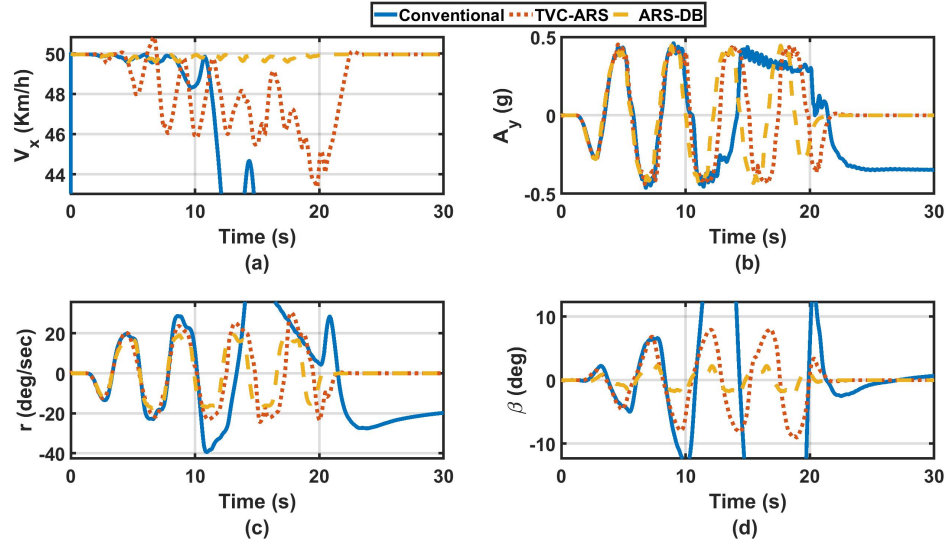


Figure 6.13: Slalom maneuver at  $\mu=0.5$  and speed 50 km/h (a) Vehicle longitudinal speed (b) lateral acceleration (c) Yaw response (d) Vehicle sideslip response

only the TVC-ARS was able to generate a yaw rate and maneuverability high enough to ensure take the maneuver successfully.

Figure 6.19 shows a smooth and uniform corrective driving moment delivered from the TVC to the right and left wheels' side. On the other hand, figure 6.20 shows the braking torque of the DB controller in the case of ARS-DB on both wheels' sides.

Even though only TVC-ARS could stabilize the controller it is memorable that ARS-DB could stabilize the vehicle when repeated the maneuver in two different cases. The first was by decreasing the desired path's amplitude from 5 to 4.9 m, and the second was by decreasing the speed to 29 km/h at the same path's amplitude (5 m).

## 6.4.2 DLC maneuver

### 6.4.2.1 DLC at $\mu = 0.85$ and $V = 100$ km/h:

Still in the closed-loop-tests, a DLC maneuver is performed at dry asphalt with Cof 0.85 and high speed of 100 km/h. According to the vehicle trajectory and lateral error at figures 6.21 (a) and (b), almost all cases pass the maneuver with the same lateral error.

Because of the assisting moment generated by TVC in the case of TVC-ARS, the steering angle of the 1<sup>st</sup> axle is less than other cases, as shown in figure 6.22 (a). Furthermore,

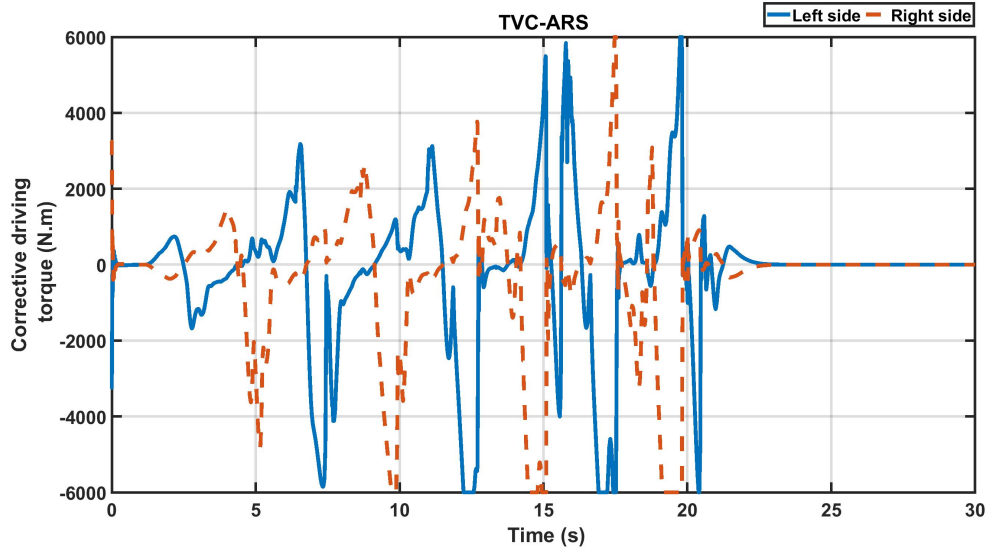


Figure 6.14: Slalom maneuver at  $\mu=0.5$  and speed 50 km/h; Corrective driving torque of the right and left wheels' side

figures 6.22 (b) and (c) show that the ARS was not engaged in either case according to the coordination laws.

The engagement of TVC in the case of TVC-ARS lead to the largest drop in the vehicle's speed (6 km/h), followed by the effect of the DB associated with the ARS-DB (4 km/h), as can be noticed in figure 6.23 (a). Despite that drop, the TVC-ARS stabilize the vehicle a little bit faster than other cases as shown in other subfigures. In addition, the TVC generated the least yaw rate and sideslip, as presented in figures 6.23 (c) and (d), respectively.

The corresponding corrective driving torque to the TVC-ARS controller is presented in figure 6.24. It can be seen that the distribution is not equally distributed on both sides due to the different normal load distribution on each side, which is a key factor in distributing the torque in the TVC allocation (TVC lower controller).

In the case of the ARS-DB in figure 6.25, it can be noticed that the braking is only applied on the first axle, which means that is no wheel's slip due to braking and consequently no excessive braking is applied.

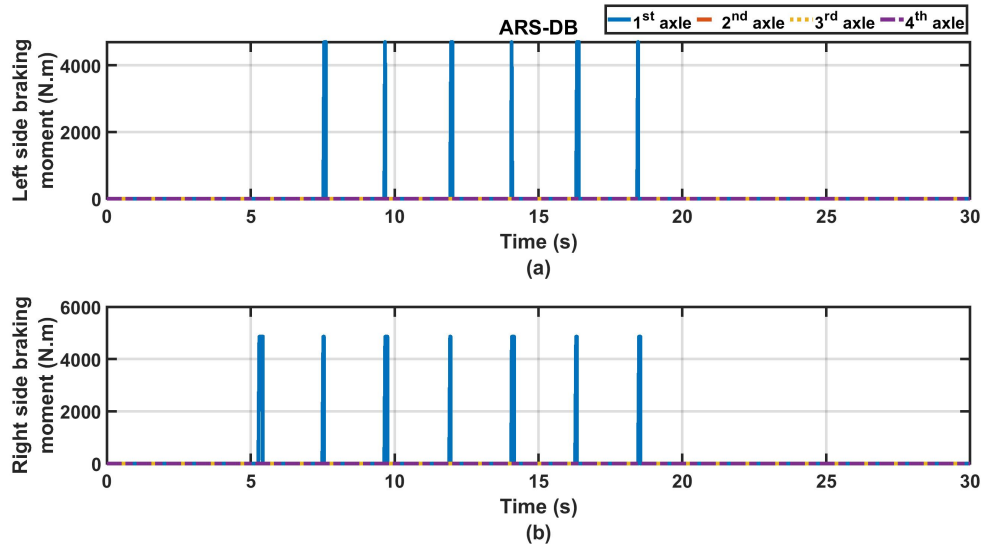


Figure 6.15: Slalom maneuver at  $\mu=0.5$  and speed 50 km/h; Braking forces at each wheel

#### 6.4.2.2 DLC at $\mu = 0.5$ and $V = 100 \text{ km/h}$ :

By performing the DLC maneuver at  $\mu = 0.5$  with a driving speed of 100 km/h and following the vehicle trajectory in figure 6.26 (a), the oscillation of the conventional vehicle can be observed. On the other hand, other cases show a more stable trajectory with less lateral deviation from the desired path, as presented in figure 6.26 (b).

The 1<sup>st</sup> axle steering angle for the controlled vehicle were less than its counterpart in the conventional vehicle, based on figure 6.27 (a). Moreover, the contribution of the ARS in case of ARS-DB is larger than TVC-ARS due to the larger steering presented in figures 6.27 (b) and (c) (from 0.5 to 3 degrees for the 3<sup>rd</sup> and 4<sup>th</sup> axles, respectively).

Based on figure 6.28 (a), it is notable that the effect of the controllers led to a decrease in the desired speed less than the drop in the case of the conventional vehicle (almost 5 km/h). This drop is from about 2.1 to 3 km/h in the case of ARS-DB TVC-ARS, respectively. By observing the dynamic response in other figures, it can be seen that the TVC-ARS could stabilize the vehicle faster than the ARS-DB by almost 0.3 seconds, which is faster than the conventional vehicle by 4 seconds. Furthermore, both controllers maintain low yaw rate and sideslip as shown in figures 6.28 (c) and (d), respectively.

In the case of the TVC, unequal torque on the right and left sides due to unequal lateral



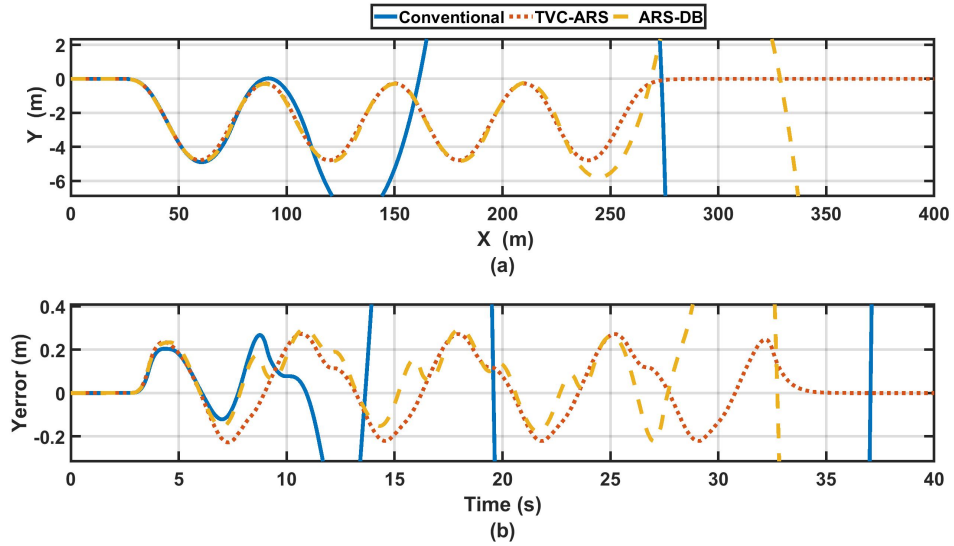


Figure 6.16: Slalom maneuver at  $\mu=0.2$  and speed 30 km/h (a) Vehicle trajectory (b) Lateral error

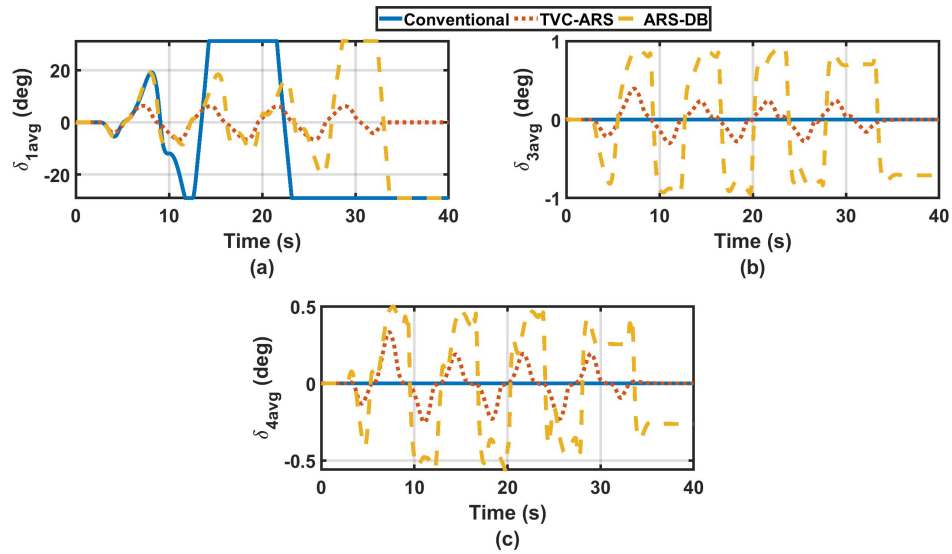


Figure 6.17: Slalom maneuver at  $\mu=0.2$  and speed 30 km/h (a) Average Steering angle of the 1<sup>st</sup> axle (b) Average Steering angle of the 3<sup>rd</sup> axle (c) Average Steering angle of the 4<sup>th</sup> axle

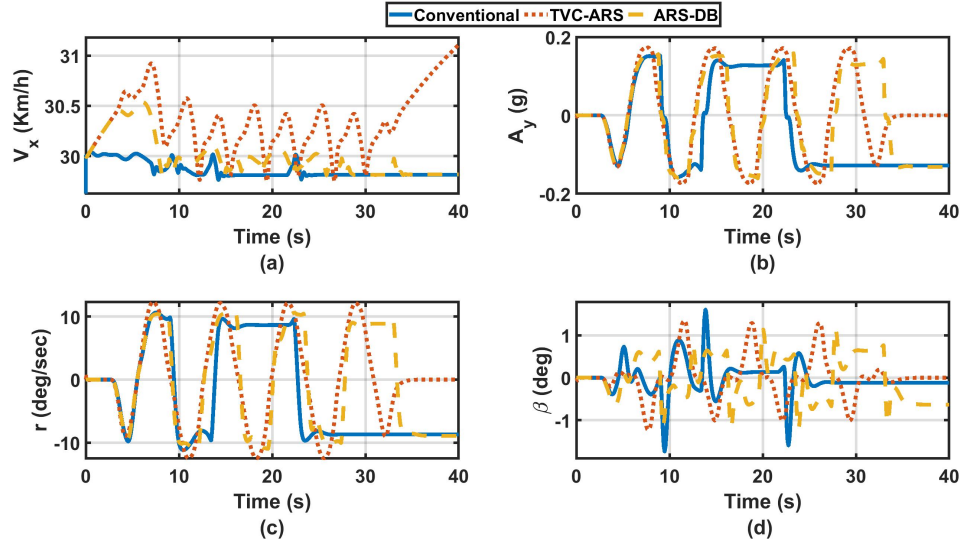


Figure 6.18: Slalom maneuver at  $\mu=0.2$  and speed 30 km/h (a) Vehicle longitudinal speed (b) lateral acceleration (c) Yaw response (d) Vehicle sideslip response

load transfer are also observed in figure 6.29. Meanwhile, it can be seen in figure 6.30 that the contribution of the DB in the ARS-DB controller was very small and occurs on only the 1<sup>st</sup> axle's right wheel during the time 3.7 to 4.1 seconds.

#### 6.4.2.3 DLC at $\mu = 0.2$ and $V = 100 \text{ km/h}$ :

The maneuver is performed on a slippery road with CoF 0.2 at driving speed 100 km/h and the vehicle trajectory and corresponding lateral error are presented in figures 6.31 (a) and (b), respectively. Based on the coordination, at such low friction and high speed, it is more effective to apply the ARS than other controllers. Therefore, the controlled vehicle's behaviour is almost the same. It is also noticed that the uncontrolled vehicle failed to stabilize after performing the maneuver.

By observing the 1<sup>st</sup>, 2<sup>nd</sup>, and 3<sup>rd</sup> axles' average steering angle in figures 6.32 (a), (b), and (c), respectively, it can be assured that all controllers behaves the same and have the same steering without any contribution from the TVC or the DB controllers.

The dynamic response in figure 6.33 shows that the ARS activation resulted in a negligible change in the vehicle's longitudinal speed and maintain low lateral acceleration, yaw rate, and sideslip that kept the vehicle's stability as presented in figures 6.33 (a), (b), (c), and (d).

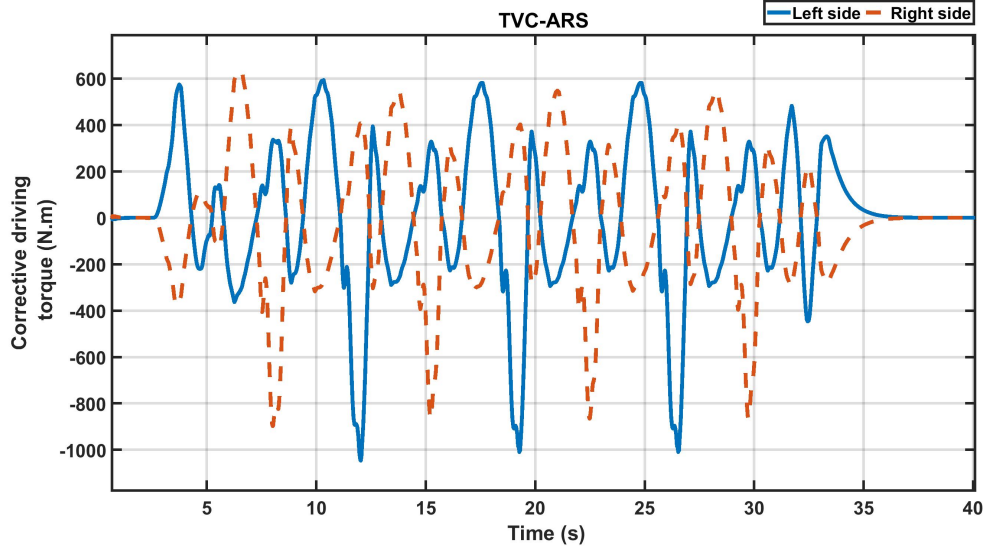


Figure 6.19: Slalom maneuver at  $\mu=0.2$  and speed 30 km/h; Corrective driving torque of the right and left wheels' side

### 6.4.3 FMVSS maneuver

#### 6.4.3.1 FMVSS at $\mu = 0.85$ and $V = 100 \text{ km/h}$ :

For open-loop testing, the FMVSS maneuver is conducted at first. Figure 6.34 (a) presents the trajectory generated by the vehicle for all cases. In general, it can be noticed that the TVC-ARS has less maneuverability than other cases. Figure 6.34 (b) is a close-up on the trajectory that is presented in figure 6.34 (a) ( $X=0:80 \text{ m}$ ) to show the lateral offset that is taken by each case. It can be confirmed that the TVC-ARS has the least by 2.2m followed by the ARS-DB by almost 3m and the conventional vehicle by 3.15 m.

Figure 6.35 (a) shows the 1<sup>st</sup> axle's steering angle which indicates that all cases exposed to the same driver's input. Figures 6.35 (b) and (c) show that the ARS has not been activated in neither cases.

While the vehicle's speed is dropped to almost the same value for all cases, the TVC-ARS seems to affect it faster than the ARS-DB, as shown in figure 6.36 (a). Moreover, by observing the vehicle's dynamic response in figure 6.36 (a), (b), and (c), it can be noticed that the less lateral offset (maneuverability) resulted in the least lateral acceleration, yaw rate, and sideslip, respectively. This leads to faster stabilization.

The corrective torque applied on each vehicle's side in the case of the TVC-ARS is

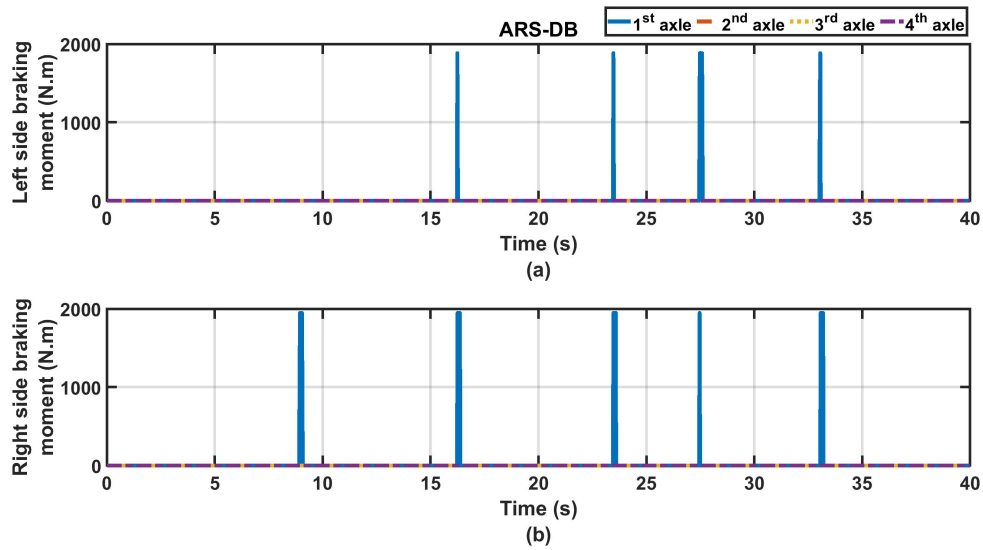


Figure 6.20: Slalom maneuver at  $\mu=0.2$  and speed 30 km/h; Braking forces at each wheel

presented in figure 6.37. Meanwhile, the braking torque applied in the case of the ARS-DB is presented in figure 6.38, which is only applied to the 1<sup>st</sup> axle.

#### 6.4.3.2 FMVSS at $\mu = 0.5$ and $V = 100 \text{ km/h}$ :

When repeating the maneuver at lower CoF, It can be seen from figures 6.39 (a) and (b) that the TVC-ARS has the highest lateral offset (2.4m), while the ARS-DB has the least (2m).

For the same steering input that is reflected on the 1<sup>st</sup> axle's steering angle in figure 6.40 (a), The steering angles of the 3<sup>rd</sup> and 4<sup>th</sup> axles were high in case of the ARS-DB in comparison with the TVC-ARS, as shown in figure 6.40 (b) and (c).

Figure 6.41 (a) shows a very small drop in the vehicle's speed in the case of the ARS-DB, while the drop reached 5 km/h and 16 km/h in the case of the TVC-ARS and the uncontrolled vehicle, respectively. In figure 6.41 (b), (c), and (d), it can be noticed that the TVC-ARS has almost the same lateral acceleration, yaw rate, and sideslip as in the case of the ARS-DB. In addition, it almost stabilizes at the same time despite the higher lateral offset presented in figure 6.39.

In this test, the contribution of the corrective driving torque applied by the TVC, as shown in figure 6.42 in the case of the TVC-ARS controller resulted in less steering at

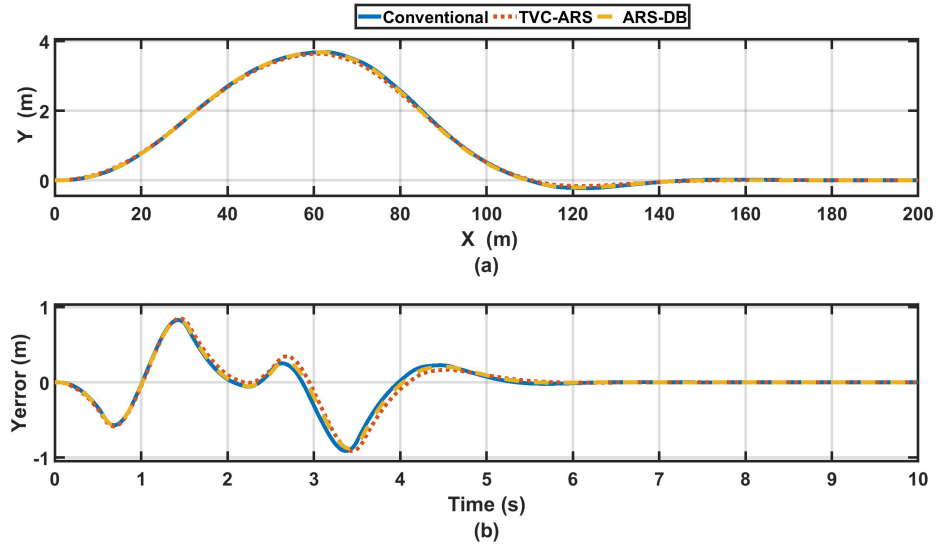


Figure 6.21: DLC maneuver at  $\mu=0.85$  and speed 100 km/h (a) Vehicle trajectory (b) Lateral error

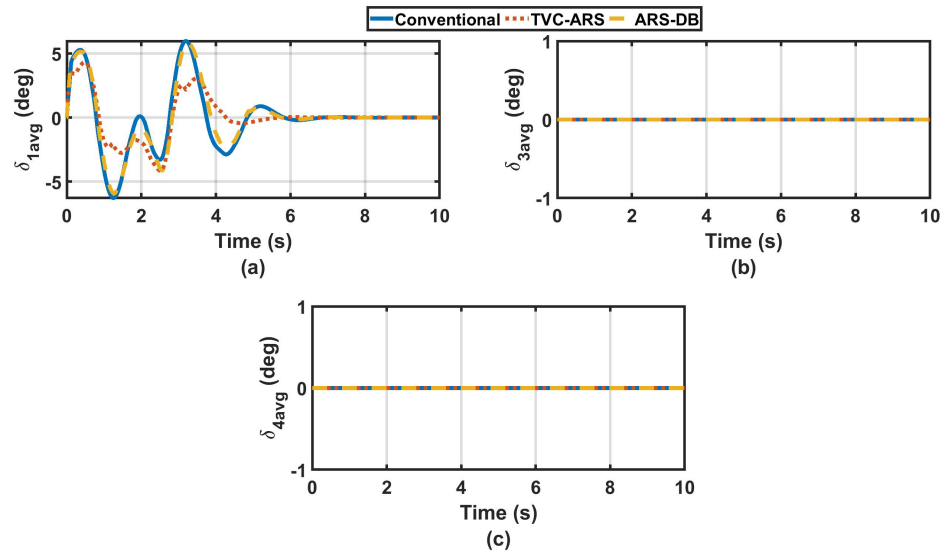


Figure 6.22: DLC maneuver at  $\mu=0.85$  and speed 100 km/h (a) Average Steering angle of the 1<sup>st</sup> axle (b) Average Steering angle of the 3<sup>rd</sup> axle (c) Average Steering angle of the 4<sup>th</sup> axle

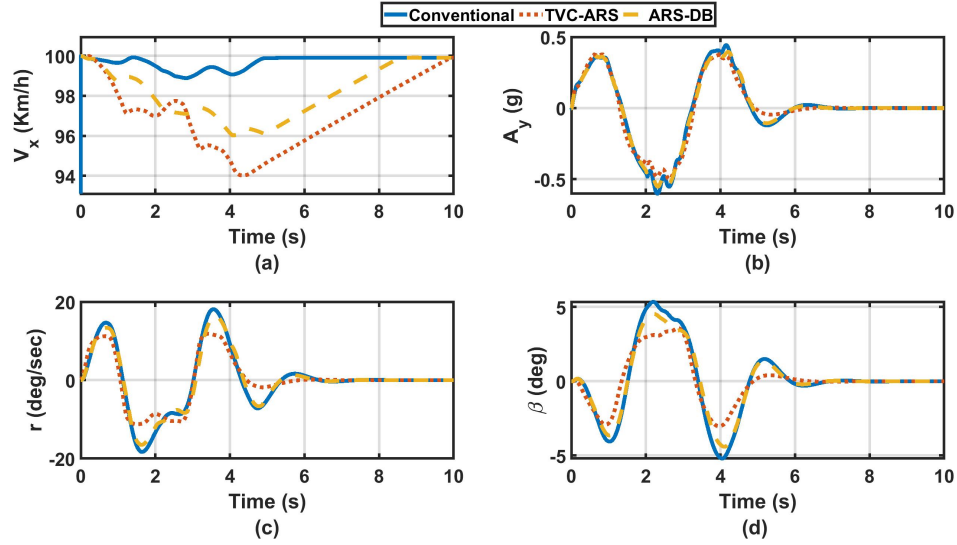


Figure 6.23: DLC maneuver at  $\mu=0.85$  and speed 100 km/h (a) Vehicle longitudinal speed (b) lateral acceleration (c) Yaw response (d) Vehicle sideslip response

the rear axles and higher lateral offset (maneuverability).

#### 6.4.3.3 FMVSS at $\mu = 0.2$ and $V = 100$ km/h:

From figure 6.43 (a), and (b) it can be noticed that the lateral offset that is exhibited by the vehicle is limited at slipper road with CoF 0.2. It reaches a 0.81m in the case of conventional vehicle and decreased to 0.62m for other cases.

Figure 6.44 show the average steering angles of each axle, which is almost identical in the case of the controlled vehicle due to the activation of ARS only.

Despite that the lateral offset difference is less than 20cm ( $<0.2$ m) in favour of the conventional vehicle, the controlled vehicle showed a tremendous improvement in the vehicle's dynamic response. This can appear in the negligible speed drop, less lateral acceleration, yaw rate, sideslip, and faster stabilization by almost 6 seconds, as can be seen in figure 6.45 (a), (b), (c), and(d), respectively.

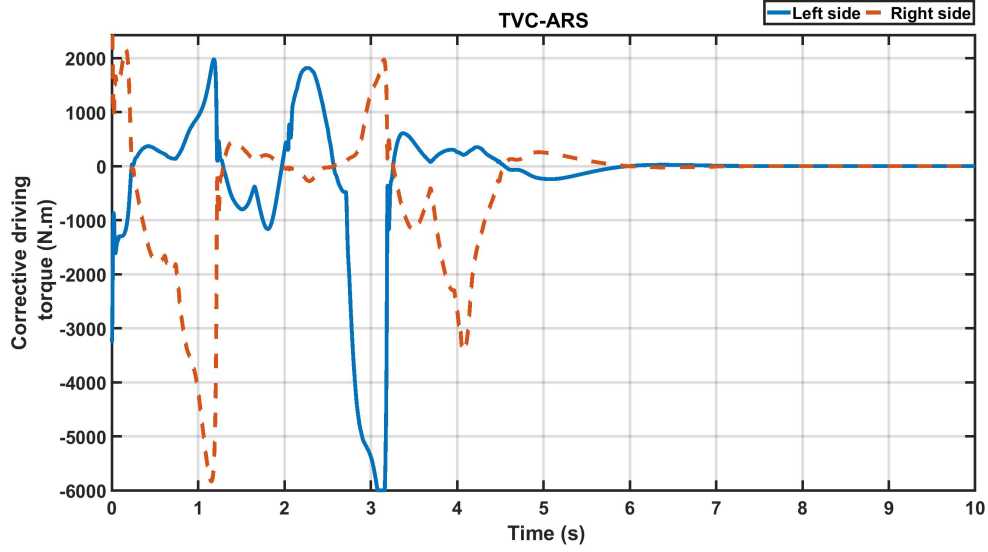


Figure 6.24: DLC maneuver at  $\mu=0.85$  and speed 100 km/h; Corrective driving torque of the right and left wheels' side

#### 6.4.4 J-turn maneuver

##### 6.4.4.1 J-turn at $\mu = 0.85$ and $V = 100 \text{ km/h}$ :

The second closed loop maneuver conducted is the J-turn maneuver. At first, the test is performed at high speed and dry asphalt with CoF 0.85. The vehicle path is shown in figure 6.46, where the TVC-ARS performed the tightest maneuver followed by the ARS-DB, then the conventional vehicle.

Figure 6.47 (a) shows the steering angle at the 1<sup>st</sup> axle, which is the same for all cases. Figure 6.47 (a) and (b) shows that the ARS didn't activate or engage in the controllers, which means that only TVC and DB were active in the TVC-ARS and ARS-DB, respectively.

The dynamic response shows a significant drop in the vehicle's speed that varies from 28 to 50 km/h in the case of the conventional vehicle and the TVC-ARS, respectively, as shown in figure 6.48 (a). Figure 6.48 (b) shows that the TVC-ARS generated lower lateral acceleration, while the ARS-DB and the conventional vehicle reached the same maximum acceleration. In addition, The TVC-ARS has the highest yaw rate and least sideslip, as shown in figures 6.48 (c) and (d).

In the case of the TVC-ARS, a higher load is transferred to the vehicle's left side. This

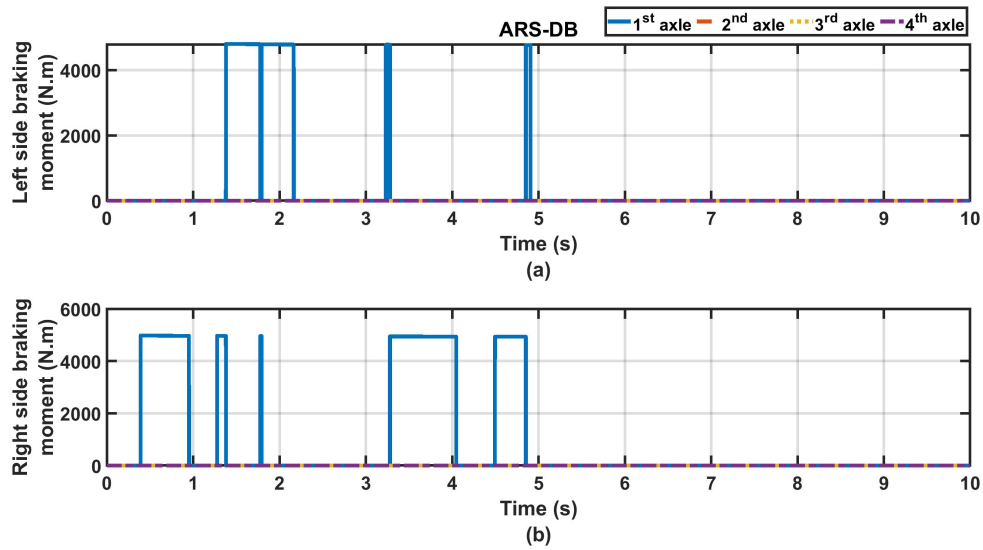


Figure 6.25: DLC maneuver at  $\mu=0.85$  and speed 100 km/h; Braking forces at each wheel

resulted in applying higher corrective driving torque to the left side in comparison to the right side, as presented in figure 6.49.

Figure 6.50 shows the braking torque applied on each axle in the case of the ARS-DB. It can be seen that the 1<sup>st</sup> axle's right wheel start to slip and the controller starts braking the 2<sup>nd</sup> axle's right wheel until the slip decreased.

#### 6.4.4.2 J-turn at $\mu = 0.5$ and $V = 100 \text{ km/h}$ :

The maneuver is also performed on wet asphalt with CoF 0.5, the vehicle path is shown in figure 6.51 for all cases. It can be seen that the TVC-ARS has the highest maneuverability, while the ARS-DB has the least.

In figure 6.52, for the same 1<sup>st</sup> axle steering angle, as shown in figure 6.52 (a), the rear axles' steering angles are different. In case of the TVC-ARS, the 3<sup>rd</sup> axle's steering angle is higher than the ARS-DB, while the 4<sup>th</sup> axle's steering angle is less, as shown in figures 6.52 (b) and (c). This can be related to the different contribution of TVC and DB in both controllers.

Notably, the TVC-ARS has the least drop in the vehicle's speed in comparison with other cases, as shown in figure 6.53 (a), even though it has the highest maneuverability. The higher maneuverability and speed yield higher lateral acceleration, as presented in



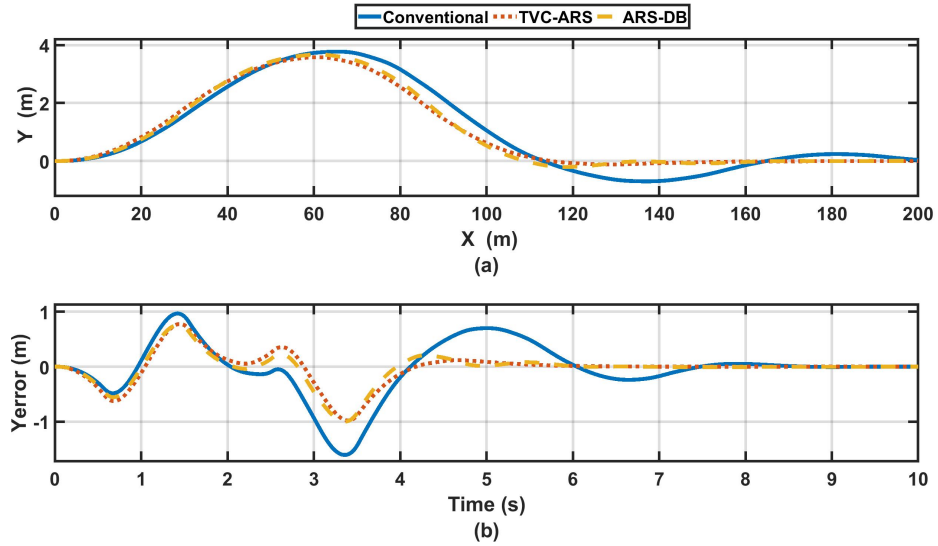


Figure 6.26: DLC maneuver at  $\mu=0.5$  and speed 100 km/h (a) Vehicle trajectory (b) Lateral error

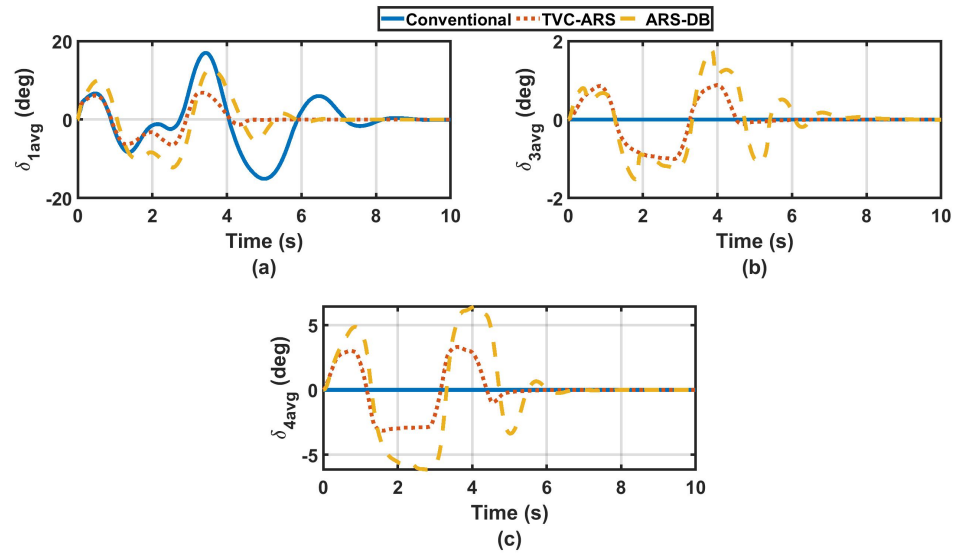


Figure 6.27: DLC maneuver at  $\mu=0.5$  and speed 100 km/h (a) Average Steering angle of the 1<sup>st</sup> axle (b) Average Steering angle of the 3<sup>rd</sup> axle (c) Average Steering angle of the 4<sup>th</sup> axle

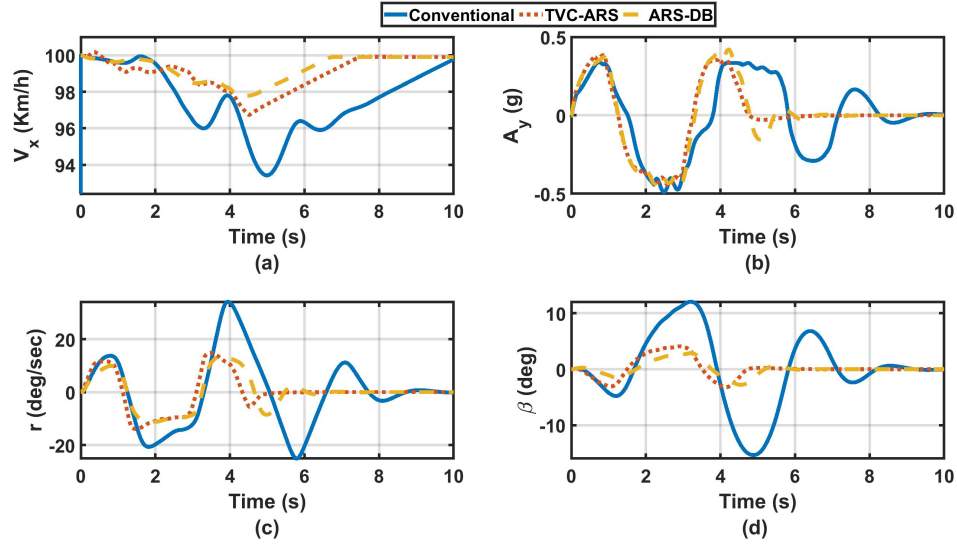


Figure 6.28: DLC maneuver at  $\mu=0.5$  and speed 100 km/h (a) Vehicle longitudinal speed (b) lateral acceleration (c) Yaw response (d) Vehicle sideslip response

figure 6.53 (b). In addition, the TVC-ARS has a higher yaw rate and sideslip than the ARS-DB, as can be seen in figures figure 6.53 (c) and (d), respectively.

Figure 6.54 shows the corrective torque applied on the right and left wheels' sides. Despite the high oscillation at the beginning of the maneuver, the controller was able to stabilize fast and reach a steady value.

#### 6.4.4.3 J-turn at $\mu = 0.2$ and $V = 100 \text{ km/h}$ :

The J-turn maneuver is repeated on an icy road with a CoF 0.2 and the vehicles' path in figure 6.55 shows very low maneuverability for all-cases.

The steering angles of the 1<sup>st</sup> axle is shown in figure 6.56 (a), where all cases has the same input. Meanwhile, the 3<sup>rd</sup> and 4<sup>th</sup> axles' steering angle are presented in figures 6.56 (b) and (c), respectively. It can be observed that the rear axles' steering angles are almost the same for the TVC-ARS and the ARS-DB, which means that the TVC and DB are not activated in both controllers.

A navigable drop in the vehicle's speed is shown in figure 6.57 (a). Meanwhile, the controlled vehicles show a lower lateral acceleration than the conventional vehicle, as in figure 6.57 (b), and more stabilized yaw rate and minimum sideslip (almost zero), as can be seen in figures 6.57 (c) and (d), respectively.

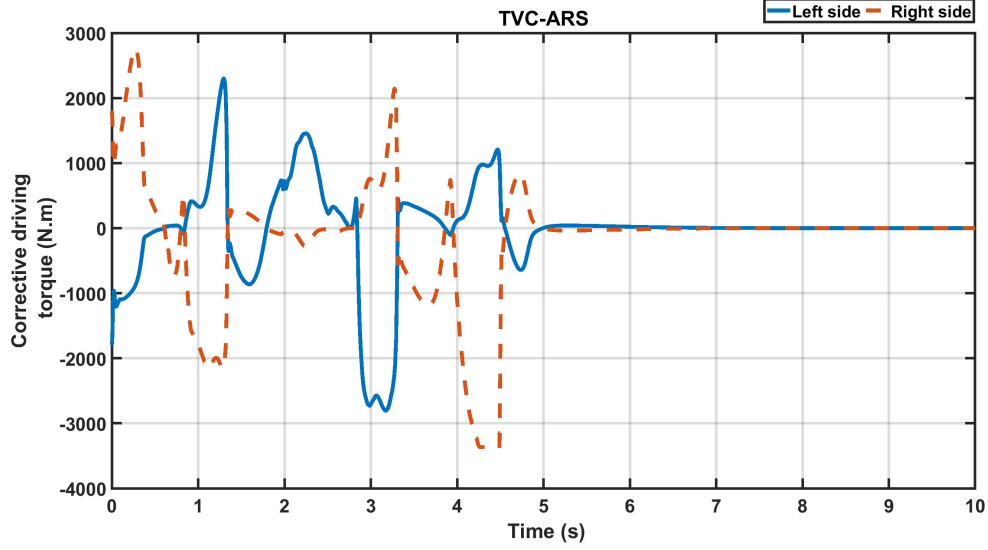


Figure 6.29: DLC maneuver at  $\mu=0.5$  and speed 100 km/h; Corrective driving torque of the right and left wheels' side

and subtracted from the right and left wheels' side for ICC

### 6.4.5 Increased-step Slalom

The increased step slalom is a severe open-loop test in which the driver applies an increased sine wave-like steering wheel angle followed by constant steering when driving on a road with CoF 0.85 with a speed of 65 km/h. The vehicle trajectory to the same steering input is shown in figure 6.58. It can be observed from the figure that the conventional vehicle didn't complete the maneuver, while the controlled vehicles did.

Figure 6.59 (a) shows the same steering input on the 1<sup>st</sup> for all cases. Furthermore, figures 6.59 (b) and (c) show no contribution of the ARS in all controllers.

Figure 6.60 (a) shows that the vehicle's speed is dropped drastically in all cases, however, the drop in case of the ARS-DB (dropped to 28 km/h) is a little higher than the TVC-ARS (34 km/h). Meanwhile, all controllers kept the lateral acceleration below the rollover threshold and prevent the vehicle from rollover. On the contrary, the conventional vehicle's lateral acceleration exceeded that threshold and rollover occurred, as can be seen in figure 6.60 (b). It is also noticed that the ARS-DB controller resulted in a higher yaw rate than the TVC-ARS, which lead to a higher sideslip, as shown in figures 6.60 (c) and (d), respectively. However, the ARS-DB shows a lower steady-state

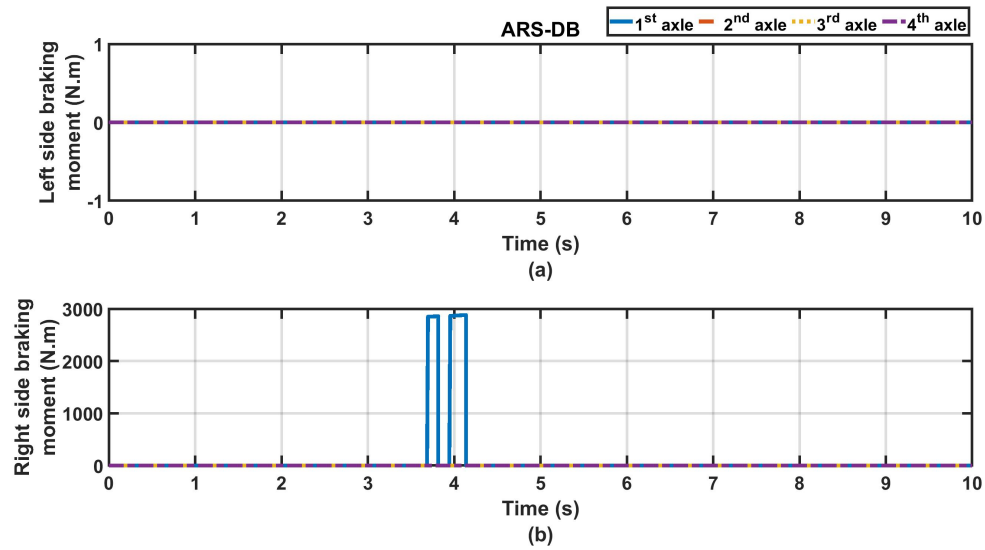


Figure 6.30: DLC maneuver at  $\mu=0.5$  and speed 100 km/h; Braking forces at each wheel

sideslip than the TVC-ARS.

The corrective driving torque distribution on each wheels' side in the case of the TVC controller is presented in figure 6.61. The figure shows a higher torque on the left side that tends to stabilize and reach a constant value at a time of more than 25 seconds, while the right side reached zero. This can be related to the circular path at the end of the maneuver as shown in figure 6.58.

The braking torque associated with the activation of the DB controller can be observed in figure 6.62. The figure shows a high braking effort applied by the controller to maintain stability and prevent rollover, which made the breaking be applied to the 1<sup>st</sup> to 4<sup>th</sup> axle on the left side and to the 2<sup>nd</sup> axle on the right side due to the high braking wheels' slip.

## 6.5 Chapter summary

In this chapter, a novel multi-chassis controllers coordinator based on genetic programming was presented to control the lateral stability of the 8x8 combat vehicle. In addition, a performance map that shows a qualitative evaluation for TVC and ARS was presented based on a series of simulation-based maneuvers. This map was processed through a new coordination equation and used to generate Neuro-fuzzy based control rules. To

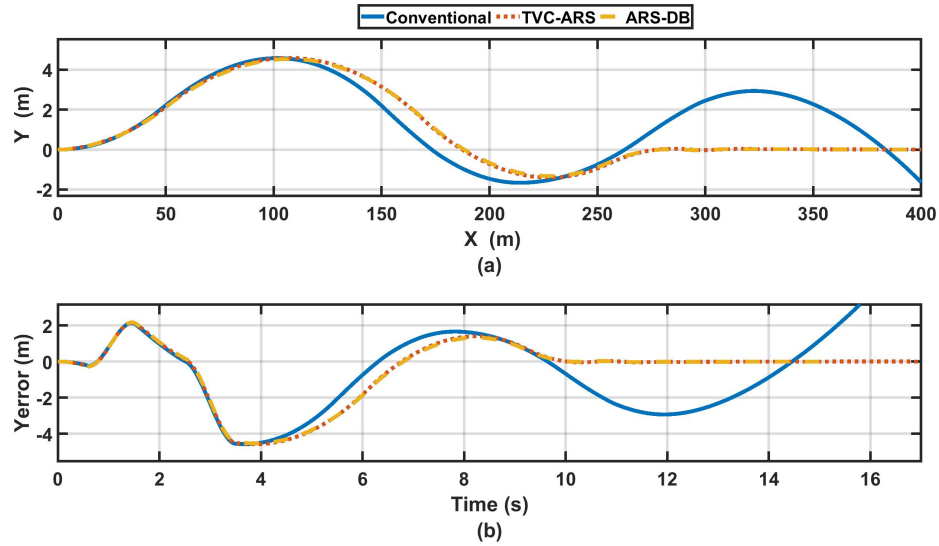


Figure 6.31: DLC maneuver at  $\mu=0.2$  and speed 100 km/h (a) Vehicle trajectory (b) Lateral error

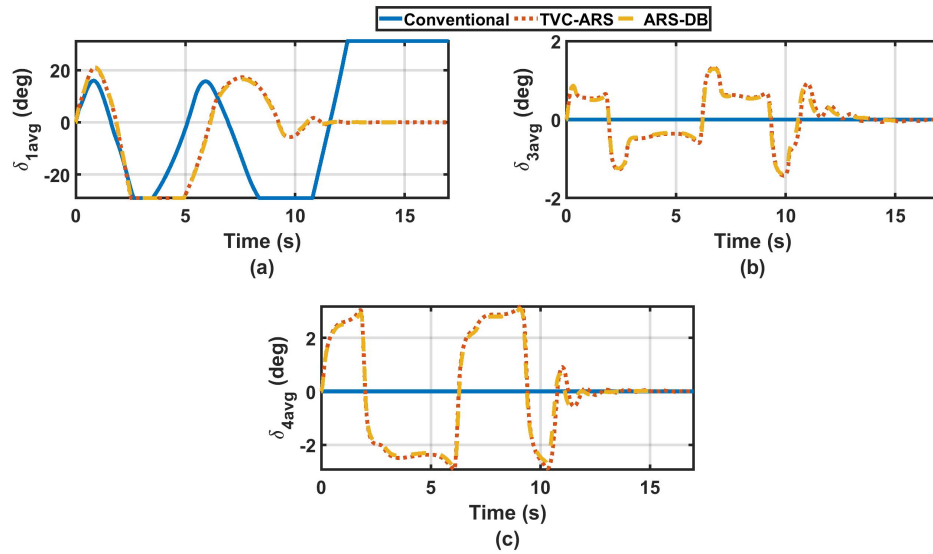


Figure 6.32: DLC maneuver at  $\mu=0.2$  and speed 100 km/h (a) Average Steering angle of the 1<sup>st</sup> axle (b) Average Steering angle of the 3<sup>rd</sup> axle (c) Average Steering angle of the 4<sup>th</sup> axle

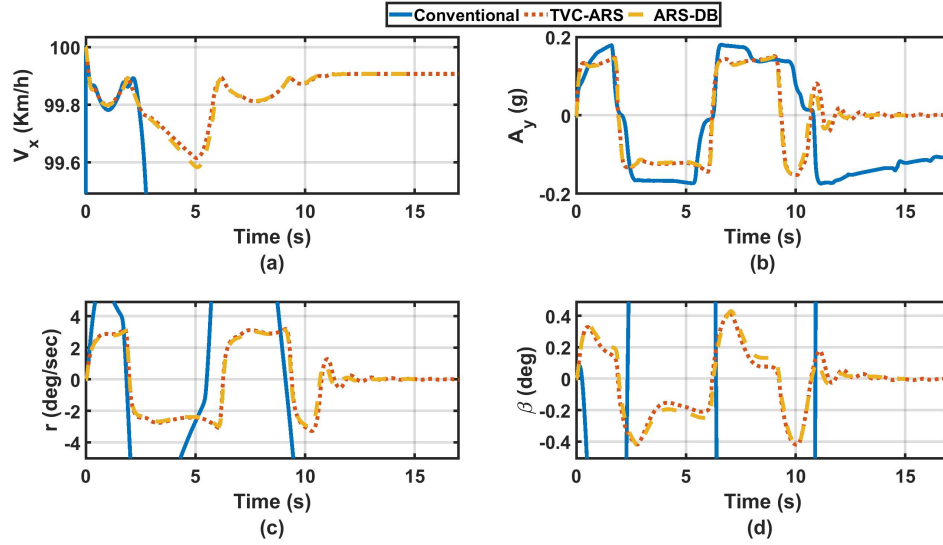


Figure 6.33: DLC maneuver at  $\mu=0.2$  and speed 100 km/h (a) Vehicle longitudinal speed (b) lateral acceleration (c) Yaw response (d) Vehicle sideslip response

ease future hardware implementation, the Neuro-fuzzy coordinator's rules were simplified to three equations using genetic programming-based software, which showed a significant reduction in the processing time. Moreover, a simple fuzzy-based coordinator was used to coordinate the differential braking and ARS controllers based on the road friction coefficient.

After that, the integrated controllers were tested by conducting several maneuvers on dry, slippery, and icy roads at high speed in comparison with the uncontrolled vehicle using slalom, DLC, FMVSS, J-turn, and step slalom maneuvers. The simulations showed that the vehicle stability was extremely enhanced by the controllers in comparison with the uncontrolled vehicle.

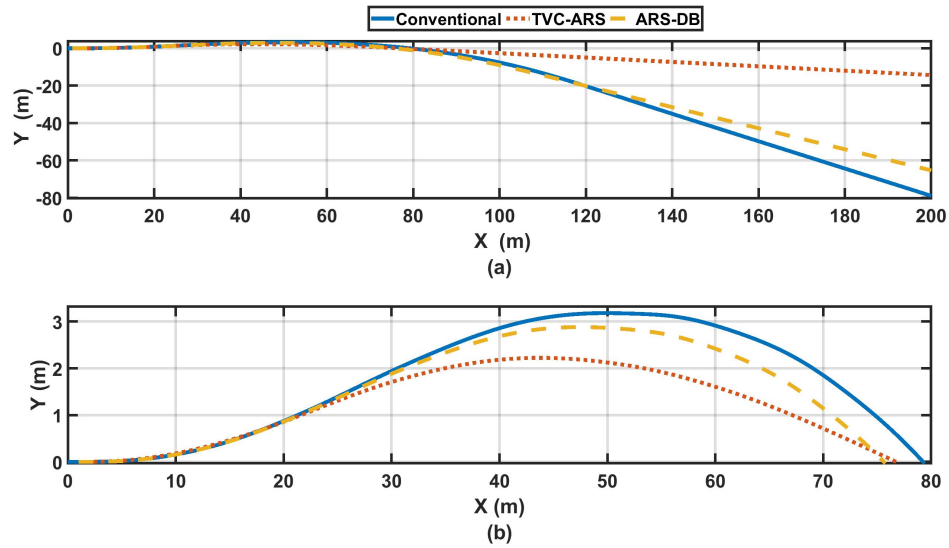


Figure 6.34: FMVSS maneuver at  $\mu=0.85$  and speed 100 km/h (a) Vehicle trajectory (b) Close up to the vehicle's lateral shift

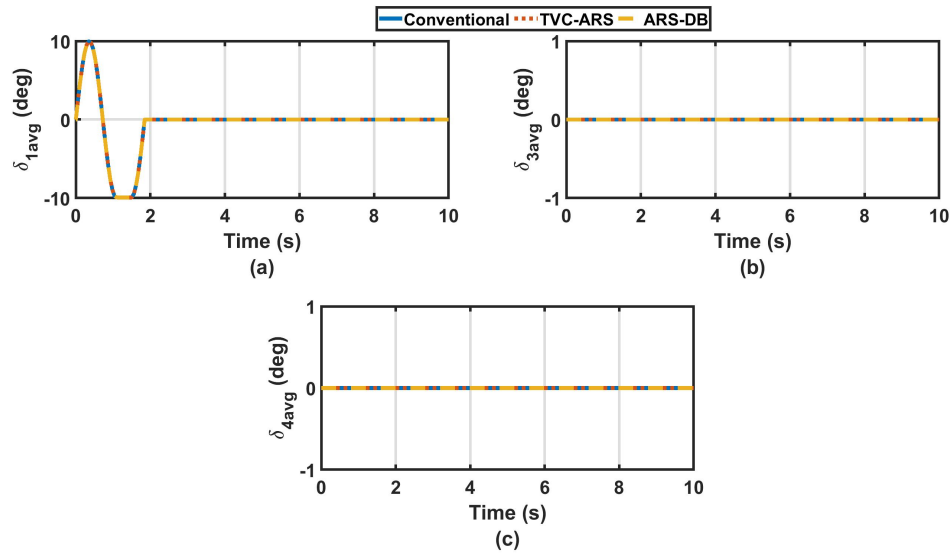


Figure 6.35: FMVSS maneuver at  $\mu=0.85$  and speed 100 km/h (a) Average Steering angle of the 1<sup>st</sup> axle (b) Average Steering angle of the 3<sup>rd</sup> axle (c) Average Steering angle of the 4<sup>th</sup> axle

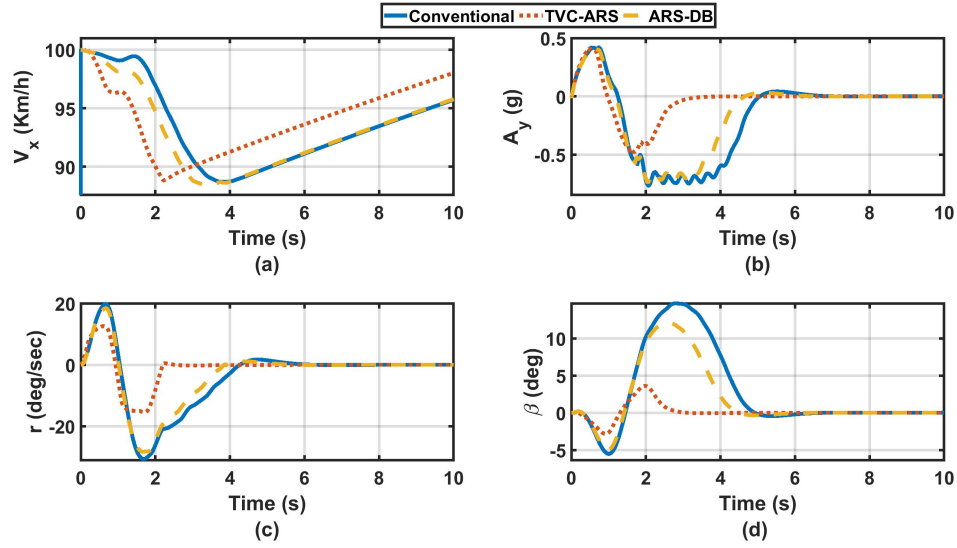


Figure 6.36: FMVSS maneuver at  $\mu=0.85$  and speed 100 km/h (a) Vehicle longitudinal speed (b) lateral acceleration (c) Yaw response (d) Vehicle sideslip response

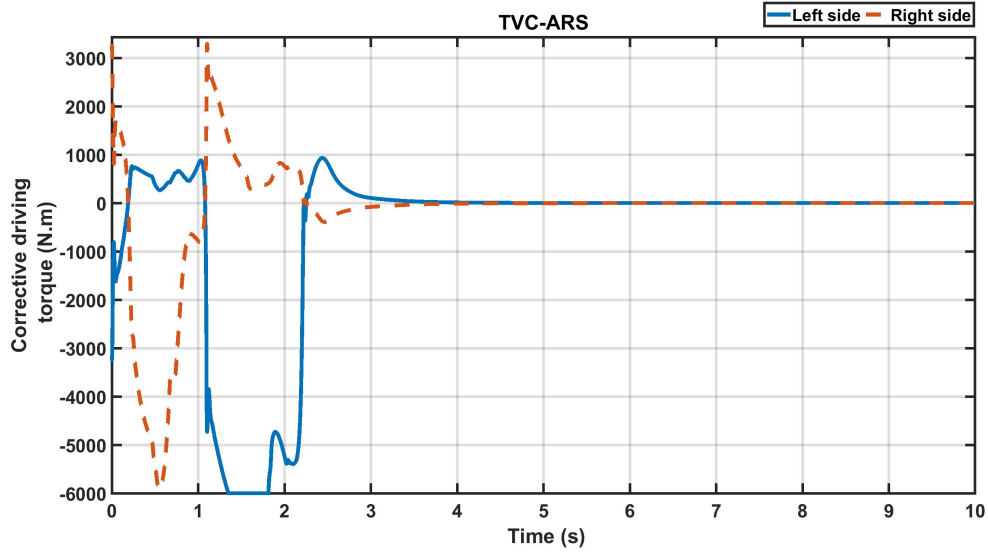


Figure 6.37: FMVSS maneuver at  $\mu=0.85$  and speed 100 km/h; Corrective driving torque of the right and left wheels' side



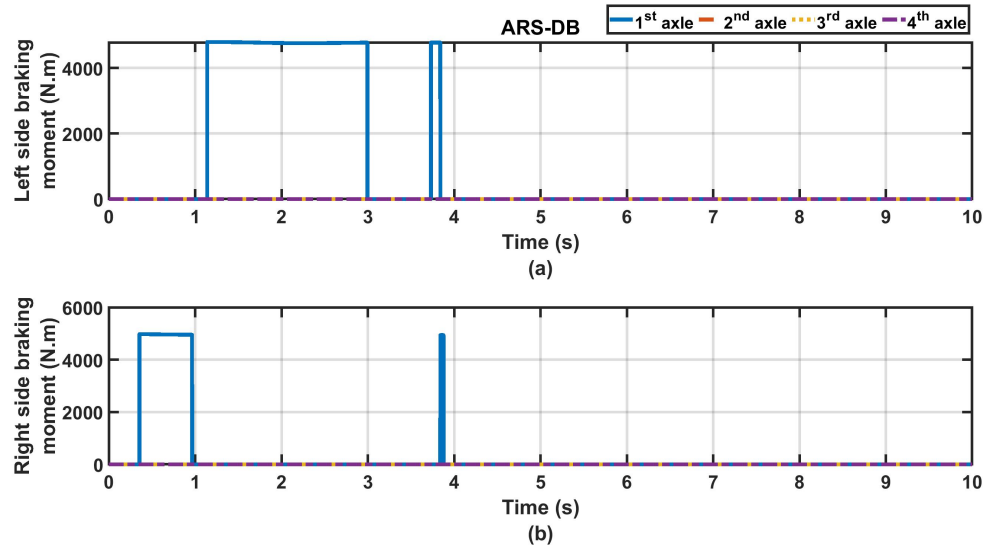


Figure 6.38: FMVSS maneuver at  $\mu=0.85$  and speed 100 km/h; Braking forces at each wheel

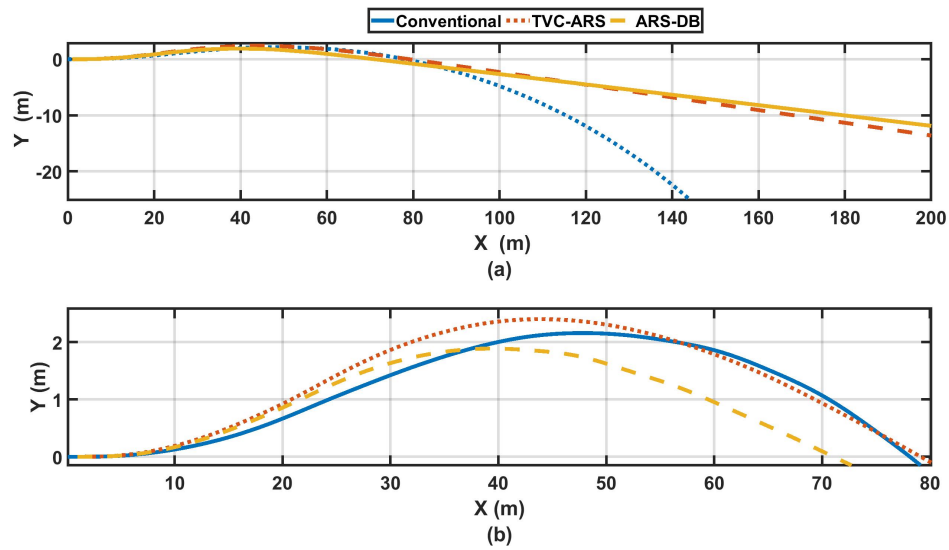


Figure 6.39: FMVSS maneuver at  $\mu=0.5$  and speed 100 km/h (a) Vehicle trajectory (b) Close up to the vehicle's lateral shift

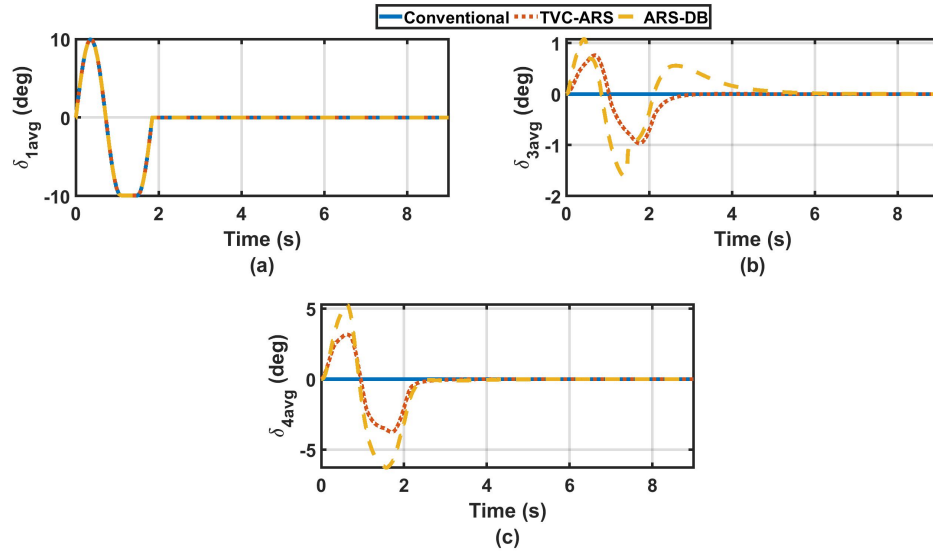


Figure 6.40: FMVSS maneuver at  $\mu=0.5$  and speed 100 km/h (a) Average Steering angle of the 1<sup>st</sup> axle (b) Average Steering angle of the 3<sup>rd</sup> axle (c) Average Steering angle of the 4<sup>th</sup> axle

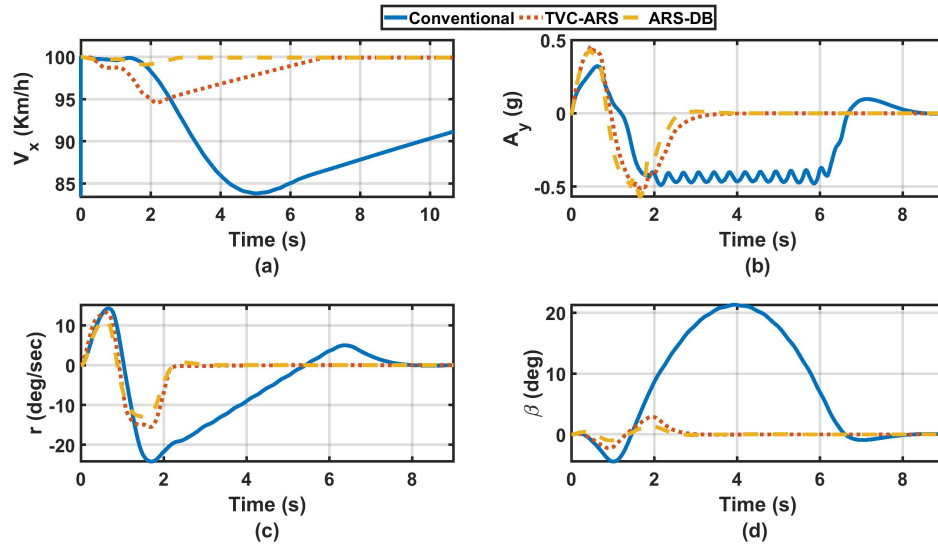


Figure 6.41: FMVSS maneuver at  $\mu=0.5$  and speed 100 km/h (a) Vehicle longitudinal speed (b) lateral acceleration (c) Yaw response (d) Vehicle sideslip response

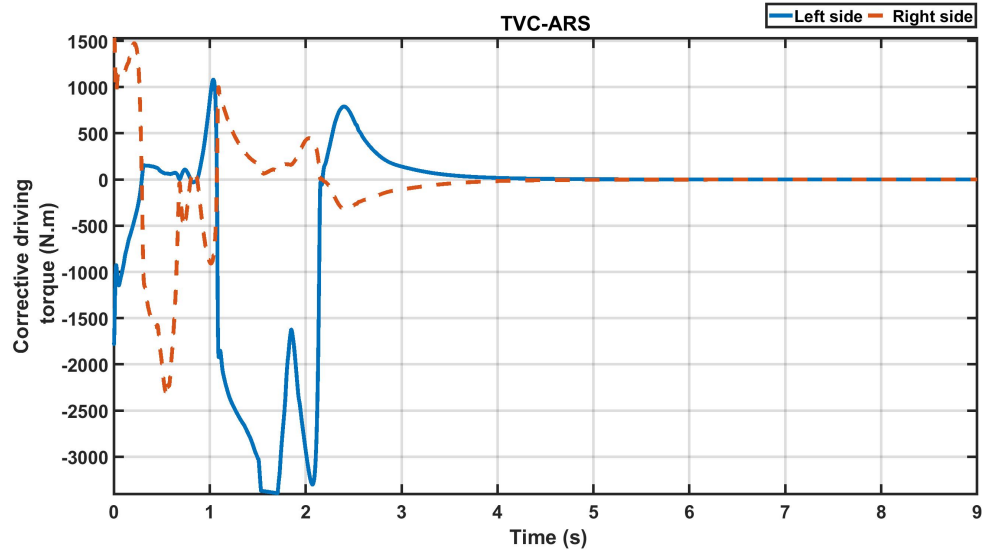


Figure 6.42: FMVSS maneuver at  $\mu=0.5$  and speed 100 km/h; Corrective driving torque of the right and left wheels' side

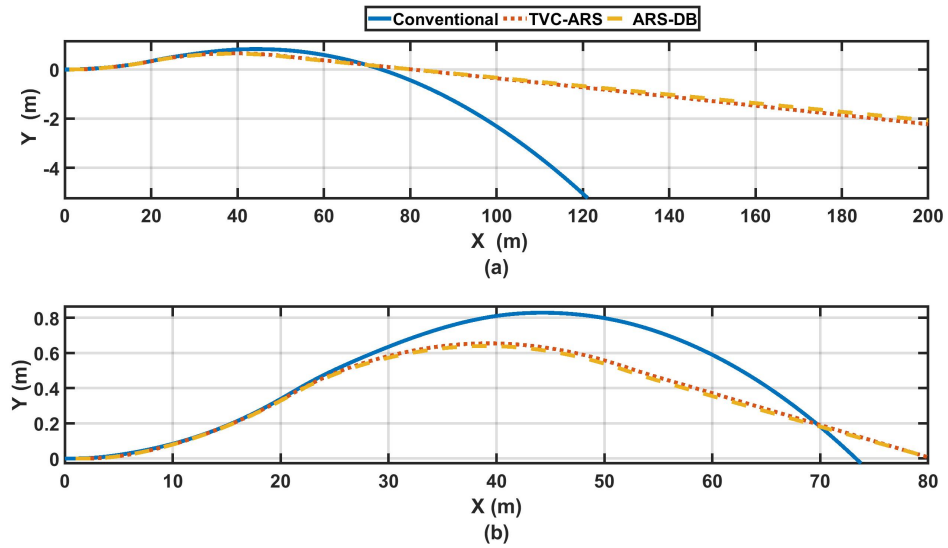


Figure 6.43: FMVSS maneuver at  $\mu=0.2$  and speed 100 km/h (a) Vehicle trajectory (b) Close up to the vehicle's lateral shift

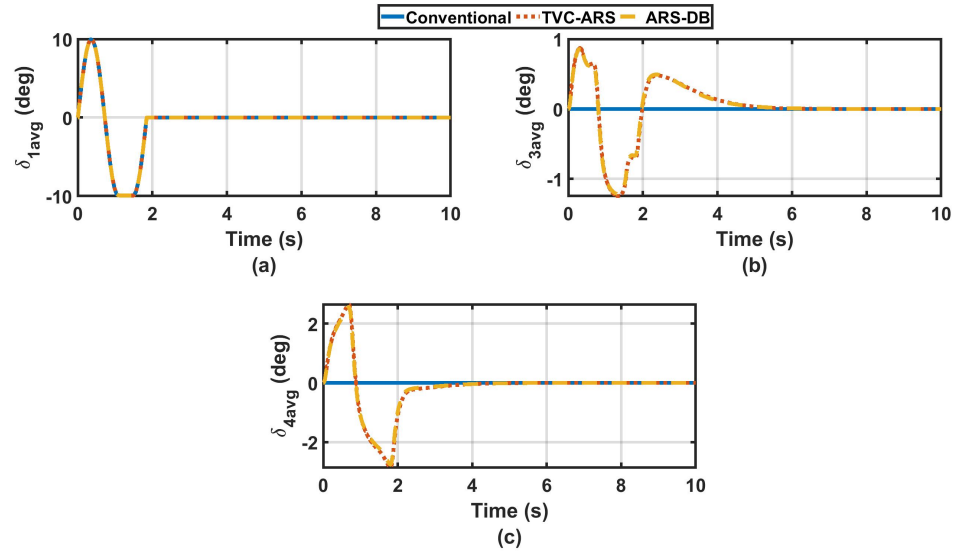


Figure 6.44: FMVSS maneuver at  $\mu=0.2$  and speed 100 km/h (a) Average Steering angle of the 1<sup>st</sup> axle (b) Average Steering angle of the 3<sup>rd</sup> axle (c) Average Steering angle of the 4<sup>th</sup> axle

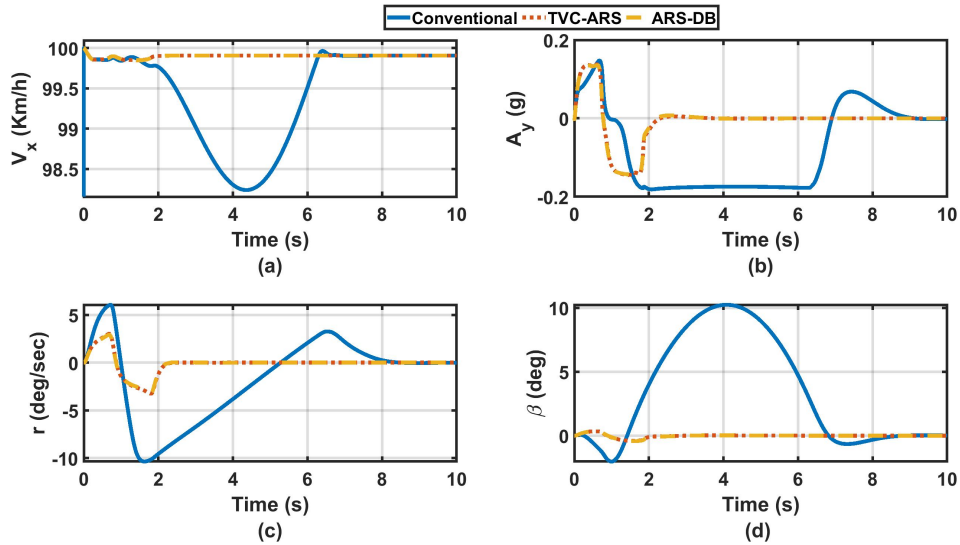


Figure 6.45: FMVSS maneuver at  $\mu=0.2$  and speed 100 km/h (a) Vehicle longitudinal speed (b) lateral acceleration (c) Yaw response (d) Vehicle sideslip response

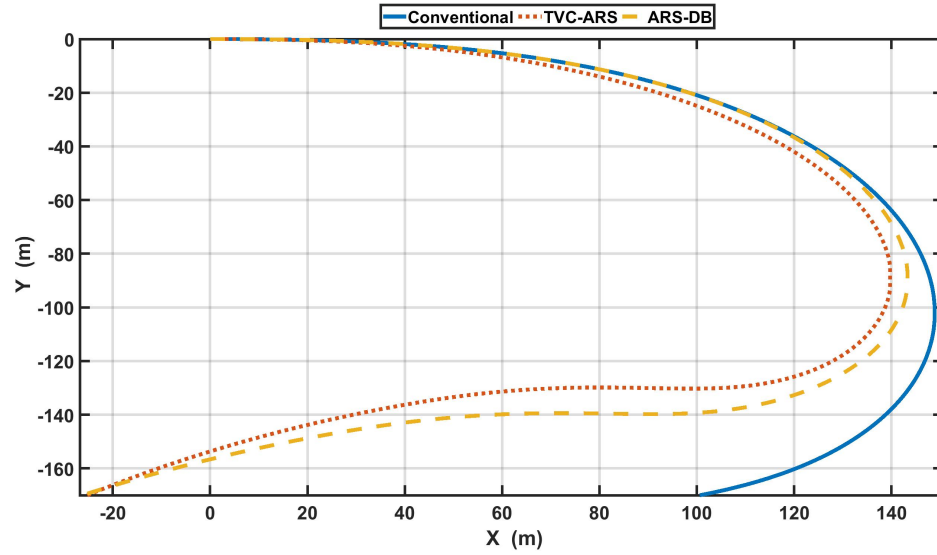


Figure 6.46: J-turn maneuver at  $\mu=0.85$  and speed 100 km/h (a) Vehicle trajectory (b) Close up to the vehicle's lateral shift

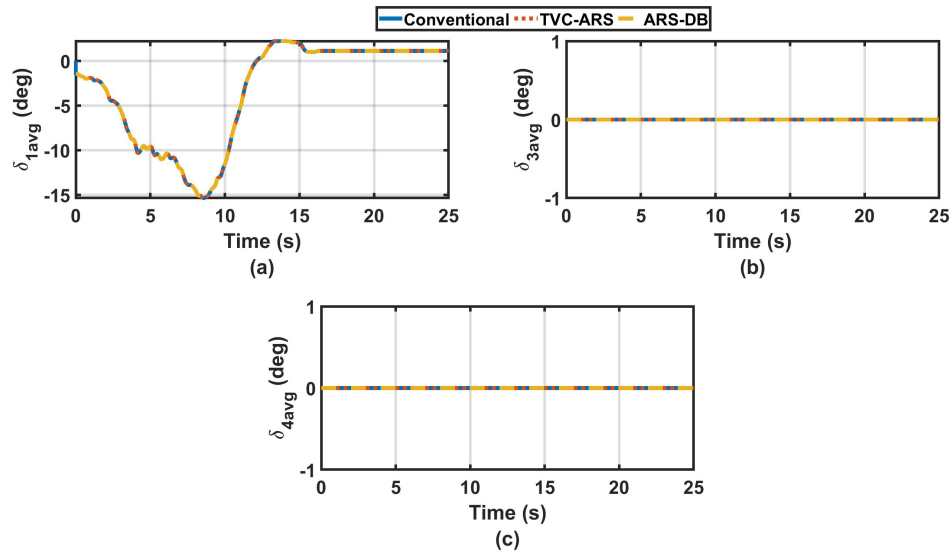


Figure 6.47: J-turn maneuver at  $\mu=0.85$  and speed 100 km/h (a) Average Steering angle of the 1<sup>st</sup> axle (b) Average Steering angle of the 3<sup>rd</sup> axle (c) Average Steering angle of the 4<sup>th</sup> axle

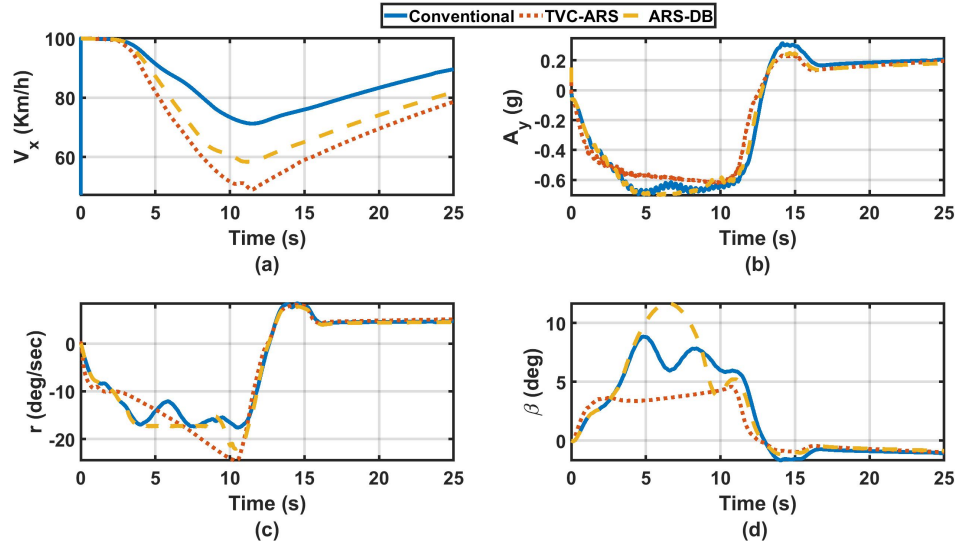


Figure 6.48: J-turn maneuver at  $\mu=0.85$  and speed 100 km/h (a) Vehicle longitudinal speed (b) lateral acceleration (c) yaw response (d) vehicle sideslip response

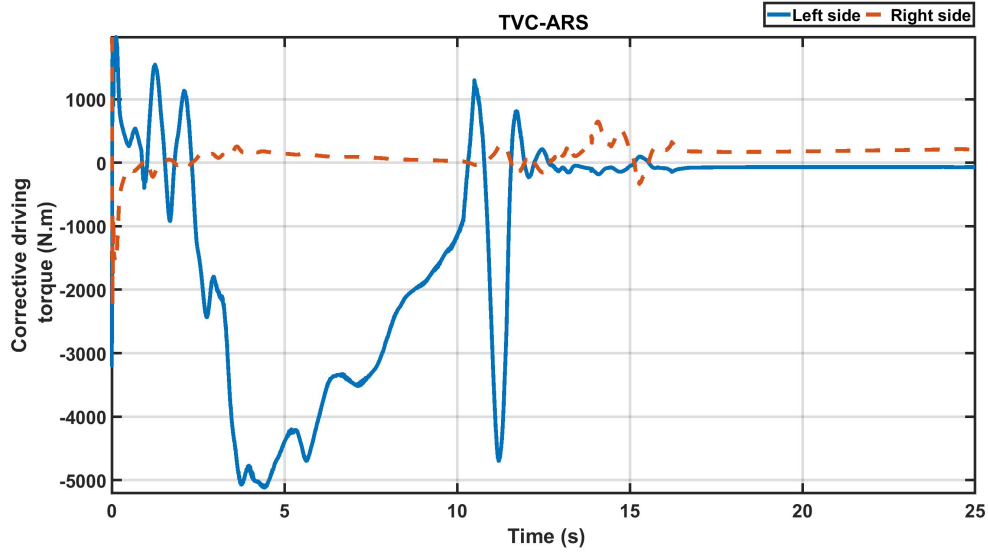


Figure 6.49: J-turn maneuver at  $\mu=0.85$  and speed 100 km/h; Corrective driving torque of the right and left wheels' side

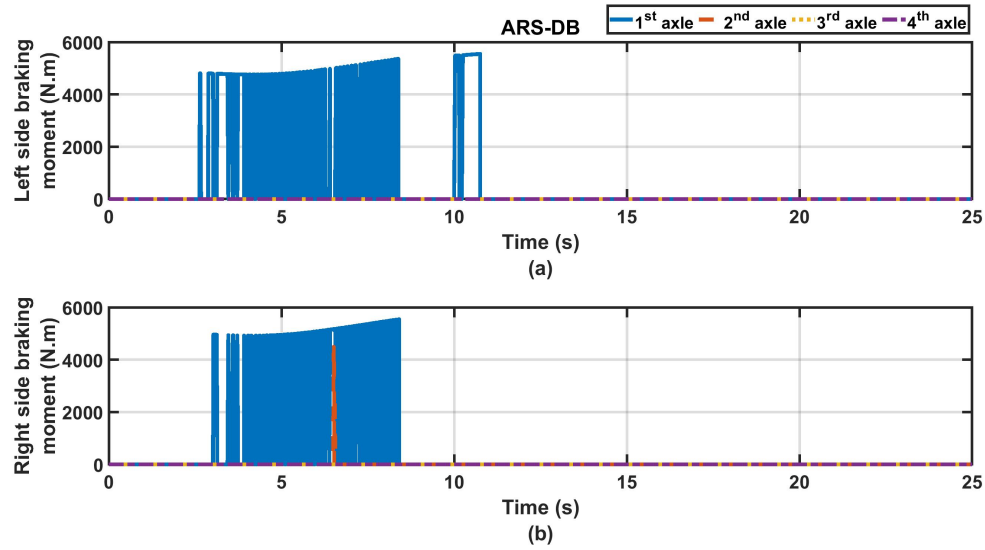


Figure 6.50: J-turn maneuver at  $\mu=0.85$  and speed 100 km/h; Braking forces at each wheel

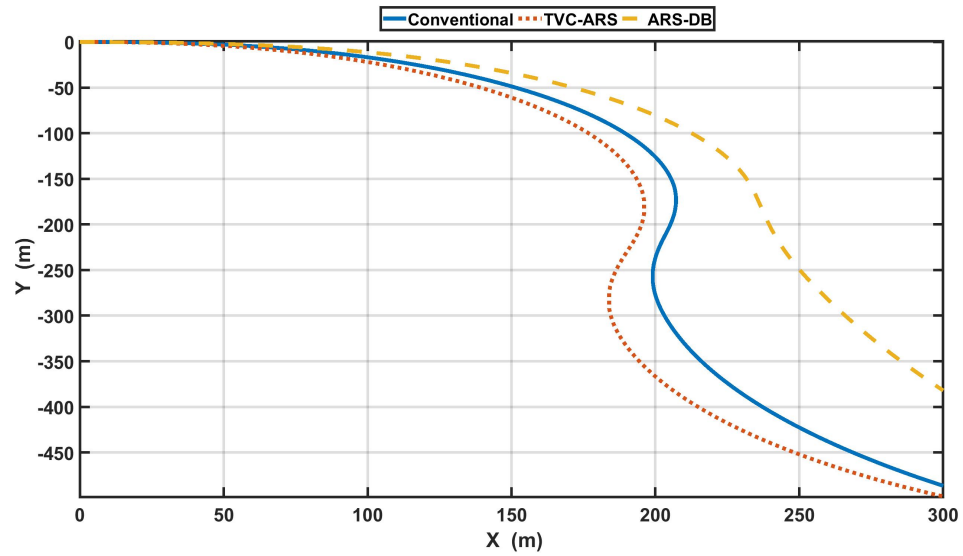


Figure 6.51: J-turn maneuver at  $\mu=0.5$  and speed 100 km/h (a) Vehicle trajectory (b) Close up to the vehicle's lateral shift

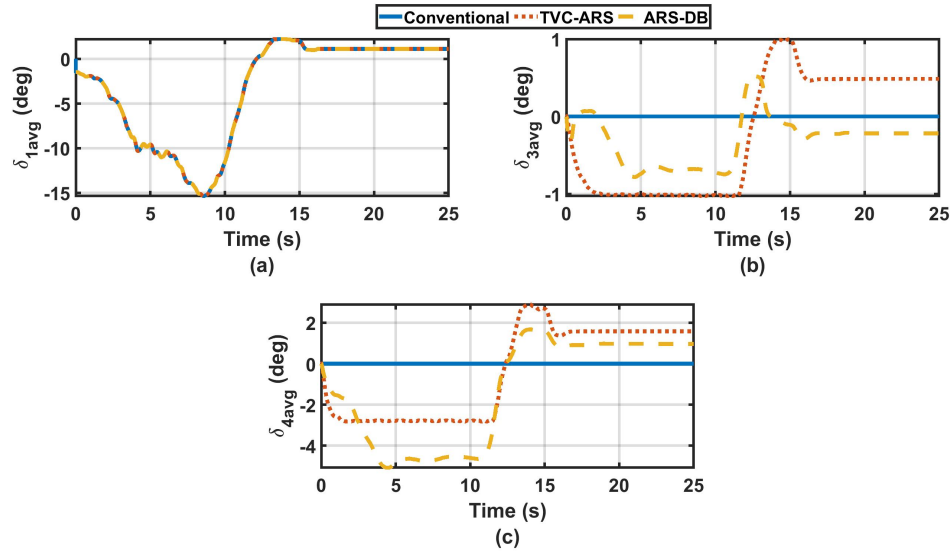


Figure 6.52: J-turn maneuver at  $\mu=0.5$  and speed 100 km/h (a) Average Steering angle of the 1<sup>st</sup> axle (b) Average Steering angle of the 3<sup>rd</sup> axle (c) Average Steering angle of the 4<sup>th</sup> axle

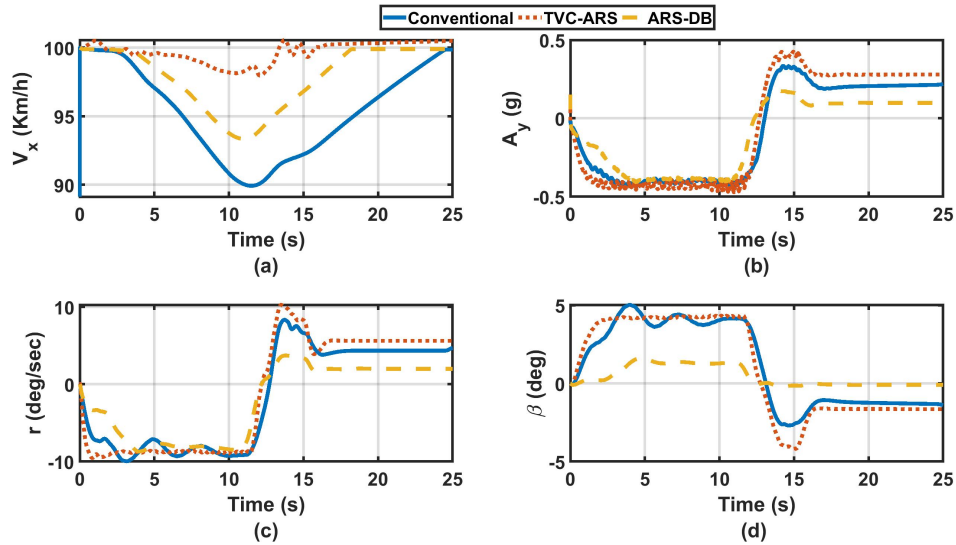


Figure 6.53: J-turn maneuver at  $\mu=0.5$  and speed 100 km/h (a) Vehicle longitudinal speed (b) lateral acceleration (c) Yaw response (d) Vehicle sideslip response



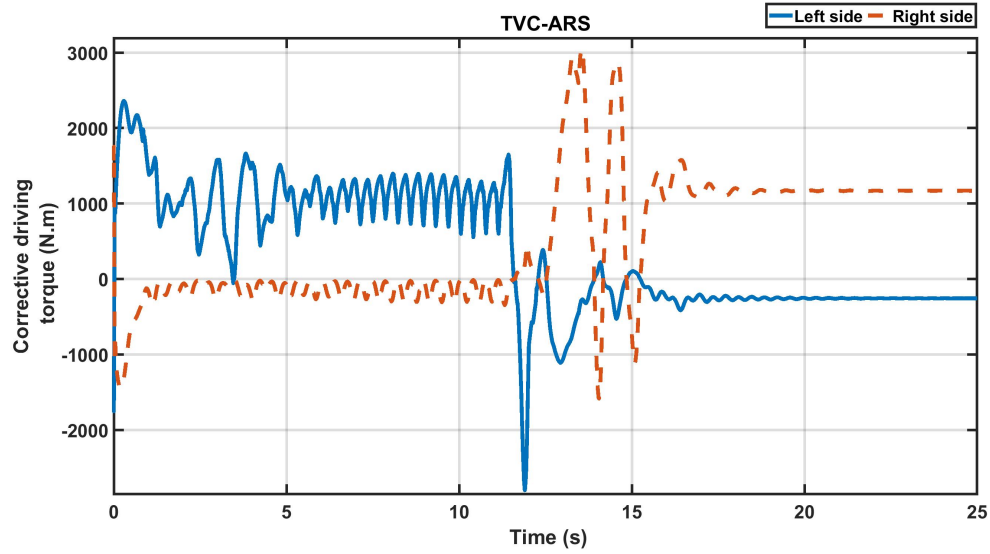


Figure 6.54: J-turn maneuver at  $\mu=0.5$  and speed 100 km/h; Corrective driving torque of the right and left wheels' side

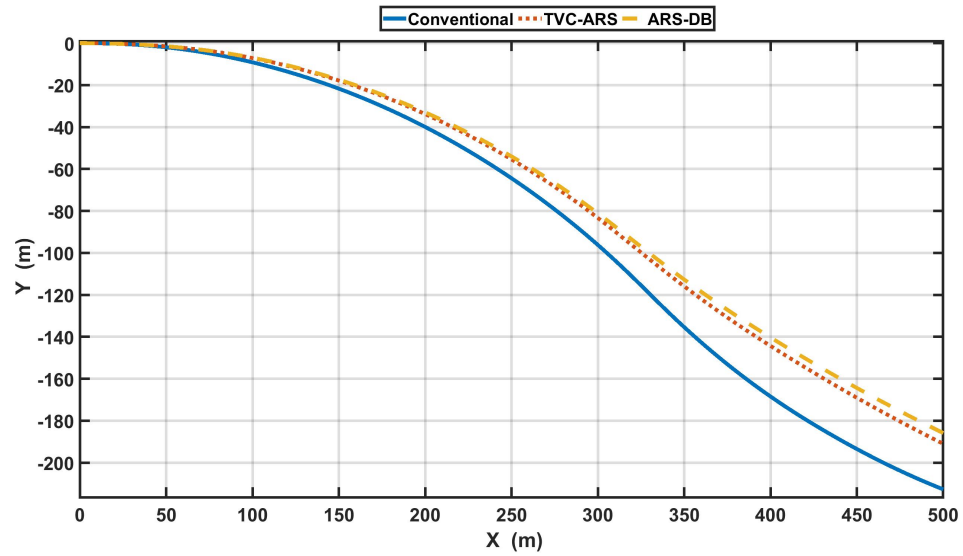


Figure 6.55: J-turn maneuver at  $\mu=0.2$  and speed 100 km/h (a) Vehicle trajectory (b) Close up to the vehicle's lateral shift

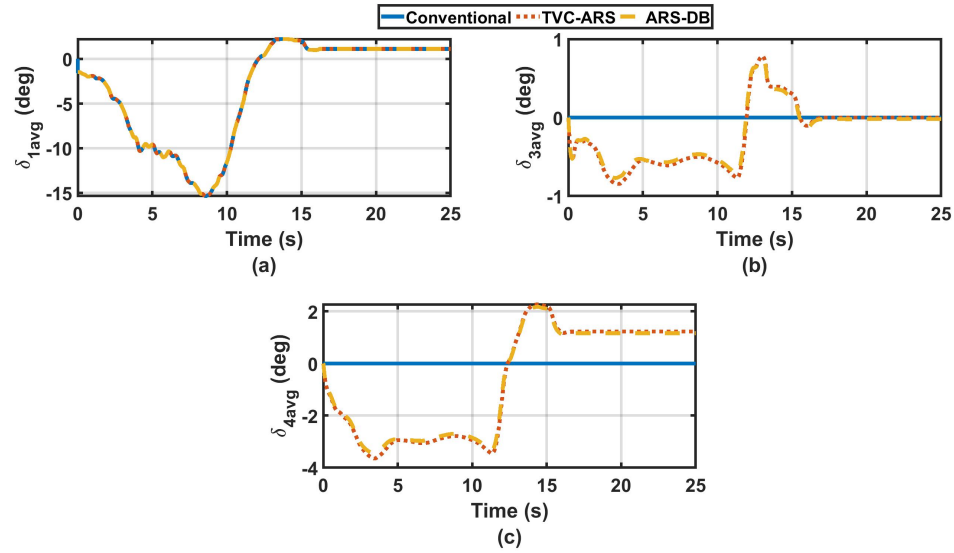


Figure 6.56: J-turn maneuver at  $\mu=0.2$  and speed 100 km/h (a) Average Steering angle of the 1<sup>st</sup> axle (b) Average Steering angle of the 3<sup>rd</sup> axle (c) Average Steering angle of the 4<sup>th</sup> axle

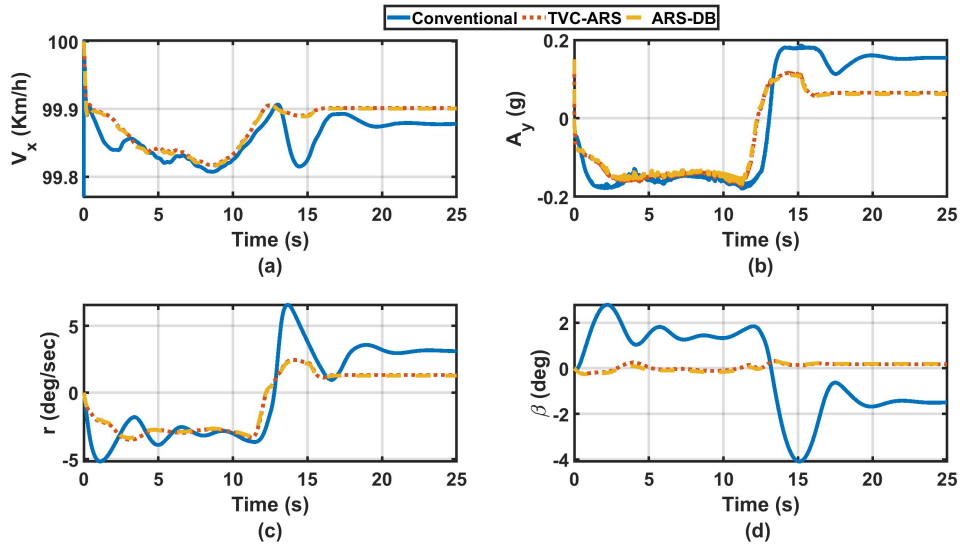


Figure 6.57: J-turn maneuver at  $\mu=0.2$  and speed 100 km/h (a) Vehicle longitudinal speed (b) lateral acceleration (c) Yaw response (d) Vehicle sideslip response

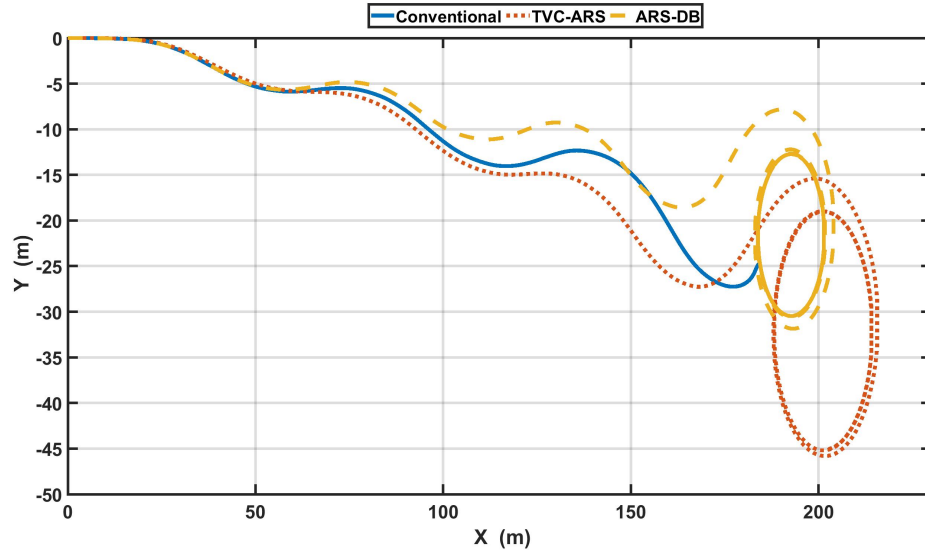


Figure 6.58: Step slalom maneuver at  $\mu=1$  and speed 65 km/h

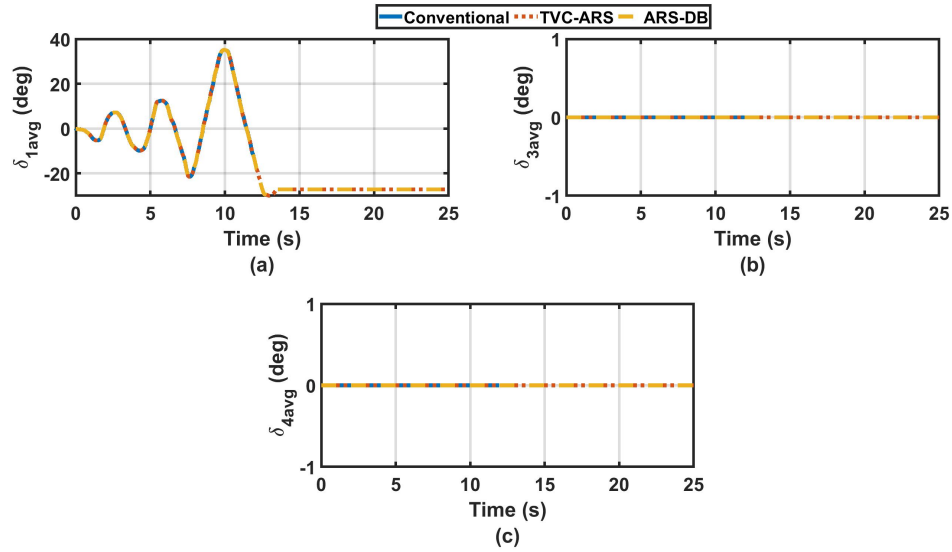


Figure 6.59: Step slalom maneuver at  $\mu=1$  and speed 65 km/h (a) Average Steering angle of the 1<sup>st</sup> axle (b) Average Steering angle of the 3<sup>rd</sup> axle (c) Average Steering angle of the 4<sup>th</sup> axle

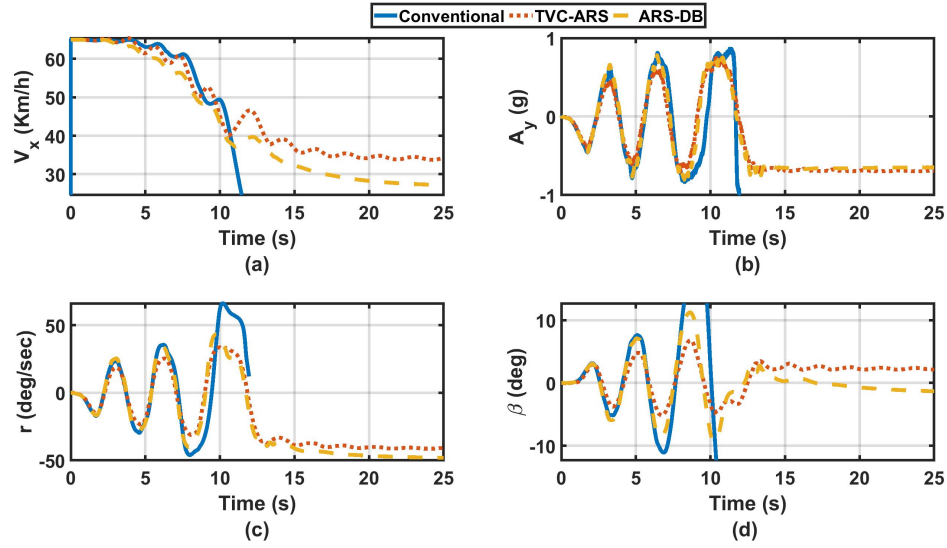


Figure 6.60: Step slalom maneuver at  $\mu=1$  and speed 65 km/h (a) Vehicle longitudinal speed (b) lateral acceleration (c) Yaw response (d) Vehicle sideslip response

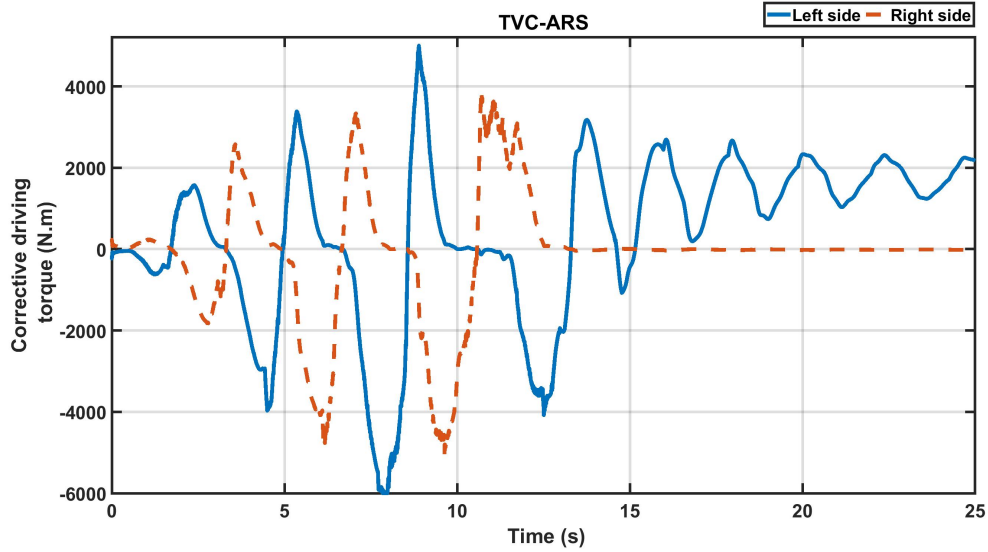


Figure 6.61: Step slalom maneuver at  $\mu=1$  and speed 65 km/h; Corrective driving torque of the right and left wheels' side

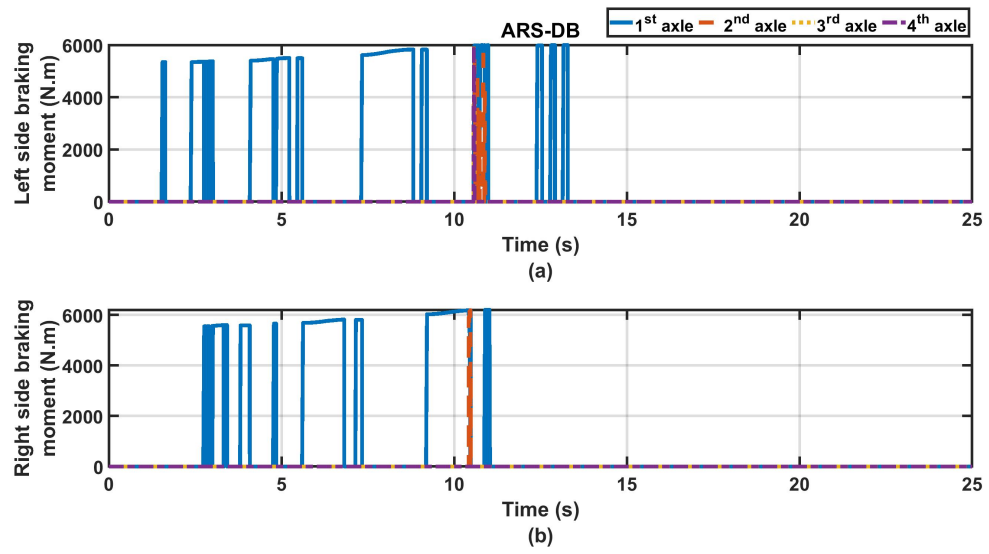


Figure 6.62: Step slalom maneuver at  $\mu=1$  and speed 65 km/h; Braking forces at each wheel

# CHAPTER 7

## Conclusions and Future Work

This chapter presents the conclusions that are arisen from this study. Then, the major contributions and recommendations for future work are introduced. Finally, the refereed journals and conferences paper are listed.

### 7.1 Conclusions

In this study, the maneuverability and lateral stability of an 8x8 combat vehicle were investigated. The maneuverability was assessed under operation with several passive steering modes at low-speed maneuvers. In addition, three different lateral stability controller strategies; Active Rear Steering (ARS), Differential Braking (DB), and Torque Vectoring Control (TVC), are introduced. The controllers showed a recognizable enhancement in the vehicle's lateral stability. Moreover, two Integrated Chassis Controllers (ICCs) using ARS-DB and TVC-ARS were presented and evaluated ant limited handling driving conditions. The important conclusions from this research study are listed below:

1. The literature review showed that there is a paucity in publications regarding:
  - (a) Investigating the vehicle's maneuverability for multiple steering configurations.
  - (b) The dependency of the lateral stability controllers on the yaw reference model and control objectives contradiction.
  - (c) Considering the lateral stability for autonomous multi-axle vehicles.
  - (d) Exploit advance machine learning techniques, especially Genetic-Programming (GP), in the lateral stability control field.
2. The maneuverability investigation of different passive steering configurations at very low speed showed that:

- (a) The highest maneuverability was obtained by counter All-Wheel Steering (AWS) configuration.
  - (b) Counter-AWS generates almost zero sideslip.
  - (c) Parallel steering is beneficial for performing a zero yaw motion, with no rear-end swing.
- 3. The utilization of the independent active steering of the 3<sup>rd</sup> and 4<sup>th</sup> axles is more effective than only actively steering the 4th axle in terms of:
  - (a) Better exploitation of the axles in decreasing the vehicle sideslip.
  - (b) High improvement in the vehicle transient response.
  - (c) Prevent the vehicle rollover and increase the vehicle stability.
- 4. The synthesized cost function to optimize the Gain-Scheduled Linear Quadratic Regulator (GSLQR) gains resulted in attaining the vehicle stability with minimum steering of the rear axles. Moreover, replacing the scheduled gains with simple GP-based equations led to a smooth transition between the control gains at various driving conditions.
- 5. The developed AISMC was effective in enhancing the vehicle stability on rough terrain and was able to compensate for the yaw disturbances.
- 6. Steering the 3<sup>rd</sup> and 4<sup>th</sup> axles effectively enhanced the path-following accuracy than conventional front-steering controller, such as:
  - (a) Tightening the design requirements to achieve better tracking performance.
  - (b) Adding constraints to the integration of the position and heading angle tracking error for better stabilization at high-speed tracking.
- 7. The integration between ARS stability controllers with the conventional front-steering improves the path-following performance during high-speed operation.
- 8. The developed activation criterion based on the phase portrait (phase-plane) analysis of the vehicle's nonlinear model was efficient in achieving less use of the braking torque and consequently enhancing the vehicle's longitudinal dynamics.
- 9. The proposed Genetic Programming (GP) technique showed more effectiveness than the Neuro-Fuzzy (NF) one in terms of:

- (a) Train the GP algorithm with a lower-dimensional dataset in comparison to Neuro-Fuzzy (NF) control method.
  - (b) The ability of the GP algorithm to interpolate and extrapolate for the provided dataset, which resulted in better performance than the NF-based controller when tested in driving conditions beyond the trained dataset.
  - (c) Resulted in developing a controller with less processing time than the NF-based one.
10. Limiting the vehicle sideslip drastically enhanced the TVC performance.
  11. The developed ICCs significantly improved the vehicle stability at severe driving conditions without contradiction between the controllers.
  12. The developed TVC-ARS controller has higher capabilities in stabilizing the vehicle at almost all the driving conditions than ARS-DB. However, the advantage of the low-cost implementation of the braking controller over TVC makes the use of ARS-DB preferable.

## 7.2 Future work and recommendations

The future work and recommendations include a list of research ideas that can maximize the vehicle's and controllers' performance:

1. Assess the vehicle maneuverability using the developed steering modes over soft-terrain.
2. Develop an active suspension system to be integrated with the developed ARS for better off-road operation.
3. Use advanced optimization techniques to reach the optimal driving and braking tire forces for torque vectoring and differential braking controllers.
4. Implement the developed steering configurations in a trajectory planning algorithm and test the tracking performance for off-road operation.
5. Use new machine learning techniques such as deep learning in the vehicle stability-related research, i.e. estimation of the road conditions and friction coefficient, which will enhance the controller performance.



6. The integration between lateral, longitudinal, and vertical dynamics controllers and deriving a 3-dimension performance map to the vehicle can lead to achieve optimal utilization of the combat vehicle in the operation field.
7. Perform a sensitivity analysis for the effect of changing the rear wheels' kinematics on the ARS controller's performance.

# LIST OF PUBLICATIONS

The publications completed during the course of PhD are listed below:

## Referred journal papers

1. **Ahmed M.**, El-Gindy, M. and Lang, H. "A novel adaptive-rear axles steering controller for an 8X8 combat vehicle." Proceedings of the Institution of Mechanical Engineers, Part C: Journal of Mechanical Engineering Science. May 2021. doi:10.1177/09544062211009926
2. **Ahmed M**, El-Gindy M, Lang H. "A novel Genetic-programming based differential braking controller for an 8x8 combat vehicle." International Journal of Dynamics and Control. 2020 Dec;8(4):1102–1116. <https://doi.org/10.1007/s40435-020-00693-0>
3. **Ahmed M**, El-Gindy M, Lang H." Path-Following Enhancement of an 8x8 Combat Vehicle Using Different Rear Axles Steering Strategies. Proceedings of the Institution of Mechanical Engineers, Part K: Journal of Multi-body Dynamics. 2021;235(4):539-552. doi:10.1177/14644193211036455
4. **Ahmed M**, El-Gindy M, Lang H. "Vehicles Directional Stability Control: Literature Survey". Int. J. Vehicle Systems Modelling and Testing, (In Press)
5. **Ahmed M**, Omar M, El-Gindy. "Investigation of Various Passive Steering Modes for a multi-wheeled Combat Vehicle". Int. J. Vehicle Systems Modelling and Testing, (In Press)

## Referred conference papers

1. **Ahmed M**, El-Gindy M, Lang H, Omar M. "Development of Active Rear Axles Steering Controller For 8X8 Combat Vehicle." SAE Technical Paper 2020-01-0174, 2020, <https://doi.org/10.4271/2020-01-0174>.
2. **Ahmed M**, El-Gindy M, Lang H. Handling performance of an 8x8 combat vehicle. In IOP Conference Series: Materials Science and Engineering 2020 Nov 1 (Vol. 973, No. 1, p. 012009). IOP Publishing.

3. **Ahmed M**, El-Gindy M, Lang H. "A Novel Coordination method for an Integrated Chassis Controller of an 8x8 Combat Vehicle." SAE Technical Paper No. 22MIL-0009, WCX SAE World Congress Experience, April 5-7, 2022, Detroit, Michigan, USA - (Submitted)

## LIST OF REFERENCES

- [1] National Highway Traffic Safety Administration et al. 2019 fatal motor vehicle crashes: overview, 2019.
- [2] Alena Høyee. The effects of electronic stability control (esc) on crashes—an update. *Accident Analysis & Prevention*, 43(3):1148–1159, 2011.
- [3] Santokh Singh. Critical reasons for crashes investigated in the national motor vehicle crash causation survey. Technical report, 2015.
- [4] Brett Russell. Development and analysis of active rear axle steering for 8x8 combat vehicle. Thesis, University of Ontario Institute of Technology, 2018.
- [5] Peter D’Urso. Development of h infinity control strategy for a multi-wheeled combat vehicle. Thesis, University of Ontario Institute of Technology, 2016.
- [6] W. J. Manning and D. A. Crolla. A review of yaw rate and sideslip controllers for passenger vehicles. *Transactions of the Institute of Measurement and Control*, 29:117–135, 2007.
- [7] Yasuji Shibahata, Kazuhiko Shimada, and Tatsuhiko Tomari. Improvement of vehicle maneuverability by direct yaw moment control. *Vehicle System Dynamics*, 22(5-6):465–481, 1993.
- [8] Yoshihiro Ikushima and Kaoru Sawase. A study on the effects of the active yaw moment control. *SAE Transactions*, 104:425–433, 1995.
- [9] Shoji Inagaki, Ikuo Kushiro, and Masaki Yamamoto. Analysis on vehicle stability in critical cornering using phase-plane method. *Jsae Review*, 2(16):216, 1995.
- [10] Ken Koibuchi, Masaki Yamamoto, Yoshiki Fukada, and Shoji Inagaki. Vehicle stability control in limit cornering by active brake. Report 0148-7191, SAE technical paper, 02 1996.
- [11] Weon-Young Youn and Jae-Bok Song. Improvement of vehicle directional stability in cornering based on yaw moment control. *KSME international journal*, 14(8):836–844, 2000.
- [12] Masato Abe, Yoshio Kano, Yasuji Shibahata, and Yoshimi Furukawa. Improve-

- ment of vehicle handling safety with vehicle side-slip control by direct yaw moment. *Vehicle System Dynamics*, 33(sup1):665–679, 1999.
- [13] Kyongsu Yi, Taeyoung Chung, Jeontae Kim, and Seungjong Yi. An investigation into differential braking strategies for vehicle stability control. *Proceedings of the Institution of Mechanical Engineers, Part D: Journal of Automobile Engineering*, 217(12):1081–1093, 2003.
  - [14] Jean-Jacques E Slotine and Weiping Li. *Applied nonlinear control*, volume 199. Prentice hall Englewood Cliffs, NJ, 1991.
  - [15] Yuri Shtessel, Christopher Edwards, Leonid Fridman, and Arie Levant. *Sliding mode control and observation*. Springer, 2014.
  - [16] Jinkun Liu and Xinhua Wang. *Advanced sliding mode control for mechanical systems*. Springer, 2012.
  - [17] S. Zhao, Y. Li, L. Zheng, and S. Lu. Vehicle lateral stability control based on sliding mode control. In *2007 IEEE International Conference on Automation and Logistics*, pages 638–642, 2007.
  - [18] Aria Noori Asiabar and Reza Kazemi. A direct yaw moment controller for a four in-wheel motor drive electric vehicle using adaptive sliding mode control. *Proceedings of the Institution of Mechanical Engineers, Part K: Journal of Multi-body Dynamics*, 233(3):549–567, 2019.
  - [19] Shou-Tao Li, Hui Liu, Di Zhao, Qiu-Yuan Li, Yan-Tao Tian, De-Jun Wang, and Ding-Li Yu. Adaptive sliding mode control of lateral stability of four wheel hub electric vehicles. *International Journal of Automotive Technology*, 21(3):739–747, 2020.
  - [20] M. T. Raharijaona, M. G. Duc, and M. S. Mammar. Linear parameter-varying control and h-infinity synthesis dedicated to lateral driving assistance. In *IEEE Intelligent Vehicles Symposium, 2004*, pages 407–412, 2004.
  - [21] M. Canale, L. Fagiano, A. Ferrara, and C. Vecchio. Comparing internal model control and sliding-mode approaches for vehicle yaw control. *IEEE Transactions on Intelligent Transportation Systems*, 10(1):31–41, 2009.
  - [22] Yonathan Weiss, Liron I Allerhand, and Shai Arogeti. Yaw stability control for

- a rear double-driven electric vehicle using lpv-h infinity methods. *Science China Information Sciences*, 61(7):70206, 2018.
- [23] Jinhua Zhang, Weichao Sun, and Zhiguang Feng. Vehicle yaw stability control via  $h_\infty$  gain scheduling. *Mechanical Systems and Signal Processing*, 106:62–75, 2018.
  - [24] Zhengyuan Wang, Umberto Montanaro, Saber Fallah, Aldo Sorniotti, and Basilio Lenzo. A gain scheduled robust linear quadratic regulator for vehicle direct yaw moment control. *Mechatronics*, 51:31–45, 2018.
  - [25] Tor A. Johansen and Thor I. Fossen. Control allocation—a survey. *Automatica*, 49(5):1087–1103, 2013.
  - [26] D. Kasinathan, A. Khajepour, S. Chen, and B. Litkouhi. Constrained holistic cornering control. In *2014 American Control Conference*, pages 3899–3904, 2014.
  - [27] D. Kasinathan, A. Kasaiezadeh, A. Wong, A. Khajepour, S. Chen, and B. Litkouhi. An optimal torque vectoring control for vehicle applications via real-time constraints. *IEEE Transactions on Vehicular Technology*, 65(6):4368–4378, 2016.
  - [28] Milad Jalali, Amir Khajepour, Shih ken Chen, and Bakhtiar Litkouhi. Integrated stability and traction control for electric vehicles using model predictive control. *Control Engineering Practice*, 54:256–266, 2016.
  - [29] Mathias Metzler, Davide Tavernini, Aldo Sorniotti, and Patrick Gruber. An explicit nonlinear mpc approach to vehicle stability control. In *Proceedings of The 14th International Symposium on Advanced Vehicle Control*, page 7. Tsinghua University, 2018.
  - [30] Wongun Kim, Kyongsu Yi, and Jongseok Lee. Drive control algorithm for an independent 8 in-wheel motor drive vehicle. *Journal of Mechanical Science and Technology*, 25(6):1573, 2011.
  - [31] Hossam Ragheb. *Torque control strategy for off-road vehicle mobility*. Thesis, 2014.
  - [32] Jun Ni and Jibin Hu. Handling performance control for hybrid 8-wheel-drive vehicle and simulation verification. *Vehicle System Dynamics*, 54(8):1098–1119,

2016.

- [33] E. Ono, S. Hosoe, H. D. Tuan, and S. doi. Robust stabilization of vehicle dynamics by active front wheel steering control. In *Proceedings of 35th IEEE Conference on Decision and Control*, volume 2, pages 1777–1782 vol.2, 1996.
- [34] Kai-Ten Feng, Han-Shue Tan, and M. Tomizuka. Automatic steering control of vehicle lateral motion with the effect of roll dynamics. In *Proceedings of the 1998 American Control Conference. ACC (IEEE Cat. No.98CH36207)*, volume 4, pages 2248–2252 vol.4, 1998.
- [35] Said Mammar and Damien Koenig. Vehicle handling improvement by active steering. *Vehicle System Dynamics*, 38(3):211–242, 2002.
- [36] WanZhong Zhao, Yi Lin, JianWei Wei, and GuoBiao Shi. Control strategy of a novel electric power steering system integrated with active front steering function. *Science China Technological Sciences*, 54(6):1515, 2011.
- [37] WanZhong Zhao, MiLi Fan, ChunYan Wang, Zhilin Jin, and Yufang Li.  $H_{\infty}$ /extension stability control of automotive active front steering system. *Mechanical Systems and Signal Processing*, 115:621–636, 2019.
- [38] Yasuji Shibahata, Namio Irie, Hideo Itoh, and Kenji Nakamura. The development of an experimental four-wheel-steering vehicle. *SAE Transactions*, 95:862–869, 1986.
- [39] Yutaka Hirano and Katsumi Fukatani. Development of robust active rear steering control for automobile. *JSME International Journal Series C*, 40(2):231–238, 1997.
- [40] Kozo Fujita, Kaoru Ohashi, Katsumi Fukatani, Syouichi Kamei, Yasuhiro Kaga, and Hideo Mori. Development of active rear steer system applying  $h_{\infty}$ - $\mu$  synthesis. *SAE Transactions*, 107:1694–1701, 1998.
- [41] M Canale and L Fagiano. Comparing rear wheel steering and rear active differential approaches to vehicle yaw control. *Vehicle System Dynamics*, 48(5):529–546, 2010.
- [42] K. Yi K. Park, E. Joa. Rear-wheel steering control for enhanced maneuverability of vehicles. 04 2019.

- [43] K Huh, J Kim, and J Hong. Handling and driving characteristics for six-wheeled vehicles. *Proceedings of the Institution of Mechanical Engineers, Part D: Journal of Automobile Engineering*, 214(2):159–170, 2000.
- [44] BC Chen, CC Yu, and WF Hsu. Steering control of six-wheeled vehicles using linear quadratic regulator techniques. *Proceedings of the Institution of Mechanical Engineers, Part D: Journal of Automobile Engineering*, 221(10):1231–1240, 2007.
- [45] Lance Bredthauer and David Lynch. Use of active rear steering to achieve desired vehicle transient lateral dynamics. Technical report, SEA Vehicle Dynamics Division, 04 2018.
- [46] Masao Nagai, Yutaka Hirano, and Sachiko Yamanaka. Integrated control of active rear wheel steering and direct yaw moment control. *Vehicle System Dynamics*, 27(5-6):357–370, 1997.
- [47] Masao Nagai, Yutaka Hirano, and Sachiko Yamanaka. *Vehicle System Dynamics*, 29(sup1):416–421, 1998.
- [48] D. Selmanaj, M. Corno, O. Senname, and S. Savaresi. Advantages of rear steer in lti and lpv vehicle stability control. In *52nd IEEE Conference on Decision and Control*, pages 3523–3528, 2013.
- [49] R. Wang, H. Zhang, and J. Wang. Linear parameter-varying controller design for four-wheel independently actuated electric ground vehicles with active steering systems. *IEEE Transactions on Control Systems Technology*, 22(4):1281–1296, 2014.
- [50] H. Zhang and J. Wang. Vehicle lateral dynamics control through afs/dyc and robust gain-scheduling approach. *IEEE Transactions on Vehicular Technology*, 65(1):489–494, 2016.
- [51] Hui Zhang and Junmin Wang. Chapter 10 - robust gain-scheduling control of vehicle lateral dynamics through afs/dyc. In Hui Zhang, Dongpu Cao, and Haiping Du, editors, *Modeling, Dynamics and Control of Electrified Vehicles*, pages 339–368. Woodhead Publishing, 2018.
- [52] Hui Jing, Rongrong Wang, Junmin Wang, and Nan Chen. Robust  $h_\infty$  dy-



- namic output-feedback control for four-wheel independently actuated electric ground vehicles through integrated afs/dyc. *Journal of the Franklin Institute*, 355(18):9321–9350, 2018. Special Issue on Control and Signal Processing in Mechatronic Systems.
- [53] W. Zhao, X. Qin, and C. Wang. Yaw and lateral stability control for four-wheel steer-by-wire system. *IEEE/ASME Transactions on Mechatronics*, 23(6):2628–2637, 2018.
  - [54] Abbas Chokor, Reine Talj, Moustapha Doumiati, Ali Hamdan, and Ali Charara. A comparison between a centralised multilayer l<sub>pv</sub>/ $h_{\infty}$  and a decentralised multilayer sliding mode control architectures for vehicle’s global chassis control. *International Journal of Control*, 0(0):1–16, 2020.
  - [55] S. Cheng, L. Li, C. Liu, X. Wu, S. Fang, and J. Yong. Robust lmi-based h-infinite controller integrating afs and dyc of autonomous vehicles with parametric uncertainties. *IEEE Transactions on Systems, Man, and Cybernetics: Systems*, pages 1–10, 2020.
  - [56] Ossama Mokhiamar and Masato Abe. Simultaneous optimal distribution of lateral and longitudinal tire forces for the model following control. *J. Dyn. Sys., Meas., Control*, 126(4):753–763, 2004.
  - [57] Junmin Wang and Raul G Longoria. Coordinated and reconfigurable vehicle dynamics control. *IEEE Transactions on Control Systems Technology*, 17(3):723–732, 2009.
  - [58] Johannes Tjonnas and Tor A Johansen. Stabilization of automotive vehicles using active steering and adaptive brake control allocation. *IEEE Transactions on Control Systems Technology*, 18(3):545–558, 2009.
  - [59] Qinghua Meng, Tingting Zhao, Chunjiang Qian, Zong-yao Sun, and Panpan Ge. Integrated stability control of afs and dyc for electric vehicle based on non-smooth control. *International Journal of Systems Science*, 49(7):1518–1528, 2018.
  - [60] Jaewon Nah and Seongjin Yim. Optimization of control allocation with esc, afs, ars and tvd in integrated chassis control. *Journal of Mechanical Science and Technology*, pages 2941–2948, 2019.

- [61] J. Feng, S. Chen, and Z. Qi. Coordinated chassis control of 4wd vehicles utilizing differential braking, traction distribution and active front steering. *IEEE Access*, 8:81055–81068, 2020.
- [62] Milad Jalali, Saeid Khosravani, Amir Khajepour, Shih-ken Chen, and Bakhtiar Litkouhi. Model predictive control of vehicle stability using coordinated active steering and differential brakes. *Mechatronics*, 48:30–41, 2017.
- [63] Hossein Mirzaeinejad, Mehdi Mirzaei, and Sadra Rafatnia. A novel technique for optimal integration of active steering and differential braking with estimation to improve vehicle directional stability. *ISA Transactions*, 80:513–527, 2018.
- [64] Mansour Ataei, Amir Khajepour, and Soo Jeon. Model predictive control for integrated lateral stability, traction/braking control, and rollover prevention of electric vehicles. *Vehicle System Dynamics*, 58(1):49–73, 2020.
- [65] Hamid Taghavifar, Chuan Hu, Leyla Taghavifar, Yechen Qin, Jing Na, and Chongfeng Wei. Optimal robust control of vehicle lateral stability using damped least-square backpropagation training of neural networks. *Neurocomputing*, 384:256–267, 2020.
- [66] Jiaxu Zhang, Shiyong Zhou, Fengjun Li, and Jian Zhao. Integrated nonlinear robust adaptive control for active front steering and direct yaw moment control systems with uncertainty observer. *Transactions of the Institute of Measurement and Control*, 42(16):3267–3280, 2020.
- [67] Yuji Yokoya, Ryohei Kizu, Hiroshi Kawaguchi, Kaoru Ohashi, and Hiroyuki Ohno. Integrated control system between active control suspension and four wheel steering for the 1989 celica. Technical report, 09 1990.
- [68] Hiroshi Kawakami, Hiroki Sato, Masaaki Tabata, Hideo Inoue, and Hidenori Itimaru. Development of integrated system between active control suspension, active 4ws, trc and abs. Technical report, 02 1992.
- [69] Junjie He, David A Crolla, MC Levesley, and WJ Manning. Coordination of active steering, driveline, and braking for integrated vehicle dynamics control. *Proceedings of the Institution of Mechanical Engineers, Part D: Journal of Automobile Engineering*, 220(10):1401–1420, 2006.

- [70] Hussein Termous, Hassan Shraim, Reine Talj, Clovis Francis, and Ali Charara. Coordinated control strategies for active steering, differential braking and active suspension for vehicle stability, handling and safety improvement. *Vehicle System Dynamics*, 57(10):1494–1529, 2019.
- [71] Z. Yu, Y. Hou, B. Leng, L. Xiong, and Y. Li. Disturbance compensation and torque coordinated control of four in-wheel motor independent-drive electric vehicles. *IEEE Access*, 8:119758–119767, 2020.
- [72] Jeonghoon Song. Design and comparison of afs controllers with pid, fuzzy-logic, and sliding-mode controllers. *Advances in Mechanical Engineering*, 5:401548, 2013.
- [73] Jeonghoon Song. Development and comparison of integrated dynamics control systems with fuzzy logic control and sliding mode control. *Journal of Mechanical science and Technology*, 27(6):1853–1861, 2013.
- [74] Jeonghoon Song. Integrated vehicle dynamic controls using active rear wheel steering and four wheel braking. *International Journal of Vehicle Systems Modelling and Testing*, 13(1):26–43, 2018.
- [75] Shahab Rahimi and Mahyar Naraghi. Design of an integrated control system to enhance vehicle roll and lateral dynamics. *Transactions of the Institute of Measurement and Control*, 40(5):1435–1446, 2018.
- [76] Xu Zhang, Chuanxue Song, Shixin Song, Jingwei Cao, Silun Peng, Chunyang Qi, Feng Xiao, and Da Wang. Stability control for vehicle dynamic management with multi-objective fuzzy continuous damping control. *Applied Sciences*, 10(21), 2020.
- [77] Xiujuan Yang, Zengcai Wang, and Weili Peng. Coordinated control of afs and dyc for vehicle handling and stability based on optimal guaranteed cost theory. *Vehicle System Dynamics*, 47(1):57–79, 2009.
- [78] Arash Hosseinian Ahangarnejad, Stefano Melzi, and Mehdi Ahmadian. Integrated vehicle dynamics system through coordinating active aerodynamics control, active rear steering, torque vectoring and hydraulically interconnected suspension. *International Journal of Automotive Technology*, 20(5):903–915, 2019.

- [79] W Kim, K Yi, and J Lee. An optimal traction, braking, and steering coordination strategy for stability and manoeuvrability of a six-wheel drive and six-wheel steer vehicle. *Proceedings of the Institution of Mechanical Engineers, Part D: Journal of Automobile Engineering*, 226(1):3–22, 2012.
- [80] Wei Liu, Hongwen He, Fengchun Sun, and Jiangyi Lv. Integrated chassis control for a three-axle electric bus with distributed driving motors and active rear steering system. *Vehicle System Dynamics*, 55(5):601–625, 2017.
- [81] J. Guldner, V. I. Utkin, and J. Ackermann. A sliding mode control approach to automatic car steering. In *Proceedings of 1994 American Control Conference - ACC '94*, volume 2, pages 1969–1973 vol.2, 1994.
- [82] E. H. M. Lim and J. K. Hedrick. Lateral and longitudinal vehicle control coupling for automated vehicle operation. In *Proceedings of the 1999 American Control Conference (Cat. No. 99CH36251)*, volume 5, pages 3676–3680 vol.5, 1999.
- [83] G. Tagne, R. Talj, and A. Charara. Higher-order sliding mode control for lateral dynamics of autonomous vehicles, with experimental validation. In *2013 IEEE Intelligent Vehicles Symposium (IV)*, pages 678–683, 2013.
- [84] H. Wang, Y. Huang, A. Khajepour, Y. Zhang, Y. Rasekhipour, and D. Cao. Crash mitigation in motion planning for autonomous vehicles. *IEEE Transactions on Intelligent Transportation Systems*, 20(9):3313–3323, 2019.
- [85] R. Wang, C. Hu, F. Yan, and M. Chadli. Composite nonlinear feedback control for path following of four-wheel independently actuated autonomous ground vehicles. *IEEE Transactions on Intelligent Transportation Systems*, 17(7):2063–2074, 2016.
- [86] Chuan Hu. *ROBUST PATH FOLLOWING CONTROL FOR INDEPENDENTLY ACTUATED AUTONOMOUS GROUND VEHICLES WITH TRANSIENT PERFORMANCE IMPROVEMENT*. Thesis, 2017.
- [87] Jun Liu, Liang Gao, Junjie Zhang, and Feng Yan. Super-twisting algorithm second-order sliding mode control for collision avoidance system based on active front steering and direct yaw moment control. *Proceedings of the Institution of Mechanical Engineers, Part D: Journal of Automobile Engineering*, 235(1):43–54, 2021.

- [88] P. Wang, S. Gao, L. Li, S. Cheng, and L. Zhao. Automatic steering control strategy for unmanned vehicles based on robust backstepping sliding mode control theory. *IEEE Access*, 7:64984–64992, 2019.
- [89] Armin Norouzi, Milad Masoumi, Ali Barari, and Saina Farrokhpour Sani. Lateral control of an autonomous vehicle using integrated backstepping and sliding mode controller. *Proceedings of the Institution of Mechanical Engineers, Part K: Journal of Multi-body Dynamics*, 233(1):141–151, 2019.
- [90] G. V. Raffo, G. K. Gomes, J. E. Normey-Rico, C. R. Kelber, and L. B. Becker. A predictive controller for autonomous vehicle path tracking. *IEEE Transactions on Intelligent Transportation Systems*, 10(1):92–102, 2009.
- [91] Taehyun Shim, Ganesh Adireddy, and Hongliang Yuan. Autonomous vehicle collision avoidance system using path planning and model-predictive-control-based active front steering and wheel torque control. *Proceedings of the Institution of Mechanical Engineers, Part D: Journal of automobile engineering*, 226(6):767–778, 2012.
- [92] Qingjia Cui, Rongjun Ding, Bing Zhou, and Xiaojian Wu. Path-tracking of an autonomous vehicle via model predictive control and nonlinear filtering. *Proceedings of the Institution of Mechanical Engineers, Part D: Journal of Automobile Engineering*, 232(9):1237–1252, 2018.
- [93] Chuanyang Sun, Xin Zhang, Lihe Xi, and Ying Tian. Design of a path-tracking steering controller for autonomous vehicles. *Energies*, 11(6), 2018.
- [94] Junho Lee and Hyuk-Jun Chang. Analysis of explicit model predictive control for path-following control. *PloS one*, 13(3):19, 2018.
- [95] Hong Wang, Yanjun Huang, Amir Khajepour, Yadollah Rasekhipour, Yubiao Zhang, and Dongpu Cao. Crash mitigation in motion planning for autonomous vehicles. *IEEE Transactions on Intelligent Transportation Systems*, 2019.
- [96] Lu Yang, Ming Yue, and Teng Ma. Path following predictive control for autonomous vehicles subject to uncertain tire-ground adhesion and varied road curvature. *International Journal of Control, Automation and Systems*, 17(1):193–202, 2019.

- [97] ERIK Wachter. *Lateral Path Tracking in Limit Handling Condition using SDRE Control*. Thesis, 2016.
- [98] ChunYan Wnag, WanZhong Zhao, ZhiJiang Xu, and Guan Zhou. Path planning and stability control of collision avoidance system based on active front steering. *Science China Technological Sciences*, 60(8):1231–1243, 2017.
- [99] Pengpeng Feng, Jianwu Zhang, and Weimiao Yang. Observer-based state-feedback robust control for path following of autonomous ground vehicles. *Proceedings of the Institution of Mechanical Engineers, Part I: Journal of Systems and Control Engineering*, 234(2):222–239, 2020.
- [100] J. Ni, J. Hu, and C. Xiang. Robust path following control at driving/handling limits of an autonomous electric racecar. *IEEE Transactions on Vehicular Technology*, 68(6):5518–5526, 2019.
- [101] Y. Chen, S. Chen, H. Ren, Z. Gao, and Z. Liu. Path tracking and handling stability control strategy with collision avoidance for the autonomous vehicle under extreme conditions. *IEEE Transactions on Vehicular Technology*, 69(12):14602–14617, 2020.
- [102] Matthew J Hillegass, James G Faller, Mark S Bounds, Moustafa El-Gindy, and Abhishek S Joshi. Validating the directional performance of multi-wheeled combat vehicle computer simulation models. In *ASME 2004 International Mechanical Engineering Congress and Exposition*, number IMECE2004-60168, pages 781–789. American Society of Mechanical Engineers Digital Collection, 2004.
- [103] Matthew J Hillegass, James G Faller, Mark S Bounds, Moustafa El-Gindy, and Seokyong Chae. Validating the vertical dynamic performance of a multi-wheeled combat vehicle computer simulation model. In *ASME 2005 International Mechanical Engineering Congress and Exposition*, number IMECE2005-79170, pages 31–40. American Society of Mechanical Engineers Digital Collection, 2005.
- [104] Arnold Odrigo. Development of multi-wheel drivetrain control system for future electric combat vehicle. Thesis, University of Ontario Institute of Technology, 2017.
- [105] Amr Mohamed. *Design and Development of Advanced Control Techniques for*

- an Unmanned Ground Vehicle*. Thesis, University of Ontario Institute of Technology, 2018.
- [106] Carl-Johann Van Eeden et al. *The steering relationship between the first and second axles of a 6x6 off-road military vehicle*. Doctoral dissertation, 2007.
  - [107] Weimiao Yang, Pengpeng Feng, and Jianwu Zhang. A comprehensive active-steering control method for improvement of vehicle handling performance. *Proceedings of the Institution of Mechanical Engineers, Part K: Journal of Multi-body Dynamics*, 232(3):413–425, 2018.
  - [108] Y. Zhang, J. Ni, and J. Hu. A robust yaw moment controller design for autonomous ground vehicle aiming to changing directions with high mobility. In *2018 Chinese Control And Decision Conference (CCDC)*, pages 6392–6396, 2018.
  - [109] Daniel Eugene Williams. Generalised multi-axle vehicle handling. *Vehicle System Dynamics*, 50(1):149–166, 2012.
  - [110] Stanley M Shinnars. *Modern control system theory and design*. John Wiley & Sons, 1998.
  - [111] Sandro Bruno Duarte Alves. *Helicopter flight modeling and robust autonomous control with uncertain dynamics*. PhD thesis, Universidade da Beira Interior, 2012.
  - [112] Richard M Murray. Optimization-based control. *California Institute of Technology, CA*, pages 111–128, 2009.
  - [113] A. Kalbat. Linear quadratic gaussian (lqg) control of wind turbines. In *2013 3rd International Conference on Electric Power and Energy Conversion Systems*, pages 1–5, 2013.
  - [114] Ian R Manchester. Amme4500: Guidance, navigation, and control course notes university of sydney. Technical report, Technical report, University of Sydney, 2013.
  - [115] Joao P Hespanha. *Linear systems theory*. Princeton university press, 2018.
  - [116] Rajesh Rajamani. *Vehicle dynamics and control*. Springer Science & Business Media, 2011.

- [117] Alrik L Svenson and Aleksander Hac. Influence of chassis control systems on vehicle handling and rollover stability. *Enhanced safety of vehicles, NHTSA*, (05-0324):4, 2005.
- [118] DA Panke, NH Ambhore, and RN Marathe. Review on handling characteristics of road vehicles. *Journal of Engineering Research and Applications (Int J Eng Res Appl)*, 4(7):178–182, 2014.
- [119] National Highway Traffic Safety Administration. Fmvss no. 126: Electronic stability control systems. *Final Regulatory Impact Analysis*. March, 2007.
- [120] Irene Sardellitti, Gustavo A Medrano-Cerda, N Tsagarakis, Amir Jafari, and Darwin G Caldwell. Gain scheduling control for a class of variable stiffness actuators based on lever mechanisms. *IEEE Transactions on Robotics*, 29(3):791–798, 2013.
- [121] El-Ghazali Talbi and El-Ghazali. *Metaheuristics: From Design to Implementation*, volume 74. John Wiley & Sons, 06 2009.
- [122] Ali Zilouchian and Mohammad Jamshidi. *Intelligent Control Systems Using Soft Computing Methodologies*. CRC Press, Inc., USA, 1st edition, 2000.
- [123] R. C. Rafaila and G. Livint. H-infinity control of automatic vehicle steering. In *2016 International Conference and Exposition on Electrical and Power Engineering (EPE)*, pages 031–036. IEEE, 2016.
- [124] Da-Wei Gu, Petko Petkov, and Mihail M Konstantinov. *Robust control design with MATLAB®*. Springer Science & Business Media, 2013.
- [125] J He. Integrated vehicle dynamics control using active steering, driveline and braking. 2005.
- [126] Robert Fullér. *Introduction to neuro-fuzzy systems*, volume 2. Springer Science & Business Media, 2000.
- [127] Fakhreddine Karray, Fakhreddine O Karray, and Clarence W De Silva. *Soft computing and intelligent systems design: theory, tools, and applications*. Pearson Education, 2004.
- [128] G. S. Sandhu and K. S. Rattan. Design of a neuro-fuzzy controller. In *1997 IEEE International Conference on Systems, Man, and Cybernetics. Computational Cy-*



*bernetics and Simulation*, volume 4, pages 3170–3175. IEEE, 1997.

- [129] Olaf Wolkenhauer and John M Edmunds. A fuzzy systems toolbox for use with matlab. In *IEE Colloquium on Fuzzy Logic Controllers in Practice*, number 5485336, pages 9/1–9/4. IET, 1996.
- [130] Jo Yung Wong. *Theory of ground vehicles*. John Wiley & Sons, 2008.
- [131] L. A. Zadeh. Outline of a new approach to the analysis of complex systems and decision processes. *IEEE Transactions on Systems, Man, and Cybernetics*, SMC-3(1):28–44, 1973.